SANDIA REPORT
SAND2021-11193
Printed September 2021

Sandia National Laboratories

ASC P&EM FY21 L2 Milestone 7836: Constitutive Model Development for Aging Polymer Encapsulants

Kenneth N. Cundiff, Kevin N. Long, Jamie M. Kropka, Shianne Carroll, and Catherine Groves

Prepared by
Sandia National Laboratories
Albuquerque, New Mexico 87185
Livermore, California 94550

Issued by Sandia National Laboratories, operated for the United States Department of Energy by National Technology & Engineering Solutions of Sandia, LLC.

Available to DOE and DOE contractors from

U.S. Department of Energy
Office of Scientific and Technical Information
P.O. Box 62
Oak Ridge, TN 37831

Telephone: (865) 576-8401
Facsimile: (865) 576-5728
E-Mail: reports@osti.gov
Online ordering: http://www.osti.gov/scitech

Available to the public from

U.S. Department of Commerce
National Technical Information Service
5301 Shawnee Road
Alexandria, VA 22312

Telephone: (800) 553-6847
Facsimile: (703) 605-6900
E-Mail: orders@ntis.gov
Online order: https://classic.ntis.gov/help/order-methods

ABSTRACT

This SAND report fulfills the completion requirements for the ASC Physics and Engineering Modeling Level 2 Milestone 7836 during Fiscal Year 2021.

The Sandia Simplified potential energy clock (SPEC) non-linear viscoelastic constitutive model was developed to predict a whole host of polymer glass physical behaviors in order to provide a tool to assess the effects of stress on these materials over their lifecycle. Polymer glasses are used extensively in applications such as electronics packaging, where encapsulants and adhesives can be critical to device performance. In this work, the focus is on assessing the performance of the model in predicting material evolution associated with long-term physical aging, an area that the model has not been fully vetted in. These predictions are key to utilizing models to help demonstrate electronics packaging component reliability over decades long service lives, a task that is very costly and time consuming to execute experimentally. The initiating hypothesis for the work was that a model calibration process can be defined that enables confidence in physical aging predictions under ND relevant environments and timescales without sacrificing other predictive capabilities.

To test the hypothesis, an extensive suite of calibration and aging data was assembled from a combination of prior work and collaborating projects (Aging and Lifetimes as well as the DoD Joint Munitions Program) for two mission relevant epoxy encapsulants, 828DGEBA/DEA and 828DGEBA/T403. Multiple model calibration processes were developed and evaluated against the entire set of data for each material. A qualitative assessment of each calibration's ability to predict the wide range of aging responses was key to ranking the calibrations against each other. During this evaluation, predictions that were identified as non-physical, i.e., demonstrated something that was qualitatively different than known material behavior, were heavily weighted against the calibration performance. Thus, unphysical predictions for one aspect of aging response could generate a lower overall rating for a calibration process even if that process generated better quantitative predictions for another aspect of aging response. This insurance that all predictions are qualitatively correct is important to the overall aim of utilizing the model to predict residual stress evolution, which will depend on the interplay amongst the different material aging responses. The DSC-focused calibration procedure generated the best all-around aging predictions for both materials, demonstrating material models that can qualitatively predict the whole host of different physical aging responses that have been measured. This step forward in predictive capability comes from an unanticipated source, utilization of calorimetry measurements to specify model parameters. The DSC-focused calibration technique performed better than compression-focused techniques that more heavily weigh measurements more closely related to the structural responses to be predicted. Indeed, the DSC-focused calibration procedure was only possible due to recent incorporation of the enthalpy and heat capacity features into SPEC that was newly verified during this L2 milestone.

Fundamentally similar aspects of the two material model calibrations as well as parametric studies to assess sensitives of the aging predictions are discussed within the report. A perspective on the next steps to the overall goal of residual stress evolution predictions under stockpile conditions closes the report.

ACKNOWLEDGMENT

The authors would like to thank the Milestone Review Committee: Nicholas Wyatt (PI), Coby Davis, Brenton Elisberg, Jason Dugger, and Mike Neilsen for providing feedback, guidance, and discussion at the four project review meetings. Guidance and support on uncertainty quantification calculations from Alyssa Skulborstad and support in deriving and understanding the heat capacity behavior in the SPEC model from Brandon Talamini were both important to the milestone success. The authors would also like to thank program support from Aging and Lifetime as well as the Joint Munitions Program which enabled a new and clean set of calibration data to be produced in conjunction with this milestone. We also thank the ASC P&EM program for the opportunity to dive deep into this topic.

CONTENTS

LIST OF FIGURES

LIST OF TABLES

NOMENCLATURE

Table 0-1. Nomenclature

Abbreviation	Definition
828DEA (or 828DGEBA/DEA)	Epon 828 digylcidyl ether of bisphenol A (DGEBA) cross-linked with diethanolamine
828T403 (or 828DGEBA/T403)	Epon 828 digylcidyl ether of bisphenol A (DGEBA) cross-linked with polyetheramine (Jeffamine T-403, Huntsman)
ASC	Advanced Simulation and Computing
CTE	Coefficient of Thermal Expansion
DOE	Department of Energy
DOD	Department of Defense
DSC	Differential Scanning Calorimeter
$f_1(t)$, τ_1, β_1	Volumetric (bulk) relaxation function and associated KWW time and width parameters
$f_2(t)$, τ_2, β_2	Shear relaxation function and associated KWW time and width parameters
$f_3(t)$, τ_3, β_3	Thermal expansion relaxation function and associated KWW time and width parameters
$f_4(t)$, τ_4, β_4	Isochoric heat capacity relaxation function (also referred to as the "thermal relaxation function") and associated KWW time and width parameters
KWW	Kohlrausch–Williams–Watts (KWW) or stretched-exponential function, $\exp\left(-\left(\frac{t}{\tau}\right)^{\beta}\right)$
NLVE	Non-Linear Viscoelastic
ND	Nuclear Deterrence
PEC	Potential Energy Clock model
P&EM	Physics and Engineering Modeling
SPEC	Simplified Potential Energy Clock model
Tg	Glass Transition Temperature
TTS	Time–Temperature Superposition
TMA	Thermo-Mechanical Analyzer

1. INTRODUCTION

Glasses physically age, which means they structurally rearrange at the molecular level to pack more tightly during their service lifetime. This process can impact the reliability of devices that depend on these materials to perform specific functions over the decades-long lifetimes of Nuclear Deterrent (ND) components and space vehicles. Inorganic glasses and many polymer adhesives and encapsulants spend their lifetimes below their glass transition temperature (Tg), "trapping" their processing history into their "memory" and driving continuous evolution through the physical aging process over their lifetime. Both the processing history and the aging that occurs can substantially impact the thermal-mechanical behavior of the material, particularly in the non-linear response regime and in the failure behavior [5, 20].

The extent to which a material physically ages depends upon factors such as the proximity of the material's Tg to temperatures it is exposed to, the time over which the material experiences the temperature, and the breadth of the material's glass transition. During physical aging, a glass forming material shrinks when it is unconfined. When it is confined and prevented from shrinking, the residual stress state within it changes, which may deleteriously affect surrounding materials. From a design perspective, loss of dimensional conformance, interfacial debonding, and cracking within the glass or cracking of fragile components that the glass is interacting with are all concerns that must be avoided.

Testing to assess the reliability of components/devices over lifetimes that extend decades is impractical. Rather, specific material aging mechanisms must be accelerated in the laboratory while tracking the material evolution. Such datasets enable the assessment of science-based models' abilities to predict the effect of the aging mechanism on the material. Once material evolution prediction is demonstrated, simple, component-like structural tests can be designed (computationally or from scientific intuition) and used to validate the ability of the model to make structural predictions. Success in all the aforementioned stages enables a tool that can confidently predict component reliability concerns over lifetimes that extend over decades in a much more efficient (time and cost) manner than experimental assessments.

Sandia has invested decades into developing physically based non-linear viscoelastic (NLVE) models to predict glass thermal-mechanical behavior. This is accomplished through a close and enduring collaboration between Engineering Sciences (1500) and Materials Science (1800) in which iteration between experimental and computational findings defines the required fidelity at which the material physics must be represented in order to generate structural predictions of interest to SNL engineering design and assessment. Over this time period, a theoretical framework has been developed and the resulting constitutive model has been shown to adequately predict specific material NLVE behavior, such as temperature and strain rate dependence of yield, creep, cooling history dependence of thermal-mechanical response, etc. of as-manufactured samples ([3, 6, 16]). A simplified version of the model ([4]), which eases experimental efforts for

material calibration and reduces computational processing power requirements, has also been demonstrated to be similarly predictive and is currently used in engineering design and problem-solving simulations across SNL mission space. We focus on this Simplified Potential Energy clock model (SPEC) in this report.

While these modeling tools incorporate a history dependent shift factor, or "material clock", that has the potential to account for physical aging of the material, limitations of the model's ability to accurately predict the effects of short-term aging on material response have been noted ([3]). Decades-long predictions of aging effects of relevance to SNL mission areas have not been adequately pursued to date. In this work, we examine whether the impediment to quantitative aging predictions can be reduced by adding fidelity to the model calibration process. We then study how different calibration choices impact the quality of physical aging predictions across a diverse suite of aging data. Additionally, two known gaps in model form are addressed. First, we explore adjusting the definition of equilibrium shift factors below Tg to enable the model to equilibrate (cease changing with time) as observed experimentally, and second, we improve the model credibility for predicting heat capacity changes. We focus on two epoxy glasses common to the Sandia mission space, 828DGEBA/DEA and 828DGEBA/T403. But this work has relevance to other materials that exhibit the same aging mechanisms.

It is worth noting that outside of Sandia in the open literature, the Sandia developed SPEC model has outperformed other non-linear viscoelastic and viscoplastic models in round robin predictions of physical aging. See in particular chapters 4 and 14 from [20] wherein the Sandia NLVE model is referred to as the "TVEM" model, for thermoviscoelastic model. But, while the authors of those studies note that the TVEM model performs well across many common predictions, they indicate its performance is far from perfect. Given the complexity of constitutive model forms and how to calibrate it, it is difficult to know if the calibrations used today for different materials are the "best" calibrations or if there is another calibration elsewhere in the model parameter space that is better. Recent work has identified deficiencies in the current 828DGEBA/DEA calibration when it comes to aging predictions [26, 22]. Those finding, which are referred to in more detail in the appropriate sections of this report, motivated the postulation that a more specific material calibration could improve aging predictions. Of course, improved aging predictions cannot come at the cost of other predictive capabilities necessary to represent the full lifecycle of the material. This led to the initiating *hypothesis* for the current Level 2 Milestone that *a model calibration process can be defined that enables confidence in physical aging predictions under ND relevant environments and timescales without sacrificing other predictive capabilities*. Throughout the rest of this report, the process of evaluating that hypothesis and the resulting findings are discussed.

This work specifically addressed the completion of FY21 ASC P&EM L2 Milestone 7836, the language of which is reproduced verbatim in the following two sections.

1.1. Milestone Description

Polymer encapsulation physically ages (changes physical properties and thermal-mechanical behavior without a composition change over time) in the stockpile. In many cases, the degree of physical aging is controlled by the proximity of the glass transition to the component

environmental temperature, the breadth of the material's glass transition, and the thermal-mechanical history it withstood to arrive in the glassy state. These factors influence the residual stress and its evolution as components age. In order to assess the reliability of aging polymer encapsulated components against failure or a change in function, it is important to be able to predict the physical aging behavior associated with specified thermal and aging histories. The main goal of this milestone is to establish the capability to which Sandia's Simplified Potential Energy Clock (SPEC) Non-Linear Viscoelastic model will predict various manifestations of physical aging in polymer encapsulation. We will calibrate models for three materials to new, batch-consistent sets of characterization data and use these calibrations to predict different measures of physical aging. Moreover, a deficiency of the model's sub-glass-transition equilibration behavior will be addressed through theory development, code modification, and documentation. These efforts will be deployed on extensive data collected on Sandia workhorse encapsulants, such as 828 DGEBA/DEA, and filled encapsulants under relevant manufacturing and aging thermal-mechanical conditions. The project will leverage both DOE Aging and Lifetime and DoD/Joint Munitions Programs experimental funding, which will collect the new, high quality calibration data for the materials studied.

1.2. Milestone Completion Criteria

The sub-glass-transition equilibrated behavior of the SPEC model will be altered to reflect Arrhenius behavior observed experimentally. With this model enhancement, a new set of calibrations for 828 DGEBA/DEA, 828 DGEBA/T403, and 828 DGEBA/DEA Filled with glass microballoons (the third material a stretch goal) will be produced and documented. These calibrations will then be subjected to a suite of physical aging predictions with available data (different for each material) including: enthalpy peaks in aged differential scanning calorimetry samples, stress-free thermal strain relaxation, stress-free aging and subsequent yield strength predictions, and as a stretch goal, predictions of creep (mechanical aging) below the glass transition. In addition to the "best fit" parameters, we will also examine how parameterizations are changed when the model calibrations are tailored directly to physical aging data. The project concludes successfully with a SAND Report at the end of FY21.

1.3. Outline of Report

The report is laid out as follows. The SPEC model formalization is reviewed, and model enhancements related to sub-Tg equilibration and heat capacity calculations are discussed in chapter 2. Then, in chapter 3, a summary of experimental data collected for this project, as well as data collected and documented previously, is presented for both 828DEA and 828T403. These data are used in chapter 4 to explore different approaches for calibrating the SPEC model that best fits all the calibration data available for 828T403. Calibrated models for each approach are catalogued and then compared based on their ability to predict different physical aging experiments. In chapter 5, the calibration and physical aging prediction processes are repeated for 828DEA. Parametric studies are then executed in chapter 6 to determine relationships between

parameters that are important for physical aging predictions and check which calibration procedures uphold the uncovered relationships. The work is then concluded with discussion on major findings, remaining gaps, and possible future efforts in chapter 7.

2. CONSTITUTIVE MODEL REVIEW AND ENHANCEMENTS

All of the present milestone simulation work used a research version of the Simplified Potential Energy Clock (SPEC) constitutive model [4] within Sierra Solid Mechanics Finite Element code [25] within the Lame constitutive model library [21]. The workhorse SPEC model implementation, named the `universal polymer` model, only allows for two relaxation functions, one relaxation function represents both the bulk and thermal expansion relaxation functions, and another represents the shear relaxation function. Thermal terms suitable for comparison to DSC experiments are not implemented. Hence, we used the `spectacular` model which is nearly the same as the `universal polymer` model except that it involves four independent relaxation functions: bulk, shear, thermal expansion, and heat capacity. Moreover, the `spectacular model` is a complete thermal-mechanical constitutive model of a single phase material as it calculates not only the stress but also the entropy and dissipation needed for energy balance calculations. For complete details on these terms that do not exist in the SPEC (`universal polymer`) model, see [24].

It is worth noting that during the original development of the parent PEC (Potential Energy Clock) Model [6, 3], four independent relaxation functions were considered and the definition of the shift factor was substantially more complicated than the shift factor definition used in the SPEC models here (which are the same between the `universal polymer` and `spectacular`). Hence, the `spectacular` model represents a model form that is between the complexity of PEC and SPEC. The added complexity of `spectacular` was thought to be needed in order to better represent the various types of experimental data the model must fit and predict. Through the course of presenting results, we will evaluate the benefits of adding these additional relaxation functions as well as specific model form enhancements in the context of whether these enhancements significantly improve model fitting and predictions.

The purpose of this chapter is to present new contributions added to the `spectacular` model specifically to address prediction of thermal behavior (enthalpy, heat capacity, etc.) as well as deficiencies in sub-Tg equilibration behavior. The chapter is organized as follows. In section 2.1, the full thermal-mechanical constitutive model theory is reviewed in the context of the first and second laws of thermodynamics. All necessary terms are identified needed for both momentum and energy balance partial differential equations. Implementation of the model is not discussed but can be found in suitable detail in prior work under the `universal polymer` model [21]. Then, verification testing is presented for simulations of a constant volume temperature sweep in section 2.2. Simulations of constant pressure temperature sweeps, as is usually tested in a differential scanning calorimetry test, are presented in section 2.3. Since the constitutive equations are derived from the Helmholtz free energy, it is difficult to formulate analytical solutions for a constant pressure temperature sweep. Therefore, parameters are incrementally activated in section 2.3 to demonstrate the diversity of contributions to the constant pressure heat

capacity. Then, in section 2.4, a new formulation of the sub-Tg shift factor is developed and verified under simple scenarios.

2.1. Review of the Complete Thermal-Mechanical SPEC Constitutive Model

Here we briefly review the augmented SPEC model theory that includes additional thermal terms. The model theory is documented in detail in [24] and much of this section is taken directly from that source.

2.1.1. Thermodynamically Consistent Modeling of Thermo-Mechanical Effects in the SPEC Model Framework

The SPEC model belongs to the class of constitutive models with fading memory [10]. We begin briefly with the first and second laws of thermodynamics of a homogenous, single phase continuum. Then, we present the Helmholtz Free Energy that is the foundation of the SPEC model with the extra thermal terms. The Coleman and Noll procedure are used within the context of the Clausius-Duhem form of the Second Law to determine the stress and entropy. We only report these two thermodynamic forces (work conjugate to the strain rate and temperature rate respectively) here for brevity. Finally, with an appropriate Legendre transform, when the constitutive model is put into the first law and recast it into a form where the temperature is the fundamental unknown field, one arrives at the partial differential equation for the temperature field. We report the equations and important terms that arise directly from the constitutive model evolution including the heat capacity (which will be compared with experiments in this report). Many details are skipped and can be found in recent work [24].

2.1.2. Thermomechanical Constitutive Equations

The mass, momentum, and energy balance continuum field equations require closure relations, which the SPEC constitutive model provides (except for the heat flux constitutive equation). Since we wish to work with the strain and the temperature as the independent variables associated with the usual solution variables for linear momentum and energy balance finite element procedures, we formulate our constitutive model with a Helmholtz free energy $\Psi = E - \theta\eta$ as the relevant thermodynamic potential, and therefore we regard quantities such as the internal energy density, E, and enthalpy density, χ, as derived quantities. All densities are per reference

(undeformed) volume. The full set of constitutive equations to be developed are

$$\Psi = \Psi(\boldsymbol{h}) \tag{2.1}$$
$$\boldsymbol{\Sigma} = \boldsymbol{\Sigma}(\boldsymbol{h}) \tag{2.2}$$
$$\eta = \eta(\boldsymbol{h}) \tag{2.3}$$
$$\boldsymbol{Q} = \boldsymbol{Q}(\boldsymbol{C}, \theta, \nabla\theta) \tag{2.4}$$
$$E = E(\boldsymbol{h}) \tag{2.5}$$
$$\chi = \chi(\boldsymbol{h}). \tag{2.6}$$

The symbol $\boldsymbol{h}$ represents the entire histories of the Hencky strain and the temperature $\{\boldsymbol{H}(s), \theta(s)\}_{s=0}^{s=t}$.

The full SPEC Helmholtz Free Energy per reference volume including the new heat capacity term (see for comparison [3]) is,

$$\begin{aligned}\Psi = \Psi_\infty(\boldsymbol{H}, \theta) &+ \frac{1}{2} K_D(\theta) \int_0^t \int_0^t f_1(t^* - s^*, t^* - u^*) \frac{dI_1}{ds} \frac{dI_1}{du} ds du \\ &- L_D(\theta) \int_0^t \int_0^t f_3(t^* - s^*, t^* - u^*) \frac{d\theta}{ds} \frac{dI_1}{du} ds du \\ &+ G_D(\theta) \int_0^t \int_0^t f_2(t^* - s^*, t^* - u^*) \frac{d\boldsymbol{H}^{\text{dev}}}{ds} : \frac{d\boldsymbol{H}^{\text{dev}}}{du} ds du \\ &- \frac{C_D(\theta)}{2\theta_{\text{ref}}} \int_0^t \int_0^t f_4(t^* - s^*, t^* - u^*) \frac{d\theta}{ds} \frac{d\theta}{du} ds du.\end{aligned} \tag{2.7}$$

The fourth hereditary integral is new in this work, and significant efforts were allotted during the milestone to verify and exercise this thermal parts of the model. The deviatoric part of the Hencky strain is $\boldsymbol{H}^{\text{dev}}$, and its trace is indicated by I_1. The functions $f_i(s,u)$, $i = \{1,2,3,4\}$ are the relaxation functions, which are symmetric in their arguments. For convenience, we will make use of the notational simplification

$$f_i(s) := f_i(s,0) = f_i(0,s)$$

when one of the arguments vanishes. Notationally, a subscript of "D" indicates the difference between a parameter's glassy value and its equilbrium value. For example, for a generic parameter Z, $Z_D = Z_g - Z_\infty$, where Z_g indicates the glassy value and Z_∞ indicates the equilibrium value. K_D is thus the (temperature dependent) difference in the bulk modulus, L_D is $K_g\delta_g - K_\infty\delta_\infty$, where the δ symbols are related to the volumetric coefficient of thermal expansion, G_D is the difference in the shear modulus, and C_D is the difference in the volumetric heat capacities, measured at the reference temperature θ_{ref}. Finally, $()_\infty$ and $()_g$ represent an equilibrated and glassy quantities, respectively.

The star on the time variables is used to indicate that the time has been transformed from laboratory time to material time via a single viscoelastic shift factor (which affects all relaxation processes similarly). That shift factor is unmodified from the SPEC model formulation in [4] and

is reproduced here along with the relationship between material and laboratory time,

$$\begin{aligned}
\log_{10} a &= \frac{-C_1 N}{C_2 + N}, && (2.8)\\
N &= \left(\theta - \theta_{\text{ref}} - \int_0^t f_3\left(t^* - s^*\right)\frac{d\theta}{ds}ds\right) && (2.9)\\
&\quad + C_3\left(I_1 - \int_0^t f_1\left(t^* - s^*\right)\frac{dI_1}{ds}ds\right)\\
&\quad + C_4\int_0^t ds\int_0^t f_2\left(t^* - s^*, t^* - u^*\right)\frac{d\boldsymbol{H}^{\text{dev}}}{ds}\frac{d\boldsymbol{H}^{\text{dev}}}{du}ds\,du\\
t^* - s^* &= \int_{u=s}^{u=t}\frac{du}{a[u]} && (2.10)
\end{aligned}$$

The temperature dependence of the material properties is assumed to be at most linear, e.g.,

$$K_g(\theta) = K_{g,\text{ref}} + K_g'(\theta - \theta_{\text{ref}}), \tag{2.11}$$

with $K_{g,\text{ref}}$ is the value of the glassy bulk modulus measured at the reference temperature θ_{ref} and K_g' represents the (constant) rate of change of the glassy bulk modulus with temperature. The symbol " $'$ " is used here to denote a derivative with respect to temperature, e.g., $Z_D'(\theta) = dZ_D(\theta)/d\theta$. For the glassy and equilibrium differences in the bulk modulus, shear modulus, and volumetric heat capacity,

$$K_D' = K_g' - K_\infty', \tag{2.12}$$

$$G_D' = G_g' - G_\infty', \tag{2.13}$$

$$C_D' = C_g' - G_\infty'. \tag{2.14}$$

Since $L_D(\theta)$ is a product of two properties that each depend linearly on temperature, $L_D(\theta)$ has a quadratic dependence on temperature:

$$L_D'(\theta) = K_{g,\text{ref}}\delta_g' + K_g'\delta_{g,\text{ref}} + 2K_g'\delta_g'(\theta - \theta_{\text{ref}}) - K_{\infty,\text{ref}}\delta_\infty' - K_\infty'\delta_{\infty,\text{ref}} - 2K_\infty'\delta_\infty'(\theta - \theta_{\text{ref}}), \tag{2.15}$$

$$L_D'' = 2K_g'\delta_g' - 2K_\infty'\delta_\infty'. \tag{2.16}$$

In writing (2.7), it is implied that heat capacity terms are added to the equilibrium free energy; in particular we take

$$\begin{aligned}
\Psi_\infty(\boldsymbol{H},\theta) = G_\infty(\theta)\boldsymbol{H}^{\text{dev}} : \boldsymbol{H}^{\text{dev}} + \frac{K_\infty(\theta)}{2}I_1^2 - K_\infty(\theta)\delta_\infty(\theta)(\theta - \theta_{\text{sf}})I_1\\
- C_{\infty,\text{ref}}\theta\left(\log\frac{\theta}{\theta_{\text{ref}}} - 1\right) - C_{\infty,\text{ref}}\theta_{\text{ref}} - \frac{C_\infty'}{2}\left(\theta - \theta_{\text{ref}}\right)^2,
\end{aligned} \tag{2.17}$$

where $C_{\infty,\text{ref}}$ is the equilibrium volumetric heat capacity measured at the reference temperature θ_{ref}, and C_∞' is a parameter representing the (assumed constant) rate of change of the equilbrium heat capacity with temperature. This form is chosen such that the equilibrium heat capacity will also vary linearly with temperature.

The material time derivative of the Helmholtz Free Energy density will be needed for use with the Second Law of thermodynamics and the Coleman and Noll procedure (to identify the stress and entropy). That time derivative will have three terms that for brevity we have already identified through the Coleman and Noll procedure to be associated with the work conjugate pairs of stress and strain, entropy and temperature, and the dissipation.

$$\dot{\Psi} = \boldsymbol{\Sigma}(\boldsymbol{h}) : \dot{\boldsymbol{H}} + \eta(\boldsymbol{h})\dot{\theta} - \mathscr{D}_{TM}(\boldsymbol{h}), \tag{2.18}$$

where

$$\begin{aligned}\boldsymbol{\Sigma}(\boldsymbol{h}) =& \frac{\partial \Psi_\infty(\boldsymbol{H},\theta)}{\partial \boldsymbol{H}} + K_D(\theta)\,\mathbf{1}\int_0^t f_1(t^*-s^*)\frac{dI_1}{ds}ds \\ &+ 2G_D(\theta)\int_0^t f_2(t^*-s^*)\frac{d\boldsymbol{H}^{\mathrm{dev}}}{ds}ds \\ &- L_D(\theta)\,\mathbf{1}\int_0^t f_3(t^*-s^*)\frac{d\theta}{ds}ds,\end{aligned} \tag{2.19}$$

$$\begin{aligned}\eta(\boldsymbol{h}) =& -\frac{\partial \Psi_\infty(\boldsymbol{H},\theta)}{\partial \theta} + L_D(\theta)\int_0^t f_3(t^*-s^*)\frac{dI_1}{ds}ds \\ &+ \frac{C_D(\theta)}{\theta_{\mathrm{ref}}}\int_0^t f_4(t^*-s^*)\frac{d\theta}{ds}ds \\ &- \frac{1}{2}K_D'\int_0^t\int_0^t f_1(t^*-s^*,t^*-u^*)\frac{dI_1}{ds}\frac{dI_1}{du}dsdu \\ &- G_D'\int_0^t\int_0^t f_2(t^*-s^*,t^*-u^*)\frac{d\boldsymbol{H}^{\mathrm{dev}}}{ds} : \frac{d\boldsymbol{H}^{\mathrm{dev}}}{du}dsdu \\ &+ L_D'\int_0^t\int_0^t f_3(t^*-s^*,t^*-u^*)\frac{d\theta}{ds}\frac{dI_1}{du}dsdu \\ &+ \frac{C_D'}{2\theta_{\mathrm{ref}}}\int_0^t\int_0^t f_4(t^*-s^*,t^*-u^*)\frac{d\theta}{ds}\frac{d\theta}{du}dsdu,\end{aligned} \tag{2.20}$$

and

$$\begin{aligned}\mathscr{D}_{\mathrm{TM}} =& -\frac{K_D(\theta)}{2}\int_0^t\int_0^t \frac{\partial f_1(t^*-s^*,t^*-u^*)}{\partial t}\frac{dI_1}{ds}\frac{dI_1}{du}dsdu \\ &- G_D(\theta)\int_0^t\int_0^t \frac{\partial f_2(t^*-s^*,t^*-u^*)}{\partial t}\frac{d\boldsymbol{H}^{\mathrm{dev}}}{ds} : \frac{d\boldsymbol{H}^{\mathrm{dev}}}{du}dsdu \\ &+ L_D(\theta)\int_0^t\int_0^t \frac{\partial f_3(t^*-s^*,t^*-u^*)}{\partial t}\frac{d\theta}{ds}\frac{dI_1}{du}dsdu \\ &+ \frac{C_D(\theta)}{2\theta_{\mathrm{ref}}}\int_0^t\int_0^t \frac{\partial f_4(t^*-s^*,t^*-u^*)}{\partial t}\frac{d\theta}{ds}\frac{d\theta}{du}dsdu.\end{aligned} \tag{2.21}$$

2.1.3. Energy Balance Field Equation

The energy balance (first law) can be written such that temperature is the independent variable (see [24] for details),

$$\bar{C}(\boldsymbol{h})\dot{\theta} = -\operatorname{Div}\boldsymbol{Q} + Q + \mathscr{D}_{\mathrm{TM}}(\boldsymbol{h}) + \mathscr{C}(\boldsymbol{h}) + \theta\mathscr{H}(\boldsymbol{h}). \tag{2.22}$$

Here, for convenience, we have collected terms into the heat capacity-like quantity

$$\begin{aligned}\bar{C}(\boldsymbol{h}) = {} & C_{\infty,\mathrm{ref}} + C'_{\infty}\theta + \frac{\theta}{\theta_{\mathrm{ref}}}C_D(\theta) + 2I_1\theta(K'_{\infty}\delta_{\infty}(\theta) + K_{\infty}(\theta)\delta'_{\infty}) + 2K'_{\infty}\delta'_{\infty}I_1\theta(\theta-\theta_{\mathrm{sf}}) \\ & + 2L'_D\theta\int_0^t f_3(t^*-s^*)\frac{dI_1}{ds}ds + 2\frac{C'_D\theta}{\theta_{\mathrm{ref}}}\int_0^t f_4(t^*-s^*)\frac{d\theta}{ds}ds \\ & + L''_D\dot{\theta}\int_0^t\int_0^t f_3(t^*-s^*,t^*-u^*)\frac{d\theta}{ds}\frac{dI_1}{du}dsdu,\end{aligned} \tag{2.23}$$

a heat source due to temperature-rate dependent heat capacity hereditary integrals,

$$\begin{aligned}\mathscr{C}(\boldsymbol{h}) = {} & -C_D(\theta)\frac{\theta}{\theta_{\mathrm{ref}}}\int_0^t\frac{\partial f_4(t^*-s^*)}{\partial t}\frac{d\theta}{ds}ds \\ & -\frac{C'_D\theta}{2\theta_{\mathrm{ref}}}\int_0^t\int_0^t\frac{\partial f_4(t^*-s^*,t^*-u^*)}{\partial t}\frac{d\theta}{ds}\frac{d\theta}{du}dsdu,\end{aligned} \tag{2.24}$$

and a heat source associated with thermomechanical entropic effects, given by

$$\begin{aligned}\mathscr{H}(\boldsymbol{h}) = {} & -K_g(\theta)\delta_g(\theta)\dot{I}_1 - (K'_{\infty}\delta_{\infty}(\theta) + K_{\infty}(\theta)\delta'_{\infty})(\theta-\theta_{\mathrm{sf}})\dot{I}_1 \\ & + 2G'_{\infty}\boldsymbol{H}^{\mathrm{dev}} : \dot{\boldsymbol{H}}^{\mathrm{dev}} + K'_{\infty}I_1\dot{I}_1 \\ & + K'_D\dot{I}_1\int_0^t f_1(t^*-s^*)\frac{dI_1}{ds}ds + 2G'_D\dot{\boldsymbol{H}} : \int_0^t f_2(t^*-s^*)\frac{d\boldsymbol{H}^{\mathrm{dev}}}{ds}ds \\ & - L'_D\dot{I}_1\int_0^t f_3(t^*-s^*)\frac{d\theta}{ds}ds - L_D(\theta)\int_0^t\frac{\partial f_3(t^*-s^*)}{\partial t}\frac{dI_1}{ds}ds \\ & + \frac{1}{2}K'_D\int_0^t\int_0^t\frac{\partial f_1(t^*-s^*,t^*-u^*)}{\partial t}\frac{dI_1}{ds}\frac{dI_1}{du}dsdu \\ & + G'_D\int_0^t\int_0^t\frac{\partial f_2(t^*-s^*,t^*-u^*)}{\partial t}\frac{d\boldsymbol{H}^{\mathrm{dev}}}{ds} : \frac{d\boldsymbol{H}^{\mathrm{dev}}}{du}dsdu \\ & - L'_D\int_0^t\int_0^t\frac{\partial f_3(t^*-s^*,t^*-u^*)}{\partial t}\frac{d\theta}{ds}\frac{dI_1}{du}dsdu.\end{aligned} \tag{2.25}$$

Equation (2.22) is a generalization of the heat equation, and is the additional PDE that must be solved in conjunction with the linear momentum balance.

The internal energy can be computed directly from the Helmholtz Free Energy density, entropy density, and temperature. The enthalpy can then be calculated from the internal energy, the stress, and the strain. See [24] for details.

2.1.4. Specification of Relaxation Functions

In the `spectacular` model, each relaxation function is specified by the sum of a Prony series,

$$f_i(s,u) = \sum_{k=1}^{N} w_{i,k} \exp\left(\frac{-s}{\tau_{i,k}}\right) \exp\left(\frac{-u}{\tau_{i,k}}\right), \tag{2.26}$$

$$f_i(s,0) = f_i(0,s) = f_i(s) = \sum_{k=1}^{N} w_{i,k} \exp\left(\frac{-s}{\tau_{i,k}}\right), \tag{2.27}$$

where $f_i(s,u)$ is the i^{th} relaxation function, $\tau_{i,k}$ is the k^{th} Prony time of the i^{th} relaxation function, and $w_{i,k}$ is it's weight. However, it is often convenient to described a relaxation function using a stretched exponential,

$$f_i(s) = \exp\left[-\left(\frac{s}{\tau_i}\right)^{\beta_i}\right], \tag{2.28}$$

where τ_i is the characteristic time of the stretched exponential and β_i is the stretching exponent. Stretched exponentials cannot be directly used by the `spectacular` model, so they must be approximated by a Prony series. The stretched exponentials are converted to approximate Prony series fits externally to the model using custom Python tools. In the context of this report, $\tau_{i,k}$ (with two indices) represents a characteristic time in a Prony series, while τ_i (with one index) indicates a characteristic time for a stretched exponential.

2.2. Analytic Verification of Constant-Volume Heat Capacity Calculations

A verification test for the constant volume heat capacity is presented in [24]. That verification test considered the volumetric heat capacity during a constant temperature ramp using a calibration where no material parameters depended on temperature, there was no time–temperature superposition ($C_1 = 0$), and the relaxation functions consisted of a single Prony term. An expanded verification effort is presented here that includes temperature-dependent material properties and relaxation functions that consist of a Prony series.

The thermomechanical history considered for verification is cooling at a constant temperature rate while the volume is held fixed;

$$\dot{\theta}(t) = q, \quad I_1(t) = 0, \quad \boldsymbol{H}^{\text{dev}} = \boldsymbol{0}. \tag{2.29}$$

For the history described in Equation (2.29), Equations (2.7), (2.19), (2.20), (2.21), (2.23), (2.24), and (2.25) simplify to

$$\begin{aligned}\Psi(t) = &-C_\infty^{\text{ref}}\theta\left(\log\frac{\theta}{\theta_{\text{ref}}} - 1\right) - C_\infty^{\text{ref}}\theta_{\text{ref}} - \frac{C'_\infty}{2}\left(\theta - \theta_{\text{ref}}\right)^2 \\ &- \frac{C_D(\theta)}{2\theta_{\text{ref}}}\dot{q}^2 \int_0^t \int_0^t f_4(t-s, t-u)\, ds\, du,\end{aligned} \tag{2.30}$$

$$\Sigma_{\mathrm{h}}(t) = \frac{1}{3}\operatorname{tr}\boldsymbol{\Sigma}(t) = -K_{\infty}(\theta)\,\delta_{\infty}(\theta)\,(\theta-\theta_{\mathrm{sf}}) - L_D(\theta)\,q\int_0^t f_3(t-s)\,ds, \tag{2.31}$$

$$\begin{aligned}\eta(t) = {} & C_{\infty}^{\mathrm{ref}}\log\left(\frac{\theta}{\theta_{\mathrm{ref}}}\right) + C'_{\infty}(\theta-\theta_{\mathrm{ref}}) + \frac{C_D(\theta)}{\theta_{\mathrm{ref}}}q\int_0^t f_4(t-s)ds \\ & + \frac{C'_D}{2\theta_{\mathrm{ref}}}q^2\int_0^t\int_0^t f_4(t-s,t-u)dsdu,\end{aligned} \tag{2.32}$$

$$\mathscr{D}_{\mathrm{TM}}(t) = \frac{C_D(\theta)}{2\theta_{\mathrm{ref}}}q^2\int_0^t\int_0^t \frac{\partial f_4(t-s,t-u)}{\partial t}dsdu, \tag{2.33}$$

$$\bar{C}(t) = C_{\infty}^{\mathrm{ref}} + C'_{\infty}\theta + \frac{\theta}{\theta_{\mathrm{ref}}}C_D(\theta) + 2C'_D\frac{\theta}{\theta_{\mathrm{ref}}}q\int_0^t f_4(t-s)\,ds, \tag{2.34}$$

$$\mathscr{C}(t) = -C_D(\theta)\frac{\theta}{\theta_{\mathrm{ref}}}q\int_0^t \frac{\partial f_4(t-s)}{\partial t}ds - \frac{C'_D}{2}\frac{\theta}{\theta_{\mathrm{ref}}}q^2\int_0^t\int_0^t \frac{\partial f_4(t-s,t-u)}{\partial t}dsdu, \tag{2.35}$$

and

$$\mathscr{H}(t) = 0. \tag{2.36}$$

Since there time–temperature superposition is turned off, $t^* = t$. Without time–temperature superposition, the hereditary integrals in Equations (2.30)–(2.36) are much easier to evaluate analytically. Their expressions are

$$\int_0^t f_i(t-s)ds = \sum_{k=1}^{N}\left[w_{i,k}\tau_{i,k}\left(1-\exp\left(\frac{-t}{\tau_{i,k}}\right)\right)\right], \tag{2.37}$$

$$\int_0^t\int_0^t f_i(t-s,t-u)dsdu = \sum_{k=1}^{N}\left[w_{i,k}\tau_{i,k}^2\left(1-\exp\left(\frac{-t}{\tau_{i,k}}\right)\right)^2\right], \tag{2.38}$$

$$\int_0^t \frac{\partial f_i(t-s)}{\partial t}ds = \sum_{k=1}^{N}\left[-w_{i,k}\left(1-\exp\left(\frac{-t}{\tau_{i,k}}\right)\right)\right], \tag{2.39}$$

$$\int_0^t \frac{\partial f_i(t-s,t-u)}{\partial t}dsdu = \sum_{k=1}^{N}\left[-2w_{i,k}\tau_{i,k}\left(1-\exp\left(\frac{-t}{\tau_{i,k}}\right)\right)^2\right]. \tag{2.40}$$

Solutions for $\Psi(t)$, $\Sigma_{\mathrm{h}}(t)$, $\eta(t)$, $\mathscr{D}_{\mathrm{TM}}(t)$, $\bar{C}(t)$, and $\mathscr{C}(t)$ were calculated using the `spectacular` model in Sierra and were compared to Equations (2.30)–(2.35). All calculations used a temperature history that started at 375 K and cooled to 225 K at a rate of $q = -0.1\,\mathrm{K/s}$. A parameter set based on a calibration for 828DGEBA/DEA from [26] was used, with some modifications. First, the reference temperature was set to $\theta_{\mathrm{ref}} = 300\,\mathrm{K}$. Second, as previously mentiond, time–temperature superposition was deactivated ($C_1 = 0$) to facilitate analytical solutions to the hereditary integrals. Third, in [26], a two-function calibration was used; $f_1(t) = f_3(t)$. To increase the complexity of the validation, $f_1(t) \neq f_3(t)$ was used here. The separate $f_3(t)$ was taken from [22]. Finally, heat capacity inputs and $f_4(t)$ were taken from [3], since [26] uses the `universal polymer` model, which does not include full thermo-mechanical coupling. A table with the parameters used for verification are shown in Table 2-1. Relaxation functions $f_1(t)$, $f_3(t)$, and $f_4(t)$ were speified by Prony series that were fit

Table 2-1. Parameters used for verification of thermal terms under constant-volume cooling.

Parameter Name	Parameter	Value	Units
`bulk glassy 0`	K_g^{ref}	4.9	GPa
`bulk glassy 1`	K_g'	-12	MPa/K
`bulk rubbery 0`	K_∞^{ref}	3.2	GPa
`bulk rubbery 1`	K_∞'	-12	MPa/K
`shear glassy 0`	G_g^{ref}	0.94	GPa
`shear glassy 1`	G_g'	-2.3	MPa/K
`shear rubbery 0`	G_∞^{ref}	4.5	MPa
`shear rubbery 1`	G_∞'	0	MPa/K
`volcte glassy 0`	α_g^{ref}	170	10^{-6}/K
`volcte glassy 1`	α_g'	0.2	10^{-6}/K^2
`volcte rubbery 0`	$\alpha_\infty^{\text{ref}}$	600	10^{-6}/K
`volcte rubbery 1`	α_∞'	0.4	10^{-6}/K^2
`heat capacity glassy 0`	C_g^{ref}	1.916880	MJ/(m$^3\cdot$K)
`heat capacity glassy 1`	C_g'	4.8216	kJ/(m$^3\cdot$K^2)
`heat capacity rubbery 0`	C_∞^{ref}	2.481360	MJ/(m$^3\cdot$K)
`heat capacity rubbery 1`	C_∞'	2.8224	kJ/(m$^3\cdot$K^2)
`reference temperature`	θ_{ref}	300	K
`wlf c1`	$\hat{C}_1$	0	–
`wlf c2`	$\hat{C}_2$	1	K
`clock c3`	C_3	0	K
`clock c4`	C_4	0	K
`density`	ρ	1176	kg/m^3
	τ_1	6	s
	β_1	0.14	–
	τ_2	N/A	s
	β_2	N/A	–
	τ_3	0.0036	s
	β_3	0.259	–
	τ_4	20	s
	β_4	0.24	–

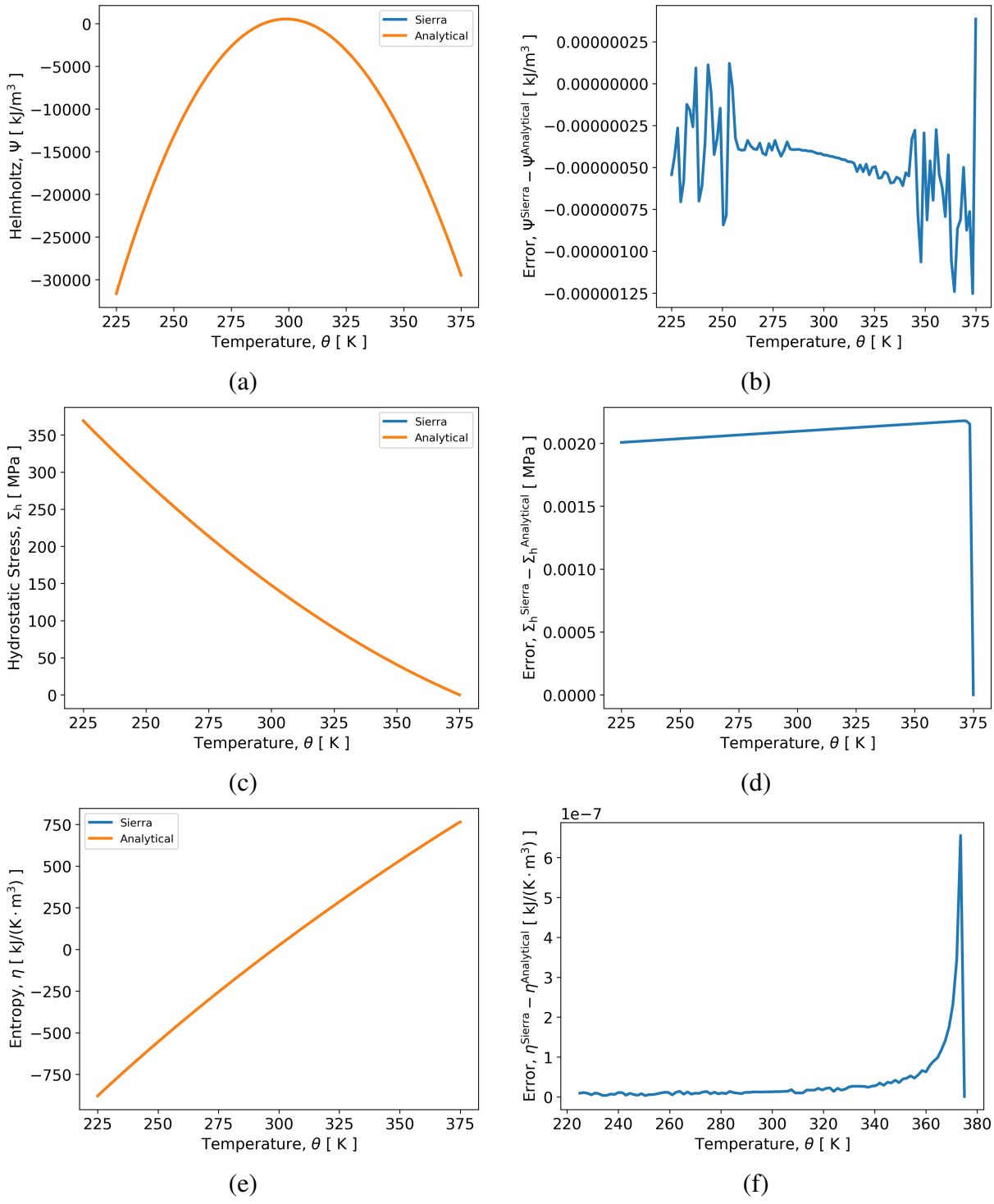

Figure 2-1. Results for a constant-volume temperature decrease at $-0.1\,\mathrm{K/s}$. Analytical results are plotted with Sierra outputs in (a), (c), and (e). Errors are small enough that the analytical and Sierra curves overlap. Errors between the analytical and Sierra results are plotted in (b), (d), (f). (a) and (b) Helmholtz free energy, Ψ. (c) and (d) hydrostatic stress, Σ_h. (e) and (f) entropy, η.

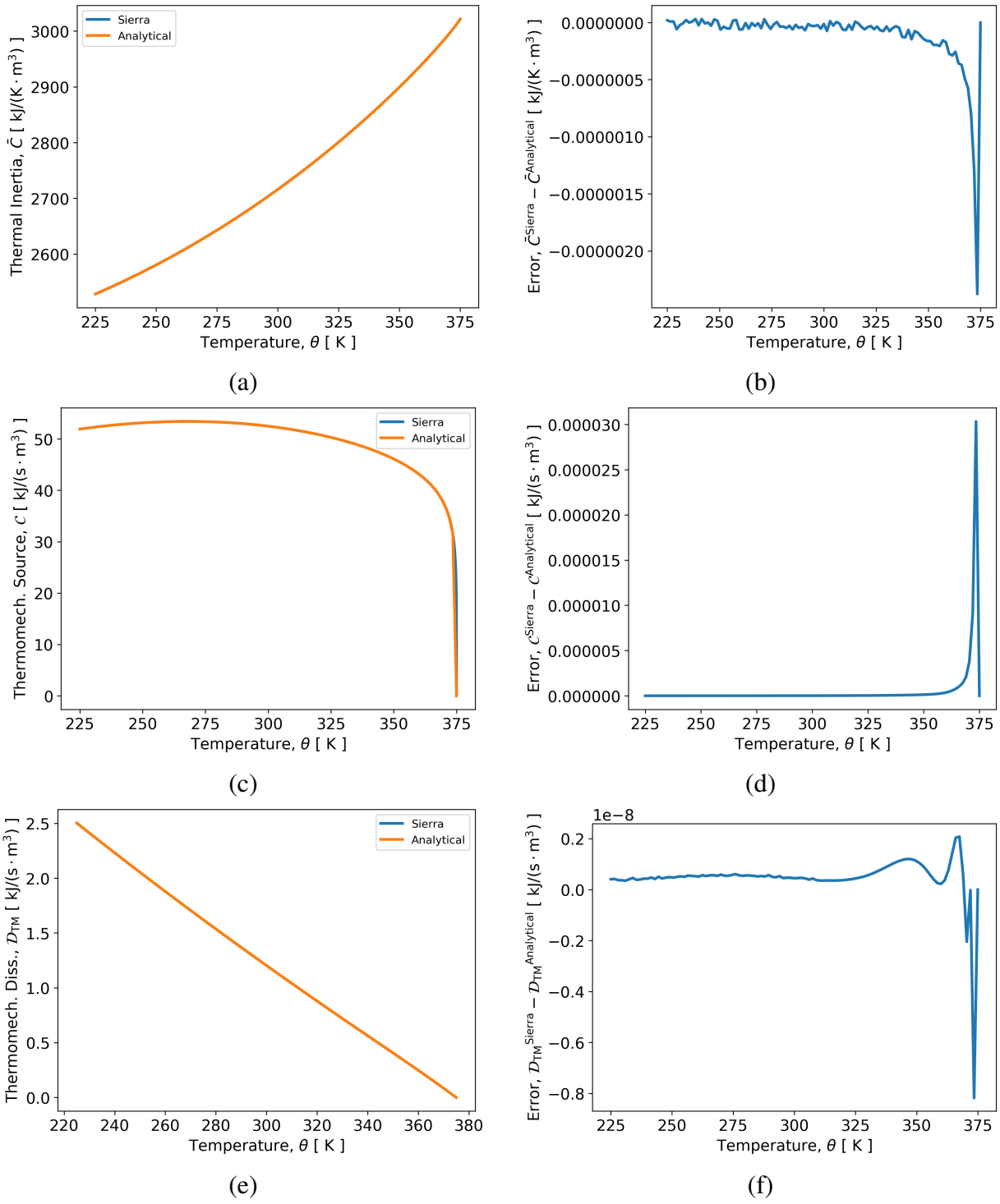

Figure 2-2. Results for a constant-volume temperature decrease at $-0.1\,\mathrm{K/s}$. Analytical results are plotted with Sierra outputs in (a), (c), and (e). Errors are small enough that the analytical and Sierra curves overlap. Errors between the analytical and Sierra results are plotted in (b), (d), (f). (a) and (b) thermal inertia, $\bar{C}$. (c) and (d) thermomechanical source, $\mathscr{C}$. (e) and (f) thermomechanical dissipation, $\mathscr{D}_{\text{TM}}$.

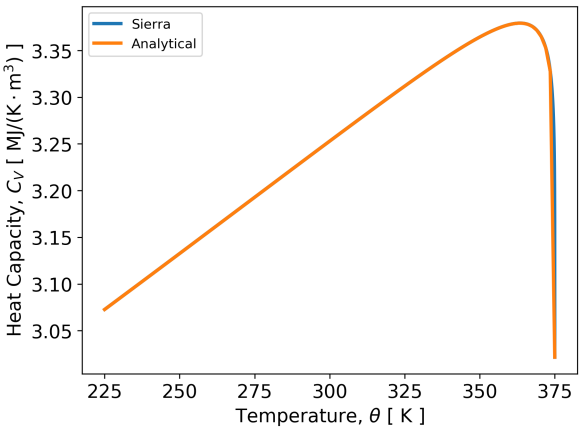

Figure 2-3. Constant-volume heat capacity calculated both analytically and by Sierra. Errors are small, so curves mostly overlap.

to stretched exponential functions. Only the stretched exponential function parameters are given in Table 2-1. No stretched exponential was used for $f_2(t)$ and its full Prony series can be found in [26], Appendix 1.

Solutions to Equations (2.30)–(2.35) and errors between the Analytical and Sierra results are shown in Figs. 2-1 and 2-2. All thermodynamic quantities are calculated per volume in the reference configuration, which is also the current configuration since the strain is fixed. For all model outputs, errors are low, demonstrating successful verification of the terms exercised by this thermomechanical history. Not all thermomechanical terms are exercised for a constant volume cool-down, since terms involving $\boldsymbol{H}$ and I_1 are zero when the strain is held constant. In the next section, constant pressure simulations are studied to understand the effects of terms involving I_1, but no formal verification is conducted.

The heat capacity under constant volume (or more generally, constant strain) can be calculated according to

$$C_V = \left| \bar{C} - \frac{1}{\dot{\theta}} \left(\mathscr{D}_{\mathrm{TM}} + \mathscr{C} + \theta \mathscr{H} \right) \right|_{\dot{\boldsymbol{H}}=\boldsymbol{0}} . \tag{2.41}$$

The derivation of for Equation (2.41) is shown in [24]. The constant-volume heat capacity for the verification problem is plotted in Fig. 2-3.

2.3. A Study of Different Contributions to the Constant-Pressure Heat Capacity Calculations

The heat capacity under constant pressure (or more generally, constant stress) can be calculated according to

$$C_p = \left| \bar{C} - \frac{1}{\dot{\theta}} \left(\mathscr{D}_{\mathrm{TM}} + \mathscr{C} + \theta \mathscr{H} \right) \right|_{\dot{\boldsymbol{\Sigma}}=\boldsymbol{0}} . \tag{2.42}$$

Table 2-2. Constant parameters for C_p testing.

Parameter Name	Parameter	Value	Units
`shear glassy 0`	G_g^{ref}	0.9	GPa
`shear glassy 1`	G_g'	-4.2	MPa/K
`shear rubbery 0`	G_∞^{ref}	4.5	MPa
`shear rubbery 1`	G_∞'	0	MPa/K
`reference temperature`	θ_{ref}	75	°C
`wlf c1`	$\hat{C}_1$	16.5	–
`wlf c2`	$\hat{C}_2$	54.5	K
`clock c3`	C_3	0	K
`clock c4`	C_4	11800	K
`density`	ρ	1176	kg/m^3
	τ_1	6	s
	β_1	0.24	–
	τ_2	0.12	s
	β_2	0.22	–
	τ_3	6	s
	β_3	0.24	–
	τ_4	20	s
	β_4	0.24	–

The derivation of for Equation (2.42) is shown in [24]. Since we are using a Helmholtz Free Energy functional to derive the model, the heat capacity at constant strain (isochoric heat capacity) is a natural quantity to produce. But, the heat capacity at constant pressure is not, and it is not simple to verify. Instead, here we take the approach of studying the effects of material parameters one by one on the isobaric heat capacity. This approach helps us build intuition about which parameters are most important for a quantity that is more easily measured experimentally with differential scanning calorimetry (where constant pressure is typically assumed).

We compute the isobaric heat capacity per unit reference volume in Sierra by sweeping a single element through a prescribed thermal history under stress-free conditions. The isobaric heat capacity is computed at each time step as the addition of multiple terms as previously discussed. Typically we divide the heat capacity per reference volume by the reference density to convert the quantity to the specific isobaric heat capacity as is more commonly done experimentally.

Four different studies were run that explore different parameters known to influence the isobaric heat capacity. In all studies, the temperature was cooled from well above Tg to well below Tg at 10 °C/min, and the isobaric heat capacity was computed at every time step. The parameters unchanged throughout the four studies are presented in Table 2-2. These parameters do not affect the isobaric heat capacity. The parameters are based on legacy 828DEA parameterizations (though not for the heat capacity terms) [26] to keep the model relevant to materials studied here.

Table 2-3. Parameters examined under constant-pressure (stress-free) cooling to assess their effects on the isobaric heat capacity predictions.

Parameter	Study 1	Study 2	Study 3	Study 4	Units
K_g^{ref}	3.2	3.2	Varies	Varies	GPa
K_g'	0	0	Varies	Varies	MPa/K
K_∞^{ref}	3.2	3.2	Varies	Varies	GPa
K_∞'	0	0	Varies	Varies	MPa/K
α_g^{ref}	0	Varies	600	170	$10^{-6}/\text{K}$
α_g'	0	Varies	0	0.4	$10^{-6}/\text{K}^2$
$\alpha_\infty^{\text{ref}}$	0	Varies	600	600	$10^{-6}/\text{K}$
α_∞'	0	Varies	0	0.2	$10^{-6}/\text{K}^2$
C_g^{ref}	Varies	1.63	1.63	1.63	$\text{kJ}/(\text{kg}\cdot\text{K})$
C_g'	Varies	0	0	0	$\text{J}/(\text{kg}\cdot\text{K}^2)$
C_∞^{ref}	Varies	2.11	2.11	2.11	$\text{kJ}/(\text{kg}\cdot\text{K})$
C_∞'	Varies	0	0	0	$\text{J}/(\text{kg}\cdot\text{K}^2)$

The parameters varied in the constant pressure heat capacity studies are collected in Table 2-3. All of these parameters can influence the constant pressure heat capacity. Four studies were pursued:

1. the isochoric heat capacity and heat capacity temperature sensitivities, C_g^{ref}, C_g', C_∞^{ref}, C_∞',
2. the volumetric coefficients of thermal expansion and their temperature derivatives α_g^{ref}, α_g', $\alpha_\infty^{\text{ref}}$, α_∞',
3. the bulk moduli, K_g^{ref}, K_g', K_∞^{ref}, K_∞', with a constant volumetric coefficient of thermal expansion, and
4. the bulk moduli with reasonable rubbery and glassy coefficients of thermal expansion.

We look at the role of glassy and rubbery isochoric heat capacities and their temperature derivatives on the predicted isobaric heat capacity during cooling in Figure 2-4. When the CTEs are turned off, there is no volume change on cooling, and so in this special case, the isochoric and isobaric heat capacities are the same, which was analytically verified previously. Here, the overall heat capacity response is constant for the first and simplest case where the isochoric heat capacity is only rubbery in Figure 2-4(a). As expected, the heat capacity is constant with temperature. As the glassy isochoric heat capacity is made different (the orange line) from rubbery, we see a reduced heat capacity in the glassy state and an unusual negative slope. Next, the glassy temperature derivative to the glassy isochoric heat capacity is turned on (the green curve). That curve shows an even bigger drop in the glassy state as the glassy heat capacity is made smaller with cooling. However, the most important and noticeable change occurs when the rubber heat capacity temperature derivative is turned on. This change shifts the heat capacity curve significantly upward.

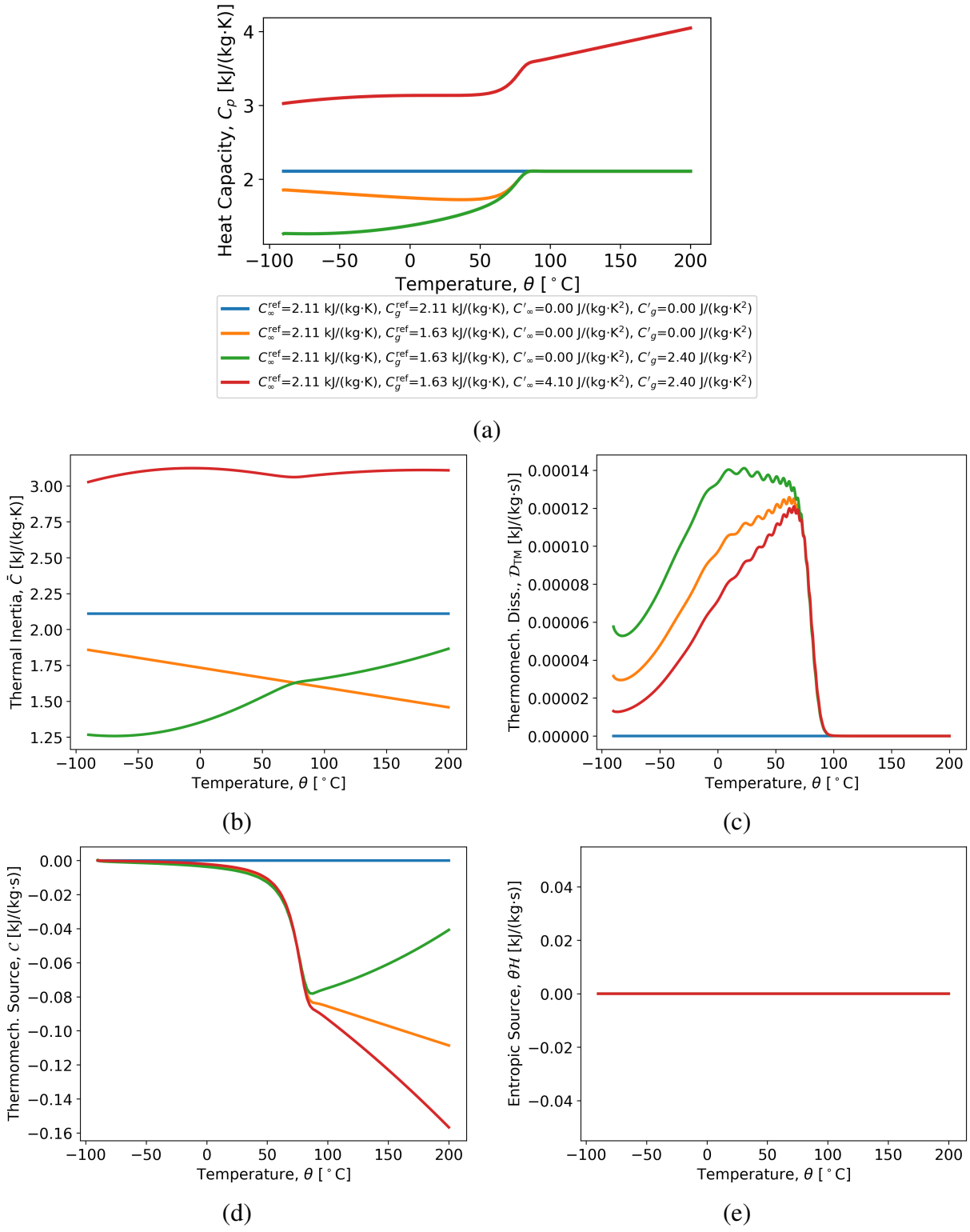

Figure 2-4. Parametric study on the role of isochoric heat capacities and their temperature derivatives on the overall isobaric heat capacity response during cooling. The four contributions to the isobaric heat capacity in Equation (2.42) **are shown term by term. Study 1 in Table 2-3.**

To gain intuition about why these changes occur, the four contributions from Equation (2.42) to the isobaric heat capacity are plotted in (b)-(e). The biggest contributor is clearly the thermal inertia term, and the reason this is so important is because there are terms in the thermal inertial associated with the isochoric heat capacity contributions that scale with the absolute temperature. Nevertheless, the combined heat capacity in (a) is reasonable across the temperature range.

In the second study, the volumetric coefficients of thermal expansion and their temperature derivatives were incrementally turned on in Figure 2-5. Here it is worth noting that the bulk modulus was a constant throughout the glass transition, but the isochoric heat capacity still has separate equilibrium and glassy values. In Figure 2-5(a), there is a mild role for the heat capacities to play, but there is a significant change when the glassy and rubbery CTEs are different. Temperature derivatives do affect the C_p slopes, but they are not as significant as the values of the CTEs themselves at the reference temperature. Again (b)-(e) show the different contributions to C_p, and again, the thermal inertial term dominates the response.

In the third study, the bulk moduli are varied with fixed and a realistic (fixed) CTE in Figure 2-6. The results in (a) are surprising. While the baseline bulk moduli have a very mild effect on the heat capacity (though not negligible), the temperature sensitivity of the bulk modulus strongly influences the C_p behavior. Simply turning on $K_g' = K_\infty' - 12\,\mathrm{MPa/K}$ changes the rubbery C_p slope from positive to negative and significantly offsets the heat capacity. This result is non-intiuitive and merits closer studies. The four contributions (b)-(e) reveal similar behavior as before. The thermal intertial is clearly the most importantant. Here, the entropic source term also becomes important in adjusting the slope from positive to negative on the rubbery side.

The fourth study is similar to the third except that realistic values of the CTE were used. But, the conclusions are unchanged. The thermal inertia term dominates, and K_g' has a huge effect

The four incremental parametric studies reveal that the prediction of the isobaric heat capacity is not trivial and is touched by many parts of the model that cannot necessarily be turned off. This finding is structural. The unusual heat capacity behavior arises from features of the model and the form of the free energy. Removing these unintuitive behaviors requires either changes to the model form or a reduced parameter space. For example, using $K_g' = K_\infty' = 0$ would make it easier to avoid the un-physical decrease of the heat capacity with increasing temperature, but would only have a minor impact of the bulk modulus.

2.4. Modifications to the Sub-Tg Equilibration Behavior

Recent efforts to predict the yield strength evolution of 828 DGEBA / DEA epoxy due to physical aging below the glass transition temperature revealed that model predictions continued to evolve many decades in time longer than experimental measurements [26]. That work suggested that the equilibrium time scale set by the viscoelastic shift factor was incorrect. Currently, the SPEC model shift factor is constitutively prescribed in Equations 2.8–2.10. We reduce the shift factor to its equilibrated form when all viscoelastic memory terms have relaxed. This equilibrated shift

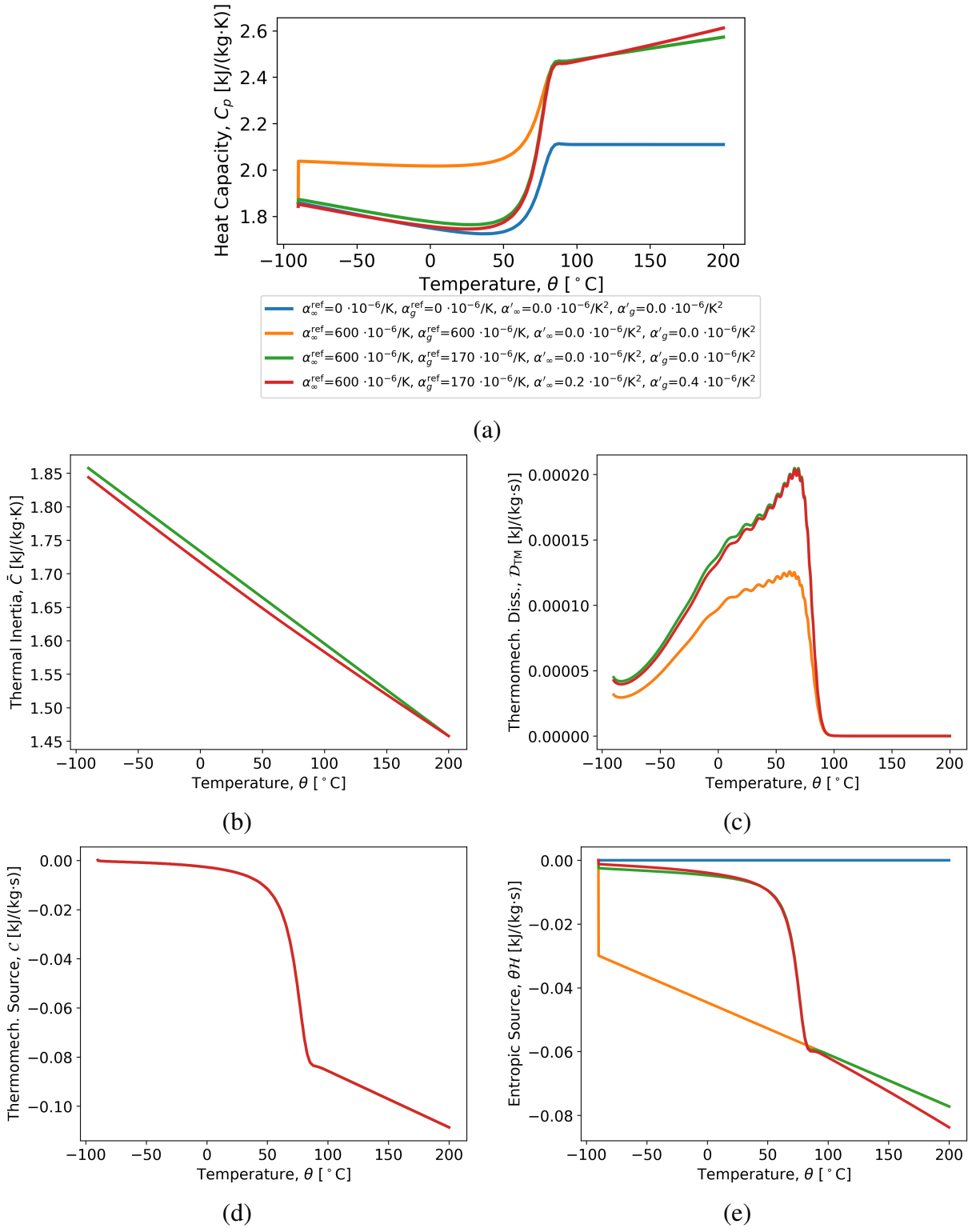

Figure 2-5. Parametric study on the role of coefficients of thermal expansion on the overall isobaric heat capacity response during cooling. The four contributions to the isobaric heat capacity in Equation (2.42) are shown term by term. Study 2 in Table 2-3.

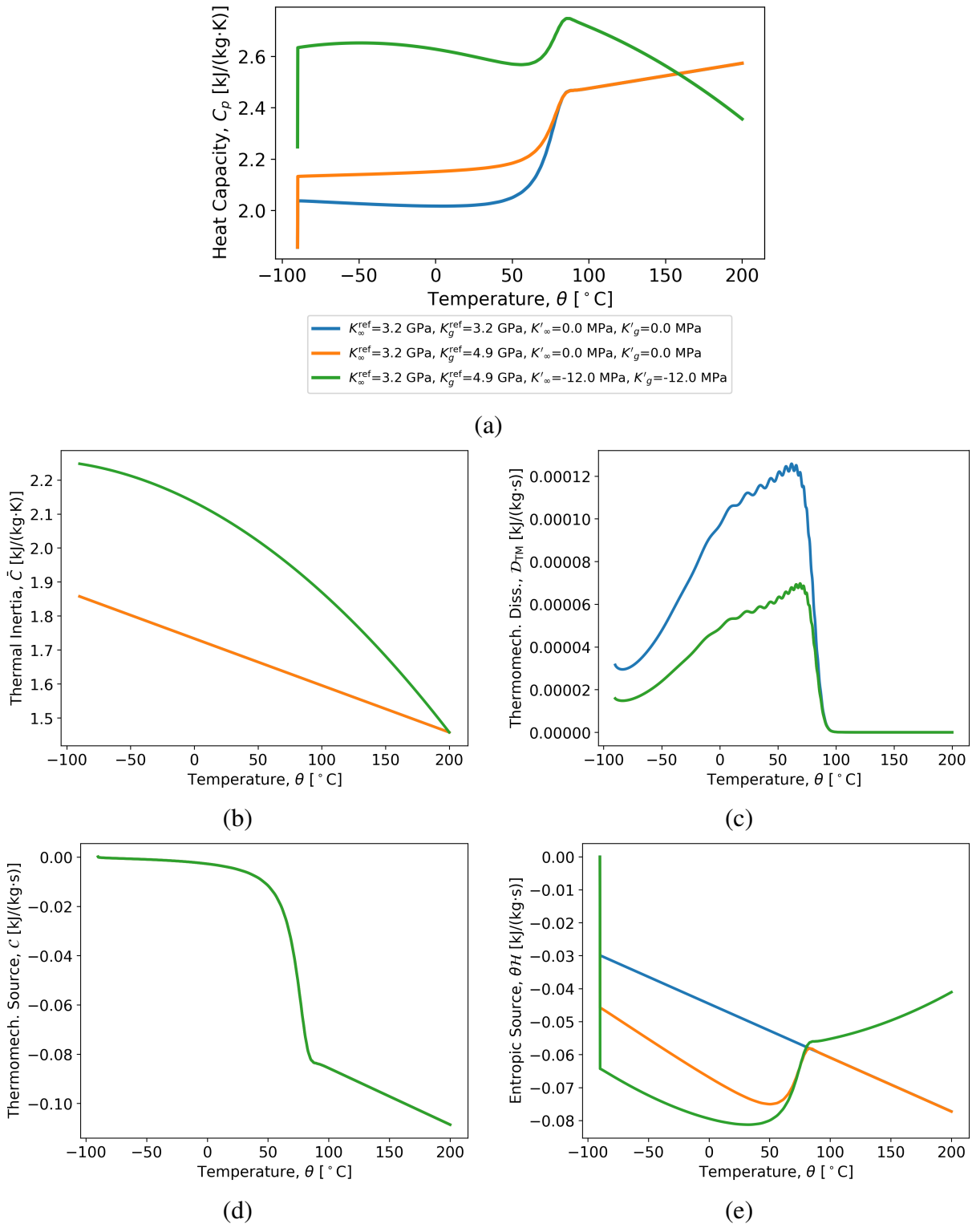

Figure 2-6. Parametric study on the role of the bulk modulus and its temperature derivatives in both the glassy and rubbery states.. The four contributions to the isobaric heat capacity in Equation (2.42) are shown term by term. Here, the CTE was chosen to be fixed at all temperatures. Study 3 in Table 2-3.

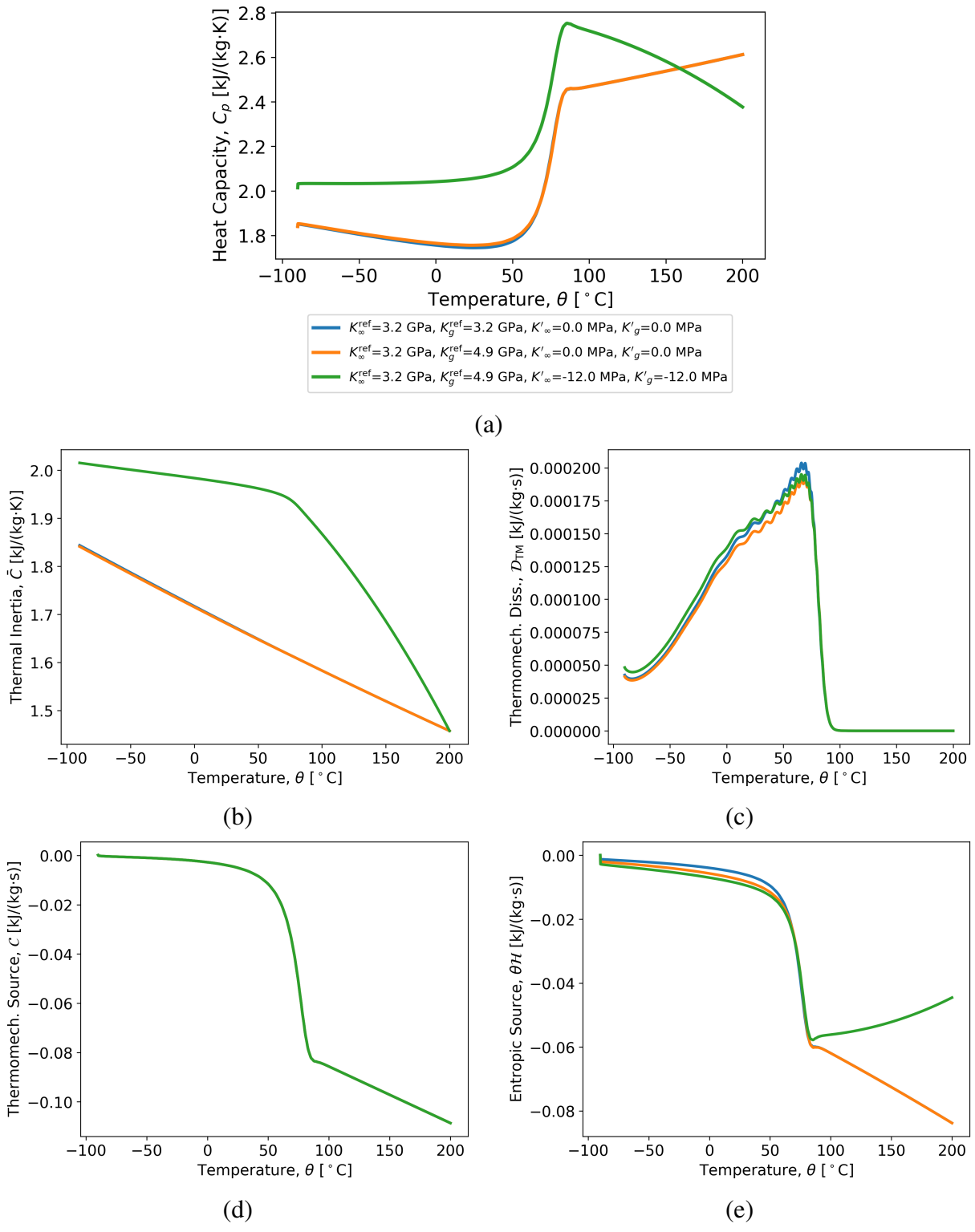

Figure 2-7. Parametric study on the role of the combination of bulk moduli and CTEs. The story is similar to Figure 2-6 with the thermal inertial term dominating. The four contributions to the isobaric heat capacity in Equation (2.42) **are shown term by term. Study 4 in Table 2-3.**

factor, which does not change in time provided the temperature and volume strain are fixed, follows the super-Arrhenius Williams-Landel-Ferry (WLF) model,

$$\log_{10} a_\infty = \frac{-C_1\left(\theta - \theta_{\text{ref}} + C_3 I_1\right)}{C_2 + \theta - \theta_{\text{ref}} + C_3 I_1} = \frac{-C_1^{\text{WLF}}\left(\theta - \theta_{\text{ref}}\right)}{C_2^{\text{WLF}} + \theta - \theta_{\text{ref}}}, \tag{2.43}$$

regardless of how far below or above the glass transition the material sits. Note in Equation 2.43, the shift factor is usually fit to time-temperature superposition data collected under ambient pressure conditions (neglected in the volume strain calculations), and so under equilibrium conditions, the volume strain $I_1 = \alpha_\infty\left(\theta - \theta_{\text{ref}}\right)$. Equation 2.43 and the associated unconfined thermal expansion conditions define the relationship between the clock C_1 and C_2 and the WLF C_1^{WLF} and C_2^{WLF} with the former used in the model and the latter set typically determined experimentally. See [21] in the `universal_polymer` section for more details. Given that Equation 2.43 diverges at $\theta = \theta_{\text{ref}} - C_2 - C_3 I_1$ or at $\theta_{\text{ref}} - C_2 - C_3\left(\theta - \theta_{\text{ref}}\right)$ under no-load conditions, the WLF form is not suitable as an equilibrated target deep in the glass. Note, we have neglected the temperature sensitivity of the rubbery volumetric coefficient of thermal expansion. In this section, we develop modifications a sub-Tg equilibration behavior for NLVE materials that is different from WLF, discuss implementation and verification in Sierra/SM/Lame, and present results using a legacy parameterization for 828DEA. Shortcomings are identified.

2.4.1. Sub-Tg Equilibration Model Theory

Literature has explored two forms of the equilibrated shift factor below the glass transition, an Arrhenius form ([18]) and a quadratic form ([12]). In these papers, near and above the glass transition behavior is observed to remain super-Arrhennius, like the WLF form now. However, below T_g, the equilibrated shift factor changes to one of two functional forms with respect to temperature (ignoring the volume strain effect). Far below the glass transition, Chandler's group argues that the quadratic form transitions back to Arrhennius behavior ([12]), but the details of the WLF-to-Quadratic-to-Arrhenius transition are unclear.

For simplicity, we will pursue Arrhenius equilibrated shift factor behavior below a transition temperature specified by the user (and WLF equilibrated behavior above that transition temperature). That is, below this user-defined transition temperature, we seek an equilibrated no-load shift factor of this form,

$$a_\infty = a_0 \exp\left(\frac{E}{R\theta}\right), \qquad \log_{10} a_\infty = \log_{10} a_0 + \frac{E}{R\theta \log 10}. \tag{2.44}$$

Equation 2.44 introduces two material parameters, E, and a_0. The user must specify the activation energy, E, as well as the temperature where the WLF and Arrhenius forms are equal under no-load conditions, θ_{match}. At the user defined matching temperature, equating the two no-load equilibrated forms determines the (constant) parameter, a_0,

$$\log_{10} a_0 = -\frac{C_1^{\text{WLF}}\left(\theta_{match} - \theta_{\text{ref}}\right)}{C_2^{\text{WLF}} + \theta_{match} - \theta_{\text{ref}}} - \frac{E}{R\theta_{match}\log 10} \tag{2.45}$$

However, there is one more subtlety. The SPEC model incorporates other non-equilibrium terms into the clock in a WLF-like form. From the SPEC model, the complete shift factor is defined in Equation 2.10, which shows that the temperature, volume strain, and shear strain history terms are all entangled in a WLF-like form in how they influence the instantaneous shift factor. Therefore, we seek an Arrhenius equilibrated form that exists within a WLF-like functional form. That is, we want under no-load equilibrium conditions,

$$\log_{10} a_\infty \;=\; \log_{10} a_0 + \frac{E}{R\theta \log 10} = \frac{-C_1\left(F\left[\theta\right] + C_3\left(\theta - \theta_{\text{ref}}\right)\right)}{C_2 + F\left[\theta\right] + C_3\left(\theta - \theta_{\text{ref}}\right)}, \tag{2.46}$$

where through some algebra, we find the equilibrium WLF form that is equivalent to a specific Arrhenius model form is,

$$F[\theta] = -\frac{C_2\left(\log_{10} a_0 + \frac{E}{R\theta\log 10}\right)}{C_1 + \log_{10} a_0 + \frac{E}{R\theta \log 10}} - C_3\alpha_\infty\left(\theta - \theta_{\text{ref}}\right) \tag{2.47}$$

Now, below the matching temperature, we replace the WLF equilibrated temperature dependence, $\theta - \theta_{\text{ref}}$, with the Arrhenius-equivalent equilibrium temperature dependence, $F\left[\theta\right]$ in Equation 2.47, such that the shift factor definition below the matching temperature (where the response is Arrhenius) is,

$$\begin{aligned} M \;&=\; F\left[\theta\right] - \int_0^t f_1\left(\theta^* - s^*\right)\frac{dT}{ds}ds + C_3\left(I_1 - \int_0^t f_1\left(\theta^* - s^*\right)\frac{dI_1}{ds}ds\right) \\ &\quad + C_4\int_0^t\int_0^t f_2\left(\theta^* - s^*, \theta^* - u^*\right)\frac{d\,\text{dev}\boldsymbol{H}}{ds} : \frac{d\,\text{dev}\boldsymbol{H}}{du}dsdu, \end{aligned} \tag{2.48}$$

$$\log_{10} a \;=\; \frac{-C_1 M}{C_2 + M}. \tag{2.49}$$

In summary, above the matching temperature, $\theta > \theta_{match}$ supplied by the user, Equations 2.8 and 2.10 furnishes the shift factor and ultimately a WLF response at equilibrium. Below the matching temperature, Equations 2.48 and 2.49, furnish the shift factor and ultimately an Arrhenius equilibrium shift factor temperature dependence.

2.4.2. Sub-Tg Equilibration Model Implementation and Verification

We discuss implementation of the Sub-Tg equilibration behavior followed by verification on simple, no-load cooling scenarios.

The sub-Tg equilibrium Arrhenius shift factor developed in the previous section was implemented into the `Spectacular` model in Sierra/SM/Lame [21]. Two new material parameters are supplied by the user, E/R (units of temperature), the ratio of the activation energy to the gas constant, and T_{match} the matching temperature where the WLF and Arrhenius equilibrium shift factors are the same. The enforcement of whether the equilibrium shift shift factor is calculated occurs through an `if` control block directly checking whether the temperature is above or below the matching temperature, which affects how the term M used in the shift factor calculation is

determined. See Equation 2.48 for the Arrhenius form and recall that if the response is WLF, then $F[\theta] = \theta - \theta_{\text{ref}}$.

The implementation of the `Spectacular` model is similar in its time integration strategy to the `universal_polymer` model [21]. A key feature of the time integration scheme is a Newton loop to determine the shift factor at the mid-step of the time discretization in which all hereditary integrals have been properly integrated with the shift factor through the time step. The WLF form has a particular temperature sensitivity during the Newton loop, and the Arrhenius form has a different sensitivity. We did not update the temperature sensitivity as we did not see a significant performance hit when we used the WLF temperature sensitivity the whole time. Hence, the implementation of the Sub-Tg equilibrated form was non-invasive and straightforward.

Analytic solutions are difficult for history dependent NLVE constitutive models. Since the shift factor definition was the only piece of the model we changed, verifying that the corrected equilibrated shift factor was produced was the focus of our verification efforts. To that end, we took a legacy calibration of 828DEA in [26] and modified the parameterization to have just one relaxation function with just a single Prony time. At this point, two different parameterizations were considered, one with a Prony time of 1 second and the other with 1 microsecond. The case with a microsecond was anticipated to remain in equilibrium much longer during cooling into the glassy state. We then considered two cases. First, the matching temperature, T_{match} was 50 °C below the reference temperature, and second, the matching temperature (71 °C) was set to 4 °C below the reference temperature (75 °C). In each case, the $E/R = 503E3/8.315 = 60493$ Kelvin based on preliminary estimates (unpublished) for the activation energy for 828DEA corresponding to this sub-Tg Arrhenius equilibration behavior. All four models (two matching temperatures by two single Prony times) were subjected to the same thermal history. The temperature started at the reference temperature (75 °C), heated to 105 °C for 30 minutes, cooled at 1 °C per minute to 50 °C , and then the temperature was held and the material was allowed to equilibrate. All steps were under stress free conditions. The shift factor temperature histories for both cases for each matching temperature condition are shown in Figure 2-8 with an independent axis chosen to show Arrhenius behavior.

For the WLF only original model in Figure 2-8(a), the one second Prony time quickly falls out of equilibrium and departs from the WLF line (purple dashed and green). When the low temperature of 50 °C is reached, the model predicts that the shift factor slowly approaches the equilibrium value ($\log_{10} a_\infty \approx 10^9$). By contrast, the one microsecond Prony time model falls out of equilibrium (stops tracking the WLF line) only briefly and then rapidly equilibrates during the hold at 50 °C . The main message from the old model was that deep in the glass, the equilibrium shift factor is very large, and most Prony times will not equilibrate. And, if the temperature is decreased further, the Prony times can never equilibrate as the equilibration target is not meaningful (goes singular and then reverses sign).

The updated model and implementation are evident when the matching temperature is much closer to the glass transition (reference temperature in this case) as shown in Figure 2-8(b). Here, the model with the one second Prony time falls out of equilibrium roughly around the temperature where the model transitions to Arrhenius equilibrium behavior. The cooling response is noticeably different below this temperature between the one second Prony time models in Figures 2-8(b) and 2-8(a) with the updated model following a much lower shift factor vs. $1000/\theta$

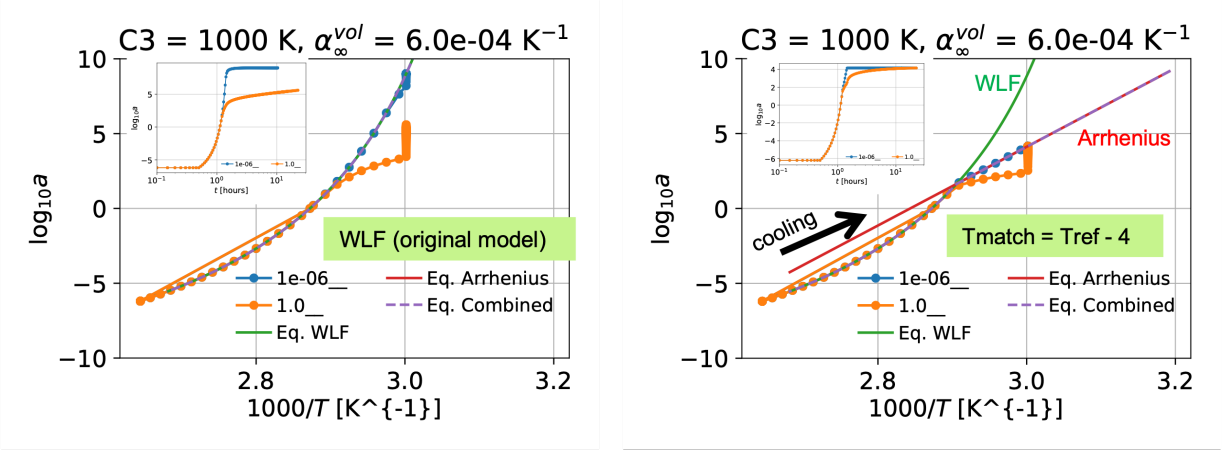

(a) (b)

Figure 2-8. Verification simulations of the original (WLF-only) model (a) and the model in which below $\theta = \theta_{\text{ref}} - 4$, the model equilibrates to the Arrhenius temperature dependence. Analytic functions are lines, and orange and blue symbols correspond to Sierra simulations. The insets show the time history of the shift factor.

tracectory on further cooling. When 50 °C is reached, the one second Prony time model is able to equilibrate fully to the Arrhenius equilibrium value of approximately 10^4 as seen in the inset. By contrast, this equilibration did not happen over the same time scale for the WLF only model. The one microsecond time Prony time model remains equilibrated during the entire simulation first following the WLF behavior and then the Arrhenius behavior.

Figure 2-8, confirms that the Sierra implementation is correctly producing the right equilibrium behavior in temperature space even when the model first falls out of equilibrium and is then given time to equilibrate.

2.4.3. Sub-Tg Arrhenius Simulations with the Legacy 828DEA Parameterization

In this section we reproduce the no-load, isothermal aging followed by compression through yield for 828DEA with the updated sub-Tg Arrhenius equilibration behavior. The model parameterization and details of aging and compression simulations were documented in detail previously [26]. He we will only briefly discuss the scenarios run and how the model parameterization was modified to reflect the updated Arrhenius equilibrium shift factor. The first step was to select a temperature below which the data suggested the equilibrium behavior was not Arrhenius. We analyzed the shift factor vs. temperature developed from both a vintage 2016 shear master curve (that was used in the previous citation) as well as from a new master curve developed in this work and reported in the experimental chapter. We found that the shift factor departed from WLF behavior near 71 °C or about 4 °C below the reference temperature. Plotting the base 10 logarithm of the shift factor against $1000/\theta$ in Figure 2-9 for both the vintage and new shear master curve time temperature superposition data, we were able to clearly identify a linear relation, which is a strong indicator of exponential behavior.

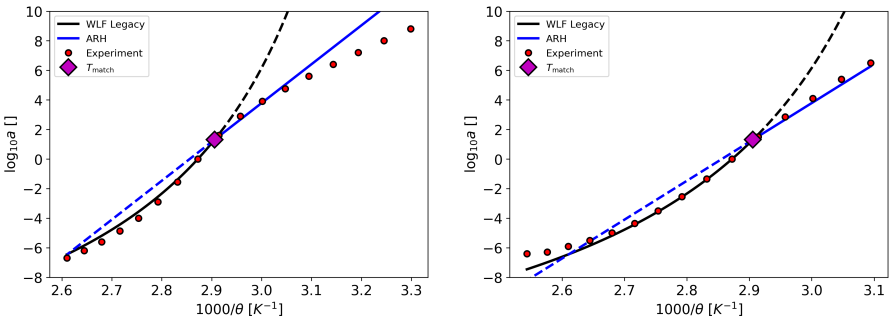

(a) Vintage shift factor (b) 2021 cold-to-hot shift factor

Figure 2-9. Estimation of the sub-Tg Arrhenius activation energy governing the equilibrium Arrhenius response for $\theta \leq \theta_{\text{match}} = \theta_{\text{ref}} - 4$. The same $E/R = 60530$ K is used for both parameterizations with a common matching temperature 71 °C (344 K). The dashed lines show the function forms that are no longer the equilibrium targets in the particular temperature regime

The activation energy is better behaved against the 2016 shift factor data compared with the 2021. Near the matching temperature, the activation energy found is reasonable for both independent shift factor data sets, but for the 2016 data, one clearly sees that the material stays in equilibrium (following the Arrhenius behavior) until at the colder temperatures, the shift factor falls below the equilibrium condition (falls out of equilbrium). For the newer data set, low enough temperatures were not reached to see the model depart from equilibrium. Since our objective is to determine the effects of this model change, we proceed with this matching temperature 71 °C or 344 K and $E/R = 60530$ K.

With this model parameterization change in the legacy model from [26], we simulated the 55 °C isothermal aging followed by compression through yield. A simpler thermal protocol was followed than was done experimentally. Specimens started at the reference temperature (75 °C), heated by 30 degrees and held for 30 minutes, cooled to 55 °C at 1 °C per minute, aged for a prescribed aging time, and then compression tested at 0.01 per minute through yield. This idealized temperature history as well as the temperature history (approximately) used experimentally are shown in Figure 2-10. Note that log time scaling is uses to show the different aging segements, but cooling and reheating segments always occur at 1 °C per minute. The results of the original model form (WLF only–column 1) and the new model form with the WLF to Arrhenius equilibrium shift factor switch are presented in Figure 2-11. As expected with the change in model form, the shift factor during cooling is very different for the model that equilibrates to the Arrhenius temperature function even though the model quickly falls out of equilibrium for both cases (WLF only and WLF–Arrhenius) in Figure 2-11 and specifically in 2-11(c) and 2-11(d). With the original (WLF only) model having a higher shift factor, yield is also correspondingly higher compared with the new model form. Clearly, the sub-Tg behavior is different and promising, but to use it, the 828DEA model must be re-parameterized.

It is finally worth noting that the rate of change of yield with respect to aging time is similar for both the WLF and WLF-Arrhenius model forms at about 4 and 5 MPa per decade of aging time in hours for the two models respectively. This rate of change is controlled by how quickly the

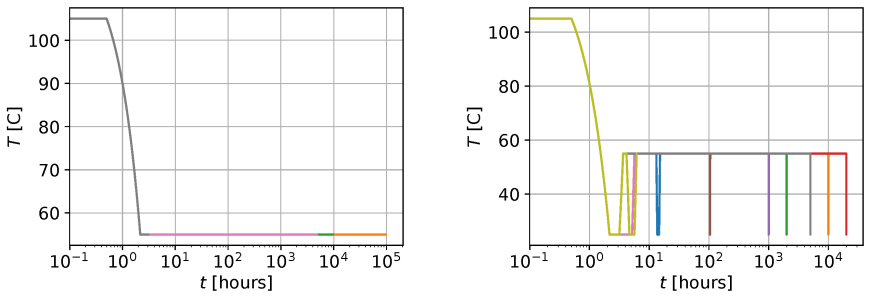

(a) Simplified Temperature History (b) Experimental Temperature History

Figure 2-10. log time temperature histories, idealized (a) and approximately experimental (b), for the no-load isothermal aging followed by compression through yield for 828DEA in [26]. Different aging times correspond to differently colored curves.

thermal hereditary integral is relaxing in the shift factor definition. This similarity occurs even though the shift factor time histories are clearly different from the two models. The fact that the WLF–Arrhenius model relaxes slightly faster is consistent with the shift factor being lower for that model.

The next step was to simulate the more complicated experimental temperature history protocol as depicted in Figure 2-10(b). Unfortunately, these simulations produced unexpected behavior on reversal of temperature (from cooling to heating) that we have yet to understand whether it is a deficiency of the theory or a bug. However, due to these unexpected behaviors, the sub-Tg model form could not be used reliably, and so it was not used throughout the rest of the SAND report. This topic remains one that must be re-examined in the future.

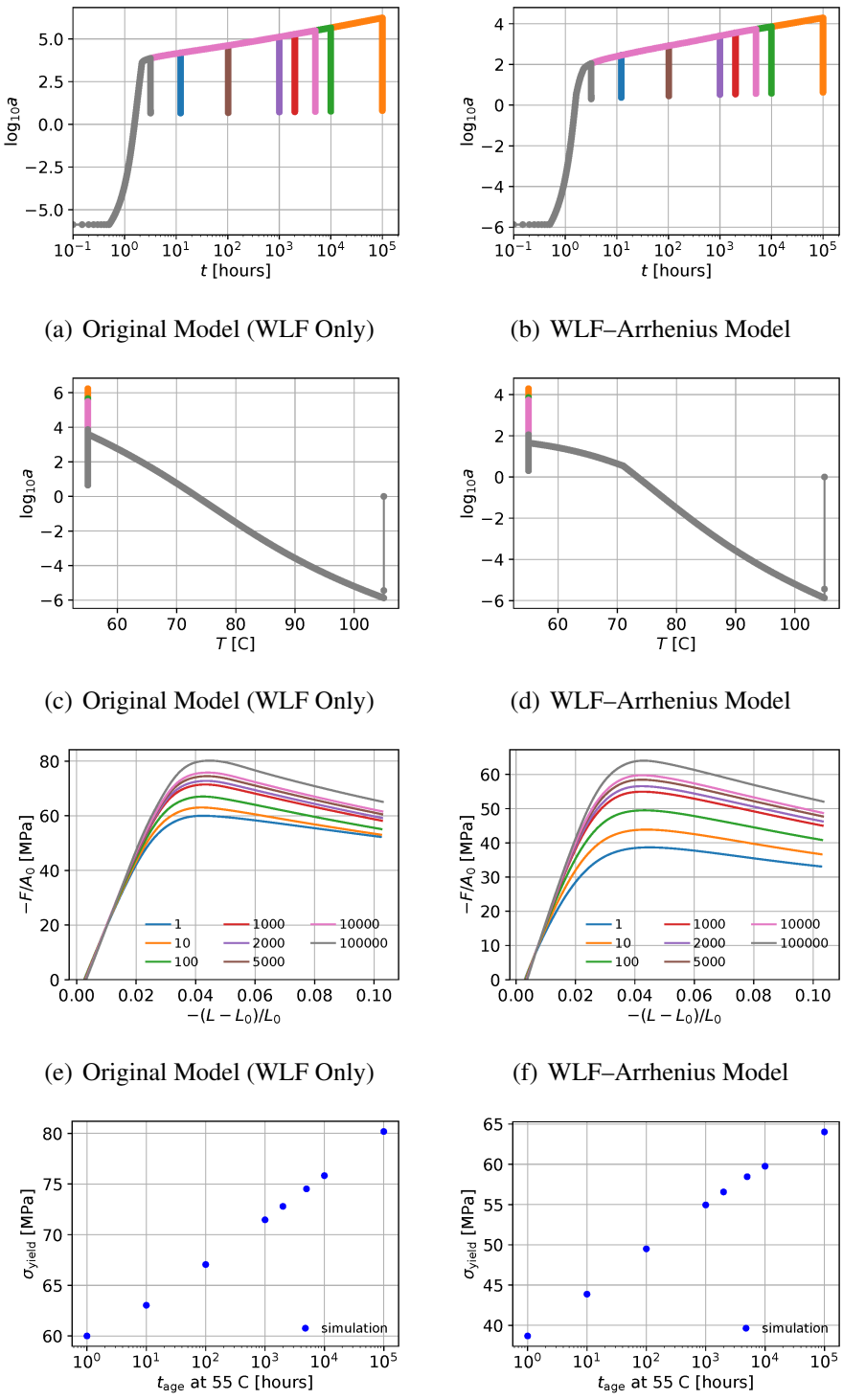

(a) Original Model (WLF Only)

(b) WLF–Arrhenius Model

(c) Original Model (WLF Only)

(d) WLF–Arrhenius Model

(e) Original Model (WLF Only)

(f) WLF–Arrhenius Model

(g) Original Model (WLF Only)

(h) WLF–Arrhenius Model

Figure 2-11. Isothermal aging at 55 °C for 828DEA followed by compression through yield. The model parameterization was taken from [26] and used to generate predictions for the original model (column 1). The WLF-Arrhenius modified parameterization is shown in column 2. Aging times are listed in the stress-strain curves with differently colored curves and number corresponding to aging times in hours at 55 °C .

3. EXPERIMENTAL CALIBRATION AND AGING DATA

In this chapter, we summarize the experimental methods, data analyses, and data archival for experiments performed in conjunction with this milestone during FY21. Additionally, experimental data that were previously collected and documented (in particular, specific physical aging tests), and that are used in this report, are also briefly summarized. By putting the data in one place and instructions to access it, we hope to expedite future modeling efforts.

Two materials were freshly experimentally characterized for the purpose of fully calibrating the SPEC constitutive model [4] as implemented in the `Spectacular` model in the finite element code Sierra/SM/Lame [21, 25]: Epon 828 Diglycidal ether of bis-phenol A (828DGEBA) cross-linked with di-ethanolamine (DEA), which we refer to as 828DEA, and 828DGEBA cross-linked with Jeffamine T403, which we refer to as 828T403. Details of the curing procedures that were followed were previously reported [17, 9]. These materials are similar. They are step-growth, amine cured epoxies with unaged glass transitions near 75 (828DEA) and 90 °C (828T403).

While 828DEA is widely used in the Sandia mission space, it has remaining reaction potential via alternative reaction pathways near and above the glass transition [17]. Therefore, experimental characterization and aging measurements of 828DEA may involve chemical changes, which can and will complicate interpretation of aging test results. We will specifically report in the last section of this chapter on targeted studies to understand how the shear master curve and time-temperature superposition are affected by chemical changes to the material during characterization testing. The known complexity of possible chemical aging both during characterization and aging measurements of 828DEA was carefully considered in tests performed in this work, but it also motivated us to consider 828T403 as a material that would be simpler to assess SPEC model physical aging predictions.

828T403 was selected as a similar high glass transition temperature epoxy thermoset suitable for electronics packaging as with 828DEA [2], but it does not have remaining reaction potential near its glass transition. Hence, our intention was that we could attribute changes in 828T403 material behavior solely to physical aging, which is the only aging mechanism that the `Spectacular` (SPEC) model predicts. As we will find, even 828T403 exhibits clear signs of chemical changes at elevated temperatures. But, for the majority of calibration and aging data presented and used for 828T403, the dominant aging mechanism was physical.

The chapter is divided into three sections. First, we present all characterization and aging data for 828DEA. Second, we present companion data for 828T403.

3.1. 828DEA Experiments

3.1.1. Isofrequency Temperature Sweep Under Oscillatory Shear

Small deformation, oscillatory shear tests were performed on 3 x 6 x 50 mm torsion bars of 828DEA using an ARES2 rheometer at 1 Hz oscillation. The specimens were taken to 200 °C to erase any viscoelastic memory and then cooled at 1 °C per minute in order to maintain thermal equilibrium (constant temperature that tracks the prescribed temperature) within the sample. When room temperature was reached, the temperature switched to heating at 1 °C per minute until 200 °C was reached. These temperature spans well encapsulated the full glass transition which was expected to be around a 30 °C span around 75 °C . During the temperature scans, the specimens were subjected to steady state oscillatory shear. The in-phase and out-of-phase (storage and loss) shear moduli were recorded using the machine software. Two repeat tests were performed, and consistent material data were extracted. An example of this isochronal temperature sweep is provided in Figure 3-1. One measure of the glass transition is the peak of the loss tangent, also referred to as "tanδ", which is the ratio to the loss and storage shear moduli [13]. In Figure 3-1, the peak of loss tangent for both initial upward sweeps is around 85 °C . After exposure to the 130 °C and 200 °C higher temperatures, the glass transition is shifted upwards such that on the down and upward sweeps, peak of the tanδ has shifted by 1 and 5 °C for the 130 and 200 °C high temperatures respectively. The obvious change in glass transition indicates that the high temperature exposure has induced chemical changes (chemical aging) in the material, and that the materiald does not represent "as-received" material after such high thermal excursions. Therefore, we will focus on the "initial up" data as an indicator of the glass transition although such data does include some viscoelastic unknown history.

3.1.2. Isothermal Frequency Sweeps and the Shear Master Curve

As in subsection 3.1.1, small deformation, oscillatory shear tests were performed on the same dimensioned torsion bars of 828DEA using an ARES2 rheometer. Here, the specimens were taken to temperatures in 5 °C increments, stepping down from 120 °C to 50 °C or from 50 °C stepping upward in 5 °C increments until 120 °C . In each case, when a temperature was reached, the specimen was held for 5 minutes to thermally equilibrate, after which, the specimen was subjected to oscillatory shear over a range of frequencies from 0.01 to 100 Hz. The storage and loss moduli were collected at each frequency and at each temperature.

Note that for both tests, the specimen was initially taken to 120 °C for 30 minutes to erase viscoelastic memory. For the case of sequential cooling, the test commenced immediately with the first frequency sweep. For the other test case, after the thirty minute hold at 120 °C , the specimen was cooled at 1 °C / min to 50 °C , allowed to soak for 5 minutes to thermally equilibrate, and then frequency sweeps commenced associated with the upward incremental temperature scan.

For both temperature history tests, the ARES2 software was used to extract the storage and loss moduli vs frequency at each temperature. Following the tests, a shear master curve from each test was constructed assuming time–temperature superposition (TTS). See [13] for more details on

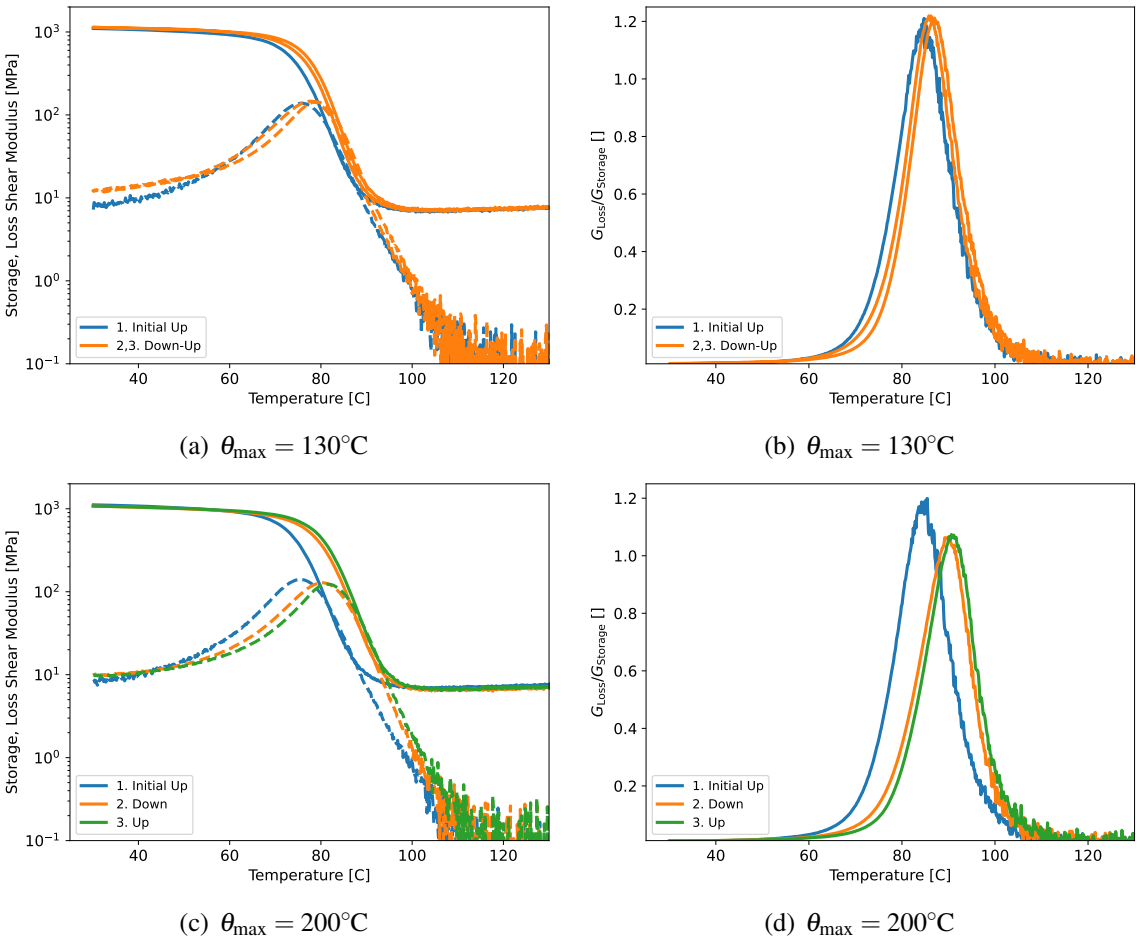

(a) $\theta_{max} = 130°C$ (b) $\theta_{max} = 130°C$

(c) $\theta_{max} = 200°C$ (d) $\theta_{max} = 200°C$

Figure 3-1. 828DEA Isofrequency temperature sweeps at 1 Hz oscillation, 1 °C per minute, 0.1% strain amplitude, and applied from room temperature to 130 or 200 °C , down to room temperature, and then back to 130 or 200 °C . The maximum temperature is clipped so that the plots focus on the glass transition.

master curve construction and TTS. In all cases, the reference temperature, where the viscoelastic shift factor is unity, was set to 75 °C .

A comparison of the shear master curves plotted at the reference temperature (75 °C) for the two temperature histories as well as a master curve constructed from legacy isothermal frequency sweep data of unknown thermal history is shown in Figure 3-2. There are significant differences between the master curves and TTS (shift factor) behavior associated with the thermal history that the specimens experienced. The green curves associated with starting hot and stepping downward spent the most amount of time (known) at elevated temperatures. In contrast, the orange curves, which cooled immediately from 120 °C to 50 °C and then collected data on heating, spent the least amount of known time at elevated temperature.

The peaks of the loss tangents (Figure 3-2(c)) were 1.6E-5, 7.9E-4, and 6.3E-4 Hz for the hot-to-cold, heat-after-cool, and vintage/unknown thermal histories respectively. Otherwise, the shear master curves had similar shapes and breadths in frequency space. This indicates that the

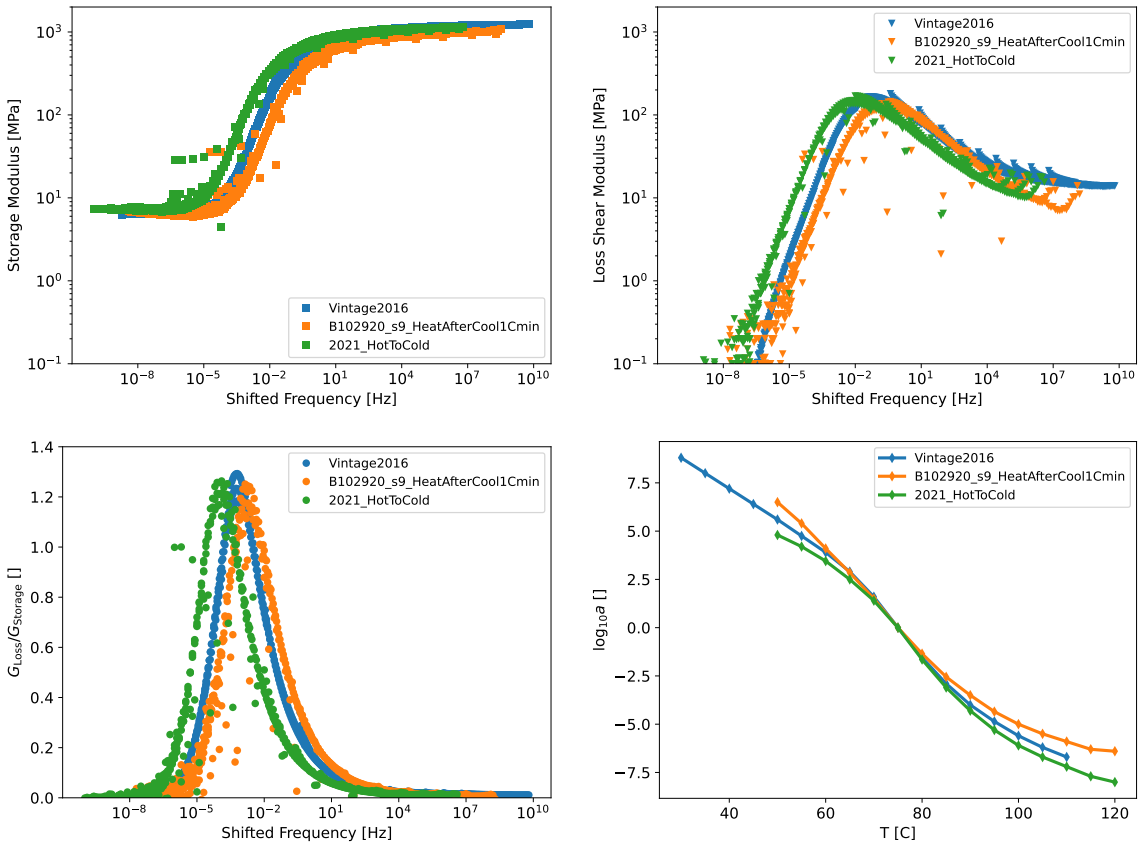

Figure 3-2. Unaged 828DEA shear master curves at the 75 °C reference temperature from three distinct temperature histories.

main effect of thermal history, which most likely arises from additional curing of the specimen during the test, is to shift the dominant relaxation time scale (dominant frequency where the loss tangent is maximized) as seen in Figure 3-2(c) at the common reference temperature of 75 °C . Here we see that the hot-to-cold dominant frequency is nearly 50 times slower than the dominant frequency of the heat-after-cool data, and the vintage data with unknown history is between the two curves. Shifting the dominant frequency downward is equivalent to increasing the dominant relaxation time which is equivalent to raising the glass transition temperature, which again confirms that time at high temperature causes 828DEA to be significantly different from the "as-manufactured" material used in the mission space.

While the master curves appear to simply shift from the different thermal histories, the time-temperature superposition behaviors (shift factor vs. temperature) are forced by construction to pass through 1 at the reference temperature of 75 °C . While the curves are distinct in Figure 3-2(d), they change by about the same amount between 50 and 100 °C , which qualitatively suggests that the TTS behavior, adjusted for the different dominant frequencies is not substantially different amongst the three thermal histories. Further work would be needed to further verify this statement.

It is worth noting that the hot-to-cold test procedure is the most desirable procedure for well

behaved, chemically inert glass forming polymers. As the material cools slowly, it stays equilibrated for a larger portion of the temperature range and delays the effects of physical aging. In contrast, the heat-after-cooling history means that physical aging is built into the material response from the initial cooling response, and the apparent glass transition would be higher given the built in physical aging. But, in this case where remaining reaction potential exists, the heat-after-cool is likely closer to measuring the shear master curve behavior that represents the as-cured 828DEA material in applications. As these characteristic frequencies (or relaxation time scales) are important to simulating specific features of physical aging, we comment that this study reveals the importance of caution when characterizing viscoelastic materials with cure potential.

3.1.3. Thermal Strain Measurements Across the Glass Transition

The thermal strain behavior across the glass transition under controlled cooling rates is typically the next measurement performed to characterize glass forming thermoset materials for parametrizing the NLVE SPEC model [4]. Here, a mechanical probe thermal mechanical analyzer (TA Instruments 800) with a 50 mN dead load was used to measure the dimensional change of an 828DEA 11.3 x 11.3 x 11.3 mm block as the temperature was swept from room temperature to 200 °C to room temperature at 1 °C per minute. Other tests swept to colder temperatures but generally followed this protocol. The first upward sweep removed viscoelastic memory, and subsequent cool and reheat steps were used to characterize the thermal strain response across the glass transition. The measured thermal strain and its derivative with respect to temperature (linear coefficient of thermal expansion) are shown for a typical measurement in figure 3-3 for both cooling from equilibrium and then reheating. The glass transition from the perspective of thermal

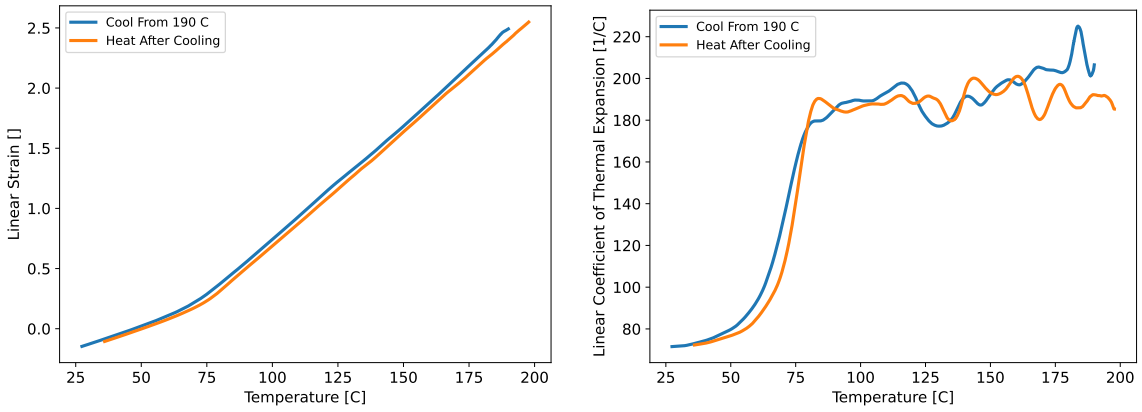

Figure 3-3. 828DEA Linear thermal strain and linear coefficient of thermal expansion from experiments on the same specimen that cooled from equilibrium to room temperature, thermally equilibrated, and then heated back well above the glass transition

strain is marked by a three fold change in apparent linear coefficient of thermal expansion (CTE), which here goes from roughly 185 parts per million per °C (PPM/°C) in the equilibrated state to approximately 70 PPM/°C in the glassy state. The transition occurs more narrowly than for the

isofrequency temperature sweep data — despite that data having problems with chemical aging. This observation will be important in the characteristic time scales for thermal expansion relaxation needed to fit the thermal strain data here. Finally, it is worth noting that the mild amount of aging from cooling acts to slightly shift the heat-after-cool data upward in temperature by a few degrees as well as to produce a small spike in the CTE as the material equilibrates (upper end of the glass transition). These features are classic physical aging signatures (see [18] or chapters 2 and 4 in [20]) and will be used in both calibration and validation.

3.1.4. Unaged Uniaxial Compression Below the Glass Transition

Uniaxial compression tests were performed at fixed temperatures and engineering strain rates on unaged 1x1 inch 828DEA cylindrical plugs on an MTS load loadframe with a 5 kN load cell. Axial strain was measured with a mechanical extensometer to remove any compliance issues within the setup. The typical testing procedure involved first a controlled thermal history to get the specimens to room temperature where they stayed for uncontrolled periods of time. Little physical aging occurs at room temperature which is 50°C below the as-cured glass transition. This low temperature holding was approximated as a 1 h hold in simulations of the specimen thermal history, but could have been neglected without loss of fidelity.

When it was time to test at a particular temperature and strain rate condition, specimens were heated or cooled from room temperature to the desired test temperature (-50, 25, and 50 °C) by placing them in the oven at the test temperature and allowing them to sit for 30 minutes to thermally equilibrate. After 30 minutes, they were subjected to uniaxial compression to 15% compressive engineering strain (0.15 inches) as limited by the extensometer range.

These tests characterized Young's modulus, the yield strength (taken to be the maximum of the engineering compressive stress vs. compressive strain curve), and compressive strain at yield for unaged specimens at specific temperatures and strain rates. Three repeats at each condition were performed. Typical compressive stress vs. compressive strain curves at -50, 25, and 50 °C , and for each condition at 1E-2, 1E-1, and 1E0 per minute compressive engineering strain rate, are provided in Figure 3-4.

In Figure 3-4, some pre-processing of the data were performed to remove the toe region of the stress-strain curves via the following method. A secant slope was calculated between 0.5 and 1% compressive strain. The strain at which this slope, applied to the location at 1% compressive strain, intersected the axis at zero stress was removed from the strain data. This analysis method was applied to all stress-strain data in this report. Typically toe regions involved strain removals of less than 0.5%.

The same method to calculate the slope for the toe region removal was used to compute the initial Young's modulus for each test. The yield strength was taken to be the maximum of the stress-strain curve, and the strain at yield was the strain at this point. Young's modulus, yield strength, and yield strain were all calculated on the corrected data. Linear regressions were fit against temperature and strain rate and reported in the charts in Figure 3-5.

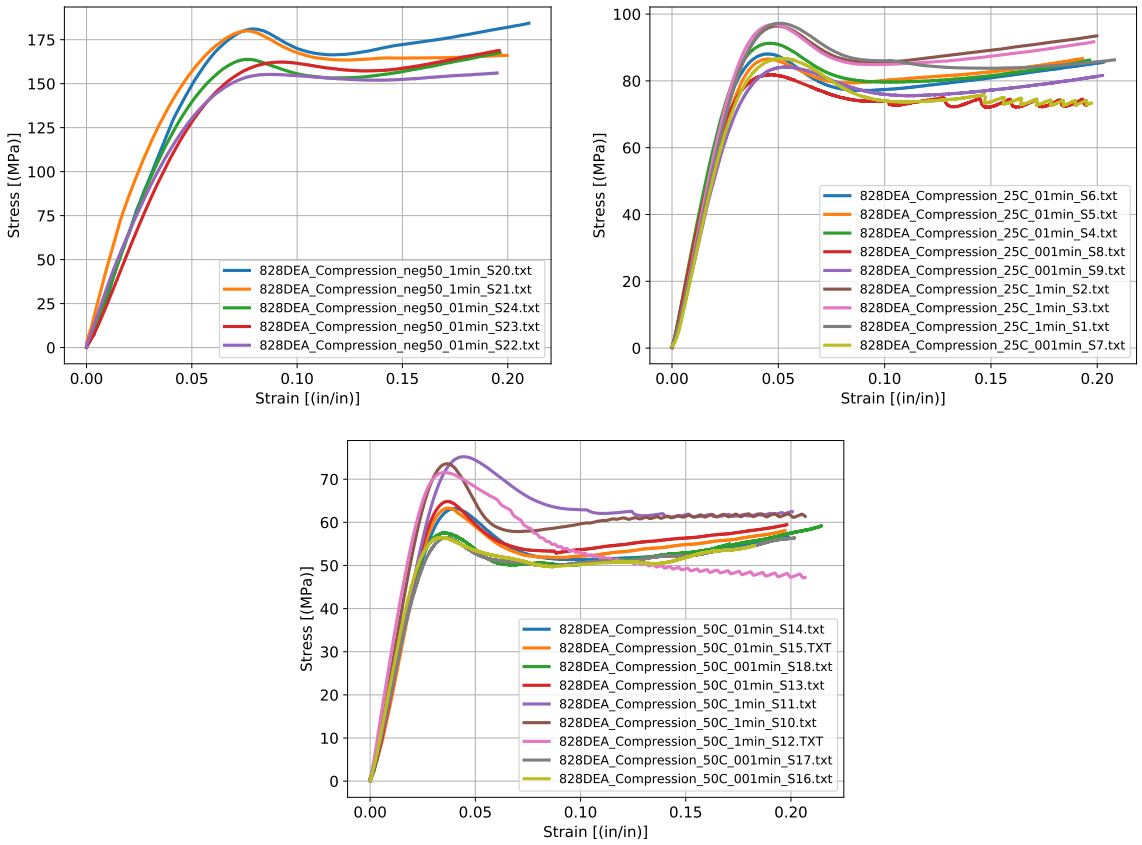

Figure 3-4. Unaged 828DEA uniaxial compression tests below the glass transition temperature at different strain rates and temperatures. All results are reported in engineering stress and strain measures.

The main findings from Figure 3-5 are that the yield strength and apparent Young's modulus increase with strain rate and reduced temperature as observed in many other glass forming polymers. However, the strain at yield does not appear to change with strain rate and only mildly changes with temperature. Note the high uncertainty at -50 °C where fewer tests were performed.

All tests show substantial softening post yield. As shown previously ([27]), this softening is associated with localization of deformation within the specimen (a "forest" of shear bands at 45 degrees from the loading direction — the maximum resolved shear direction — or a large barreled region). Quantitative data cannot be extracted from the test without modeling the test in full detail and attempting to resolve such localized deformation.

3.1.5. Unaged and Aged Uniaxial Tension

Uniaxial tension tests were performed at 50 °C in order to assess the extent to which yield is dependent on pressure or volume strain in contrast to compression tests at the same conditions.

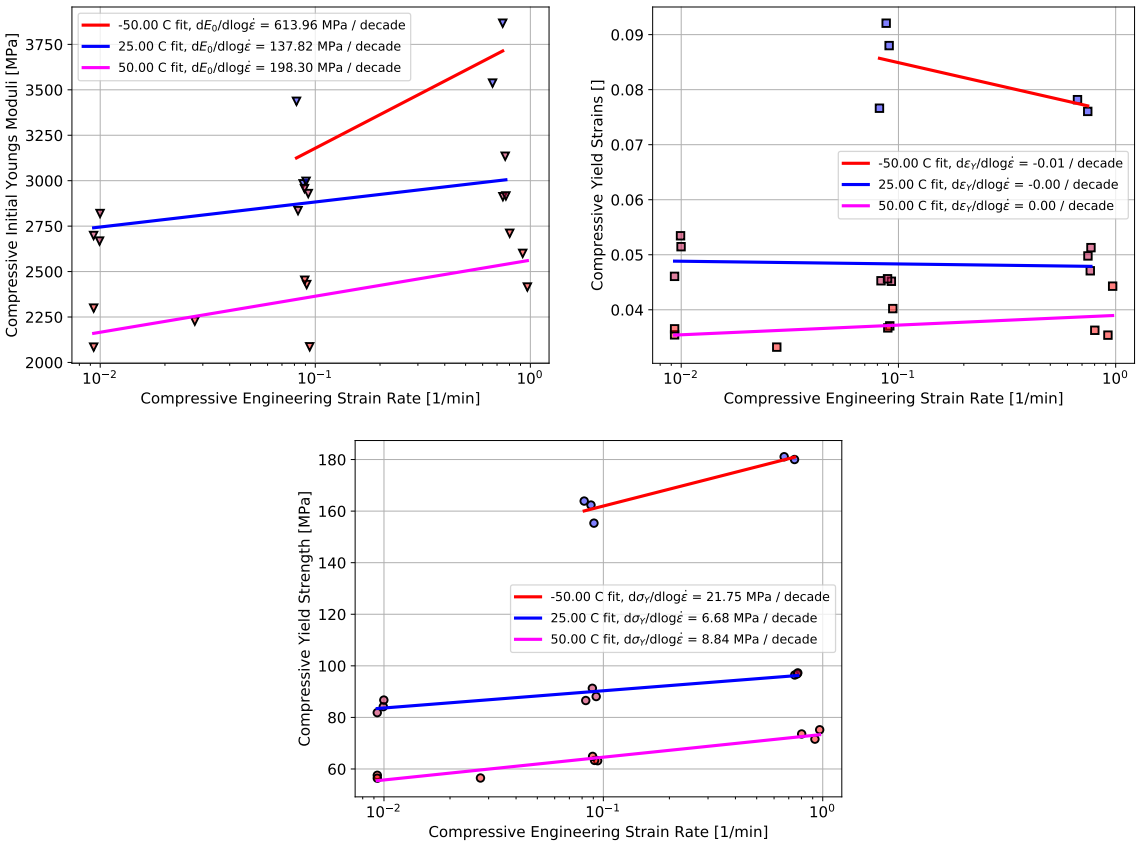

Figure 3-5. Unaged 828DEA uniaxial compression test analysis of Young's modulus, yield strength, and strain at yield across temperatures and strain rates.

Dogbone specimens following ASTM standard D638, type 1 geometry were used. Specimens were cast in the dogbone mold and cured following the standard schedule.

Two thermal protocols were used. First, specimens as cured were setup for testing, and the oven was taken to 50 °C and allowed to thermally equilibrate. These specimens have an unknown physical aging history since the condition prior to the 50 °C test are not fully know. The second set of specimens were "annealed" and essentially were cooled from 105 °C to 50 °C , allowed to thermally equilibrate for several minutes prior to testing. Specimens were tension tested in the Instron load frame with the 5 kN load cell and a mechanical extensometer to measure and control strain. The loading rate was approximately 0.01 strain per minute. Most specimens yielded before failure. Typical test results are shown in Figure 3-6. For reference to the equivalent compression tests at 50 °C , see Figure 3-4(c). The tension yield (maxima of the stress-strain curves) are slightly smaller than the compression data at the same slowest strain rate conditions when one focuses solely on the "annealed" specimens. Typical yield strengths are around 46 MPa in tension at 0.01 per minute strain rate at 50 °C vs. about 57 MPa in compression at the same strain rate and temperature. In both cases, strain at yield is nearly 3 % tension or compression.

This difference was welcomed as, at first, we thought it clearly showed the role that pressure and/or volume strain has on the material and model behaviors. But, it is worth first considering

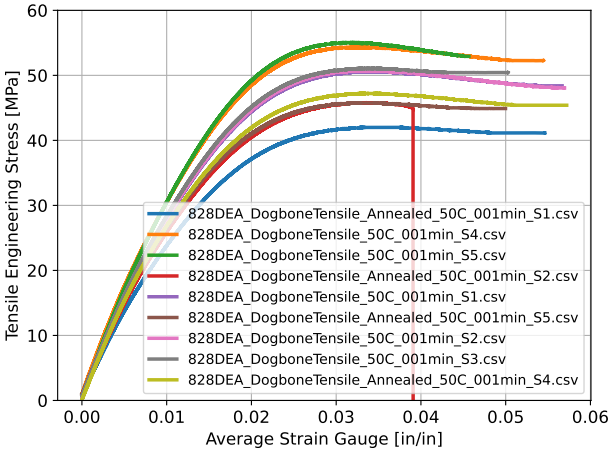

Figure 3-6. 50°C tension tests of 828DEA dogbone specimens subjected to a protocol that erased prior history ("annealed") and one with an unknown ("as received") thermal history. The sudden load drop in the red curve is associated with specimen failure.

what role geometry plays in interpreting these results. To do that, we need an estimate of the true stress at yield from both tension and compression. Noting that at 50 °C , 828DEA is 25 °C below it's glass transition, the material behavior can be idealized as glassy. From Figure 3-5(a), Young's modulus is approximately 2.2 GPa while from prior work [3], the bulk modulus was approximately measured at 5.5 GPa at 50 °C . Together, the approximate Poisson ratio is 0.433 from standard linear elasticity relations between isotropic moduli [23]. This number is reasonable given other studies of Poisson's ratio in the literature for glassy polymers [19].

Noting that the strain at yield is approximately 3% for either case, then we can estimate the area ratio between the state at yield and the undeformed area to be approximately $A/A_0 \approx 1 + 2\nu\varepsilon_{\text{yield}}$ which is 1.026 in compression and 0.974 in tension. Thus, the nominal yield strengths can be approximately transformed into true yield strengths by dividing by these area ratios. Hence, for compression, the true yield strength is approximately 54.6 MPa while in tension, the true yield strength is approximately 46.6 MPa. In other words, the relative difference in nominal stresses was 10 MPa / 56 MPa or about 18% while, the relative difference in true stresses is about 8 MPa / 56 MPa or 14%. Hence, there is a distinct difference in yield behavior between the tension and compression tests, but it is smaller when one considers (as one needs to) the true yield strengths (to remove geometry effects).

3.1.6. Differential Scanning Calorimetry of Unaged Specimens

Differential scanning calorimetry (DSC) was performed on 828DEA specimens to probe the enthalpy and heat capacity response across the glass transition. Standard transient temperature scan tests were performed in which the cooling rate was varied to affect how the specimen entered the glassy state. In a typical test, the specimen pan was placed in the chamber at room temperature, heated at 10 or 20 °C per minute to 200 °C , and immediately cooled to -90 °C at a

controlled cooling rate. The specimen was allowed to soak for 5 minutes to thermally equilibrate. Then it was reheated at 10 °C per minute to 200 °C . This test was varied in the cooling rate from 0.5 °C / minute to 10 °C / minute although the heat rate was fixed at 10 °C / minute for maximum test resolution. The data from the slower cooling rates during the cooling phase of the tests is not quantitative, but the heating behavior, which is the main test output, is quantitative from all tests. The heat capacity during the temperature scans was extracted as the relative heat flow divided by the temperature rate. Specimens were weighed prior to the tests.

Certain tests involved a single specimen subjected to repeated down-up temperature scans while other tests used unique specimen subjected to a single up-down-up temperature scan sequence as discussed above. Multiple scans on a single specimen is preferred to reduce test-to-test uncertainty, but given that specimens see time at higher temperatures, particularly when cooled at slower rates, chemical changes to the specimens are more influential in the multiple cycle, single specimen tests.

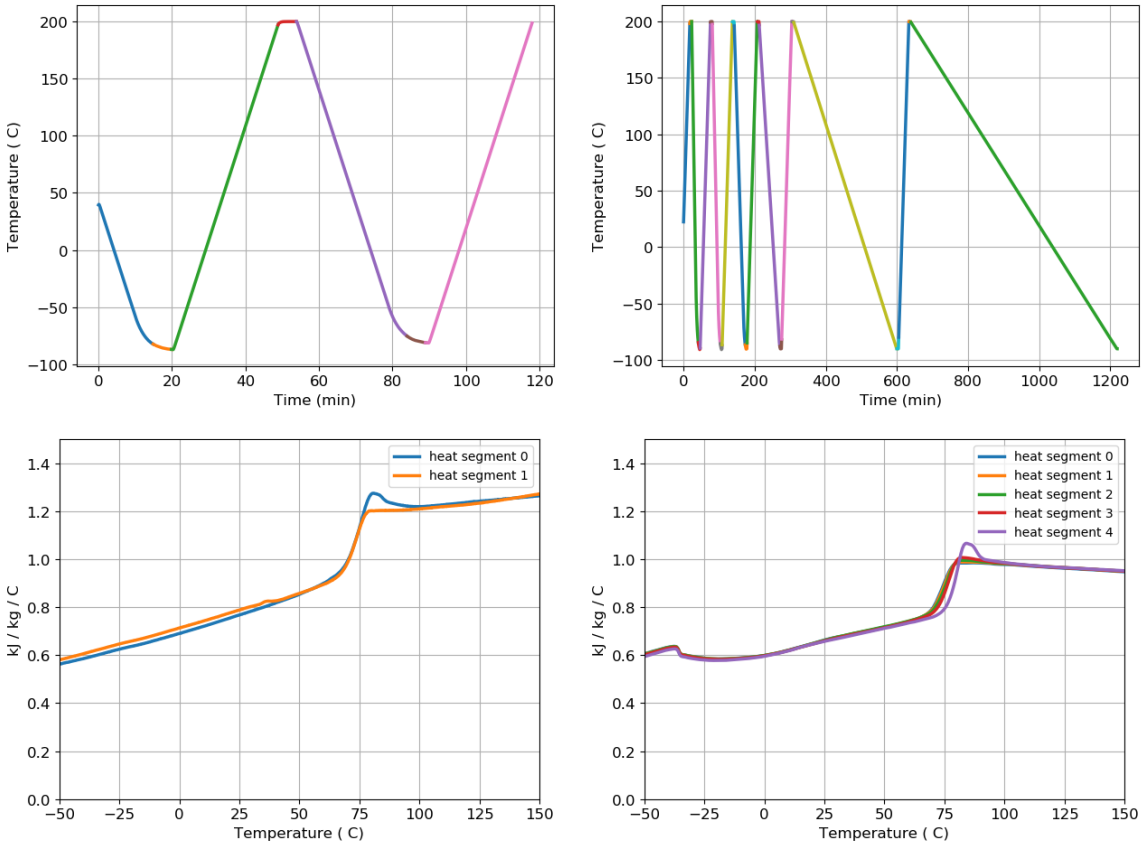

Figure 3-7. 828DEA transient DSC response under a single cooling and heating rate (a), (c), and under a variable cooling rate at a fixed heating rate (b), (d). The temperature history (top row) and specific heat capacity (heat flow / temperature rate / specimen mass) (bottom row) are shown for typical tests.

Quantitative transient DSC is tedious requiring calibrations between every run. Calibration runs were not performed between all tests. Hence, these transient DSC data sets quantitatively determine changes in the heat capacity across the glass transition, but they do not provide an

absolute value of the heat capacity itself. Because the absolute value of the heat capacity cannot be determined reliably from these tests, we used the heat capacity at 50 °C from [3] to set a common datum for all 828DEA transient DSC data sets.

Figure 3-7(c) shows that the first and second heating stage are different with the first showing an overshoot behavior. This is expected for physically aged thermoset polymer glasses [18]. The temperature history in Figure 3-7(a) shows that the first heating portion of the temperature history contains unknown thermal history prior to the test, which resulted in some physical aging. In contrast, the second heating stage occurred after the sample had been elevated well above Tg and cooled under a controlled and constant cooling rate through Tg and then reheated. These two reheating measurements show different behavior near the glass transition. Physical aging causes a delay in the recovery behavior of the sample as it is reheated, and so, much like the TMA thermal strain reheating response, a transient spike is observed in the heat capacity as the material passes through the glass transition. The height of that peak and the onset temperature during reheating at a fixed rate both shift upward the longer the material physically ages [9].

The variable cooling rate study in Figure 3-7(b) and 3-7(d) is more difficult to interpret. The expectation is that slower cooling rates would lead to higher heat capacity spikes on reheating. That is observed; increasing heating segments correspond to slower and slower cooling rates, but chemical changes also become important as a heat source and a mechanism to further cross-link the material and shift upward the glass transition. We regard the slowest cooling rate (0.5 °C per minute) as showing a combination of chemical and physical aging effects.

Specific physical aging measurements were not performed on 828DEA as measured via DSC. Hence, during the model calibration and predictions sections, we will use the variable cooling rate transient DSC measurements as a proxy for physical aging measurements.

3.1.7. Creep Under a Constant Uniaxial Engineering Stress

Creep tests were performed originally to provide data for an alternative calibration approach. But, that calibration approach was not pursued in this work. So, the creep data were used only physical aging validation. The objective of this validation was to evaluate the small deformation predictions. Under small deformation conditions, deformation induced mobility (acceleration of relaxation behavior due to deformation) is small, and the response is near linear thermoviscoelastic.

Creep experiments performed in FY21 followed a standard temperature processing history prior to the application of mechanical loads similar to the glassy compression experiments. 1x1 inch height to diameter cylindrical plugs were first held at 105 °C for thirty minutes to erase any physical memory. Then, specimens were cooled at 1 °C / min to room temperature where they were stored until testing time, at which point, specimens were placed in the oven at the desired temperature, let sit for 30 minutes to thermally equilibrate, and then were subjected to an applied engineering stress at 1 per minute strain rate until the desired stress was reached. The constant engineering stress was then held for the desired aging time, and the axial strain, as monitored by a mechanical extensometer, tracked the axial height change during the experiment. Lateral measurements were not taken. The same Instron setup used in the compression tests was used for

these creep testing. Creep was performed only at 50 °C in this test series both because the material is stiffer than when it is closer to Tg and to avoid chemical aging effects during the test.Typical creep strain and compliance measurements from the start of load application are shown in Figure 3-8.

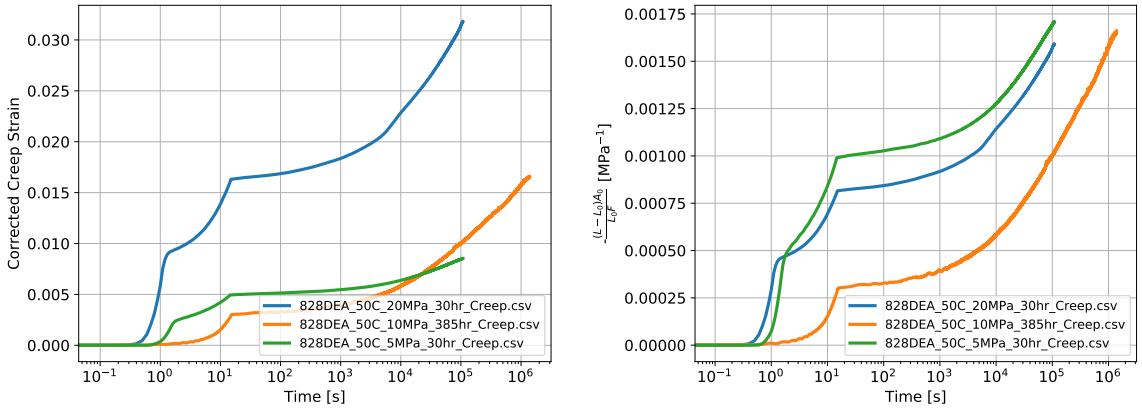

Figure 3-8. 828DEA creep response under constant uniaxial engineering stress. (a) Creep strain (b) Creep compliance time.

Although the creep strain vs. time behaves qualitatively the way we expect across each subsequently increasing applied engineering stress (Figure 3-8(a)), the creep compliance does not show the expected trend. If the material were linear thermoviscoelastic (perfectly), then all three creep compliance curves would be (nearly) identical (with errors due to finite strain kinematics). With deformation induced mobility, we expect the higher stress creep tests to exhibit non-linearly more deformation/creep compliance that the lower stress tests. It may be that within the errors of the tests (for example specimen geometry errors), the creep material response is nearly linear thermoviscoelastic.

3.1.8. Stress-Free Aging Followed by Glassy Compression Through Yield

In recent work prior to the milestone, the change in compressive yield strength under stress-free aging conditions was studied and reported in [26]. Details of these tests and measured results are reported therein along with initial modeling efforts. Here, we only briefly summarize the test and the results that will later be used for physical aging predictions in this report.

The test involves three phases: 1) programming a known thermal history, 2) isothermal stress-free aging, and 3) glassy compression at a particular test temperature (not necessarily the same as the aging temperature). First, the specimen is thermally programmed similar to the compression tests previously reported. The specimens are taken to 105 °C for thirty minutes to erase viscoelastic memory. Then, they are cooled at 0.8 °C per minute to room temperature, where they may sit for as long as a week prior to aging. When it was time to start specimen aging, the specimens were taken to the aging temperature, and let sit at the test temperature for 5 minutes to allow for thermal equilibration. Aging time was considered from this time forward. The specimens were

held for prescribed amounts of aging time under stress free conditions. Humidity was not controlled. Finally, when aging was completed, the specimens were brought back to room temperature to await testing.

When it was time for compression testing, the specimens were placed in the oven at the testing temperature instrumented with a mechanical extensometer. They were allowed to sit for 30 minutes to thermally equilibrate, and then they were compressed at 0.089 compressive strain per minute to 12% strain as limited by the extensometer. The raw compressive stress vs. compressive strain plots for different stress-free aging times are provided in Figure 3-9(a). The motion up to the maximum of the stress-strain curve was homogenous from observing tests. We consider this maximum of the stress-strain curve to be yield. However, following this maximum, the material globally softens, and experimentally extensive shear banding and/or barreling is observed. Hence, the tests are quantitative here only up through yield. The initial Young's modulus between 1 and 1.5% compressive strains (The secant slope between them), the maximum stress (yield), and the strain at yield were also of interest and plotted against aging time (one per compression curve) in Figure 3-9(b)– 3-9(d). The data were not filtered or cleaned prior to extraction of these quantities of interest.

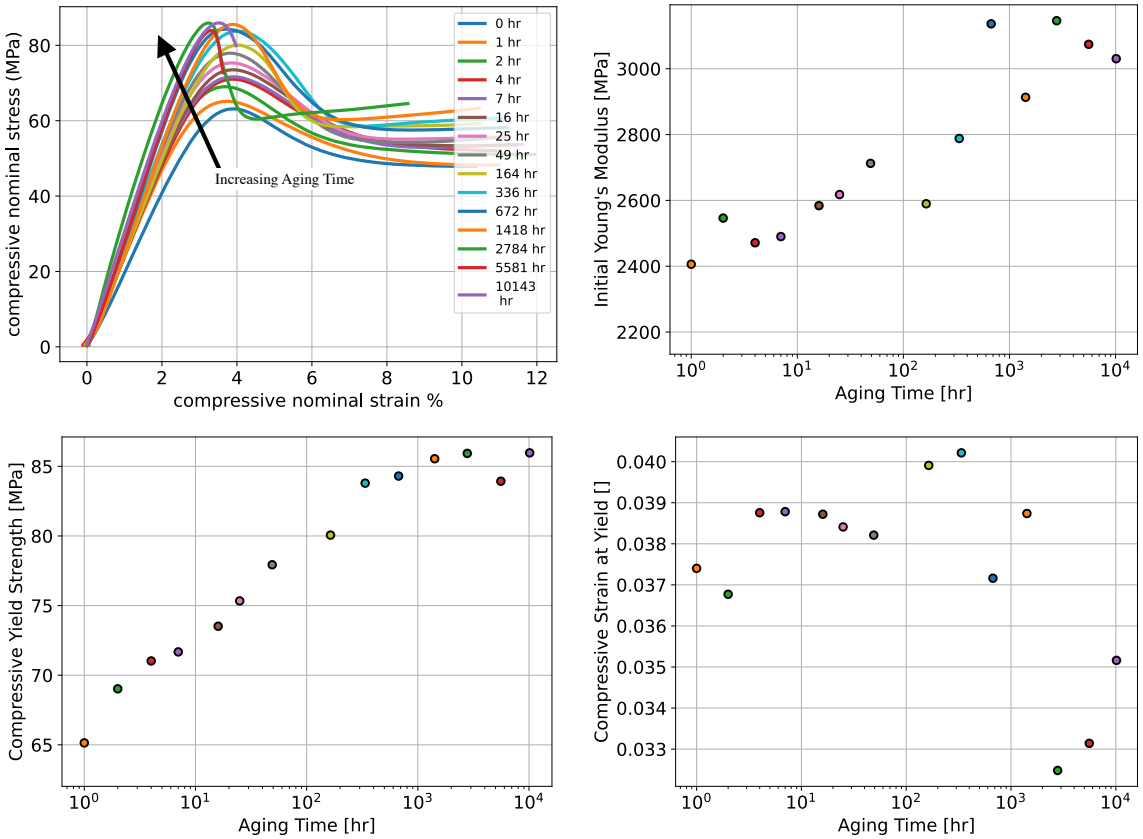

Figure 3-9. 828DEA uniaxial compression following stress-free aging. Both aging and testing were at 55°C . The raw compressive stress vs. compressive strain % data are provided in (a). From that figure, the initial Young's modulus, yield strength, and strain at yield were extracted against aging time in (c)-(d).

3.1.9. Age-Under-Load Followed by Compression Through Yield

While the tests in section 3.1.8 were aged under stress-free conditions, a complementary set of tests were also recently performed in which specimens were aged at a fixed temperature and under constant engineering stress (creep experiments) and then compressed through yielding after a preset aging time. These tests and initial modeling efforts were recently reported in detail [22]. Here we briefly describe these experiments as necessary to provide details to model the tests.

1x1 inch cylindrical plug specimens were subjected to the same temperature preconditioning as discussed in section 3.1.4. But, once specimens were brought to the aging temperature and allowed to equilibrate for 30 minutes, they were subjected to a strain rate of 0.01 per minute until a target engineering stress was reached. The engineering stress was then held for the prescribed aging time, and the axial strain response was recorded. This protocol was similar to section 3.1.7 with higher applied stresses. when the specimen had aged for the prescribed period of time, the load was removed, and the specimen was then compressed again through yield.

Typical experimental results for the creep phase of the test and the compressive-stress vs. strain behavior post-yield are taken directly from [22] and will be compared with simulations in Chapter 5. For brevity, these images are not reproduced twice.

3.1.10. Volume Relaxation Under Near Stress-Free Conditions

The last test for 828DEA involved isothermal volume relaxation using the TMA. The same kind of 11.3 x 11.3 x 11.3 mm 828DEA blocks subjected to a 50 mN deadload were used as in section 3.1.3. Specimens were taken to 105 °C , held for thirty minutes to erase viscoelastic history, and then cooled to the test temperature and allowed to rest for 5 minutes to thermally equilibrate. Then, the specimens were held under near no-load conditions, and linear strain change was monitored over time. As was done previously the specimen was assumed to be isotropic, and so we report on the volume strain vs. aging time for different temperatures. Typical volume relaxation behavior are presented in Figure 3-10. These tests were preformed over

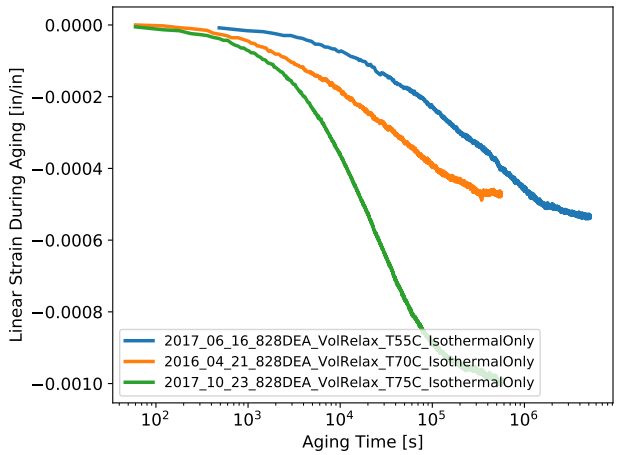

Figure 3-10. Isothermal volume relaxation of 828DEA specimens at different temperatures.

approximately 11.6 days (1 million seconds) to two months. Although the temperatures are near and below Tg and not particularly high, chemical aging appears to be very important at the upper two temperatures. At 75 °C , the material can equilibrate as we shall show later in a matter of hours (see Figure 6-12 for the baseline calibration showing the f_1 function that was fit to the TMA calibration experiment). Moreover, 75 °C is approximately the thermal strain datum. That is, at equilibrium, the thermal strain should not change if the temperature is held near this point. This datum is approximate as the material does vitrify (become glassy) during cure at 71 °C . Regardless, the expectation is that very little thermal strain should occur as the sample sits at 75°C , and if thermal strain relaxation does occur, it should track with the thermal expansion function characteristic time scale (order minutes at this temperature). However, at 75 °C , very little happens until about 1 hour by which time physical aging should be finished. Instead, from 1 hour to 24 hours, the most amount of shrinkage occurs. Hence, this particular test likely did not probe physical aging.

The story for the 70 °C test is similar although the relaxation time scale is now approximately 100 times longer (see the shift factor vs. temperature for the heat-after-cool master curve in Figure 3-2). Chemical shrinkage is likely dominant as even 100 times a few minutes is still mainly faster than the time scale over which the linear strain is changing (again 1 to 24 hours).

But at 55 °C , the shift factor in Figure 3-2 will make the relaxation time scale thousands of time slower than at the reference temperature, and there is a significant temperature shift from the strain datum of 71 °C . Hence, we do conjecture that the 55 °C relaxation behavior is dominantly physical aging. Here we can estimate the magnitude of possible strain change if the material were to equilibrate at 55 °C . A 21 °C temperature change multiplied by the approximate difference in rubbery vs. glassy linear CTEs (187 - 70 PPM/°C) gives a linear strain change of -0.0025. The measurement shows a strain change of -0.0005 approximately, which is 20% of the maximum strain we predict possible due to physical aging alone. We consider that this 55 °C test is worth using for physical aging validation.

3.2. 828T403 Experiments

Calibration and physical aging data for 828T403 followed the same methods and procedures as for 828DEA, but the tests completed frequently differed between the two materials. Here, we will clearly identify when test procedures were nearly identical (with differences arising due to the differences in glass transition of the two materials and the need to bracket that transition experimentally) as well as which procedures were only performed on 828T403. For example, uniaxial tension, creep under uniaxial compression, and age-under-load testing were not undertaken for 828T403. However, a large data set on the aged DSC transient thermal response was available and will be discussed. Similarly the stress-free aging followed by compression was more detailed than the cases for 828DEA. We follow the same layout as in section 3.1.

3.2.1. *Isofrequency Temperature Sweep*

Isofrequency temperature sweep data were collected on 828T403 torsion bars in the Ares 2 Rheomter with the same protocol as discussed for 828T403 in section 3.1.1. Typical storage and loss moduli vs. temperature are presented in Figure 3-11 for the same specimen that is first cooled from 200 °C to room temperature (labeled "down") and then reheated. The glass transition, as

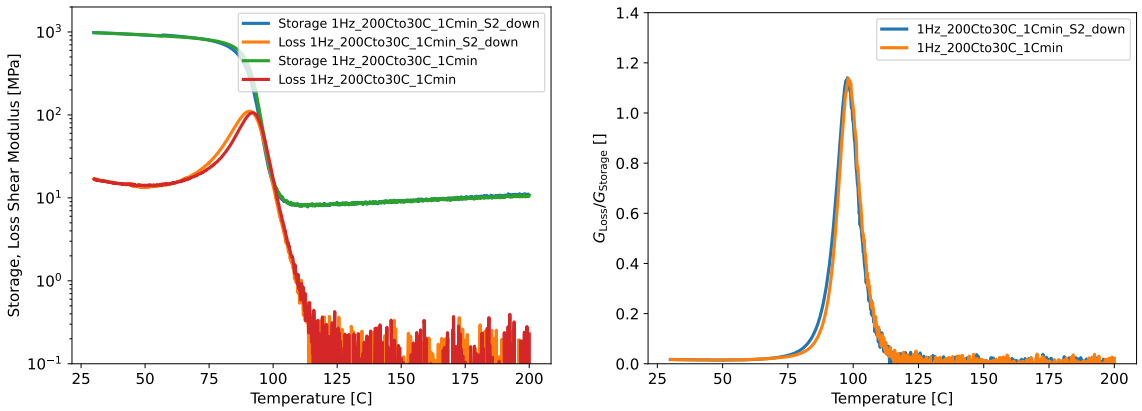

Figure 3-11. 828T403 Isofrequency temperature sweeps at 1 Hz oscillation, 1 °C per minute, 0.1% strain amplitude, and applied down and then upwards in temperature space.

defined by the peak of the loss tangent, is near 96 °C for the downward from equilibrium data and slightly higher for the upward temperature scan, which is expected due to physical aging from the downward scan. These values are nearly similar to previously measured glass transition temperatures for 828T403. For example, previous work [15] found that the glass transition, as defined by the mid-point projection of thermal-mechanical analyzer thermal strain sweep data within the glass transition, was 86 °C for "as-received" material. As the quantitative glass transition temperature depends on how one measures and defines it (see for example [20] chapter 2), we regard 96 °C as relatively close considering the difference in the two measurements. Unlike 828DEA, which clearly showed and elevated glass transition due to the high temperature processing, 828T403 is behaving similar to prior work and does not appear to be altered chemically by this particular high temperature excursion.

3.2.2. *Isothermal Frequency Sweeps and the Shear Master Curve*

As with 828DEA, a series of isothermal frequency sweeps were measured under the same two thermal profiles. First, tests starting at 120 °C and cooling downward were recorded, and then, testing that started first by heating the specimen to 120 °C for thirty minutes and then cooling the specimen to room temperature at 1 °C per minute before commencing with an upward sweep in temperature in 10 °C increments. Frequency sweeps were performed at each temperature and the storage and loss moduli were recorded.

For both cases, TTS was used with a reference temperature of 95 °C to construct a shear master curve. Both profiles produced nearly the same TTS behavior and shear mastercurve as can be seen in Figure 3-12.

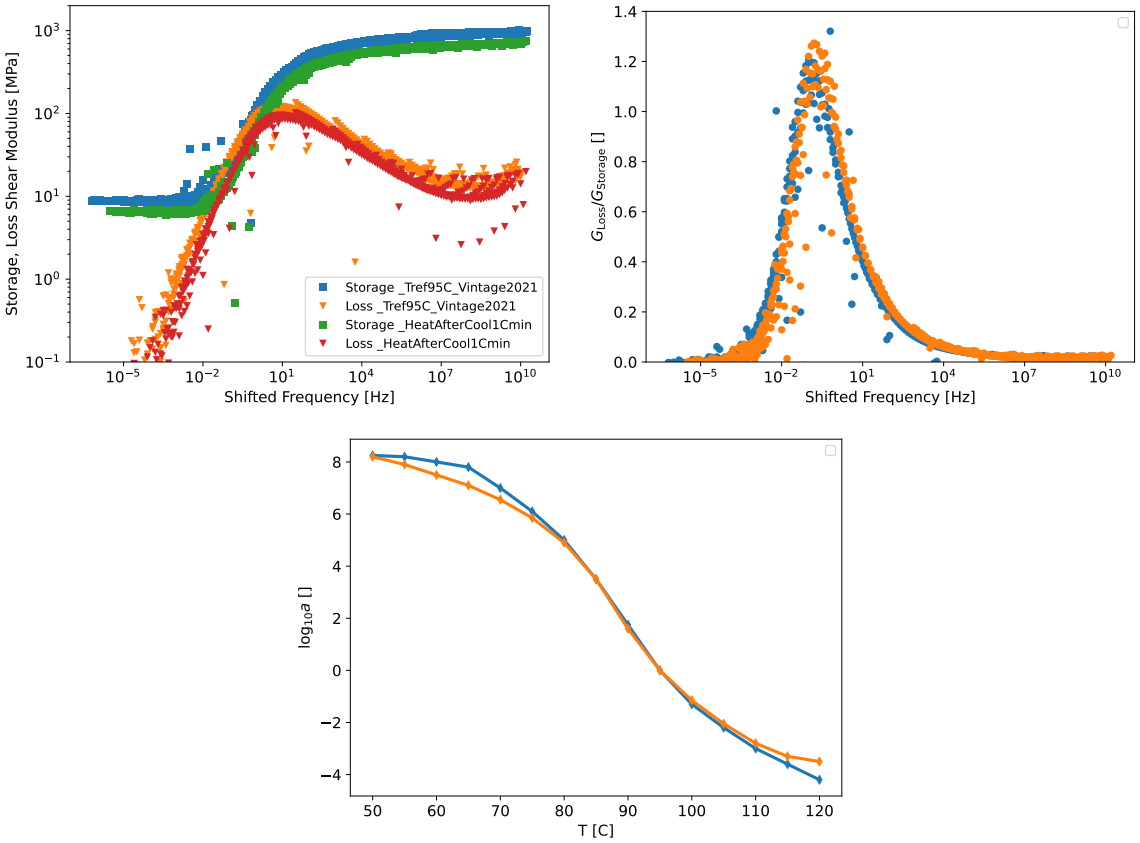

Figure 3-12. Unaged 828T403 shear master curves at the 95 °C reference temperature from two distinct temperature histories.

3.2.3. TMA Temperature Sweep

The thermal strain behavior of 828T403 was characterized using the TMA and following the same procedures as for 828DEA. See section 3.1.2. Typical thermal strain and linear coefficient of thermal expansion results are presented in Figure 3-13. The midpoint of the change in linear CTE across the glass transition, which can approximately describe the glass transition temperature, occurs when the linear CTE pass through 135 PPM/°C , which occurs at 86 °C during the cooling curve plotted, which matches prior TMA glass transition characterization for this material for this test [15].

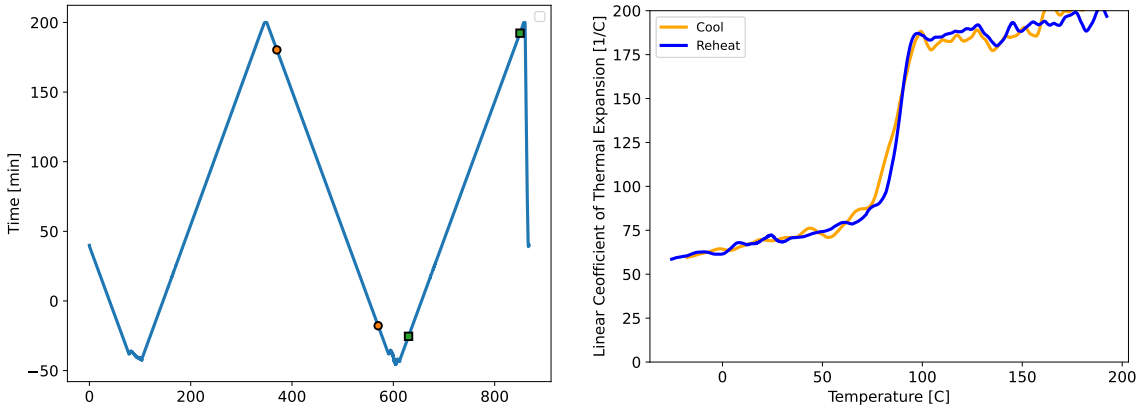

Figure 3-13. 828T403 Temperature history and linear coefficient of thermal expansion from experiments on the same specimen that cooled from equilibrium to room temperature, thermally equilibrated, and then heated back well above the glass transition. The markers show the portions of cooling and reheating two steps plotted.

3.2.4. Unaged Glassy Compression

The same thermal preconditioning (with an increased annealing temperature of 120 °C) was executed for 828T403 as discussed for 828DEA in section 3.1.4. Typical compressive stress vs. strain curves are provided in Figure 3-14 after removal of the toe region.

Again, the initial Young's modulus, yield strength, and strain rate were extracted from each test conditions and regressed to a linear fit with temperature and/or strain rate in Figure 3-15.

3.2.5. DSC and Heat Capacity Measurements

The same procedures as used for 828DEA in section 3.1.4 were used to characterize the heat capacity response of 828T403. Here we present only the variable rate tests which show well behaved and expected behavior (Figure 3-16). Namely, with slower cooling rates, the appearance of the spike in heat capacity during the reheat stage becomes evident. Substantial DSC data sets will be discussed in the next section associated with aging. The data here were used for model calibration. Chemical aging, which may have been present for the slower 828DEA cooling rates in Figure 3-7(d), does not appear to have a role. Indeed, only the slowest two cooling rates produce a distinguishable physical aging signature compared with the faster cooling rates (with rates spanning from 0.5 °C per minute up to 20 °C per minute).

3.2.6. DSC Aging Tests

Prior to this work, a detailed study of physical aging from the perspective of changes in the heat capacity response of 828T403 was performed [27]. Several different aging temperatures and times were considered. The basic thermal profile in these tests involved a similar temperature

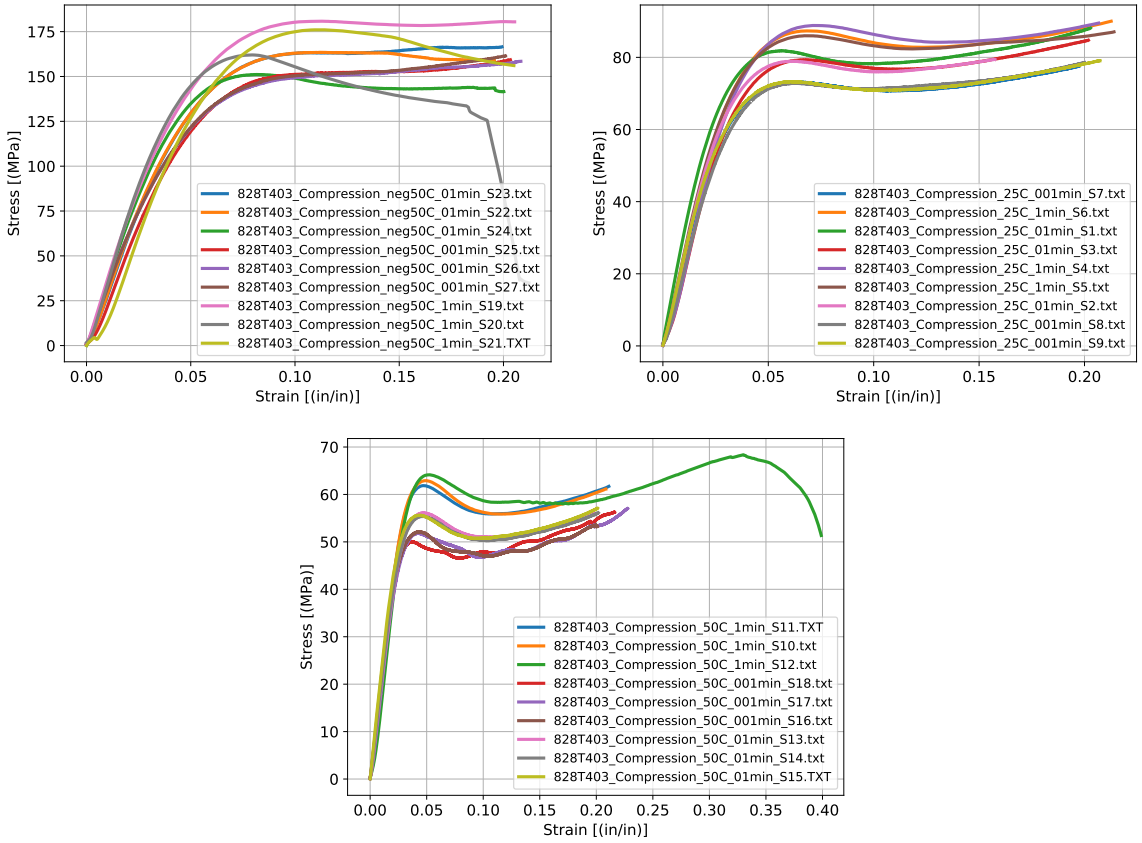

Figure 3-14. Unaged 828T403 uniaxial compression tests below the glass transition temperature at different strain rates and temperatures. All results are reported in engineering stress and strain measures.

history as discussed in the 828DEA DSC subsection 3.1.6. When aging was complete, specimens were subjected to an up-down-up transient temperature sweep at 10 °C per minute, and the two heating curves were compared. the primary quantity of interest is the specific heat capacity before and after the viscoelastic history is erased and the peak of the heat capacity spike. Typical DSC aging data for 828T403 from [27] are in Figure 3-17.

3.2.7. Stress-Free Aging Followed by Compression Through Yield

Stress-free glassy compression of 828T403 followed a similar procedure as discussed for 828DEA in section 3.1.8. However, the annealing temperature used to erase viscoelastic memory was 120 °C instead 105 °C , and the cooling rate was 1.0 °C per minute instead of 0.08 °C per minute. The experimental conditions were more extensive for 828T403 than for 828DEA and were documented as a significant contribution in Kelsey Wilson's master's thesis [27]. Several different test temperatures and aging temperatures were considered, and these were frequently different. Hence, the data are richer than the 828DEA equivalent data. Two types of stress-free aging tests were performed followed by compression through yield. First, experiments were performed where the aging temperature and loading temperature were the same using

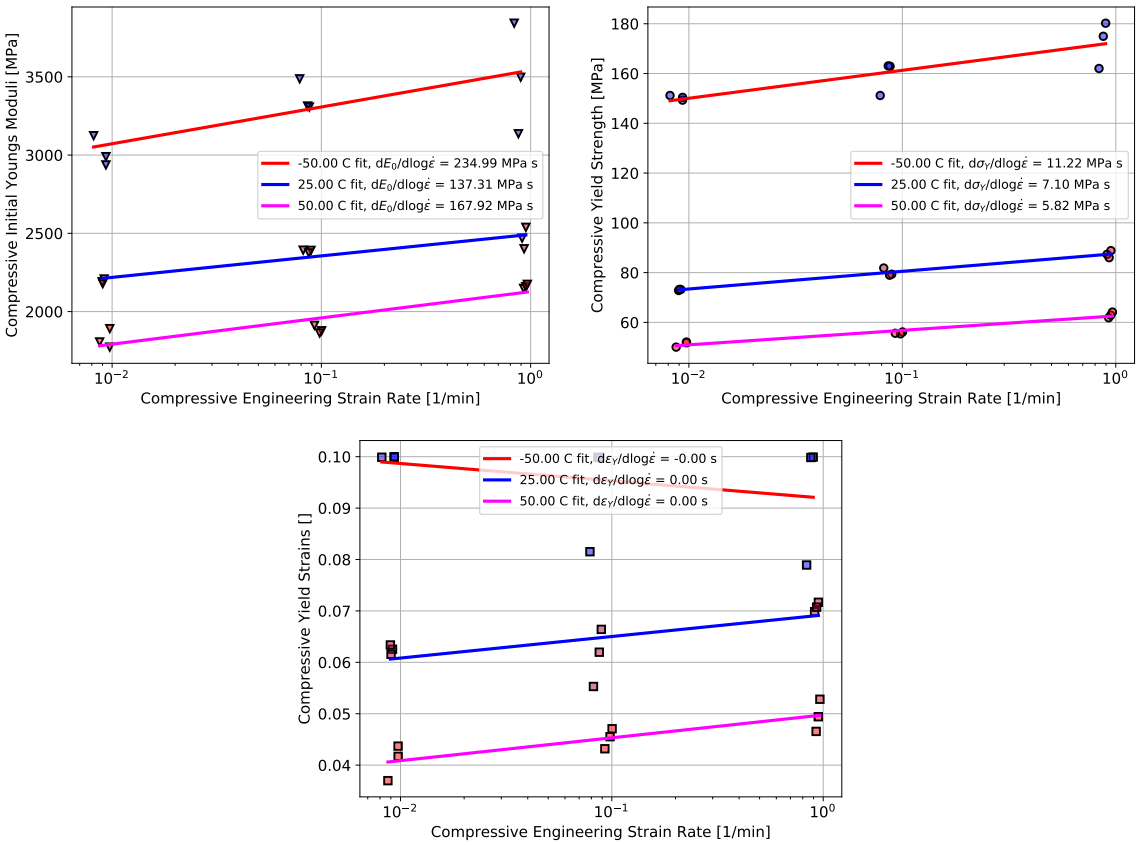

Figure 3-15. Unaged 828T403 uniaxial compression test analysis of Young's modulus, yield strength, and strain at yield across temperatures and strain rates.

temperatures of 55, 65, 76, and 83 °C . Typical stress-strain curves from these tests at the four conditions across a variety of aging times are reproduced here from that thesis in Figure 3-18,

The other significant set of studies taken from that thesis involved aging temperatures that were different followed by compression at 76 °C . Typical stress strain curves for those different aging temperatures are reproduced here in Figure 3-19.

The main observations that yield strength and the initial Young's modulus both increase with aging time are consistent 828DEA are evident in the stress-strain curves in Figure 3-18 and Figure 3-19. These features are different for the different aging and testing temperatures, and they provide quantities of interest for the model comparisons. We briefly summarize the Initial Young's moduli and yield strength evolutions from the two studies in Figure 3-20.

3.2.8. Volume Relaxation Under Near Stress-Free Conditions

A similar set of volume relaxation tests were performed on 828T403 following the same procedures for 828DEA (section 3.2.8) although at slightly different aging temperatures. The linear strain for the selection of tests is reported in Figure 3-21. 828T403 cubes were held below

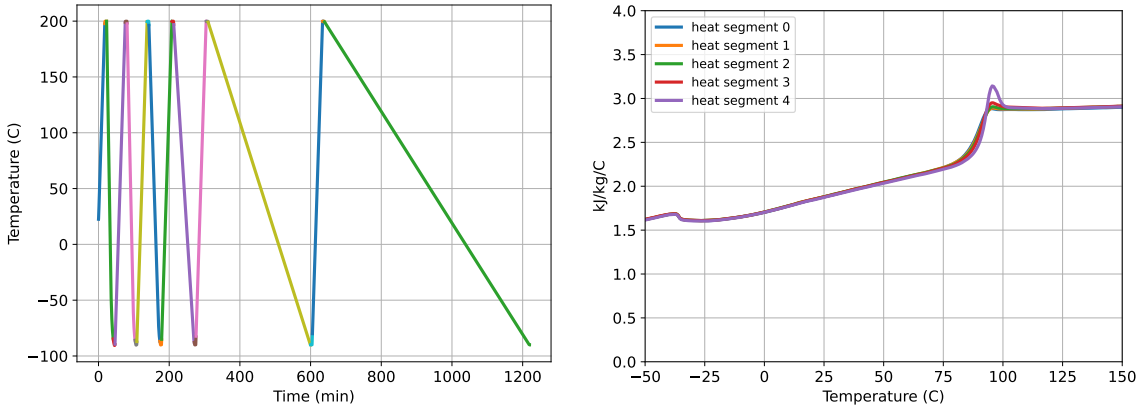

Figure 3-16. 828T403 transient DSC response under a variable cooling and heating rate on the same specimen. The temperature history (a) and specific heat capacity (heat flow / temperature rate / specimen mass) (b) are shown.

the glass transition at 83, 75, and 65 °C with a repeat at 75 °C which showed reasonable consistency between tests. All curves showed shrinkage. Again, it is worth considering how much volume strain we expect due to physical aging alone and if the sample could rest long enough to equilibrate. Assuming the thermal strain datum is near the reference temperature of 95 °C and that all of the thermal strain between the reference temperature and the aging temperature was with a glassy linear CTE, then the net amount of additional thermal strain that can accumulate is the temperature difference between the aging temperature and the reference temperature (thermal strain datum) multiplied by the difference in rubbery and glassy linear CTEs, which is approximately 100 PPM/°C . Hence, for 83 °C , we could expect a maximum volume straining due to physical aging alone of 100 PPM / °C x (-13) °C or -0.0013, which is roughly double the magnitude observed for the 83 °C test. Hence, it is possible that the volume relaxation is physical aging but that more time would be needed to reach equilibrium. Note that the back of the envelope estimate is an upper bound for the maximum available volume straining during relaxation since, in reality, the linear CTE will not be larger than the glassy limit during the cooling through the glass transition.

For the other temperatures, the same arguments hold, but the magnitude of possible thermal straining is higher. Hence, at this time, we consider these experiments worthwhile for physical aging comparisons.

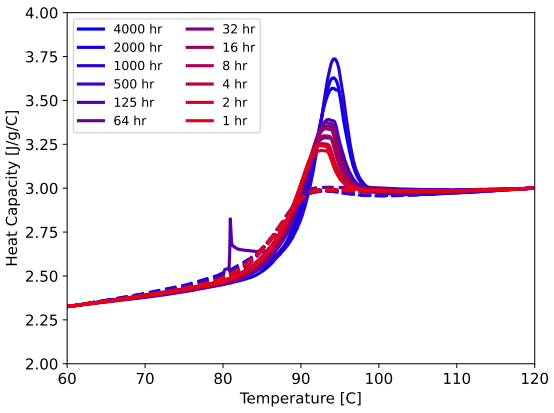

(a) T_{age} =83 °C

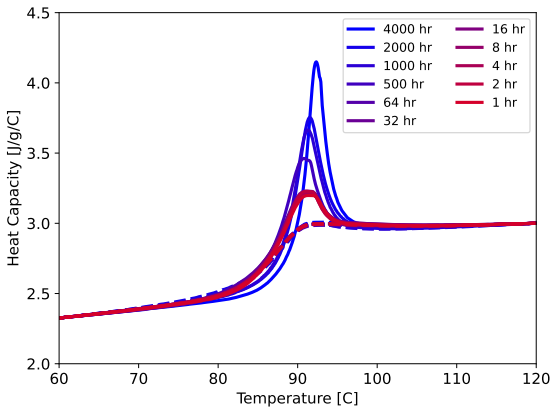

(b) T_{age} =55 °C

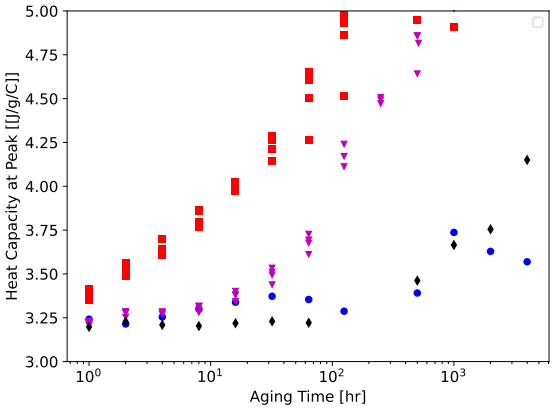

(c) Max Heat Capacity During First Reheat

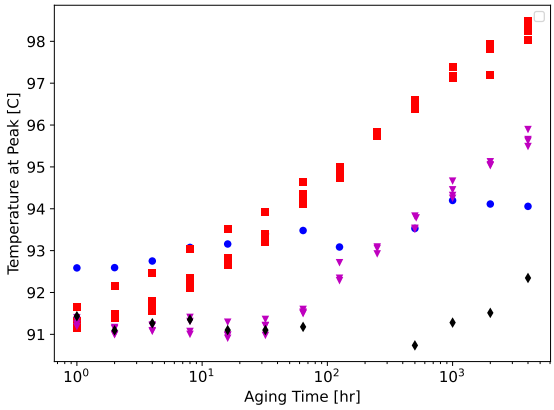

(d) Temperature at Max Heat Cap. During First Reheat

Figure 3-17. Isothermal aged 828T403 Heat Capacity responses during the first reheat (solid lines) and the second reheat (dashed lines) for aging temperatures of 83 °C (a) and 55 °C (b). The heat capacity maximum during the first reheat and the associated temperature are shown for 55, 65, 76, and 83 °C aging temperatures in (c) and (d).

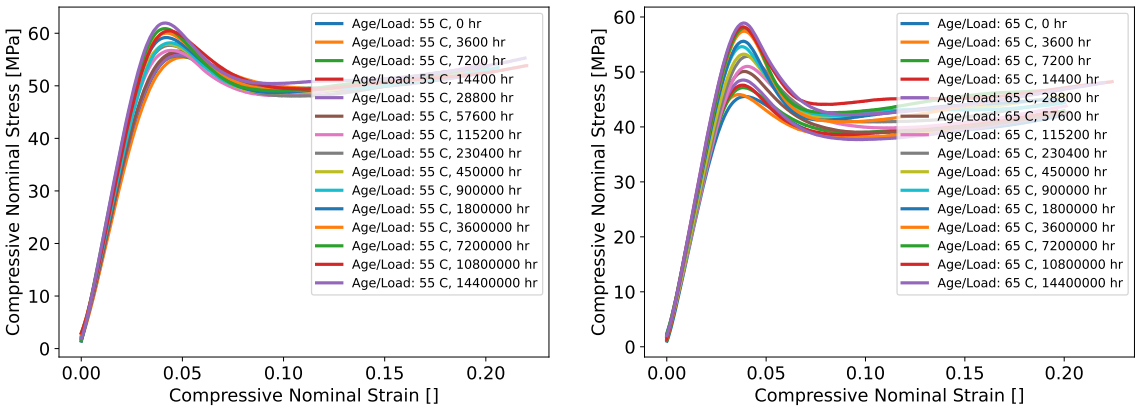

(a) $T_{age} = T_{test}$ =55 °C

(b) $T_{age} = T_{test}$ =65 °C

(c) $T_{age} = T_{test}$ =76 °C

(d) $T_{age} = T_{test}$ =83 °C

Figure 3-18. Stress-Free aged 828T403 followed by uniaxial compression at 0.089 per minute strain rate. Data replotted from [27]. Here, the aging and compression testing temperatures were the same.

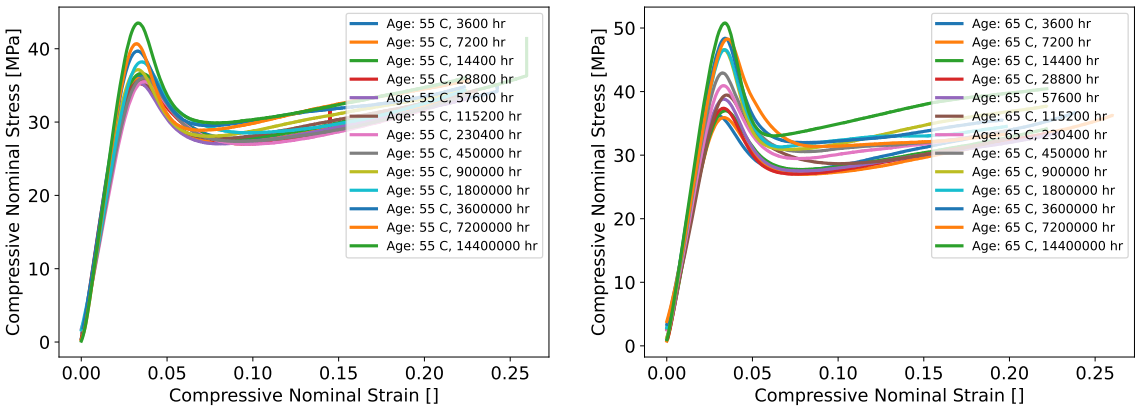

(a) T_{age} =55 °C

(b) T_{age} =65 °C

(c) T_{age} =76 °C

(d) T_{age} =83 °C

Figure 3-19. Stress-Free aged 828T403 followed by uniaxial compression at 0.089 per minute strain rate in which all tests were compressed at T_{test} = 76 °C . Data replotted from [27].

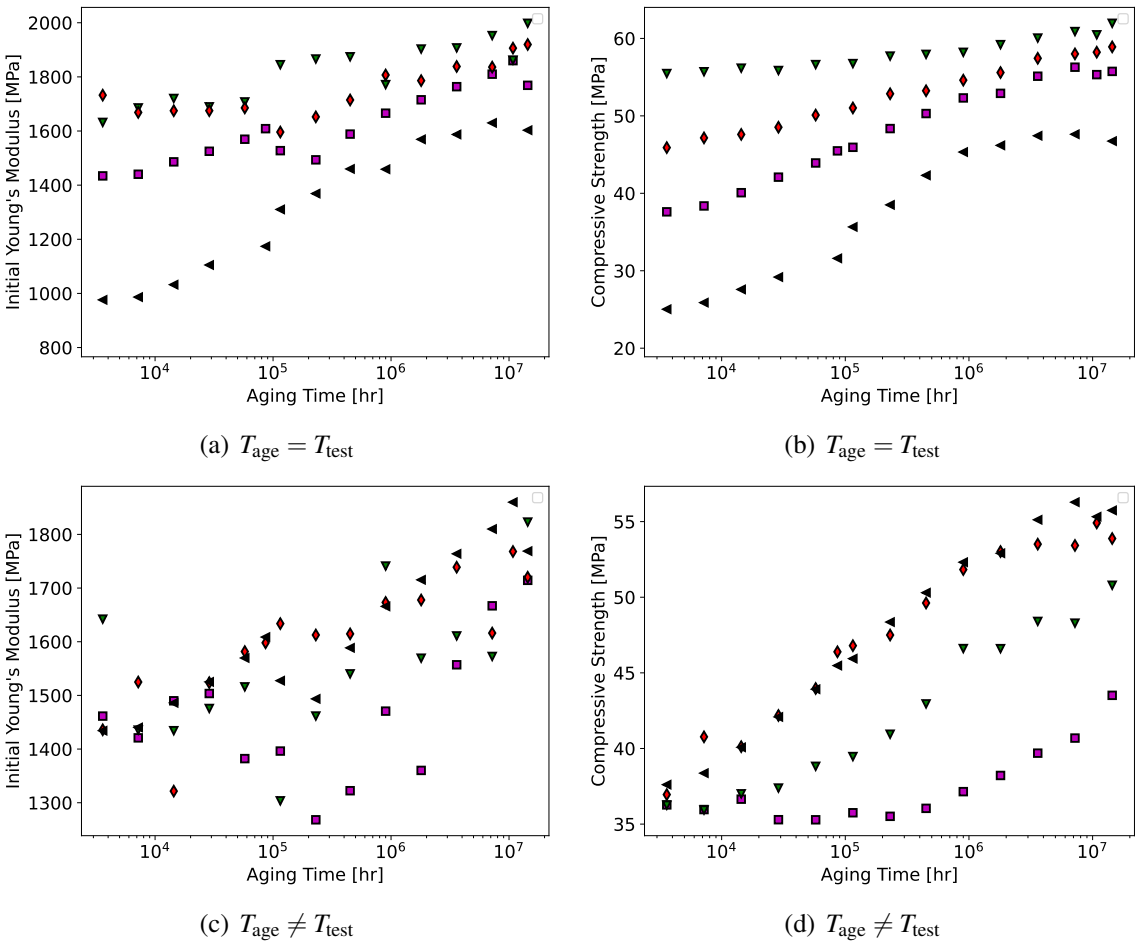

Figure 3-20. Initial Young's moduli and yield strengths for the tests in which $T_{test} = T_{age}$ (a), (b) and for the cases in which $T_{test} \neq T_{age}$ (c), (d).

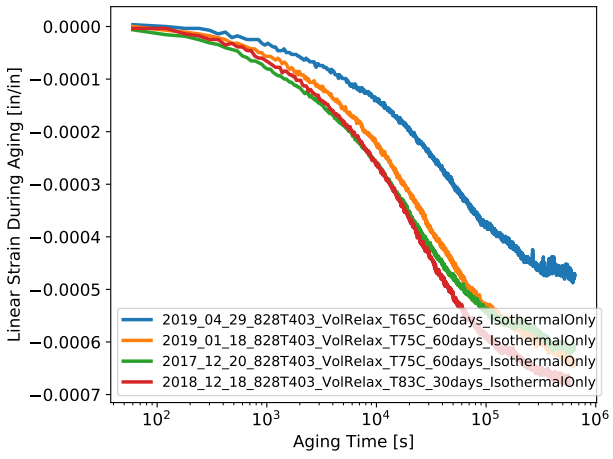

Figure 3-21. Isothermal volume relaxation of 828T403 specimens at different temperatures.

4. CALIBRATIONS AND PREDICTIONS FOR 828T403

This chapter documents the three calibration approaches executed for 828 DGEBA/T403. The first approach is referred to as the "baseline" calibration, which essentially follows the procedure historically used for the PEC and SPEC models [4, 8]. The execution of the baseline calibration procedure is documented in Section 4.1. The other two approaches attempt to improve specific behaviors that were poorly predicted by the baseline calibration by prioritizing those behaviors when fitting. The second approach focuses on improving the compressive yield stress at different strain rates and temperatures, and is therefore referred to as the "compression-focused" calibration. The execution of the compression-focused calibration procedure is documented in Section 4.2. The third approach focuses on improving the heat capacity response measured by a differential scanning calorimeter (DSC), and therefore is referred to as the "DSC-focused" calibration. The execution of the DSC-focused calibration procedure is documented in Section 4.3. In Section 4.4, the physical aging predictions from each new calibration and one legacy calibration are compared to experiments. The chapter concludes in Section 4.5 with a brief assessment of each calibration along with recommendations.

4.1. Baseline Calibration

This section presents the baseline calibration procedure for 828T403. The baseline procedure is similar to procedures commonly employed for calibrating the SPEC model [4, 8]. Fig. 4-1 shows a flowchart for the baseline calibration approach used here. Before calibration begins, a reference temperature, θ_{ref} must be chosen, see the orange box in Fig. 4-1. The value of θ_{ref} is somewhat arbitrary, but should be chosen to be slightly above the glass transition temperature where the material can exhibit equilibrium (time-independent) properties. For 828T403, a reference temperature of $\theta_{\text{ref}} = 95\,^{\circ}\text{C}$ is chosen. A full recalibration was not conducted; the parameters that have been borrowed from previous calibrations are listed in the pink box in Fig. 4-1. These borrowed parameters include the four parameters that define the bulk modulus K_g^{ref}, K_g', K_∞^{ref}, and K_∞'; the parameter controlling the sensitivity of the material clock to the volume strain, C_3; and the density, ρ. The values of borrowed parameters are listed in Table 4-1 along with references. The bulk modulus can be calibrated using a mercury pressure dilatometer [3], ultrasonic techniques, or measurements of the Poisson's ratio [4]. However, these experiments can be difficult and time consuming, so are often omitted from a standard calibration. The bulk moduli values used here are taken from Table 3-1 of [11]. The calibration of C_3 was also omitted due to the difficulty of measuring the relationship between pressure, volume, and temperature. In theory, it is possible to calibrate C_3 from the difference in yield stress between tension and compression, but this approach poses its own set of challenges, see Appendix B. As with the bulk moduli, the value of C_3 is taken from Table 3-1 of [11]. The density is also not measured, and is assumed to

be approximately equal to the density of 828DEA [3]. The density is not directly used by the SPEC model, but is necessary for converting thermodynamic quantities from a per volume value (used in the SPEC model calculations) to a per mass value (measured in experiments). As shown in the pink box in Fig. 4-1, the baseline calibration procedure assumes that the volumetric and thermal-volumetric relaxation functions are the same; $f_1(t) = f_3(t)$. This assumption is inherent to previous versions of the SPEC model [4], but in the current `spectacular` implementation, the two relaxation functions may be specified separately.

The execution of Steps 1–5 from the flowchart in Fig. 4-1 are described in detail in sections 4.1.1–4.1.5. The parameters that are produced by the baseline calibration are listed in Table 4-1. It should be noted that Table 4-1 specifies relaxation functions using stretched exponentials, which are defined by a characteristic time and a breadth, τ_i and β_i, see Eq. (2.28). However, relaxation functions must be input to the `spectacular` model as Prony series. Custom python tools convert the stretched exponential functions listed in Table 4-1 into Prony series that can be input into the `spectacular` model.

4.1.1. Isothermal Frequency Sweeps and the Shear Master Curve

Isothermal frequency sweeps and the shear master curve were used to calibrate the WLF coefficients, $\hat{C}_1$ and $\hat{C}_2$; the reference values of the glassy and rubbery shear moduli, G_g^{ref}, and G_∞^{ref}; and the shear relaxation function, $f_2(t)$. This corresponds to Step 1 in Fig. 4-1. Experimental details and results can be found in Section 3.2.2 and Fig. 3-12. Two thermal histories were used to generate the shear master curves. The high-to-low temperature history (see Fig. 3-12, label `Tref95C_Vintage2021`) was used for calibration, since this is the preferred thermal history for epoxies not likely to show significant post-manufactured additional curing or oxidation such as 828T403, see section 3.1.2.

In constructing the shear master curves, shift factors at each temperature were found, see red dots in Fig. 4-2(a). The shift factors as a function of temperature were used to calibrate the WLF coefficients. However, at low temperatures, the shift factor is too high for the material to reach its equilibrium state, therefore shift factors with $\log a > 1$ are ignored when fitting $\hat{C}_1$ and $\hat{C}_2$. It should be mentioned that WLF coefficients, $\hat{C}_1$ and $\hat{C}_2$, are fit to the shift factor versus temperature data, but the shift factor definition for the SPEC model, Eq. (2.8), uses the clock parameters, C_1 and C_2. The first clock parameter is equal to the first WLF coefficient, $C_1 = \hat{C}_1$, but the second clock parameter must be calculated from the second WLF coefficient as well as other material parameters, see [4] for details. The `spectacular` model accepts either the WLF coefficients or the first two clock parameters as inputs, so it is unnecessary to perform the conversion from WLF coefficients to clock parameters outside of the model.

Shear master curves were constructed using time–temperature superposition to shift storage and loss shear moduli at different temperatures to a reference temperature so that a smooth curve was formed. While constructing the shear master curve, data from frequencies above 20 Hz was ignored, since the accuracy of data above this frequency is suspect. The data was then smoothed using custom Python tools. The smoothed data are shown in Fig. 4-2(b, c, d). Data for G''/G' (commonly called $\tan\delta$) is shown in (b), the storage shear moduli in (c), and the loss shear

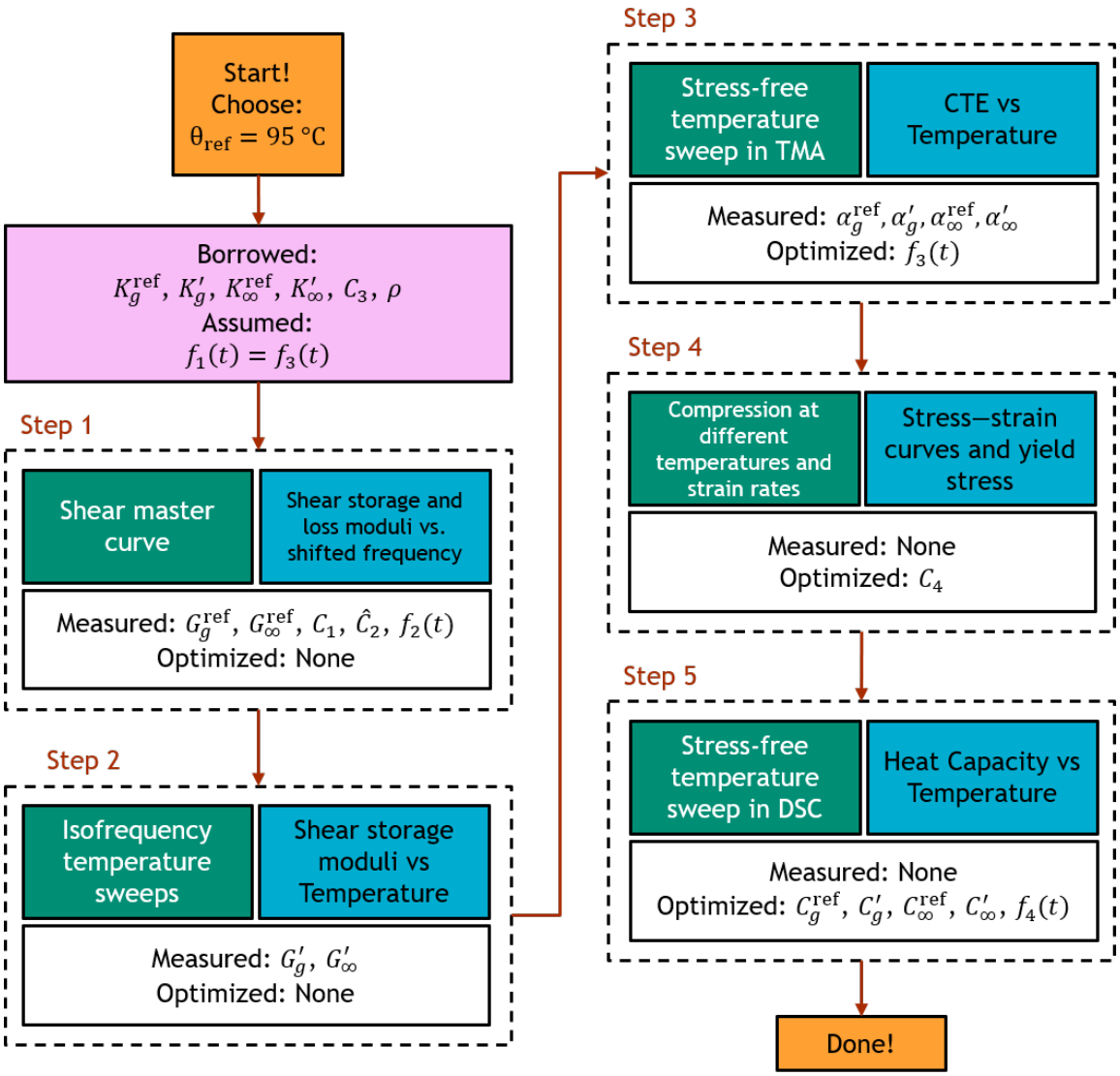

Figure 4-1. Flowchart for the baseline calibration procedure.

Table 4-1. SPEC parameters produced by the baseline calibration for 828T403.

Parameter	Value	Units	Experiment	Reference
K_g^{ref}	4.9	GPa	Legacy	[11], Table 3-1
K_g'	-12	MPa/K	Legacy	[11], Table 3-1
K_∞^{ref}	3.5	GPa	Legacy	[11], Table 3-1
K_∞'	-12	MPa/K	Legacy	[11], Table 3-1
G_g^{ref}	0.959	GPa	Shear master curve	Fig. 4-2c
G_g'	-2.959	MPa/K	Isofrequency temperature sweeps	Fig. 4-4
G_∞^{ref}	8.267	MPa	Shear master curve	Fig. 4-2c
G_∞'	22.918	kPa/K	Isofrequency temperature sweeps	Fig. 4-4
α_g^{ref}	211	$10^{-6}/\text{K}$	TMA	Fig. 4-6
α_g'	0.5	$10^{-6}/\text{K}^2$	TMA	Fig. 4-5
$\alpha_\infty^{\text{ref}}$	557	$10^{-6}/\text{K}$	TMA	Fig. 4-6
α_∞'	0.5	$10^{-6}/\text{K}^2$	TMA	Fig. 4-5
C_g^{ref}	0.695	$\text{MJ}/(\text{m}^3\cdot\text{K})$	DSC	Fig. 4-9
C_g'	1.98	$\text{kJ}/(\text{m}^3\cdot\text{K}^2)$	DSC	Fig. 4-9
C_∞^{ref}	0.991	$\text{MJ}/(\text{m}^3\cdot\text{K})$	DSC	Fig. 4-9
C_∞'	1.82	$\text{kJ}/(\text{m}^3\cdot\text{K}^2)$	DSC	Fig. 4-9
θ_{ref}	95	°C	Chosen	
$\hat{C}_1$	9.6	–	Shear master curve	Fig. 4-2a
$\hat{C}_2$	32.7	K	Shear master curve	Fig. 4-2a
C_3	900	K	Legacy	[11], Table 3-1
C_4	22500	K	Compression	Fig. 4-7
ρ	1176	kg/m^3	Legacy	[3], Table 4
τ_1	0.835	s	TMA	Fig. 4-6
β_1	0.25	–	TMA	Fig. 4-6
τ_2	0.0186	s	Shear master curve	Fig. 4-3
β_2	0.21	–	Shear master curve	Fig. 4-3
τ_3	0.835	s	TMA	Fig. 4-6
β_3	0.25	–	TMA	Fig. 4-6
τ_4	0.132	s	DSC	Fig. 4-9
β_4	0.22	–	DSC	Fig. 4-9

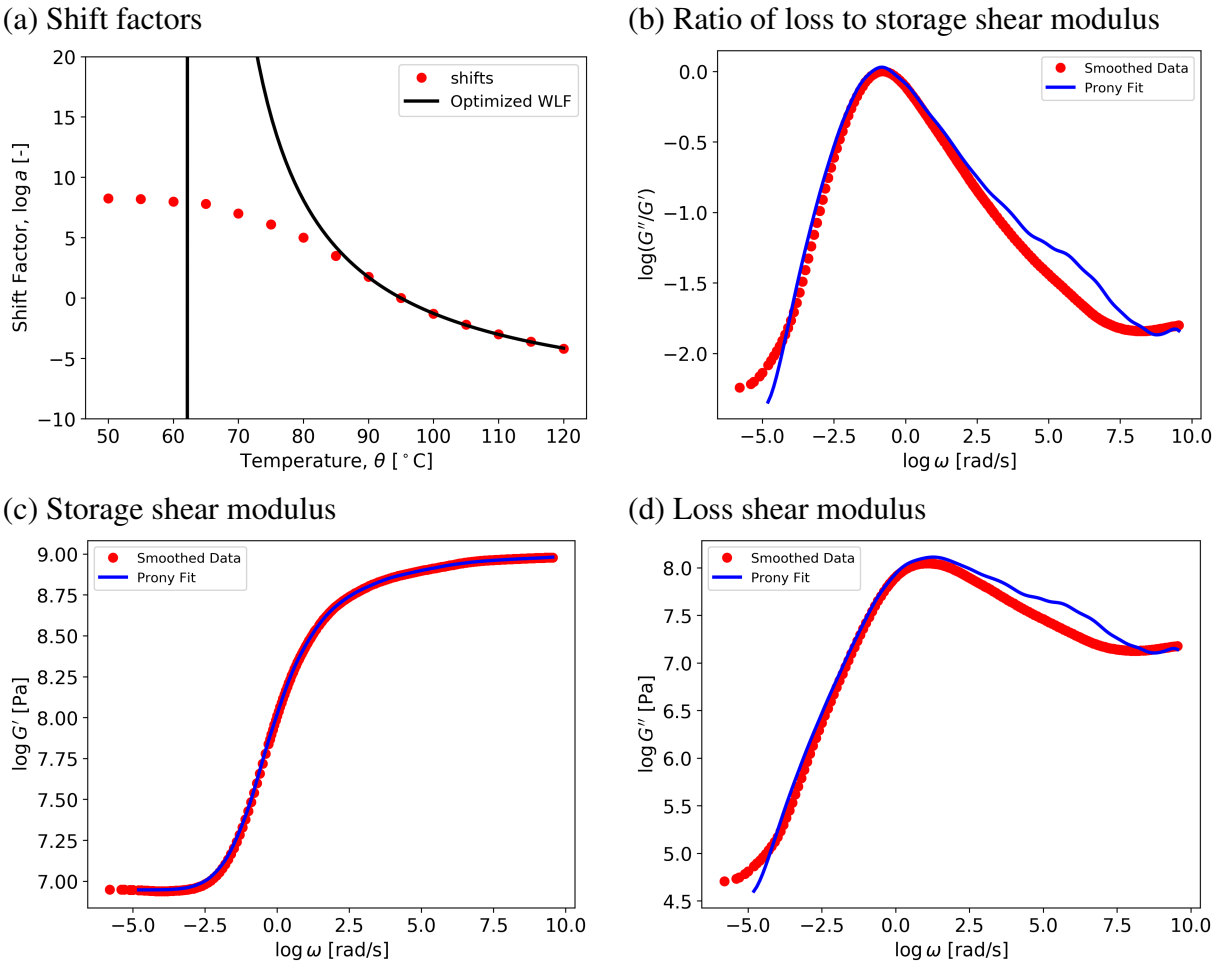

Figure 4-2. Shear master curve for 828T403 constructed from isothermal frequency sweeps. (a) The shift factor versus temperature plot used to construct the shear master curve (red dots) and the optimized WLF fit for $\log a > 1$ (black line). (b, c, d) Smoothed data versus frequency and Prony series fits for (b) G''/G' (commonly called $\tan\delta$), (c) storage moduli, G', (d) and loss moduli, G''. Experimental data from Fig. 3-12, label `Tref95C_Vintage2021`.

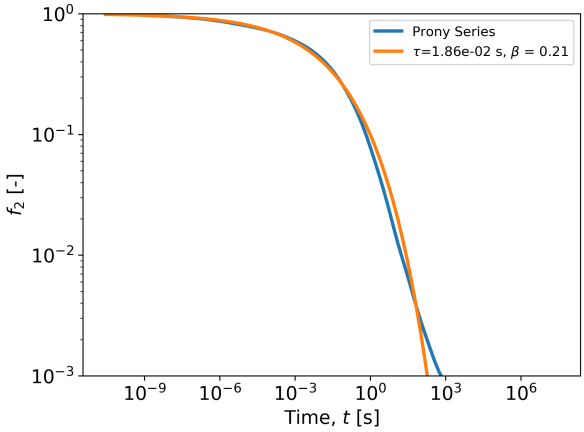

Figure 4-3. Prony series fit to the 828T403 shear master curve and the stretched exponential fit used for the baseline calibration.

moduli in (d). Reference values for the glassy and rubbery shear moduli were extracted from high and low frequency extremes of the storage shear moduli curve, see Fig. 4-2(c). To determine the shear relaxation function $f_2(t)$, a Prony series was fit to the shear master curve. The Prony series fit is plotted with the smoothed data in Fig. 4-2(b, c, d).

In forthcoming calibration steps, the other relaxation functions are calibrated by optimization. To reduce the number of parameters that need to be optimized, these relaxation functions are represented using stretched exponential functions, which are defined by two parameters, the characteristic time and the breadth, τ_i and β_i. To facilitate comparisons of all four relaxation functions across multiple calibrations, a stretched exponential is fitted to the Prony series fit to the shear master curve. The comparison of the Prony series and the stretched exponential fit are shown in Fig. 4-3.

4.1.2. Isofrequency Temperature Sweeps

The isofrequency temperature sweeps, see Section 3.2.1 and Fig. 3-11, were conducted to calibrate the temperature dependence of the shear moduli, G'_g and G'_∞. The slopes from the glassy and rubbery parts of the storage modulus curves are taken to correspond to G'_g and G'_∞. This procedure corresponds to Step 2 in Fig. 4-1. The temperature sweep from room temperature to 200 °C was used for calibration, see the green curve in Fig. 3-11, although the slopes of the up and down sweeps are essentially the same. Fig. 4-4 shows specifically how the slopes were measured from the storage modulus versus temperature curve. The measured values are $G'_g = -2.959\,\mathrm{MPa/K}$ and $G'_\infty = 22.918\,\mathrm{kPa/K}$. The positive value for G'_∞ is expected when the stiffness is driven by entropic elasticity [14], but since the magnitude of the value is small, it is often neglected, i.e. $G'_\infty = 0$.

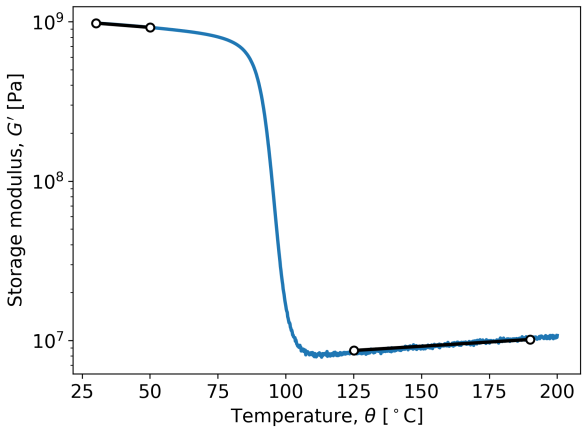

Figure 4-4. Isofrequency temperature sweep for 828T403. Black lines indicate slopes used to calibrate G'_g and G'_∞. Experimental data from Fig. 3-11, green curve.

4.1.3. Stress-Free Temperature Sweep in a Thermomechanical Analyzer

The four parameters governing the volumetric coefficient of thermal expansion (CTE); α_g^{ref}, α'_g, $\alpha_\infty^{\text{ref}}$, and α'_∞; and the thermal-volumetric relaxation function; $f_1(t) = f_3(t)$; were calibrated using a thermomechanical analyzer (TMA). This corresponds to Step 3 in Fig. 4-1. The test procedure involves measuring the linear CTE during a stress-free temperature sweep, see Section 3.2.3 and Fig. 3-13. Fig. 4-5 shows the linear CTE during an upward temperature sweep and how the four volumetric CTE parameters were measured from the experimental data. The slopes from the glassy and rubbery ends were measured to calibrate α'_g and α'_∞ and the rubbery and glassy limits were extrapolated to find the values at the reference temperature, α_g^{ref} and $\alpha_\infty^{\text{ref}}$. The SPEC model assumes isotropic behavior, so the measured linear CTE values were multiplied by three to calculate the volumetric CTE values, which are the input used by `spectacular`. The measured volumetric CTE parameters are listed in Table 4-2.

The thermal-volumetric relaxation function was calibrated by optimizing the linear CTE response of the `spectacular` model to fit the experimental data. Parameters governing the reference values for the volumetric CTEs and the thermal-volumetric relaxation function were optimized. Even though apparent values for the volumetric CTEs were measured, further adjustment through optimization were allowed. During optimization, the volumetric and thermal-volumetric relaxation functions were equal, $f_1(t) = f_3(t)$.

The TMA experiment was simulated by applying the following thermo-mechanical history to a single element in Sierra: (1) Anneal at 200 °C for 30 min, (2) cool to -50 °C at 1 °C/min, (3) hold at -50 °C for 5 min, (4) heat to 200 °C at 1 °C/min. The nominal strain was calculated from the displacement along the y-axis, and the gradient of the nominal strain was taken with respect to the temperature to calculate the linear CTE. The TMA applies a small force to the sample to measure its deformation. This the probe was modeled with a token 1 Pa stress on the $+y$-face of the element, although the specific value of the probe force is not expected to significantly impact

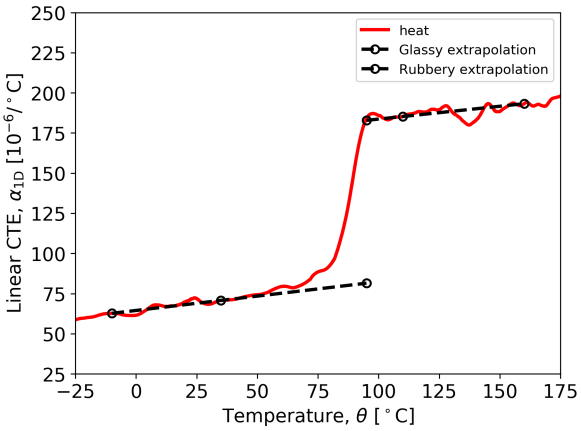

Figure 4-5. Linear coefficient of thermal expansion (CTE) measured during a temperature up-sweep in a thermomechanical analyzer (TMA) for 828T403. Black dashed lines indicate how the linear CTE reference values at 95 °C and temperarture dependence of the linear CTEs were measured. Experimental data from Fig. 3-13.

results because probe-induced deformations are negligible. The linear CTE was calculated as the thermal derivative of the nominal linear strain during the cooling and heating portions of the experiment.

The optimization procedure used a genetic algorithm, specifically the `soga` method in Dakota [1]. One-hundred generations were evaluated, with each generation having a population of one-hundred. Four parameters were optimized: the two stretched exponential parameters for $f_3(t)$ and the reference values of the volumetric CTEs, i.e. τ_3, β_3, α_g^{ref}, and $\alpha_\infty^{\text{ref}}$. The objective function was the L^2 norm of the absolute error between the simulated and experimental linear CTE between 50 °C and 120 °C. Both the linear CTE during cooling and heating were included in the objective function, and were given equal weight.

Fig. 4-6 shows the linear CTE fit upon (a) cooling and (b) heating. Black dotted lines indicate the temperature range used during optimization. The calibrated fit shows excellent agreement with the cooling curve in Fig. 4-6a. The calibrated fit on heating is also excellent, even if the transition is slightly too broad on the glassy side. At low temperatures, densification occurs as a result of physical aging. Upon reheating through the glass transition, the volume is recovered, which manifests as small CTE overshoot in the experiments. For this experiment, the overshoot is small, since no isothermal aging period was included in the experimental procedure. This small CTE overshoot also appears in the calibrated model response, demonstrating that the model is able to fit physical aging behavior when used for calibration, even if it is only a small amount of physical aging that appears here. The reference volumetric CTE values that were adjusted during optimization are compared to their measured values in Table 4-2.

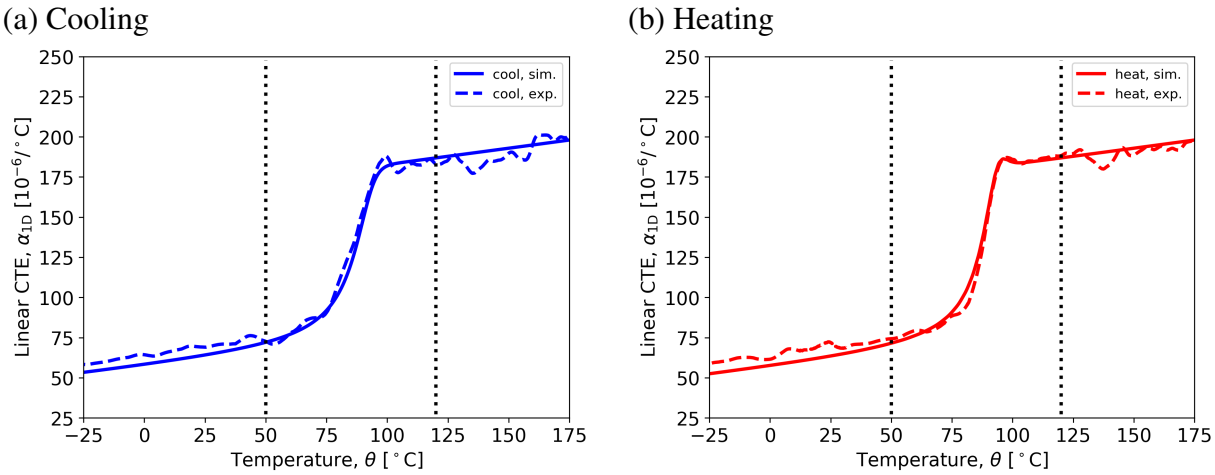

Figure 4-6. Optimized TMA response from the baseline calibration approach for 828T403. Black dotted lines represent the temperature range considered during optimization. Optimized parameters included $\tau_3 = \tau_1$, $\beta_3 = \beta_1$, α_g^{ref}, and $\alpha_\infty^{\text{ref}}$. Experimental data from Fig. 3-13.

Table 4-2. Measured volumetric coefficient of thermal expansion parameters 828T403 from Fig. 4-5 and how they are adjusted during optimization for the fit in Fig. 4-6.

Parameter	Measured	Optimized	Units
α_g^{ref}	244	211	$10^{-6}/\text{K}$
α_g'	0.5	–	$10^{-6}/\text{K}^2$
$\alpha_\infty^{\text{ref}}$	544	544	$10^{-6}/\text{K}$
α_∞'	0.5	–	$10^{-6}/\text{K}^2$

4.1.4. Glassy Compression

The clock parameter C_4 was calibrated using glassy compression experiments at different temperatures and strain rates, corresponding to Step 3 in Fig. 4-1. The parameter C_4, which controls the effect of shear strain on the material clock and is responsible for yield in the model, was calibrated so that the yield stress and Young's modulus from simulations of compression matched experimental data.

Details for the experimental procedure can be found in Section 3.2.4, with stress–strain data presented in Fig. 3-14 and linear regressions for the yield stress, yield strain, and Young's modulus in Fig. 3-15. Glassy compression was simulated in Sierra using the following thermal history applied to a single element: (1) anneal the material at 105 °C for 30 min, (2) cool at 1 °C/min to room temperature (25 °C), (3) Sit at room temperature for 60 min, (4) linearly heat to the loading temperature over 30 min, (5) at the loading temperature, apply a constant nominal strain rate in compression up to a nominal strain of 0.2. The test and simulation matrices considered included loading temperatures (−50 °C, 25 °C, 50 °C) and three strain rates (1/min, 10^{-1}/min, 10^{-2}/min) for a total of nine conditions. The simulated thermomechanical history is only an approximation of the real history. Since only a single element is used, heat transfer and inhomogeneous deformation are not considered in the model.

Since only a single parameter was calibrated, no formal Dakota procedure was used; C_4 was manually adjusted to achieve the lowest objective function. The objective function that was minimized was calculated as the sum of the relative errors of the yield stress and the Young's modulus across all nine loading conditions in the test matrix. The yield stress was calculated as the maximum nominal stress below 0.12 strain. and the Young's modulus was calculated as the average slope of the stress–strain curve between 0 and 0.2 strain. Regressions of the yield stress and Young's modulus from all experimental realizations, see Fig. 3-15, served as the reference values when calculating the relative errors. Both the yield stress and Young's moduli were weighted equally in the objective function. All loading conditions were also weighted equally in the objective function.

The simulated yield stresses after fitting C_4 are shown in Fig. 4-7. The same data is shown in Fig. 4-7a and Fig. 4-7b, but the data are organized into iso–strain rate and isothermal lines, respectively. Simulated and experimental stress–strain curves are shown in Fig. 4-8. The effect of temperature on the yield stress is too low; the calibration produces a good fit for the yield stress at 50 °C and 25 °C, but under-predicts the yield stress at −50 °C. In the model, the effect of strain rate on yield is constant at all three temperatures. However, in the experiments, the effect of strain rate on yield increases with decreasing temperature. This results in good predictions of strain rate sensitivity at higher temperatures, but the effect is too low at −50 °C. The simulated stress–strain curves are significantly broader than the experimental ones. Overall, the calibrated model produces a good fit at 50 °C and 25 °C, but a poor fit at −50 °C.

(a) Temperature Effect

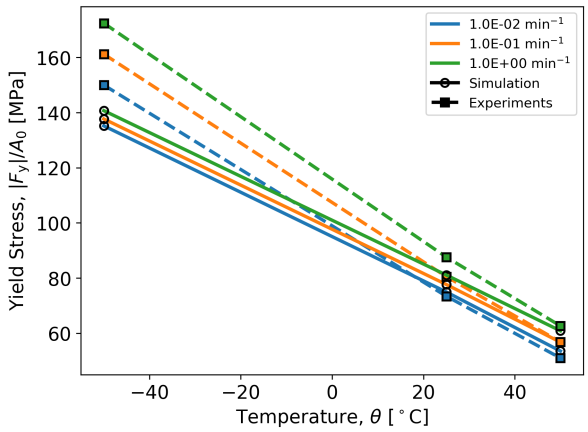

(b) Strain Rate Effect

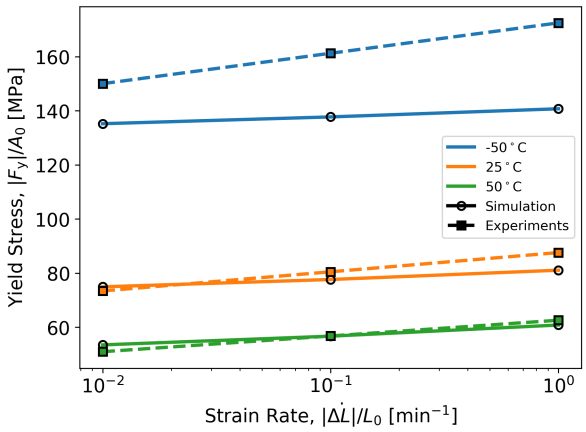

Figure 4-7. Optimized yield stress response from the baseline calibration approach for 828T403. (a) Yield stress versus temperature for constant strain rates, (b) Yield stress versus strain rate for constant temperatures. The only optimized parameter was C_4. Experimental data from Fig. 3-15.

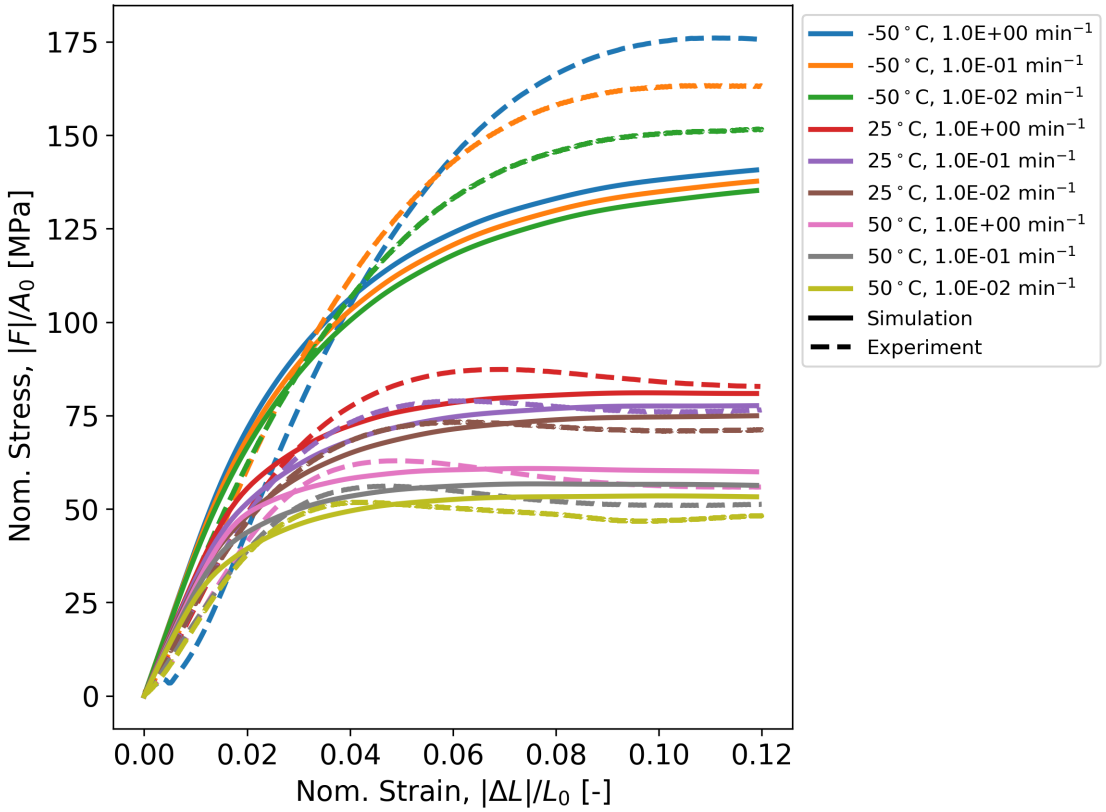

Figure 4-8. Simulated and experimental stress–strain curves. The simulated response was produced by the baseline calibration approach for 828T403. Experimental data from Fig. 3-14.

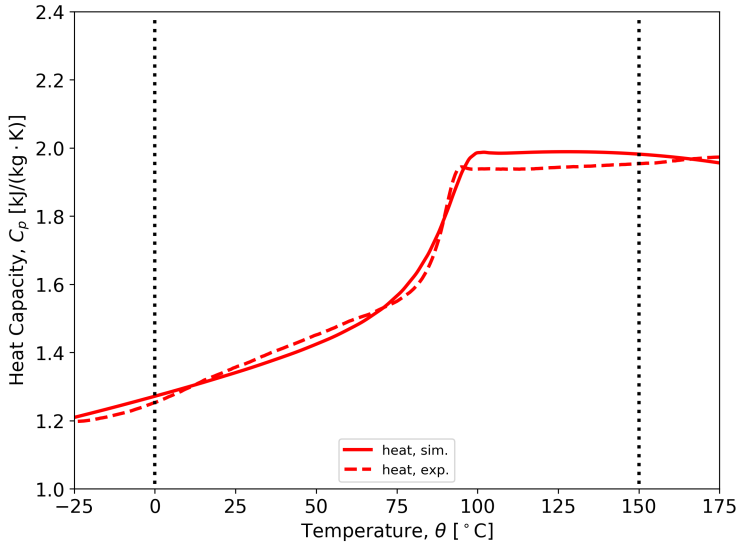

Figure 4-9. Optimized DSC response from the baseline calibration approach for 828T403. Black dotted lines represent the temperature range considered during optimization. Optimized parameters included τ_4, β_4, C_g^{ref}, C_g', C_∞^{ref}, and C_∞'. Experimental data from Fig. 3-16. The cooling rate was $15\,^\circ\text{C/min}$.

4.1.5. Stress-Free Temperature Sweep in a Differential Scanning Calorimeter

The heat capacity parameters, C_g^{ref}, C_g', C_∞^{ref}, and C_∞', as well as the thermal relaxation function, $f_4(t)$, were calibrated using measurements of the heat capacity during a stress-free temperature sweep in a differential scanning calorimeter (DSC). This corresponds to Step 5 in Fig. 4-1. Historically, this step has not been included in the standard calibration approach, as older versions of the SPEC model [4] did not include equations for thermomechanical coupling.

Details of the experimental data are found in Section 3.2.5 with heat capacity measurements shown in Fig. 3-16. The experimental heat capacity measurements were not calibrated to provide absolute values of the heat capacity. Therefore, a reference value for the heat capacity was necessary to shift the experimental data for use during optimization. Based on heat capacity measurements for 828DEA [3], all experimental data was shifted vertically to a reference value of $1527.5\,\text{J}/(\text{kg}\cdot\text{K})$ at $70\,^\circ\text{C}$. The DSC experiment was simulated by applying the following thermal history to a single element in Sierra: (1) anneal at $200\,^\circ\text{C}$ for 5 min, (2) cool at a fixed cooling rate to $-90\,^\circ\text{C}$, (3) hold the temperature constant at $-90\,^\circ\text{C}$ for 5 min, (4) heat to $200\,^\circ\text{C}$ at a heating rate of $10\,^\circ\text{C/min}$. The experimental database included temperature sweeps at multiple cooling rates. Here, only the $15\,^\circ\text{C/min}$ cooling rate was used for calibration. The constant-pressure heat capacity from the model was calculated using Eq. (2.42).

As with the TMA calibration step in Section 4.1.3, the optimization procedure used the `soga` genetic algorithm in Dakota. One-hundred generations were evaluated, with each generation having a population of one-hundred. Six parameters were optimized: the two stretched exponential function parameters for $f_4(t)$ and the four parameters governing the glassy and rubbery heat capacity, i.e., τ_4, β_4, C_g^{ref}, C_g', C_∞^{ref}, and C_∞'. The objective function that was

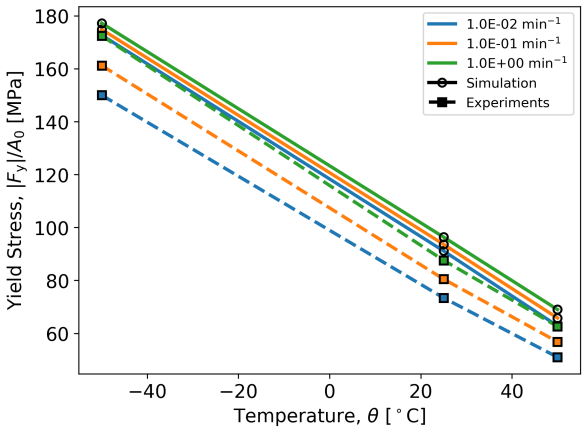

Figure 4-10. Yield stress versus temperature for a legacy calibration [11] compared to regressions of experimental data. Experimental data from Fig. 3-15.

minimized was the L^∞ norm (i.e. the maximum) of the absolute error between the simulated and experimental heat capacity between 0 °C and 150 °C. Only the heat capacity during the final heating step was included in the objective function, since accurate experimental measurements of the heat capacity are difficult to obtain during cooling.

The optimized heat capacity fit along with the corresponding experimental data are shown in Fig. 4-9. Black dotted lines are used to indicate the temperature range used in the objective function. The heat capacity transition is slightly too broad and the rubbery end of the transition is a little too high. Also, the rubbery heat capacity is constant in the experiment, but gradually decreases with temperature in the simulation. This is a result of the complicated coupling that occurs between the heat capacity, coefficients of thermal expansion, and the bulk moduli, see Section 2.3. The glassy side of the transition is well fit.

4.1.6. Motivation for a Compression-Focused Calibration Approach

The baseline calibration reasonably fit all calibration experiments, except perhaps for the yield stress in glassy compression, especially the yield stress at −50 °C. Since the yield stress was fairly accurate at higher temperatures, this suggests that the actual issue with the baseline calibration is related to the effect of temperature on the yield stress, which can been seen by comparing the slopes of yield stress versus temperature for the experiments and simulations in Fig. 4-7a. However, a legacy calibration performed much better when predicting the changes in the yield stress with temperature, which is demonstrated in Fig. 4-10. It is not a trivial task to identify the parameters that are most responsible for calibrating the changes in yield stress with temperature, but the parameters most different between the present baseline calibration and the legacy calibration were the WLF parameters, C_1 and C_2, and the thermal-volumetric relaxation function, $f_3(t)$ ($f_1(t) = f_3(t)$ in the legacy calibration). Parameters for the legacy calibration are listed in Appendix A, Table A-1. Parameter studies revealed that reasonable changes to the WLF

(a) Baseline, $\tau_1 = \tau_3 = 0.835\,\text{s}$ (b) Modified, $\tau_1 = \tau_3 = 0.001\,\text{s}$

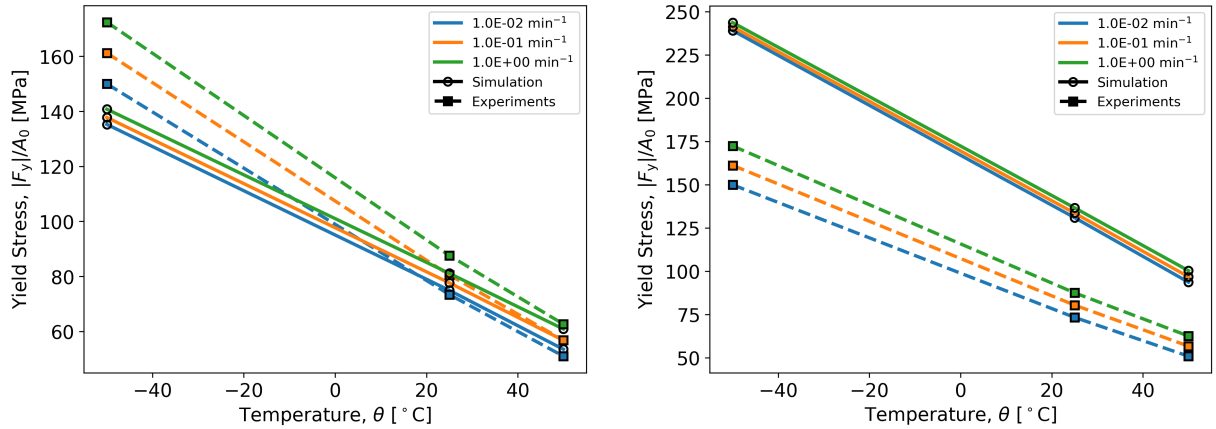

Figure 4-11. Yield stress versus temperature for two different parameter sets where $\tau_1 = \tau_3$, compared to regressions of experimental data. (a) Baseline, $\tau_1 = \tau_3 = 0.835\,\text{s}$ and (b) Modified, $\tau_1 = \tau_3 = 0.001\,\text{s}$. Experimental data from Fig. 3-15.

parameters were not able to adjust the temperature dependence of the yield stress, leaving $f_3(t)$ for investigation.

In the baseline calibration, $f_3(t)$ was calibrated from the CTE transition measured in a TMA experiment, and has the stretched exponential parameters $\tau_1 = \tau_3 = 0.835\,\text{s}$ and $\beta_1 = \beta_3 = 0.25$. On the other hand, the stretched exponential parameters for the legacy calibration are $\tau_1 = \tau_3 = 0.001\,\text{s}$ and $\beta_1 = \beta_3 = 0.20$. When the baseline calibration was modified to use the legacy bulk characteristic time, $\tau_1 = \tau_3 = 0.001\,\text{s}$, the slope of yield stress versus temperature increased, bringing it much closer to the experimental slope. This is shown in Fig. 4-12, where the yield stress versus temperature is plotted with experimental data for $\tau_1 = \tau_3 = 0.835\,\text{s}$ and $\tau_1 = \tau_3 = 0.001\,\text{s}$ (note that Fig. 4-12(a) is the same plot from Fig. 4-7(a)). Although decreasing $\tau_1 = \tau_3$ also increased the yield stress at all temperatures, the entire yield stress versus temperature curve could be shifted downward by increasing C_4, which should be refit after other relaxation functions change. Therefore, the overly high predictions of the yield stress do not alter the conclusion that using the legacy τ_3 improved the yield stress versus temperature behavior.

Fig. 4-11 indicates that either $f_1(t)$ or $f_3(t)$ is key for adjusting the relationship between temperature and yield stress. However, since both the volumetric and thermal-volumetric relaxation functions are altered in Fig. 4-11, it is unclear which one is most important. In Fig. 4-12, τ_1 and τ_3 are varied separately to understand which relaxation is more important for calibrating the yield stress versus temperature. In Fig. 4-12a, $\tau_1 = 0.001\,\text{s}$ is used, while τ_3 is kept at its original value. When τ_1 is adjusted, the yield stress rises around 10 MPa to 20 MPa, but the slope of the yield stress versus temperature is still lower than the experimental slope. On the other hand, $\tau_3 = 0.001\,\text{s}$ is used in Fig. 4-12b, and τ_1 is maintained at its original value. Here, the yield stress increases by around 40 MPa to 60 MPa and the slope of the yield stress versus temperature is now steeper than the experimental result. Clearly a value for τ_3 between 0.835 s and 0.001 s

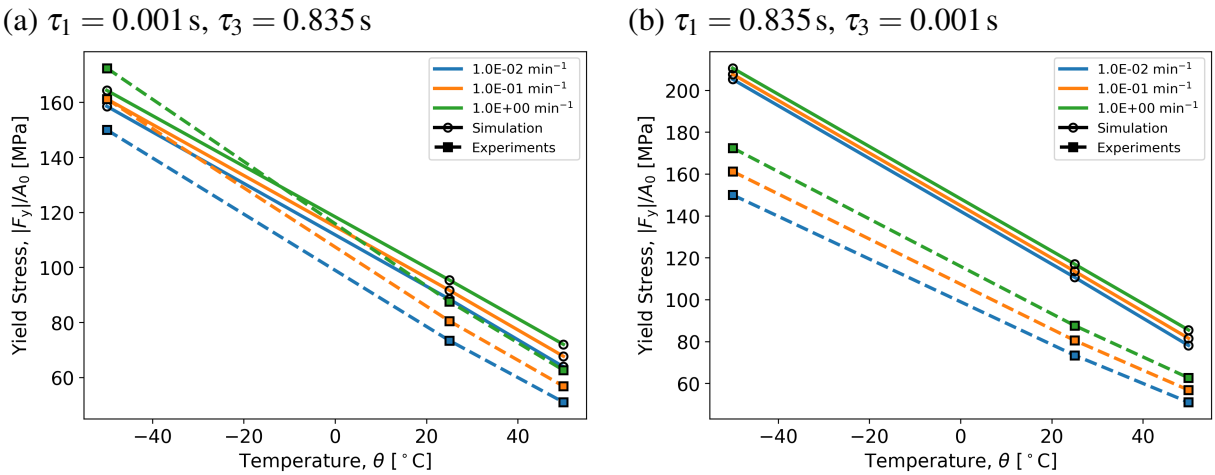

Figure 4-12. Yield stress versus temperature for two different parameter sets where $\tau_1 \neq \tau_3$, compared to regressions of experimental data. (a) Baseline, $\tau_1 = \tau_3 = 0.835\,\mathrm{s}$ and (b) Modified, $\tau_1 = \tau_3 = 0.001\,\mathrm{s}$. Experimental data from Fig. 3-15.

would correctly match the experimental slope. Fig. 4-12 clearly demonstrates that $f_3(t)$ is the more important of the two relaxation functions. This is likely because $f_3(t)$ drives the memory of the thermal history in the shift factor definition, see Eq. (2.8).

The $f_3(t)$ fit to a TMA experiment produced sub-optimal predictions of the yield stress. However, the results shown here indicate that $f_3(t)$ could be fit directly to glassy compression experiments, although it is unknown what effect this would have on predictions of the TMA experiment. This brief parameter study motivates the compression-focused calibration explored in the following section, Section 4.2.

4.2. Compression-Focused Calibration

Based on the discussion in Section 4.1.6, an alternate calibration approach was proposed where $f_3(t)$ was optimized to fit the yield stress in glassy compression at different strain rates and temperatures. The goal of this approach was to find a set of parameters that improved predictions of relationship between the yield stress and temperature, while still accurately predicting other experiments in the calibration data set.

This calibration approach diverges from the baseline approach at Step 3 in Fig. 4-1. The calibrated volumetric coefficients of thermal expansion from the baseline calibration were kept, but instead of calibrating $f_3(t)$ using the TMA experiment, $f_3(t)$ and C_4 were calibrated from the glassy compression experiments. The calibration of $f_3(t)$ and C_4 to glassy compression data are presented in Section 4.2.1. In Section 4.2.2, the DSC calibration step from the baseline approach is repeated, but new values for τ_4 and β_4 emerge given that a different $f_3(t)$ was used. After finishing the alternate calibration, the TMA simulation is re-revisited in Section 4.2.3 to assess

Table 4-3. SPEC parameters produced by the compression-focused calibration for 828T403. Only parameters that have changed from the baseline approach are listed here, see Table 4-1.

Parameter	Value	Units	Experiment	Reference
C_g^{ref}	0.983	$\text{MJ}/(\text{m}^3 \cdot \text{K})$	DSC	Fig. 4-15
C_g'	1.97	$\text{kJ}/(\text{m}^3 \cdot \text{K}^2)$	DSC	Fig. 4-15
C_∞^{ref}	1.195	$\text{MJ}/(\text{m}^3 \cdot \text{K})$	DSC	Fig. 4-15
C_∞'	1.38	$\text{kJ}/(\text{m}^3 \cdot \text{K}^2)$	DSC	Fig. 4-15
C_4	11600	K	Compression	Fig. 4-13
τ_1	129	s	Compression	Fig. 4-13
β_1	0.15	–	Compression	Fig. 4-13
τ_3	129	s	Compression	Fig. 4-13
β_3	0.15	–	Compression	Fig. 4-13
τ_4	49.8	s	DSC	Fig. 4-15
β_4	0.67	–	DSC	Fig. 4-15

what trade-offs were necessary between the CTE predictions and the yield stress predictions. Since this approach calibrates $f_3(t)$ using glassy compression data, it is referred to as the "compression-focused" calibration approach. The relaxation function $f_3(t)$ is especially important to predictions of physical aging because the thermal history is stored in the material clock via a hereditary integral with $f_3(t)$. Parameters that changed from the baseline approach are listed in Table 4-3.

4.2.1. Glassy Compression

After the CTEs are measured in Step 3 of Fig. 4-1, the compression-focused calibration departs from the baseline calibration. Instead of calibrating $f_3(t)$ using the CTE transition measured by the TMA and then calbrating C_4 using glassy compression, $f_3(t)$ and C_4 are both calibrated using glassy compression data. As with the baseline calibration approach, it is assumed that the volumetric and the thermal-volumetric functions are equal, $f_1(t) = f_3(t)$. Details for the experimental data can be found in Section 3.2.4 and results are shown in Figs. 3-14 and 3-15. All nine loading conditions from the baseline approach were also used here (loading temperatures: $-50\,^\circ$C, $25\,^\circ$C, $50\,^\circ$C and nominal strain rates: $1/\text{min}$, $10^{-1}/\text{min}$, $10^{-2}/\text{min}$) The simulations use the same thermomechanical history described in Section 4.1.4.

The optimization is conducted using the `soga` method in Dakota. One-hundred generations were evaluated, with each generation having a population of one-hundred. Three parameters were optimized: the two stretched exponential parameters for the thermal-volumetric relaxation function and the clock parameter controlling the effect of shear strain on the material clock i.e. τ_3, β_3, and C_4. The minimized objective function was composed of the relative errors of the yield stress for all nine loading conditions in the test matrix. The yield stress was calculated as the

(a) Temperature Effect

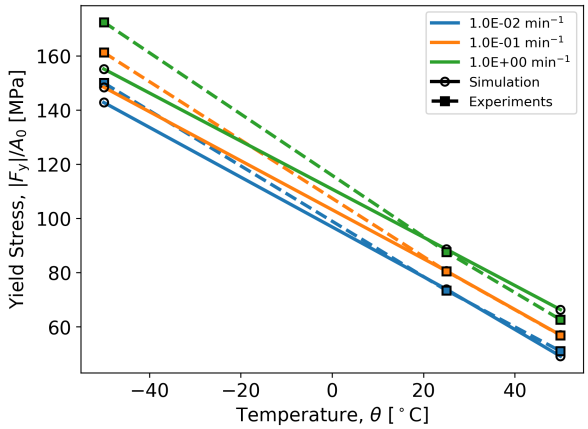

(b) Strain Rate Effect

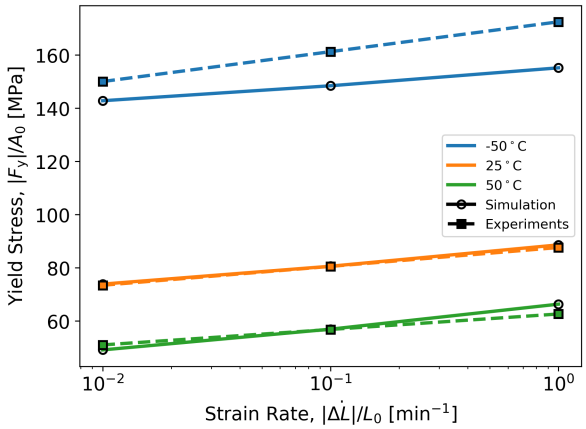

Figure 4-13. Optimized yield stress response from the compression-focused calibration approach for 828T403. (a) Yield stress versus temperature for constant strain rates, (b) Yield stress versus strain rate for constant temperatures. The optmized parameters included $\tau_1 = \tau_3$, $\beta_1 = \beta_3$, and C_4. Experimental data from Fig. 3-15.

maximum nominal stress below 0.12 strain. Linear regressions for the yield stress, see Fig. 3-15, were used as the reference value when calculating the relative errors. All nine loading conditions were weighted equally in the objective function.

The simulated yield stresses after fitting $\tau_1 = \tau_3$, $\beta_1 = \beta_3$, and C_4 are shown in Fig. 4-13. The same data is shown in Fig. 4-13a and Fig. 4-13b, but the data are organized into iso–strain rate and isothermal lines, respectively. Simulated and experimental stress–strain curves are shown in Fig. 4-14. The effect of temperature on the yield stress is increased, but is still a little too low. The yield stresses at 50 °C and 25 °C are very close, but the yield stress is still slightly too low at −50 °C. Additionally, the effect of the strain rate on yield is slightly too high at the two higher temperatures and slightly too low at the lowest temperatures. Overall, the strain rate effect seems to be an average across all temperatures. Compare this result to the baseline approach in Fig. 4-8, where the optimizer prioritized accurately reproducing the strain rate effect at the two high temperatures, but the effect is significantly under-predicted at the lowest temperature. The compression-focused calibration also predicts the maximum stress at an earlier strain level than in the experiments, but the post-peak stress decrease is more gradual in the simulations than the experiments. This could be a result of using a single element, incapable of inhomogeneous deformation, to model the compression cylinder. Overall, the compression-focused calibration exhibits improved yield stress predictions relative to the baseline approach, compare Fig. 4-14 to Fig. 4-8.

The optimized parameters for the glassy compression step of the compression-focused approach were $\tau_3 = 129\,\text{s}$, $\beta = 0.15$, and $C_4 = 11\,600\,\text{K}$. Compare this to the baseline parameters of $\tau_3 = 0.835\,\text{s}$, $\beta_3 = 0.25$, and $C_4 = 22\,500\,\text{K}$. The compression-focused $f_3(t)$ is significantly longer and broader than the $f_3(t)$ produced by the baseline calibration.

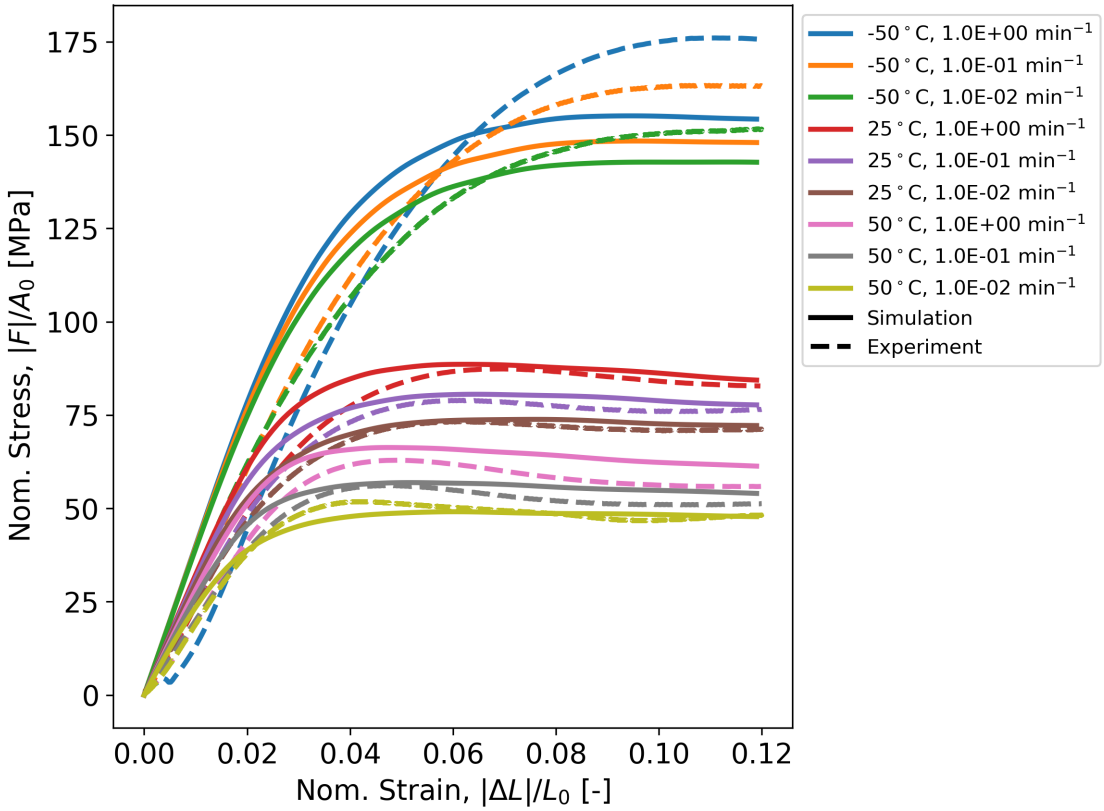

Figure 4-14. Simulated and experimental stress–strain curves. The simulated response was produced by the compression-focused calibration approach for 828T403. Experimental data from Fig. 3-14.

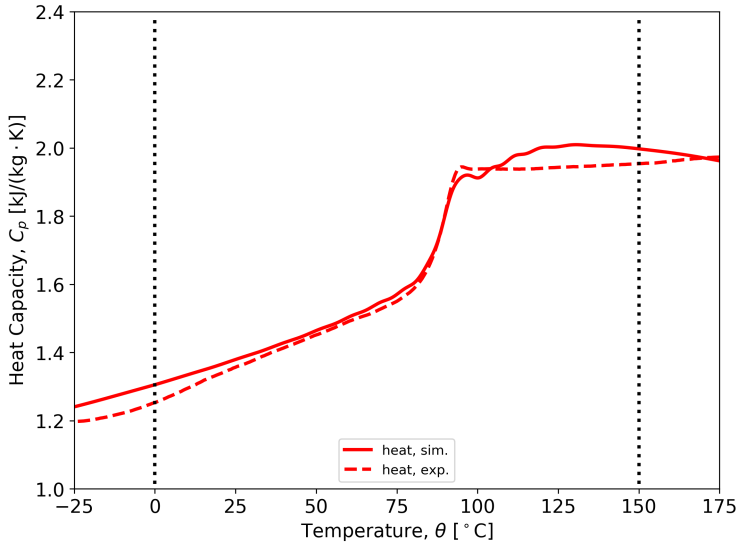

Figure 4-15. Optimized DSC response from the baseline calibration approach for 828T403. Black dotted lines represent the temperature range considered during optimization. Optimized parameters included τ_4, β_4, C_g^{ref}, C_g', C_∞^{ref}, and C_∞'. Experimental data from Fig. 3-16. The cooling rate was $15\,^\circ\text{C}/\text{min}$.

4.2.2. Stress-Free Temperature Sweep in a Differential Scanning Calorimeter

For the compression-focused calibration, the DSC calibration step needs to be repeated using the new $f_3(t)$. Since $f_3(t)$ appears in the shift factor definition of the SPEC model, Eq. (2.8), it affects all viscoelastic behaviors predicted by the model, so parameters from the baseline DSC calibration can not be re-used. The exact calibration procedure described in Section 4.1.5 is repeated here.

Fig. 4-15 shows the calibrated constant-pressure heat capacity fit for the compression-focused approach. The simulated heat capacity matches the experimental result across in the glassy region and the transition region. However, there is an unusual double structure that occurs when reaching the equilibrium heat capacity. For the $f_3(t)$ optimized to the glassy compression experiments, the stretched exponential parameters for $f_4(t)$ are $\tau_4 = 49.8\,\text{s}$ and $\beta_4 = 0.67$. Compare this to the baseline results of $\tau_4 = 0.132\,\text{s}$ and $\beta_4 = 0.22$.

4.2.3. Revisit the Stress-Free Temperature Sweep in a Thermomechanical Analyzer

No relaxation function was optimized to the TMA data in the compression-focused calibration. Therefore, it is important to re-visit the TMA response to evaluate the trade-offs made in order to improve the yield stress behavior. Details on the thermal history used to simulate the TMA experiment are provided in Section 4.1.3.

Fig. 4-16 shows the simulated and experimental linear CTE on cooling (a) and heating (b). Here, the transition response is signficantly broader than the experimental behavior, which is consistent

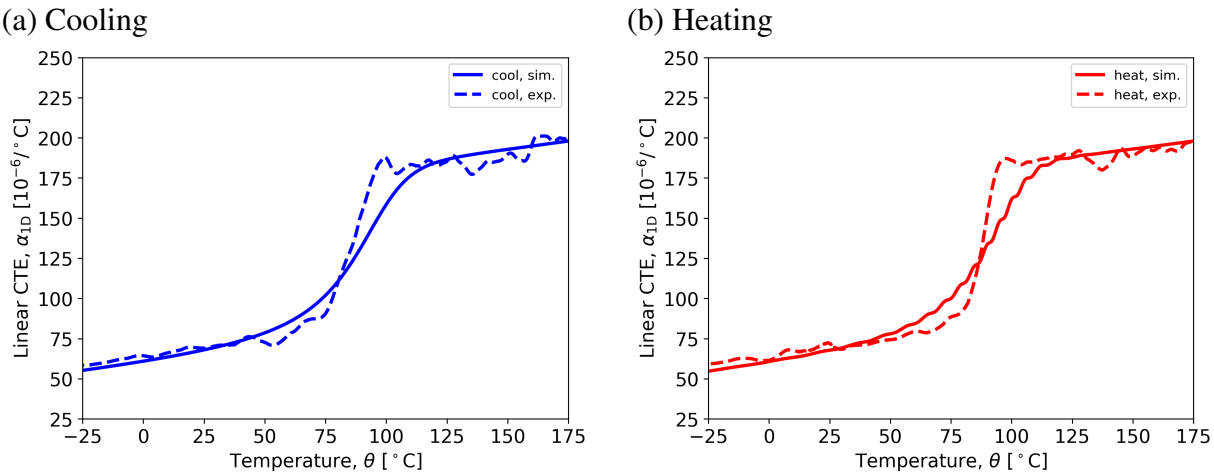

Figure 4-16. Experimental TMA response compared to the simulated response from the compression-focused calibration for 828T403 during (a) cooling and (b) heating. Experimental data from Fig. 3-13.

with increasing the $f_3(t)$, compare the compression-focused $\beta_3 = 0.14$ to the baseline value of $\beta_3 = 0.25$. When reheating, the CTE response exhibits small oscillations. This is likely because when converting a very broad (low β_i) stretched exponential into a Prony series, the Prony terms are spaced further apart (for a fixed number of terms in the Prony series). Fig. 4-16 reveals that predictions of the thermal strain are significantly worse when $f_3(t)$ is chosen to generate good predictions of the yield stress at different temperatures and strain rates.

4.3. DSC-Focused Calibration

Based on the discussion in Section 5.1.6, an alternate calibration approach was proposed where $f_3(t)$ and $f_4(t)$ were calibrated to fit the constant pressure heat capacity response from a DSC experiment using a slow cooling rate. The goal of this approach was to predict the height of the heat capacity spike that occurs on reheating when the material was cooled into the glass at a low cooling rate. However, both $f_3(t)$ and $f_4(t)$ needed to be calibrated, as adjusting $f_4(t)$ alone was not sufficient to control the height of the heat capacity spike without sacrificing the quality of the fit in other regions of the DSC response, see Section 5.1.6.

This calibration approach diverges from the baseline approach at Step 4 in Fig. 4-1. In this approach, the heat capacity fitting (Step 5) is performed first, and then the glassy compression fitting (Step 4) is performed; Steps 4 and 5 are swapped for this approach. The modified Step 5 in this approach is different in two ways. First, the experimental data that is fit during optimization uses a cooling rate of 0.5 °C/min instead of a cooling rate of 15 °C/min, which was used in Sections 4.1.5 and 4.2.2. The slower cooling rate allows some physical aging, which results in an overshoot in the constant-pressure heat capacity when the material is reheated, followed quickly by a return to the equilibrium heat capacity value. This manifests in the heat capacity curve as a "spike". Second, the thermal-volumetric and thermal relaxation functions are set equal,

Table 4-4. SPEC parameters produced by the DSC-focused calibration for 828T403. Only parameters that have chagned from the baseline approach are listed here, see Table 4-1.

Parameter	Value	Units	Experiment	Source
C_g^{ref}	0.996	$\text{MJ}/(\text{m}^3 \cdot \text{K})$	DSC	Fig. 4-17
C_g'	3.86	$\text{kJ}/(\text{m}^3 \cdot \text{K}^2)$	DSC	Fig. 4-17
C_∞^{ref}	1.180	$\text{MJ}/(\text{m}^3 \cdot \text{K})$	DSC	Fig. 4-17
C_∞'	1.54	$\text{kJ}/(\text{m}^3 \cdot \text{K}^2)$	DSC	Fig. 4-17
C_4	14700	K	Compression	Fig. 4-18
τ_3	17.6	s	DSC	Fig. 4-17
β_3	0.21	–	DSC	Fig. 4-17
τ_4	17.6	s	DSC	Fig. 4-17
β_4	0.21	–	DSC	Fig. 4-17

$f_4(t) = f_3(t)$. The bulk relaxation function during the TMA calibration step in Section 4.1.3 is not changed. Results from the modified DSC calibration step are shown in Section 4.3.1. After $f_3(t) = f_4(t)$ is fit to the DSC data using a slower cooling rate, C_4 must be adjusted to refit the glassy compression data using the new $f_3(t)$. The results from this calibration step are shown in Section 4.3.2. Finally, the TMA predictions are revisited in Section 4.3.3 using the $f_3(t)$ found from the DSC calibration step using the slower cooling rate. No relaxation functions are calibrated using the TMA data. Since this calibration approach calibrates $f_3(t)$, the relaxation function that appears in the material clock, using DSC data, it is referred to as the "DSC-focused" calibration approach. Parameters that changed from the baseline approach are listed in Table 4-4.

4.3.1. Stress-Free Temperature Sweep in a Differential Scanning Calorimeter

After calibrating $f_1(t) = f_3(t)$ using the TMA data in Step 3 of Fig. 4-1, the DSC-focused approach departs from the baseline approach. Instead of using the $f_3(t)$ found from the TMA data, $f_3(t)$ and $f_4(t)$ were calibrated using the heat capacity response measured by DSC. However, $f_1(t)$ is not changed from the TMA calibration step, and the thermal and thermal-volumetric relaxation functions were set equal, $f_3(t) = f_4(t)$.

The calibration procedure described in Section 4.1.5 is repeated here, with two exceptions. First, the experimental data used for calibration used a slower cooling rate of $0.5\,^\circ\text{C}/\text{min}$. The slower cooling was useful for invoking a physical aging response, which manifested as a spike in the heat capacity response upon reheating, since this behavior was poorly predicted in the baseline calibration, which was calibrated using an experiment with a cooling rate of $15\,^\circ\text{C}/\text{min}$. Second, the thermal and thermal-volumetric relaxation functions were set to be equal, $f_4(t) = f_3(t)$. Otherwise, the same six parameters in Section 4.1.5 were also recalibrated here, τ_4, β_4, C_g^{ref}, C_g', C_∞^{ref}, and C_∞'.

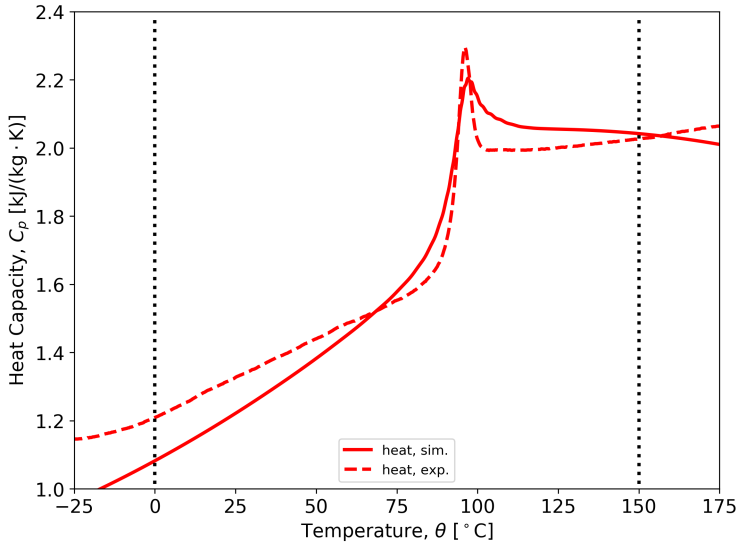

Figure 4-17. Optimized DSC response from the DSC-focused calibration approach for 828T403. Black dotted lines represent the temperature range considered during optimization. Optimized parameters included $\tau_3 = \tau_4$, $\beta_3 = \beta_4$, C_g^{ref}, C_g', C_∞^{ref}, and C_∞'. Experimental data from Fig. 3-16. The cooling rate was $0.5\,^{\circ}\text{C}/\text{min}$**.**

The optimized DSC response for the DSC-focused approach is shown in Fig. 4-17. Although the height of the heat capacity spike is fit well, the transition below and above the spike are too borad. There are other problems with the glassy and rubbery responses as well. The slope of the glassy heat capacity with temperature is too high, which makes the predictions worse at lower temperatures. The rubbery reference value appears to be too high, and then the slope with temperature is negative, whereas the experimental slope of the rubbery response is slightly positive.

4.3.2. Glassy Compression

After changing $f_3(t)$, a new C_4 is needed to best fit the glassy compression response. Only C_4 is recalibrated using the glassy compression response, so the parameter is manually adjusted within 100 K of the best fit. The best fit is defined by minimizing the relative error of the yield stress at the nine loading conditions used in Section 4.1.4. The simulated yield stress was calculated as the maximum nominal stress prior to a strain of 0.12. Regressions of the yield stress, see Fig. 3-15, served as the reference values when calculating the relative errors. All loading conditions were also weighted equally in the objective function.

The simulated yield stresses after fitting C_4 are shown in Fig. 4-18. The same data is shown in Fig. 4-18a and Fig. 4-18b, but the data are organized into iso–strain rate and isothermal lines, respectively. Simulated and experimental stress–strain curves are shown in Fig. 4-19. The fit is qualitatively similar to the baseline calibration approach, Fig. 4-8. The temperature dependence of the yield stress is too low, resulting in a good fit at higher temperatures, 50 °C and 25 °C, but

(a) Temperature Effect

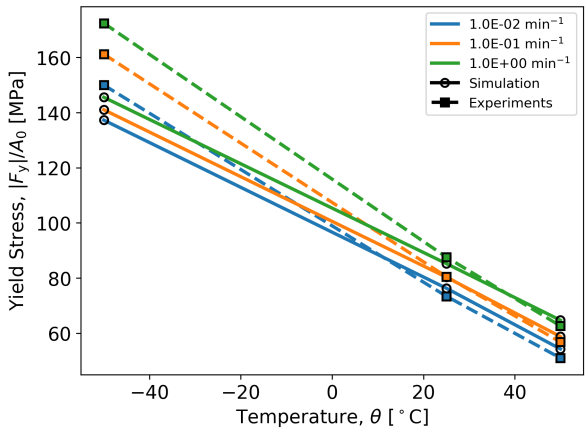

(b) Strain Rate Effect

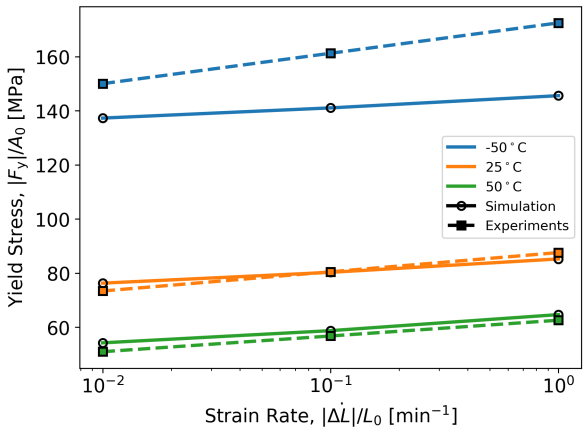

Figure 4-18. Optimized yield stress response from the DSC-focused calibration approach for 828T403. (a) Yield stress versus temperature for constant strain rates, (b) Yield stress versus strain rate for constant temperatures. The only optimized parameter was C_4. Experimental data from Fig. 3-15.

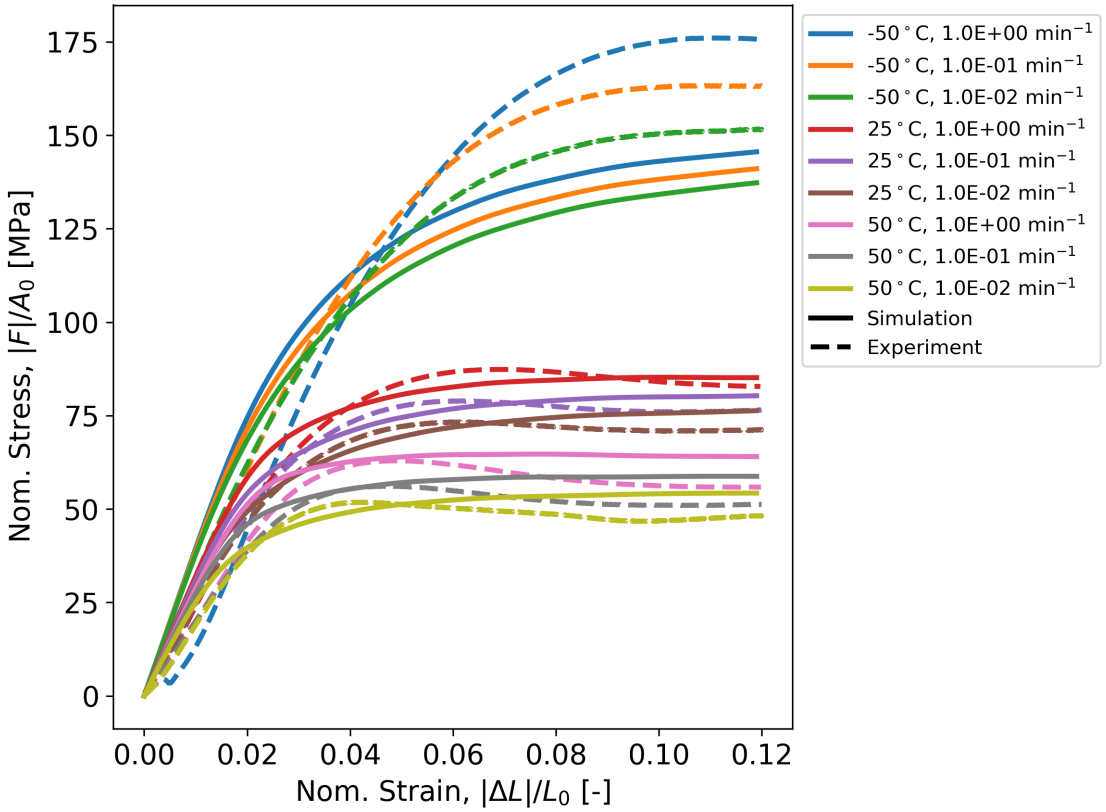

Figure 4-19. Optimized glassy compression response from the DSC-focused calibration approach for 828T403. The only optimized parameter was C_4. Experimental data from Fig. 3-14.

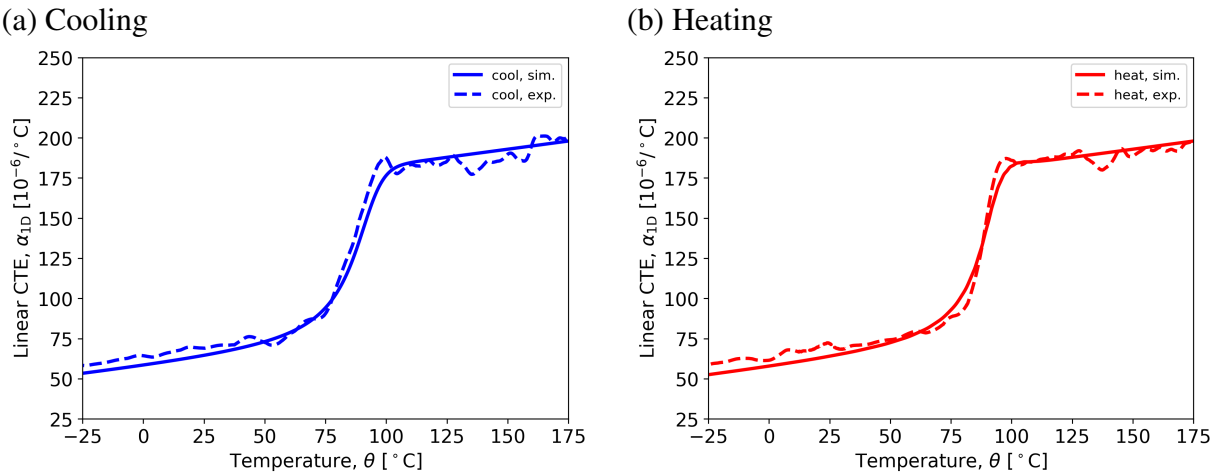

Figure 4-20. Experimental TMA response compared to the simulated response from the DSC-focused calibration for 828T403 during (a) cooling and (b) heating. Experimental data from Fig. 3-13.

the yield stress is too low at lower temperatures, −50 °C. The strain rate dependence of yield is roughly the same at all three temperatures, but in the experiments the strain rate dependence increases with decreasing temperature, so the predicted strain rate dependence is too low at −50 °C. The shape of the stress–strain curve is also still too broad.

4.3.3. Revisit stress-free temperature sweep in thermomechanical analyzer

No relaxation function was optimized to the TMA data in the DSC-focused calibration. Therefore, it is important to re-visit the TMA response to evaluate the trade-offs made in order to improve the DSC response for slow cooling rates. Details on the thermal history used to simulate the TMA experiment are provided in Section 4.1.3.

Fig. 4-20 shows the simulated and experimental linear CTEs on cooling (a) and heating (b). The DSC-focused calibration produces a good fit with the TMA data, both on heating and cooling. The transition is only slightly too broad, making it worse than the baseline prediction, Fig. 4-6, but signficiantly better than the compression-focused prediction, Fig. 4-16.

4.4. 828T403 Aging Predictions Across Calibrations

In this section, each of the three calibrations for 828T403 are subjected to a suite of physical aging simulations. The reponse from each simulation will be compared to experimental data to make qualitative assessments of the strengths and weaknesses of each calibration. In addition, predictions from a legacy calibration [11] are also presented. Parameters for the 828T403 legacy calibration can be found in Appendix A.

Table 4-5. Relaxation functions and changed parameters for all three calibration approaches for 828T403.

Parameter	Baseline	Compression-focused	DSC-focused	Units
C_g^{ref}	0.695	0.983	0.996	$\text{MJ}/(\text{m}^3 \cdot \text{K})$
C_g'	1.98	1.97	3.86	$\text{kJ}/(\text{m}^3 \cdot \text{K}^2)$
C_∞^{ref}	0.991	1.195	1.180	$\text{MJ}/(\text{m}^3 \cdot \text{K})$
C_∞'	1.82	1.38	1.54	$\text{kJ}/(\text{m}^3 \cdot \text{K}^2)$
C_4	22500	11600	14700	K
τ_1	0.835	129	0.835	s
β_1	0.25	0.15	0.25	–
τ_2	0.0186	0.0186	0.0186	s
β_2	0.21	0.21	0.21	–
τ_3	0.835	129	17.6	s
β_3	0.25	0.15	0.21	–
τ_4	0.132	49.8	17.6	s
β_4	0.22	0.67	0.21	–

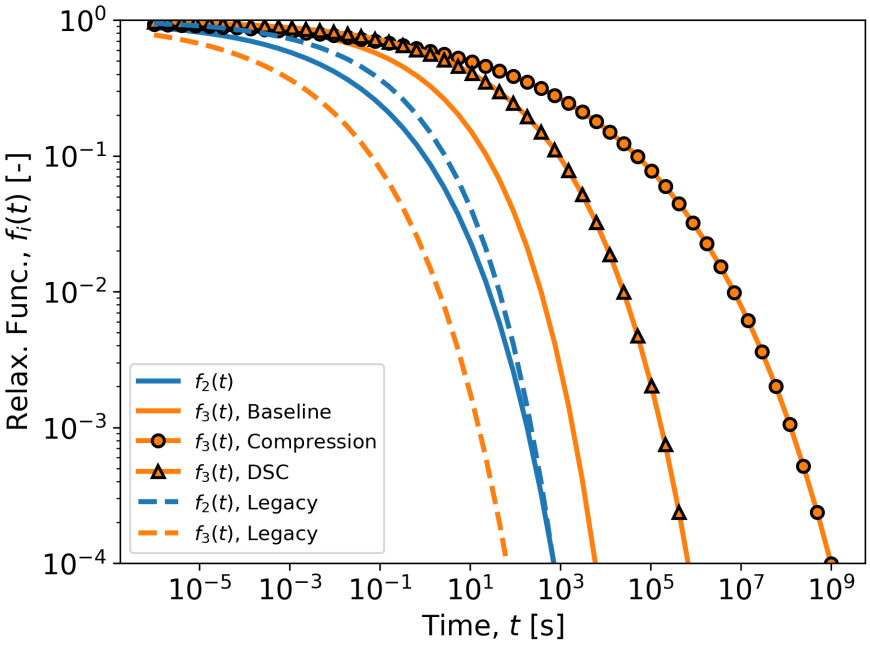

Figure 4-21. Comparison of the different functions for $f_3(t)$ found from the three calibrations of 828T403 and the $f_2(t)$ common to all three. Also shown are the $f_2(t)$ and $f_3(t)$ from a legacy calibration [11].

Prior to executing the physical aging simulations, the key differences betweeen the calibrations are highlighted. Table 4-5 lists the stretched exponential functions for all four relaxation functions from all three 828T403 calibrations and parameters that changed between each calibration. The most fundamental difference between each calibration is the type of experiment used to calibrate $f_3(t)$, which is the relaxation function that stores the thermal history in the shift factor definition, see Eq. (2.8). The characteristic time for $f_3(t)$ varies from 0.835 s to 129 s and the breadth varies from 0.15 to 0.25. Based on the parameter studies that are discussed in Sections 4.1.6 and 5.1.6, the model responses are less sensitive to $f_1(t)$ and $f_4(t)$. The shear relaxation function, $f_2(t)$, is the same across all three calibrations, since they were all calibrated from the same shear master curve. Different C_4 arise from fitting the glassy compression data based on the different $f_3(t)$ functions. As τ_3 increases, C_4 must decrease to maintain the same yield stress. Values for the heat capacity parameters also vary for each calibration, but these changes are of secondary importance to the aging response. Fig. 4-21 shows compares $f_3(t)$ for all three calibrations along with the common $f_2(t)$. The $f_3(t)$ and $f_2(t)$ from a legacy calibration are also shown. The legacy and current $f_2(t)$ are very similar, demonstrating a low amount of uncertainty from the shear master curve calibration step. On the other hand, an extremely wide range of different $f_3(t)$ are present in the four calibrations. The compression-focused calibration is the longest, followed by the DSC-focused, followed by the baseline, followed by the legacy calibration. Only the legacy $f_3(t)$ is shorter than either $f_2(t)$.

4.4.1. Stress-Free Aging Followed by Compression Through Yield

The calibrations were benchmarked against the evolution of the mechanical behavior after stress-free aging. Experimental details are found in Section 3.2.7. Two data sets were available, one where the specimen was aged and loaded at the same temperature, see Fig. 3-18, and another where the specimen was loaded at 76 °C regardless of the aging temperature, see Fig. 3-19. Aging times between 0 h and 4000 h were explored. The experimentally measured yield stress and initial Young's modulus are plotted as functions of the aging time in Fig. 3-20. Stress-free aging followed by compression through yield was simulated using the following thermomechanical history applied to a single element in Sierra: (1) anneal at 120 °C for 30 min, (2) cool to 25 °C at a rate of 1 °C/min, (3) sit at 25 °C for 30 min, (4) heat to the aging temperature, θ_{age} over 30 min, (5) hold at the aging temperature for the aging time, less 30 min for the time it took to heat to the aging temperature, (6) cool to 25 °C over 30 min, (7) sit at 25 °C for 1 h, (8) heat to the loading temperature, θ_{load} over 30 min, (9) load at a nominal strain rate of 0.89/min, corresponding to a displacement rate of 0.1 in/min for a specimen with an initial length of 1.12 in. The yield stress is chosen as a convenient metric for physical aging, which is calculated from the simulations as the local maximum in the nominal stress.

Fig. 4-22 shows the effects of the aging time on the stress–strain curves for $\theta_{\text{age}} = \theta_{\text{load}} = 65\,^{\circ}\text{C}$. The baseline calibration under predicts the amount of strengthening that occurs from aging, while the legacy calibration shows nearly no effect of aging on the stress–strain curve. On the other hand, the compression-focused and DSC-focused calibrations seem to produce good predictions of yield stress evolution. Fig. 4-23 plots the yield stress versus aging time for all conditions where $\theta_{\text{age}} = \theta_{\text{load}}$. To make it possible to display the unaged cases, $t_{\text{age}} = 0$ on a log plot, they are

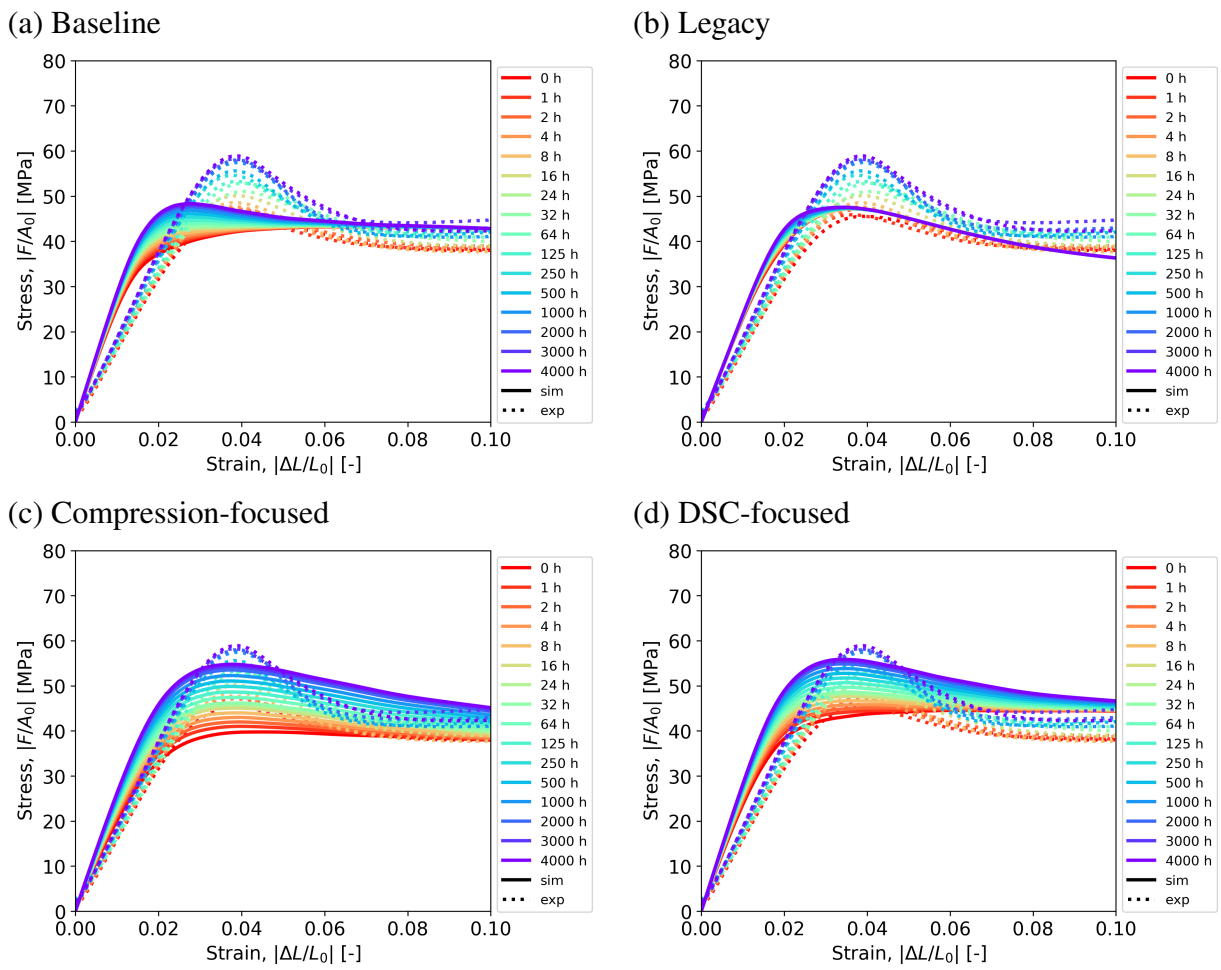

Figure 4-22. 828T403 calibration assessment of stress–strain curves after stress-free aging. (a) Baseline calibration, (b) Legacy calibration [11], (c) Compression-focused calibration, (d) DSC-focused calibration. The loading temperature and aging temperature are both 65 °C. Experimental data from Fig. 3-18b.

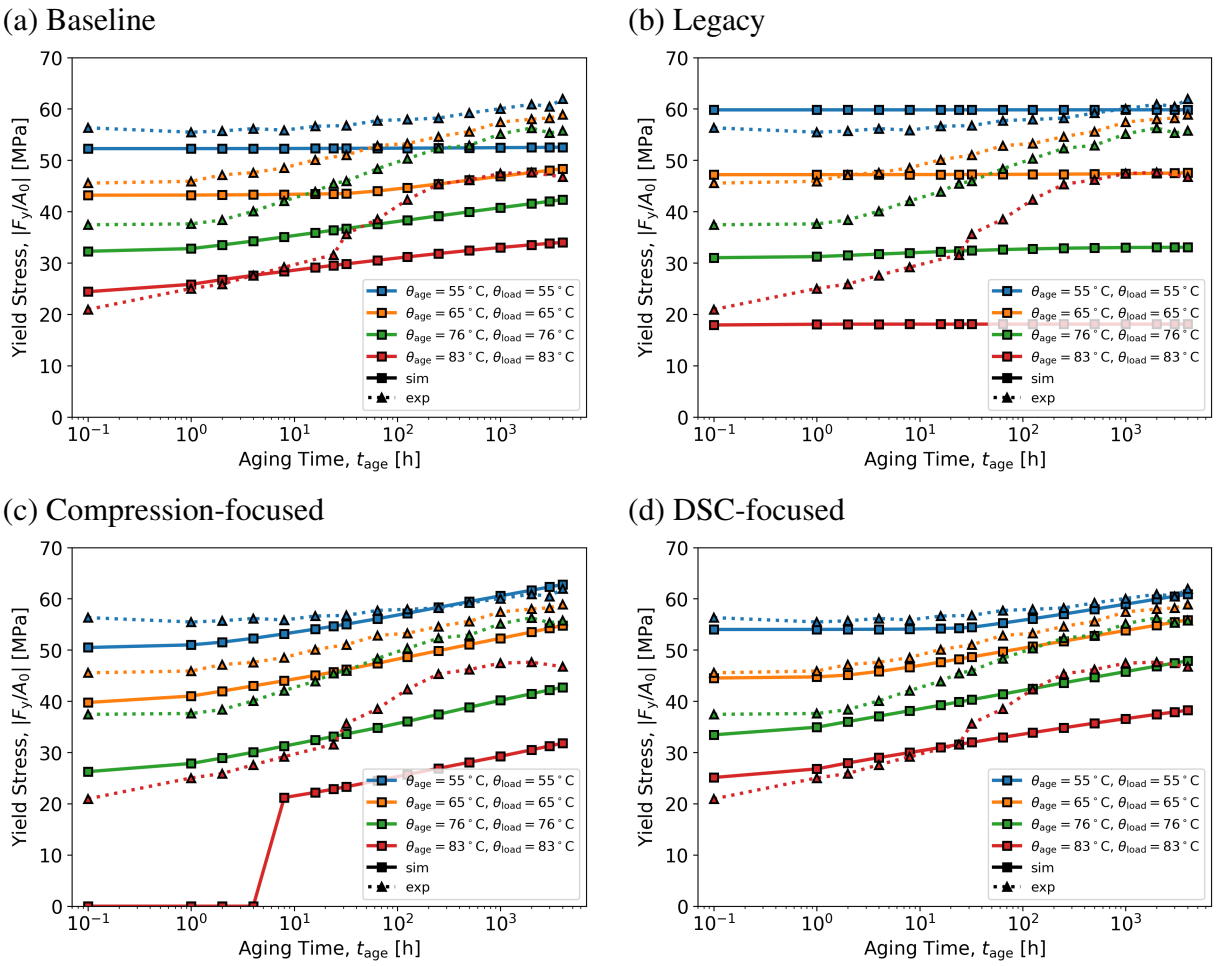

Figure 4-23. 828T403 calibration assessment for yield stress evolution with aging time for stress-free aging for the case when the aging and loading temperature are the same, $\theta_{age} = \theta_{load}$. (a) Baseline calibration, (b) Legacy calibration [11], (c) Compression-focused calibration, (d) DSC-focused calibration. A point with a yield stress of zero indicates the absence of a peak in the stress–strain curve, i.e. no apparent softening. Experimental data from Fig. 3-20b.

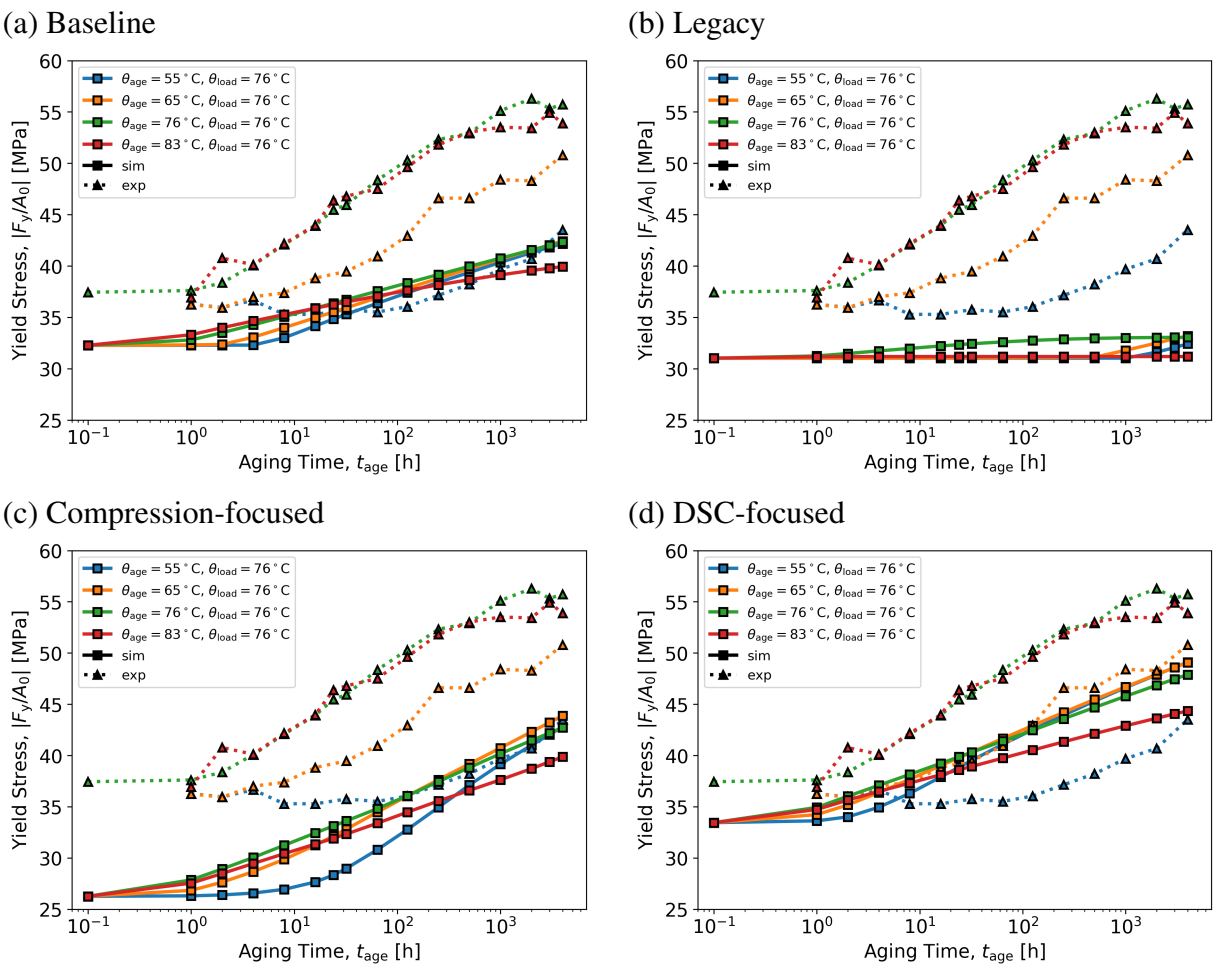

Figure 4-24. 828T403 calibration assessment for yield stress evolution with aging time for stress-free aging for the case when the aging and loading temperature are different, $\theta_{age} \neq \theta_{load}$. (a) Baseline calibration, (b) Legacy calibration [11], (c) Compression-focused calibration, (d) DSC-focused calibration. Experimental data from Fig. 3-20d.

plotted with an aging time of 0.1 h. The baseline calibration (a) shows no yield stress evolution for $\theta_{\text{age}} = 55\,^{\circ}\text{C}$ and under predicts the yield stress evolution at all other conditions. The legacy calibration (b) shows no yield stress evolution at any aging temperature. This doesn't mean that the legacy calibration produces stress–strain curves that are completely constant with respect to aging, but the different thermal histories are either erased before the peak stress or are insignificant at the peak stress. The slope of the yield stress versus aging time in the compression-focused calibration (c) matches the experiments well for the aging temperatures 55 °C and 65 °C, but is slightly too low for 76 °C and 83 °C. Also, the compression-focused calibration consistently under predicts the magnitude of the yield stress, which is peculiar since it produces the best unaged yield stress predictions for the three loading temperatures used for calibration, 50 °C, 25 °C, and −50 °C, see Fig. 4-14. For Fig. 4-23(c), the points with zero yield stress indicate that a local maximum was not found in the stress–strain curve (i.e. no apparent softening). The DSC-focused calibration (d) produces the best fit of all four calibrations. The magnitude of the unaged yield stress matches well with the experiments at all four temperatures. The slope of the yield stress with the (log) aging time is also accurate at 55 °C, 65 °C, and for low aging times with 83 °C. The slope is too low for 76 °C and and higher aging times for with 83 °C. Furthermore, the DSC-focused approach accurately predicts the different induction times (i.e. an initial time during which the yield stress does not evolve) for 55 °C, 65 °C, and 76 °C. No other calibration predicts the induction time with the same accuracy.

Fig. 4-24 plots the yield stress versus aging time for all conditions where $\theta_{\text{age}} \neq \theta_{\text{load}}$. The experimental data shows slopes of yield stress versus log aging time that are similar for the three highest aging temperatures and slightly lower for 55 °C. However, the 55 °C aging temperature has an induction time of around 100 h, the 65 °C aging time has an induction time of around 10 h, and the 76 °C and 83 °C aging temperatures show essentially no induction time. The baseline calibration approach (a) under predicts the slope of the yield stress. It does, however, get close to predicting the induction time for the $\theta_{\text{age}} = 65\,^{\circ}\text{C}$, but under-predicts the induction time for $\theta_{\text{age}} = 55\,^{\circ}\text{C}$. For all conditions except for $\theta_{\text{age}} = 55\,^{\circ}\text{C}$, the magnitude of the yield stress is too low in the baseline calibration. As with the case when $\theta_{\text{age}} = \theta_{\text{load}}$, the legacy calibration (b) shows essentially no yield stress evolution. The compression-focssed calibration (c) matches the slope well for the three highest aging temperatures, but the slope is too high for the lowest aging temperature. The induction time at 55 °C is accurate, but too short for 65 °C. For all but a few conditions, the yield stress in the compression-focused calibration is too low. The DSC-focused calibration comes the closest to predicting both the magnitude of the yield stress and its slope with the log of the aging time, but the induction time is not well predicted for 55 °C. Once again, the compression-focused and DSC-focused calibrations do the best at predicting the yield stress evolution. The compression-focused does the best at predicting the low aging temperature induction time, while the DSC-focused is more accurate regading the magnitude of the yield stress and its slope. However, both calibrations exhibit deficiencies here, specifically there is not enough variation in the aging behaviors at different aging temperatures for the $\theta_{\text{age}} \neq \theta_{\text{load}}$ case, i.e. the experiments show three distinct lines for the four aging temperatures (76 °C and 83 °C are nearly identical), while the compression-focused and DSC-focused produce four extremely similar lines for the yield stress versus aging time.

Across both the $\theta_{\text{age}} = \theta_{\text{load}}$ and $\theta_{\text{age}} \neq \theta_{\text{load}}$ cases, the DSC-focused calibration produces the best fit to the experimental data.

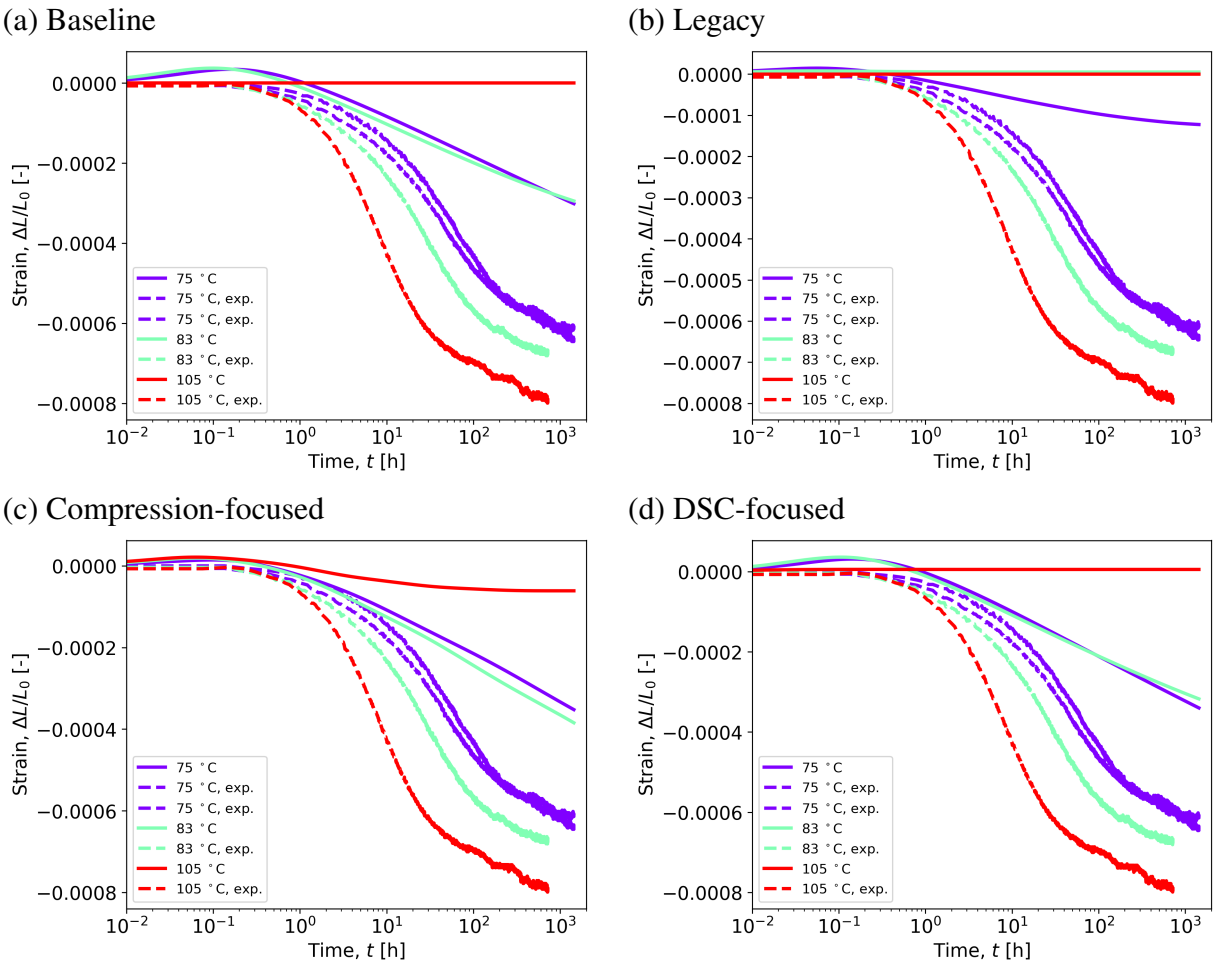

Figure 4-25. 828T403 calibration assessment for volume relaxation during a nearly stress-free isothermal hold. (a) Baseline calibration, (b) Legacy calibration [11], (c) Compression-focused calibration, (d) DSC-focused calibration. Experimental data from Fig. 3-21.

4.4.2. Isothermal Volume Relaxation Under Near Stress-Free Conditions

The calibrations were benchmarked against the evolution of the volume strain during a nearly stress-free isothermal hold. Experimental details are shown in Section 3.2.8 with experimental results shown in Fig. 3-21. The isothermal hold experiment was simulated by applying the following thermomechanical history to a single element in Sierra: (1) anneal at 150 °C for 5 min, (2) cool to 30 °C at 1 °C/min, (3) heat to the aging temperature at 1 °C/min, (4) hold at the aging temperature for 60 d. Since contact from a probe is required to measure the volume, the experiment is only nearly stress-free. A token stress of 1 Pa is applied to the $+y$-face of the element.

Fig. 4-25 compares the predictions of the evolution of the linear thermal strain during the isothermal hold to experimental data. For all calibrations, the thermal strain is essentially constant

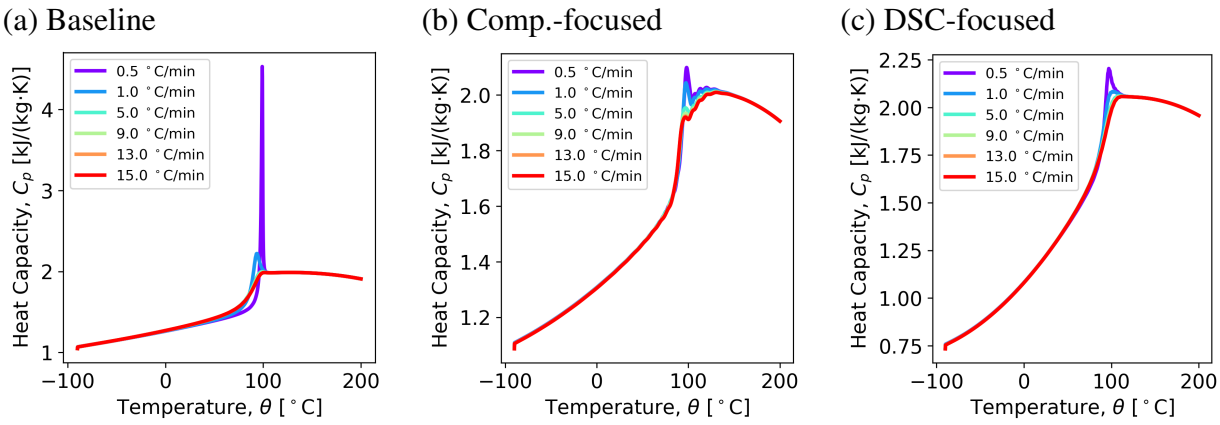

Figure 4-26. The effect of cooling rate on the constant pressure heat capacity upon reheating for three calibrations of 828T403. (a) Baseline calibration, (b) compression-focused calibration, (c) DSC-focused calibration.

for the hold at 105 °C, although a small amount of relaxation occurs in the compression-focused calibration, which has the longest $f_3(t)$. For the legacy calibration, which has the shortest $f_3(t)$, the 83 °C isothermal hold also shows no change in the thermal strain. For the three new calibrations produced here, 83 °C and 75 °C holding temperatures produce similar thermal strain histories. At the beginning of the isothermal hold, the thermal strain sometimes becomes positive. This is a memory effect occurring due to heating the material to the isothermal hold. All calibrations produce similar volume histories, which all show significantly less thermal strain relaxation than the experimental data. The increased volume change in the experiments is likely due to chemical shrinkage, which cannot be predicted by the `spectacular` model.

4.4.3. Effect of Cooling Rate on the Heat Capacity Overshoot

The calibrations were benchmarked against the heat capacity measured during a stress-free temperature increase. The thermal history involved cooling into the glass and then reheating at 10 °C/min. The experimental database included tests using different cooling rates. At slower cooling rates, a small amount of physical aging occurs, so that upon reheating, enthalpy recovery results in a spike in the heat capacity curve [9]. Experimental details can be found in Section 3.2.5 with results shown in Fig. 3-16. The DSC experiments were already used during the calibration step, but each of the three procedures used only a single cooling rate; the baseline and compression-focused calibrations used 15 °C/min, while the DSC-focused used 0.5 °C/min. Here, all three calibrations are tested at multiple cooling rates. The thermal history used to simulate these experiments is listed in Section 4.1.5, except that the applied cooling rate is variable.

Fig. 4-26 shows heat capacity upon reheating for all three calibrations. Across all three calibrations, overshoots are predicted for cooling rates 0.5 °C/min and 1.0 °C/min. At faster cooling rates, significant differences between the heat capacity response are not observed. An

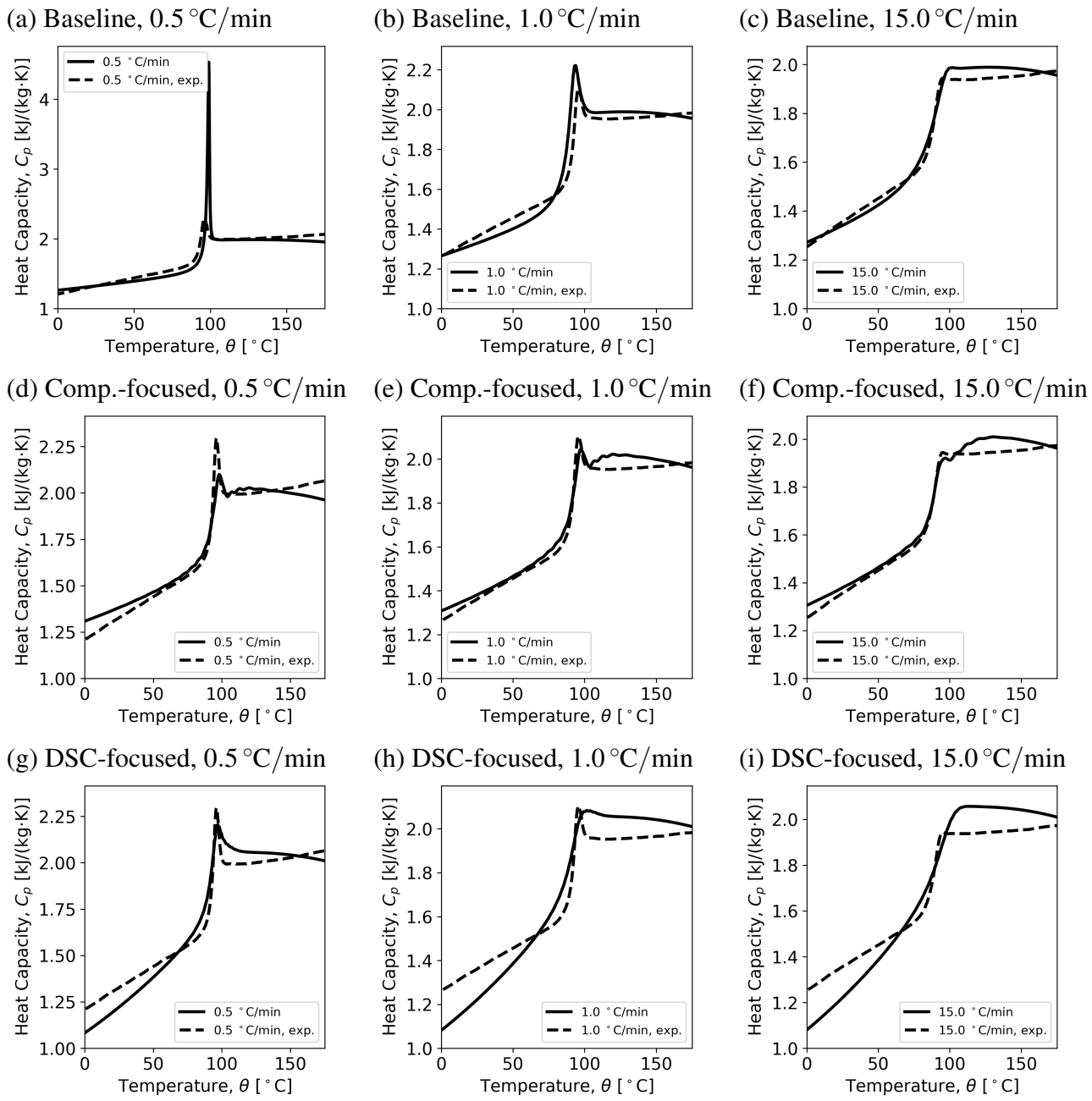

Figure 4-27. 828T403 calibration assessment for the effect of cooling rate on the constant pressure heat capacity upon reheating. The different calibrations are organized in rows; (a, b, c) basline, (d, e, f) compression-focused, (g, h, i) DSC-focused; and different cooling rates are organized in columns; (a, d, g) 0.5 °C/min**, (b, e, h)** 1.0 °C/min**, (c, f, i)** 15.0 °C/min**. Experimental data from Fig. 3-16.**

extremely large heat capacity spike is predicted for the baseline calibration at 0.5 °C/min. More reasonable overshoots are predicted for the other two calibrations. As was observed in the calibration process for the compress-focused approach, the heat capacity response exhibits an unusual double structure. Fig. 4-27 compares the model responses to experimental data. The figures are organized to show a single calibration per row and a single cooling rate per column. The baseline calibration shows reasonably good predictions for 1.0 °C/min and 15.0 °C/min, but the heat capacity spike is dramtically too large at 0.5 °C/min. On the other hand, the compression-focused calibration under predicts the height of the heat capacity spike at 0.5 °C/min, but gives good predictions of the height at 1.0 °C/min and 15.0 °C/min. However, the undesirable double structure causes bad predictions for the rubbery heat capacity at all cooling rates. The DSC-focused prediction appears to accurately predict the height of the heat capacity spike at 0.5 °C/min, but closer inspection of the other two cooling rates shows that the rubbery heat capacity is too high. Therefore, while the DSC-focused accurately predicts the the maximum heat capacity at 0.5 °C/min, the actual height of the heat capacity overshoot is under predicted. Surprisingly, the DSC-focused calibration produces the worst calibration of the heat capacity transition behavior.

4.4.4. Effect of Isothermal Aging on the Heat Capacity Overshoot

The calibrations were benchmarked against the heat capacity measured by a DSC during a stress-free temperature increase after aging during an isothermal hold. Experimental details can be found in Section 3.2.6 with results shown in Fig. 3-17. The aged DSC experiments are simulated by applying the following thermomechanical history to a single element in Sierra: (1) anneal at 120 °C for 30 min, (2) cool to 30 °C at 1 °C/min, (3) hold at 30 °C for 5 min, (4) heat to the aging temperature, θ_{age}, at 10 °C/min, (5) hold at the aging temperature, θ_{age} for the aging time, t_{age}, (6) cool to 30 °C at 10 °C/min, (7) hold at 30 °C for 5 min, (8) heat to 120 °C at 10 °C/min.

The heat capacity during the final heating step is calculated and compared to experimental results in Fig. 3-17 for aging temperatures of 55 °C and 83 °C. The aged DSC experiments were not calibrated to produce the absolute measurements of the heat capacity, so the vertical position of the experimental heat capacity curves are arbitrary. Here, a vertical offset in the experimental data is preserved to help with comparisons between the simulated and experimental response. Both the baseline (a, b) and DSC-focused (e, f) calibrations produce similar behavior. At an aging temperature of 55 °C and at long aging times, the heat capacity spike is unrealisticially too high and occurs at extremely high temperatures. In fact, for aging times greater than 1000 h in the baseline, reheating to 120 °C was not sufficient to recover to the equilibrium enthalpy. At an aging temperature of 83 °C, the peak heat capacity is still too large and occurs at too high of a temperature, but the differences between the simulated and experimental data are less dramatic for the baseline and DSC-focused calibrations. On the other hand, the compression-focused calibrations produce much more reasonable values for the heat capacity spike and the temperature at which the spike occurs. Although the compression-focused calibration exhibits an undesirable double structure, it is the only calibration that realistically models the effects of physical aging on the heat capacity.

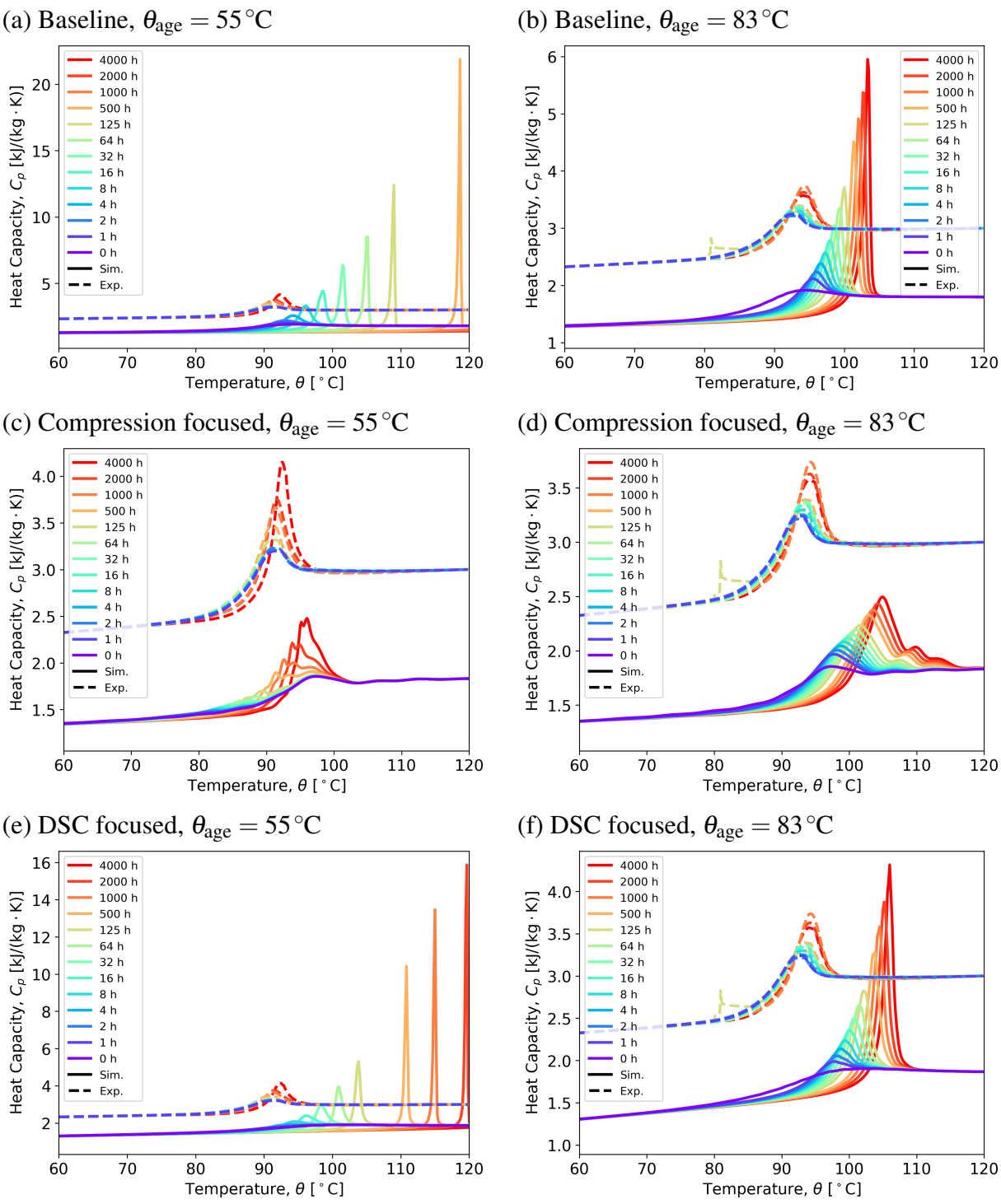

Figure 4-28. 828T403 calibration assessment for the effect of isothermal aging on the constant pressure heat capacity upon reheating. Calibrations are organized in rows; (a, b) baseline, (c, d) compression-focused, (d, e) DSC-focused, and different aging temperatures are organized in columns; (a, c, e) $\theta_{age} = 55\,^{\circ}C$ and (b, d, f) $\theta_{age} = 83\,^{\circ}C$. Experimental data from Fig. 3-17.

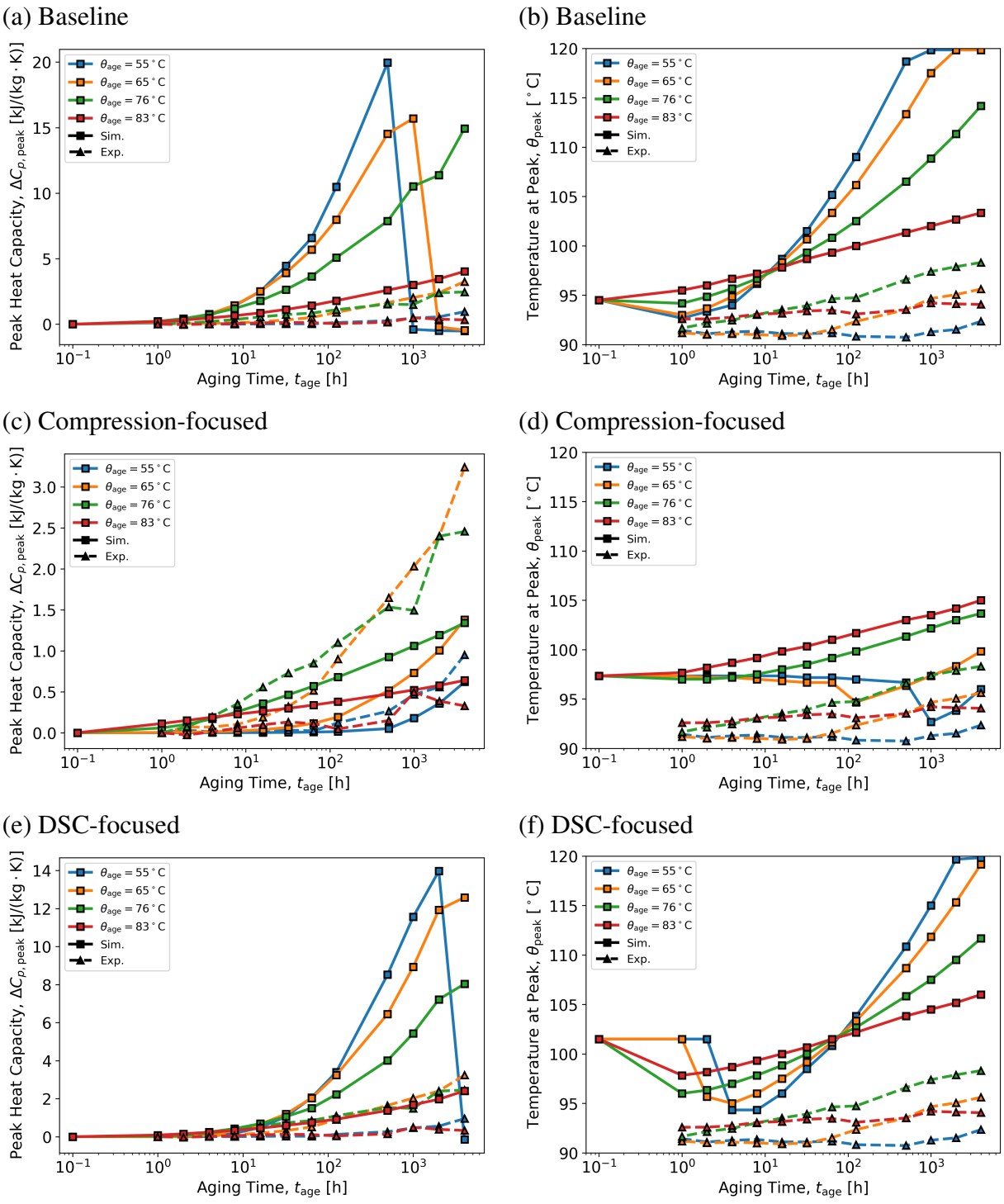

Figure 4-29. 828T403 calibration assessment for the effect of isothermal aging on the (a, c, e) peak heat capacity and (b, d, f) temperature of the peak heat capacity. Calibrations are organized in rows; (a, b) baseline, (c, d) compression-focused, (d, e) DSC-focused. Experimental data from Fig. 3-17.

4.5. 828T403 Summary and Recommendations

Three calibration procedures were executed for 828T403. The fundamental difference between each calibration procedure is the experiment used to calibrate $f_3(t)$, the relaxation function that controls the thermal memory in the shift factor definition. For the baseline approach, $f_3(t)$ is calibrated from the coefficient of thermal expansion measured by a thermo-mechanical analyzer, for the compression-focused approach, $f_3(t)$ is calibrated from the yield stress in glassy compression at different strain rates and temperatures, and for the DSC-focused approach, $f_3(t)$ is calibrated from the heat capacity measured from a differential scanning calorimeter experiment and the experiment used a procedure where the material was cooled slowly into the glass so that a heat capacity spike is observed.

The baseline calibration was fit well to both the TMA and DSC experiments, but did not predict the yield stress in compression at different temperatures and strain rates. The compression-focused calibration improved predictions of the yield stress, but the TMA predictions were considerably worsened. The DSC-focused calibration was qualitatively similar to the baseline, except that the DSC-focused could accurately predict the height of the heat capacity spike in a DSC experiment when the material is cooled slowly into the glass. However, the heat capacity transition predicted by the DSC-focused calibration is too broad. The $f_3(t)$ relaxation functions produced from the different calibrations had the following order, from shortest to longest, baseline (TMA-focused), DSC-focused, and compression-focused. From the calibration suite alone, it is difficult to determine a clear best approach, but given that the DSC-focused accurately predicts the height of the heat capacity spike on the DSC experiment with a slow cooling rate, the DSC-focused calibration is tentatively preferred for physical aging predictions.

However, across the suite of physical aging experiments, the DSC-focused approach is qualitatively the best. The DSC-focused calibration accurately predicts the magnitude of the yield stress and its evolution with stress-free aging. The compression-focused under-predicts the magnitude, while the baseline under-predicts the magnitude and rate of yield stress evolution. For DSC experiments with an isothermal hold, the baseline and DSC-focused approach once again over-predict the height of the heat capacity spike and the temperature of the spike. The compress-focused approach produces a more reasonable spike, but the transition is plagued by a double structure. Parameter studies presented later in Section 5.1.6 indicate that the very broad $f_3(t)$ produced by the compression-focused calibration may be the reason it predicts more reasonable heat capacity spikes than the other two calibrations.

5. CALIBRATION AND PREDICTIONS FOR 828DEA

This chapter documents the three calibration approaches executed for 828 DGEBA/DEA. The first approach is referred to as the "baseline" calibration, which essentially follows the procedure historically used for the PEC and SPEC models [4]. The execution of the baseline calibration procedure is documented in Section 5.1. The other two approaches attempt to improve specific behaviors poorly predicted by the baseline calibration. The second approach focuses on improving the stress–strain response in compression at different strain rates and temperatures, and is therefore referred to as the "compression-focused" calibration. The execution of the compression-focused calibration procedure is documented in Section 5.2. The third approach focuses on improving the heat capacity response measured by a differential scanning calorimeter (DSC), and therefore is referred to as the "DSC-focused" calibration. The execution of the DSC-focused calibration procedure is documented in Section 5.3. Afterwards, in Section 5.4, the physical aging predictions from each new calibration and one legacy calibration are compared to experiments. The chapter concludes in Section 5.5 with a summary brief assessment of each calibration along with recommendations.

5.1. Baseline Calibration

This section presents the baseline calibration procedure for 828DEA, which is similar to procedures commonly employed for calibrating the SPEC model [4, 8]. A flowchart for the baseline calibration procedure was previously shown in Fig. 4-1. The steps for the baseline calibration approach are re-iterated here to make this chapter more self-contained, while also highlighting a few minor differences between the approach used for 828T403 and the approach used here. Before calibration begins, a reference temperature, θ_{ref} must be chosen. The value of θ_{ref} is somewhat arbitrary, but should be chosen to be slightly above the glass transition temperature where the material can equilibrate. For 828DEA, a reference temperature of $\theta_{\text{ref}} = 75\,^{\circ}\text{C}$ is chosen. A full recalibration was not conducted; a few parameters were borrowed from other sources instead of running new experiments. These borrowed parameters include the four parameters that define the bulk modulus, K_g^{ref}, K_g', K_∞^{ref}, and K_∞'; the four parameters that define the shear modulus, G_g^{ref}, G_g', G_∞^{ref}, and G_∞'; the parameter controlling the sensitivity of the material clock to the volume strain, C_3; and the density, ρ. The values of borrowed parameters are listed in Table 5-1 along with references. The bulk modulus and C_3 are difficult to calibrate [4], and so new experiments were not performed here. Instead, their values are taken from [4], Table 3. The glassy and rubbery shear moduli can be calibrated using the shear master curve, and the temperature dependence of the shear moduli can be calibrated using the isothermal frequency sweeps, as was done for 828T403 in Chapter 4. However, it was decided that mixing elastic constants from multiple sources might lead to innacurrate values for the Young's modulus.

Therefore, the shear modulus parameters are also taken from [4], Table 3 for consistency with the bulk modulus parameters. The material density is also taken from [3], Table 4. The density is not directly used by the SPEC model, but is necessary for converting thermodynamic quantities from a per volume value (used in the SPEC model calculations) to a per mass value (measured in experiments). As shown in the pink box in Fig. 4-1, The baseline calibration procedure assummes that the volumetric and thermal-volumetric relaxation functions are the same, $f_1(t) = f_3(t)$. This assumption is inherent to previous versions of the SPEC model [4], but in the current `spectacular` implementation, the two relaxation functions may be specified separately.

The baseline calibration procedure begins by calibrating the time–temperature superposition parameters and the shear relaxation function from the isothermal frequency sweep shear master curve in Section 5.1.1. The temperature dependence of the shear moduli are measured from isofrequency temperature sweeps in Section 5.1.2, and the measurements are compared to the shear moduli parameters borrowed from [4], Table 3. The coefficients of thermal expansion and the thermal-volumetric relaxation function are calibrated using the thermal strain measured in a thermo-mechanical analyzer (TMA) in Section 5.1.3. The parameter governing the effect of shear strain on the clock, C_4, is calibrated using the yield stress at different strain rates and temperatures in Section 5.1.4. The heat capacity parameters and the thermal relaxation function are calibrated in Section 5.1.5. The parameters that are produced by the baseline calibration are listed in Table 5-1. It should be noted that Table 5-1 specifies relaxation functions using stretched exponentials, which are defined by a characteristic time and a breadth, τ_i and β_i, see Eq. (2.28). However, relaxation functions must be input to the `spectacular` model as Prony series. Custom python tools convert the stretched exponential functions listed in Table 4-1 into Prony series that can be input into the `spectacular` model.

5.1.1. Isothermal Frequency Sweeps and the Shear Master Curve

Isothermal frequency sweeps and the construction of shear master curves were used to calibrate the WLF coefficients, $\hat{C}_1$ and $\hat{C}_2$; and the shear relaxation function, $f_2(t)$. Experimental details and results can be found in Section 3.1.2 and Fig. 3-2. Two thermal histories were used to generate the shear master curves. The cold-to-hot temperature history (see Fig. 3-2, label `B102920_s9_HeatAfterCool1Cmin`) was used for calibration, since the hot-to-cold temperature history resulted in additional (undesired) curing, see Section 3.1.2.

In constructing the shear master curves, shift factors at each temperature were found, see red dots in Fig. 5-1a. The shift factors as a function of temperature were used to calibrate the WLF coefficients. However, at low temperatures, the shift factor is too high for the material to reach its equilibrium state, therefore shift factors with $\log a > 1$ are ignored when fitting $\hat{C}_1$ and $\hat{C}_2$.It should be mentioned that WLF coefficients, $\hat{C}_1$ and $\hat{C}_2$, are fit to the shift factor versus temperature data, but the shift factor definition for the SPEC model, Eq. (2.8), uses the clock parameters, C_1 and C_2. The first clock parameter is equal to the first WLF coefficient, $C_1 = \hat{C}_1$, but the second clock parameter must be calculated from the second WLF coefficient as well as other material parameters, see [4] for details. The `spectacular` model accepts either the WLF coefficients or the first two clock parameters as inputs, so it is unnecessary to perform the conversion from WLF coefficients to clock parameters outside of the model.

Table 5-1. SPEC parameters produced by the baseline calibration for 828DEA.

Parameter	Value	Units	Experiment	Reference
K_g^{ref}	4.9	GPa	Legacy	[4], Table 3
K_g'	-12	MPa/K	Legacy	[4], Table 3
K_∞^{ref}	3.2	GPa	Legacy	[4], Table 3
K_∞'	-12	MPa/K	Legacy	[4], Table 3
G_g^{ref}	0.9	GPa	Legacy	[4], Table 3
G_g'	-4.2	MPa/K	Legacy	[4], Table 3
G_∞^{ref}	4.5	MPa	Legacy	[4], Table 3
G_∞'	0	kPa/K	Legacy	[4], Table 3
α_g^{ref}	220	$10^{-6}/\text{K}$	TMA	Fig. 5-5
α_g'	0	$10^{-6}/\text{K}^2$	TMA	Fig. 5-5
$\alpha_\infty^{\text{ref}}$	562	$10^{-6}/\text{K}$	TMA	Fig. 5-4
α_∞'	0.7	$10^{-6}/\text{K}^2$	TMA	Fig. 5-4
C_g^{ref}	1.146	$\text{MJ}/(\text{m}^3\cdot\text{K})$	DSC	Fig. 5-8
C_g'	1.29	$\text{kJ}/(\text{m}^3\cdot\text{K}^2)$	DSC	Fig. 5-8
C_∞^{ref}	1.379	$\text{MJ}/(\text{m}^3\cdot\text{K})$	DSC	Fig. 5-8
C_∞'	0.65	$\text{kJ}/(\text{m}^3\cdot\text{K}^2)$	DSC	Fig. 5-8
θ_{ref}	75	°C	Chosen	
$\hat{C}_1$	12.6	–	Shear master curve	Fig. 5-1a
$\hat{C}_2$	40.1	K	Shear master curve	Fig. 5-1a
C_3	1000	K	Legacy	[4], Table 3
C_4	13700	K	Compression	Fig. 5-6
ρ	1176	kg/m^3	Legacy	[3], Table 4
τ_1	41.0	s	TMA	Fig. 5-5
β_1	0.26	–	TMA	Fig. 5-5
τ_2	1.25	s	Shear master curve	Fig. 5-2
β_2	0.23	–	Shear master curve	Fig. 5-2
τ_3	41.0	s	TMA	Fig. 5-5
β_3	0.26	–	TMA	Fig. 5-5
τ_4	6.80	s	DSC	Fig. 5-8
β_4	0.36	–	DSC	Fig. 5-8

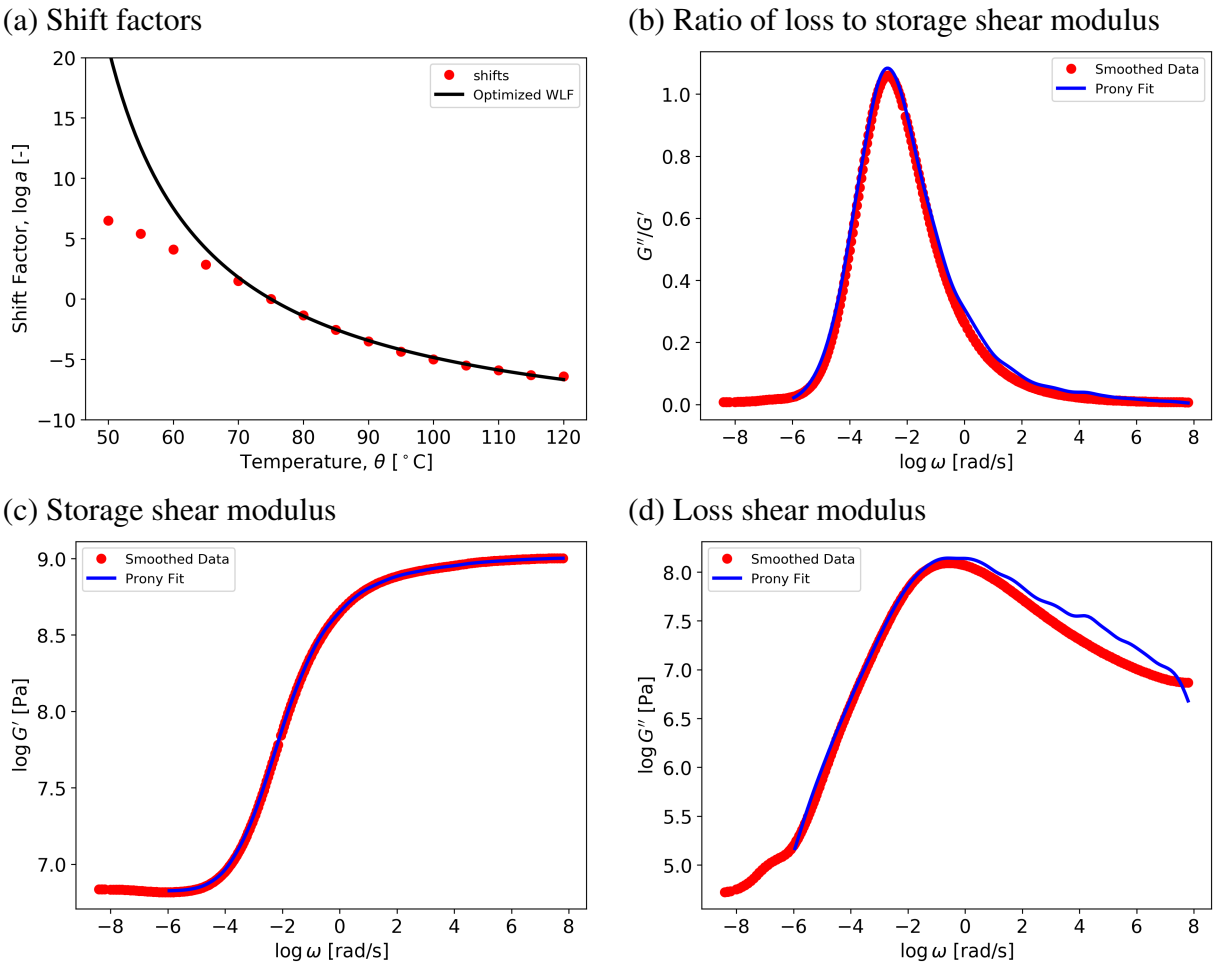

Figure 5-1. Shear master curve construction from isothermal frequency sweeps for 828DEA. (a) The shift factor versus temperature plot used to construct the shear master curve (red dots) and the optimized WLF fit for $\log a > 1$ (black line). (b, c, d) Smoothed data versus frequency and Prony series fits for (b) G''/G' (commonly called $\tan\delta$) versus frequency, (c) storage moduli, G', versus frequency, (d) and loss moduli, G'', versus frequency. Experimental data from Fig. 3-2, label `B102920_s9_HeatAfterCool1Cmin`.

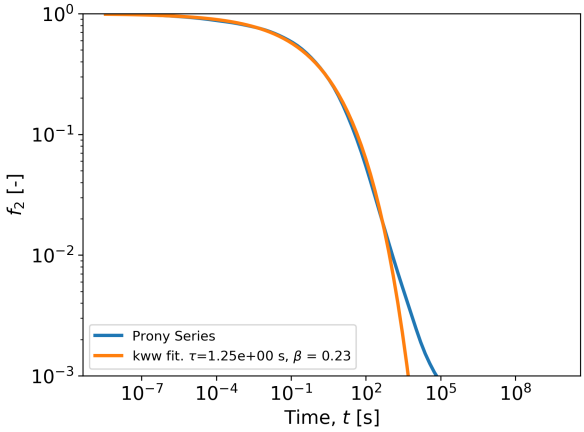

Figure 5-2. Prony series fit to the 828DEA shear master curve and the stretched exponential fit used for the baseline calibration.

Shear master curves are constructed using time–temperature superposition to shift storage and loss shear moduli at different temperatures to a reference temperature so that a smooth curve is formed. While constructing the shear master curve here, data from frequencies above 20 Hz was ignored, since the accuracy data above this frequency is suspect. The data is then smoothed using custom Python tools. The smoothed data are shown in Fig. 5-1. Data for G''/G' (commonly called $\tan\delta$) is shown in (b), the storage shear moduli in (c), and the loss shear moduli in (d). Reference values for the glassy and rubbery shear moduli are extracted from high and low frequency extremes of the storage shear moduli curve, see Fig. 4-2c. The reference shear moduli extracted from the shear master curve are $G_g^{\text{ref}} = 1.000\,\text{GPa}$ and $G_\infty^{\text{ref}} = 5.999\,\text{MPa}$. However, for consistency with the borrowed bulk moduli, the values from [4], Table 3 are used instead, $G_g^{\text{ref}} = 0.9\,\text{GPa}$ and $G_\infty^{\text{ref}} = 4.5\,\text{MPa}$ A prony series, representing the shear relaxation function $f_2(t)$, is then fit to the shear master curve. The Prony series fit is plotted with the smoothed data in Fig. 4-2b, c, d.

In forthcoming calibration steps, the other relaxation functions are calibrated by optimization. To reduce the number of parameters that need to be optimized, these relaxation functions are represented using stretched exponential functions, which are defined by two parameters, the characteristic time and the breadth, τ_i and β_i. To facilitate comparisons of all four relaxation functions accross multiple calibrations, a stretched exponential is fitted to the Prony series fit to the shear master curve. The comparison of the Prony series and the stretched exponential fit are shown in Fig. 4-3.

5.1.2. Isofrequency Temperature Sweeps

The isofrequency temperature sweeps, see Section 3.1.1, were used to measure the temperature dependence of the shear moduli, G_g' and G_∞'. However, these values were not used for calibration, but are only measured to compare with the values borrowed from [4], Table 3. The slopes from the glassy and rubbery parts of the storage modulus curves are taken to correspond to G_g' and G_∞'.

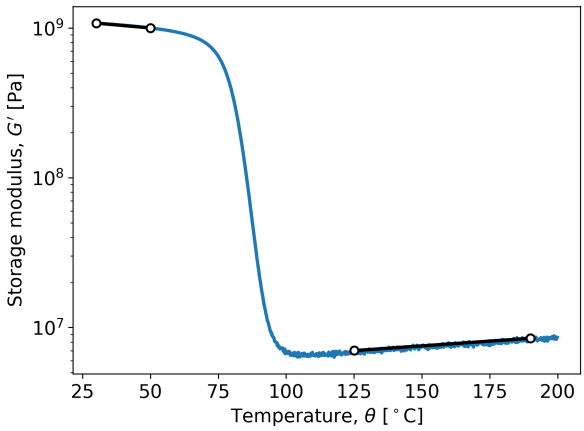

Figure 5-3. Isofrequency temperature sweep for 828DEA. Black lines indicate slopes used to measure G'_g and G'_∞.

The temperature sweep from 200 °C to room temperature was used. Although the time at this elevated temperature resulted in additional curing that increased the glass transition temperature, the additional curing had little effect on the temperature dependence of the glassy and equilibrium modulus. This is evident by comparing the high and low tempeature slopes of the blue and orange curves in Fig. 3-1. Fig. 5-3 shows specifically how the slopes were measured from the storage modulus versus temperature curve. The measured values are $G'_g = -3.9\,\text{MPa/K}$ and $G'_\infty = 23\,\text{kPa/K}$. The measured value of G'_g compares well with the value borrowed from [4], Table 3, $G'_g = -4.2\,\text{MPa/K}$ The positive value for G'_∞ is expected when the stiffness is driven by entropic elasticity [14], but since the magnitude of the value is small, it was neglected in [4], Table 3, i.e. $G'_\infty = 0$.

5.1.3. Stress-Free Temperature Sweep in a Thermomechanical Analyzer

The four parameters governing the volumetric coefficient of thermal expansion (CTE); α_g^{ref}, α'_g, $\alpha_\infty^{\text{ref}}$, and α'_∞; and the thermal-volumetric relaxation function; $f_1(t) = f_3(t)$; were calibrated using a thermomechanical analyzer (TMA). The test procedure involves measuring the linear CTE during a stress-free temperature sweep from −50 °C to 200 °C, see Section 3.1.3. Fig. 5-4 shows the linear CTE during an downward temperature sweep and how the four volumetric CTE parameters were measured from the experimental data. The slopes from the glassy and rubbery ends were measured to calibrate α'_g and α'_∞ and the rubbery and glassy limits were extrapolated to find the values at the reference temperature, α_g^{ref} and $\alpha_\infty^{\text{ref}}$. The SPEC model assumes isotropic behavior, so the measured linear CTE values were multiplied by three to calculate the volumetric CTE values, which are the input used by `spectacular`. The measured volumetric CTE parameters are listed in Table 5-2.

The thermal-volumetric relaxation function was calibrated by optimizing the linear CTE response of the `spectacular` model to fit the experimental data. Parameters governing the reference values for the volumetric CTEs and the thermal-volumetric relaxation function were optimized.

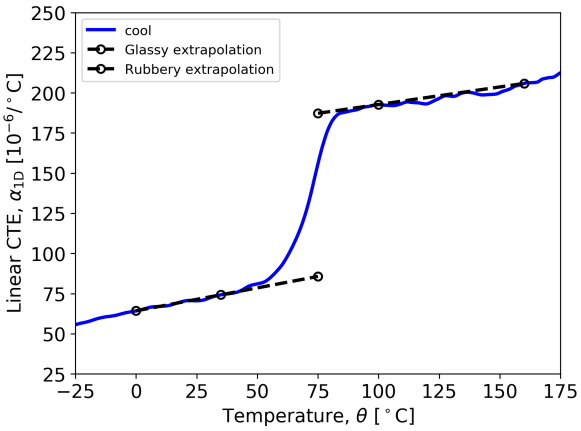

Figure 5-4. Linear coefficient of thermal expansion (CTE) measured during a temperature down-sweep in a thermomechanical analyzer (TMA) for 828DEA. Black dashed lines indicate how the linear CTE reference values at $75\,^{\circ}\mathrm{C}$ **and temperarture dependence of the linear CTEs were measured.**

Even though apparent values for the volumetric CTEs were measured, further adjustments through optimization were allowed. During optimization, the volumetric and thermal-volumetric relaxation functions were equal, $f_1(t) = f_3(t)$.

The TMA experiment was simulated by applying the following thermo-mechanical history to a single element in Sierra: (1) Anneal at $200\,^{\circ}\mathrm{C}$ for 30 min, (2) cool to $-50\,^{\circ}\mathrm{C}$ at $1\,^{\circ}\mathrm{C}/\mathrm{min}$, (3) hold at $-50\,^{\circ}\mathrm{C}$ for 5 min, (4) heat to $200\,^{\circ}\mathrm{C}$ at $1\,^{\circ}\mathrm{C}/\mathrm{min}$. The nominal strain was calcualted from the displacement along the y-axis, and the gradient of the nominal strain was taken with respect to the temperature to calculate the linear CTE. The TMA applies a small force to the sample to measure its deformation. This the probe was modeled with a token 1 Pa stress on the $+y$-face of the element, although the specific value of the probe force is not expected to signficiantly impact results. The linear CTE was calculated as the thermal derivative of the nominal linear strain during the heating and cooling portions of the experiment.

The optimization procedure used a genetic algorithm, specifically the `soga` method in Dakota [1]. One-hundred generations were evaluated, with each generation having a population of one-hundred. Four parameters were optimized: the two stretched exponential parameters for $f_3(t)$ and the glassy volumetric CTE parameters, i.e. τ_3, β_3, α_g^{ref}, and α_g'. The objective function was the L^2 norm of the absolute error between the simulated and experimental linear CTE between $50\,^{\circ}\mathrm{C}$ and $120\,^{\circ}\mathrm{C}$. Both the linear CTE during cooling and heating were included in the objective function, and were given equal weight.

Fig. 5-5 shows the linear CTE fit upon (a) cooling and (b) heating. Black dotted lines indicate the temperature range used during optimization. Overall, the optimized fit is close to the experimental data. The model fit on cooling through the glass transition is excellent. On heating, the transition at low temperatures is slightly too broad, but the volume recovery that occurs when heating into the rubbery state is accurately predicted, which is apparent by the small CTE overshoot in Fig. 5-5b. The optimizer found that $\alpha_g' = 0$ produced the best fit. On cooling, the

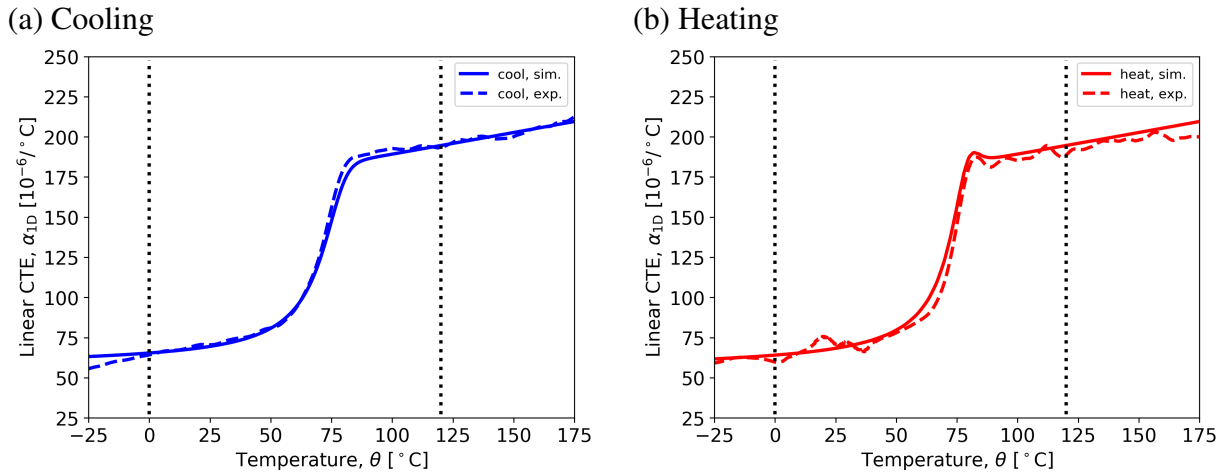

Figure 5-5. Optimized TMA response from the baseline calibration approach for 828DEA. Black dotted lines represent the temperature range considered during optimization. Optimized parameters included $\tau_1 = \tau_3$, $\beta_1 = \beta_3$, α_g^{ref}, and α_g'. Experimental data from Fig. 3-3.

Table 5-2. Measured volumetric coefficient of thermal expansion parameters for 828T403 from Fig. 4-5 and how they are adjusted during optimziation for the fit in Fig. 4-6.

Parameter	Measured	Optimized	Units
α_g^{ref}	257	220	$10^{-6}/\text{K}$
α_g'	0.8	0	$10^{-6}/\text{K}^2$
$\alpha_\infty^{\text{ref}}$	562	–	$10^{-6}/\text{K}$
α_∞'	0.7	–	$10^{-6}/\text{K}^2$

slope of the glassy CTE is close until 0 °C, but below 0 °C (where data was not used for optimization), the experimental slope of the CTE is higher than slope from the model. However, the slope of the heating curve seems well matched for the full range of data appearing in the plot. The reference volumetric CTE values that were adjusted during optimziation are compared to their measured values in Table 5-2.

5.1.4. Glassy Compression

The clock parameter C_4 was calibrated using glassy compression experiments at different temperatures and strain rates. The parameter C_4, which controls the effect of shear strain on the material clock and is responsible for yield in the model, was calibrated so that the yield stress and Young's modulus from simulations of compression matched experimental data.

Details for the experimental procedure can be found in Section 3.1.4, with stress–strain data presented in Fig. 3-4 and linear regressions for the yield stress, yield strain, and Young's modulus in Fig. 3-5. Glassy compression was simulated in Sierra using the following thermal history applied to a single element: (1) anneal the material at 105 °C for 30 min, (2) cool at 1 °C/min to room temperature (25 °C), (3) Sit at room temperature for 60 min, (4) linearly heat to the loading temperature over 30 min, (5) at the loading temperature, apply a constant nominal strain rate in compression up to a nominal strain of 0.2. The test and simulation matrices included three loading temperatures (−50 °C, 25 °C, 50 °C) and three strain rates (1/min, 10^{-1}/min, 10^{-2}/min). Eight loading conditions in compression were used, since no experiment was run for −50 °C, 10^{-2}/min. A single loading condition in tension was also available for 50 °C, 10^{-2}/min. Experimental details for the tension experiments can be found in Section 3.1.5 with stress–strain curves shown in Fig. 3-6. The simulated thermomechanical history is only an approximation of the real history. Since only a single element is used, heat transfer and inhomogenous deformation are not considered in the model.

Since only a single parameter was calibrated, no formal Dakota procedure was used; C_4 was manually adjusted to achieve the lowest objective function. The objective function that was minimized was calculated as the sum of the relative errors of the yield stress accross all eight compressive loading conditions in the test matrix. All compression experiments were weighted equally in the objective function, but the tensile loading condition was not included in the objective function. The yield stress was calculated as the maximum nominal stress below 0.12 strain. Regressions of the yield stress from all experimental realizations, see Fig. 3-5, served as the reference values when calculating the relative errors.

The simulated yield stress after fitting C_4 are shown in Fig. 4-7. The same data is shown in Fig. 4-7a and Fig. 4-7b, but the data are organized into iso–strain rate and isothermal lines, respectively. Simulated and experimental stress–strain curves are shown in Fig. 4-8. The yield stress predicted by the model fit is close to experimental data. The predicted yield stresses are slightly too low at high temperatures, slightly too high at low temperatures, and on-target for the middle temperature. This indicates that the temperature dependence of the yield stress is slightly too high. At the two highest temperatuers, the strain rate dependence of the yield stress is close to the experimental effect, but the yield stress is not sensitive enough to the strain rate. The model

(a) Temperature Effect

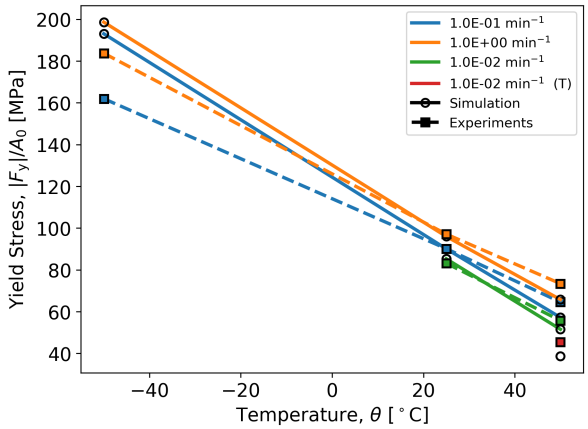

(b) Strain Rate Effect

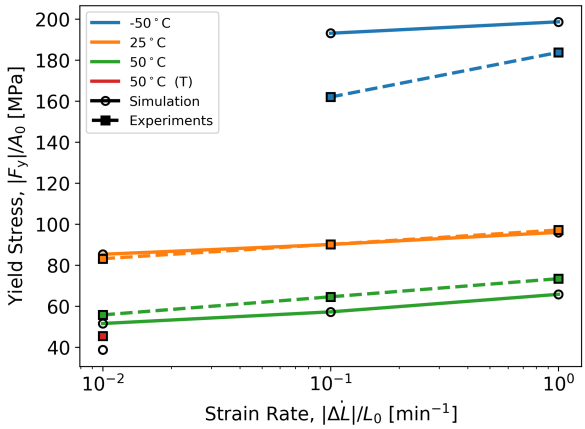

Figure 5-6. Optimized yield stress response from the baseline calibration approach for 828DEA. (a) Yield stress versus temperature for constant strain rates, (b) Yield stress versus strain rate for constant temperatures. In the legend, "(T)" denotes tensile experiments. All other experiments are compressive. The only optimized parameter was C_4. Experimental data from Fig. 3-5.

predicts that sensitivity of the yield stress to the strain rate is similar at all temperatures, but the experiments show that the strain rate sensitivity increases as the temperature decreases, so the effect is too low at $-50\,^\circ$C. Asymetry of the tensile and compressive yield stress emerge from the model as a result of C_3, which controls the effect of the volume strain on the material clock. Here, C_3 is kept fixed. Both the model and experiment show a 10 MPa difference between the tensile and compressive nominal yield stress. The simulated stress–strain curves are too broad.

5.1.5. Stress-Free Temperature Sweep in a Differential Scanning Calorimeter

The heat capacity parameters as well as the thermal relaxation function were calibrated using measurements of the heat capacity during a stress-free temperature sweep in a differential scanning calorimeter (DSC). Historically, this step has not been included in the standard calibration approach, as older versions of the SPEC model [4] did not include separate functions for the volumetric, thermal-volumetric, and thermal relaxation functions. or even equations for thermomechanical coupling.

Details of the experimental data are found in Section 3.1.6 with heat capacity measurements shown in Fig. 3-7. The experimental heat capacity measurements were not calibrated to provide absolute values of the heat capacity. Therefore, a reference value for the heat capacity was necessary to shift the experimental data for use during optimization. Based on heat capacity measurements for 828DEA [3], all experimental data was shifted vertically to a reference value of $1527.5\,\mathrm{J/(kg\cdot K)}$ at $50\,^\circ$C. The DSC experiment was simualted by applying the following thermal history to a single element in Sierra: (1) anneal at $200\,^\circ$C for 5 min, (2) cool at a fixed cooling rate to $-90\,^\circ$C, (3) hold the temperature constant at $-90\,^\circ$C for 5 min, (4) heat to $200\,^\circ$C at a heating

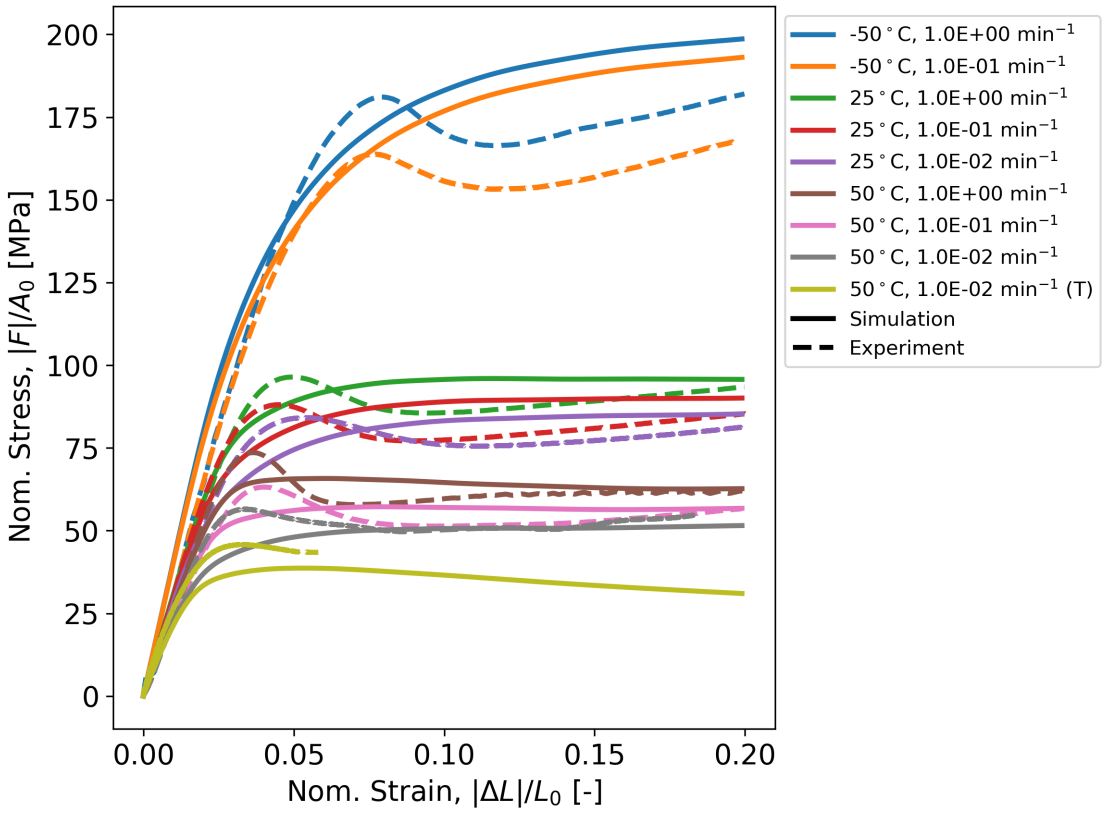

Figure 5-7. Simulated and experimental stress–strain curves. The simulated response was produced by the baseline calibration approach for 828DEA. In the legend, "(T)" denotes tensile experiments. All other experiments are compressive. Experimental data from Fig. 3-4.

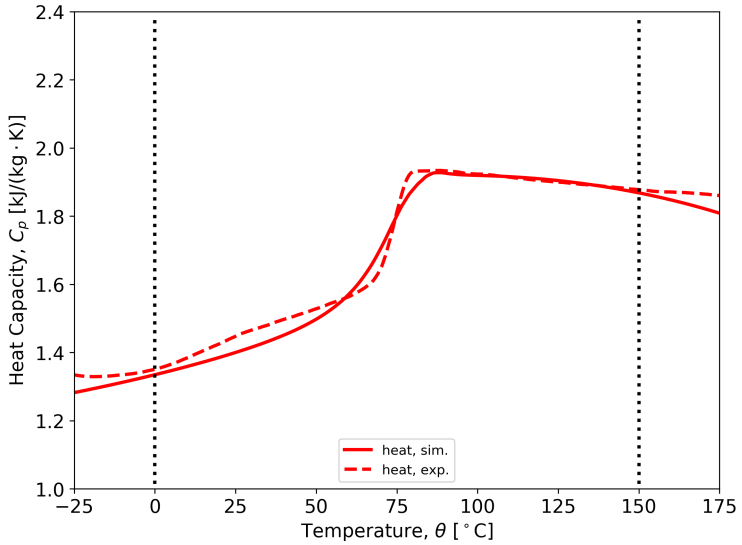

Figure 5-8. Optimized DSC response from the baseline calibration approach for 828DEA. Black dotted lines represent the temperature range considered during optimization. Optimized parameters included τ_4, β_4, C_g^{ref}, C_g', C_∞^{ref}, and C_∞'. The cooling rate was $15\,^\circ\text{C/min}$. Experimental data from Fig. 3-7.

rate of $10\,^\circ\text{C/min}$. The experimental database included temperature sweeps at multiple cooling rates. Here, only the $15\,^\circ\text{C/min}$ cooling rate was used for calibration. The constant-pressure heat capacity from the model was calculated using Eq. (2.42).

As with the TMA calibration step in Section 5.1.3, the optimization procedure used the `soga` genetic algorithm in Dakota. One-hundred generations were evaluated, with each generation having a population of one-hundred. Six parameters were optimized: the two stretched exponential function parameters for $f_4(t)$ and the four parameters governing the glassy and rubbery heat capacity, i.e., τ_4, β_4, C_g^{ref}, C_g', C_∞^{ref}, and C_∞'. The objective function that was minimized was the L^∞ norm (i.e. the maximum) of the absolute error between the simulated and experimental heat capacity between $0\,^\circ\text{C}$ and $150\,^\circ\text{C}$. Only the heat capacity during the final heating step was included in the objective function, since accurate experimental measurements of the heat capacity are difficult to obtain during cooling.

The optimized heat capacity fit along with the corresponding experimental data are shown in Fig. 5-8. Black dotted lines are used to indicate the temperature range used in the objective function. The glass transition is fit well, even if it is slightly too broad. The glassy heat capacity is slightly lower than the experiments, but the slope with temperature is good. The rubbery heat capacity is matched very well to the experiments, however, the negative slope in the experimental data is undesirable and likely an effect of chemical changes. The ability of the model to fit the negative slope is not a positive feature.

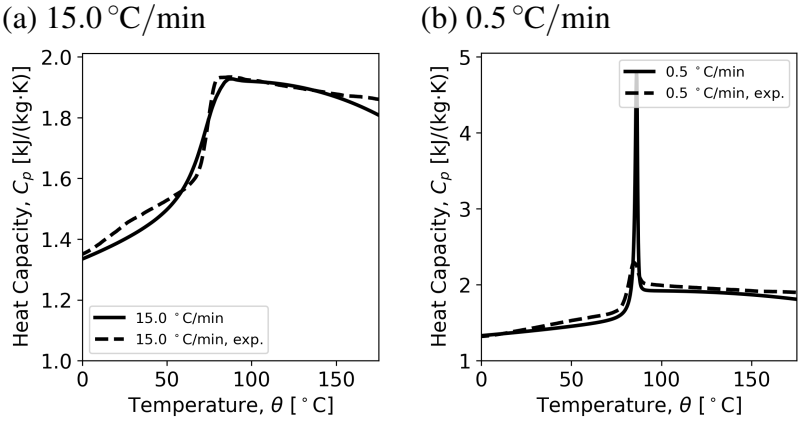

Figure 5-9. Baseline calibration exercised against DSC measurements of the heat capacity for experiments using a cooling rate of (a) $0.5\,^{\circ}\mathrm{C/min}$ **(used for fitting the baseline calibration) and (b)** $15.0\,^{\circ}\mathrm{C/min}$**. Experimental data from Fig. 3-7.**

Table 5-3. Heat capacity related parameters fit to experiments using a cooling rate of $15.0\,^{\circ}\mathrm{C/min}$ **and** $0.5\,^{\circ}\mathrm{C/min}$**.**

Parameter	$15.0\,^{\circ}\mathrm{C/min}$	$0.5\,^{\circ}\mathrm{C/min}$	Units
C_g^{ref}	1.146	0.553	$\mathrm{MJ/(m^3 \cdot K)}$
C_g'	1.29	4.22	$\mathrm{MJ/(m^3 \cdot K^2)}$
C_∞^{ref}	1.379	0.355	$\mathrm{MJ/(m^3 \cdot K)}$
C_∞'	0.65	3.47	$\mathrm{MJ/(m^3 \cdot K^2)}$
τ_4	6.80	169	s
β_4	0.36	0.53	–

5.1.6. Motivation for a DSC-Focused Calibration Approach

The baseline calibration for 828DEA was reasonably fit to the DSC heat capacity measurements when the cooling rate was $15.0\,^{\circ}\mathrm{C/min}$. Part of the suite of physical aging experiments included DSC experiments that used slower cooling rates, which created heat capacity overshoots upon reheating. The full set of predictions of DSC experiments using different cooling rates are shown later in Section 5.4.5, Fig. 5-30, but a subset of results are shown here for the purpose of motivating the DSC-focused approach. Although the fit for $15.0\,^{\circ}\mathrm{C/min}$ was good, when exercising the baseline calibration against DSC experiments with the lowest used cooling rate, $0.5\,^{\circ}\mathrm{C/min}$, the baseline calibration predicted an unrealistically high heat capacity spike, shown in Fig. 5-9. The DSC-focused approach was formulated to help improve the fit at slower cooling rates.

In an attempt to improve the heat capacity behavior for all available cooling rates, the DSC

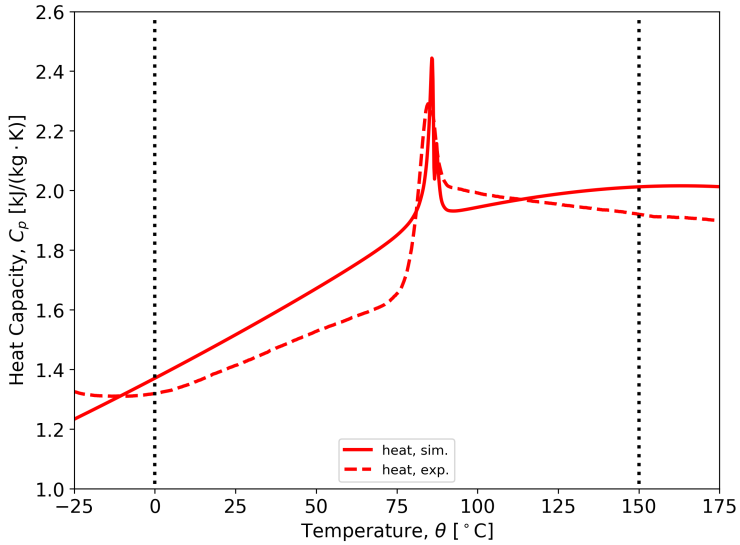

Figure 5-10. Optimized DSC response using the heat capacity measured on reheating when a cooling rate of $0.5\,^{\circ}\mathrm{C/min}$ was used. Black dotted lines represent the temperature range considered during optimization. Optimized parameters included τ_4, β_4, C_g^{ref}, C_g', C_∞^{ref}, and C_∞'. Experimental data from Fig. 3-7.

calibration step (presented in Section 5.1.5) was repeated using the $0.5\,^{\circ}\mathrm{C/min}$ cooling rate condition instead of $15.0\,^{\circ}\mathrm{C/min}$. The appearance of the heat capacity spike upon reheating for a cooling rate of $0.5\,^{\circ}\mathrm{C/min}$ is likely more discerning for calibrating the thermal relaxation functions, $f_4(t)$. The optimized heat capacity fit to the slower cooling rate is shown in Fig. 5-10 and Table 5-3 compares the parameters produced from the original DSC calibration step in Section 5.1.5 to the parameters found when fitting directly to the experiment with a slower cooling rate. Although the peak heat capacity is much closer to the experimental value, there are other significant problems with the fit. Notably, the glassy heat capacity is much too high. In fact, $C_g^{\mathrm{ref}} > C_\infty^{\mathrm{ref}}$, which is not physical. In fitting to the experiment with a slow cooling rate, the characteristic thermal relaxation time increased by an order of magnitude (τ_4 changed from 6.80 s to 169 s) and the relaxation function became significantly more narrow (β_4 changed from 0.36 to 0.53).

A quick-fix to the high glassy heat capacity was explored by manually adjusting C_g^{ref} and C_g' to see if the glassy heat capacity could be lowered while preserving the improved peak heat capacity. First the, the slope of the glassy heat capacity, C_g' was adjusted. The adjustment is shown in Fig. 5-11a (blue to orange curve). Adjusting the glassy heat capacity slope had a minimal impact on other parts of the response, although the peak heat capacity did increase slightly. Next, the reference value of the glassy heat capacity, C_g^{ref} was adjusted. The adjustment is shown in Fig. 5-11a (blue to orange curve). Now, the glassy heat capacity matches the experimental data very well, but lowering C_g' drastically increased the peak heat capacity. The increase is high enough that the peak heat capacity is overestimated by the same amount as the original DSC calibration fit to the faster cooling rate experiment which exhibited no heat capacity overshoot.

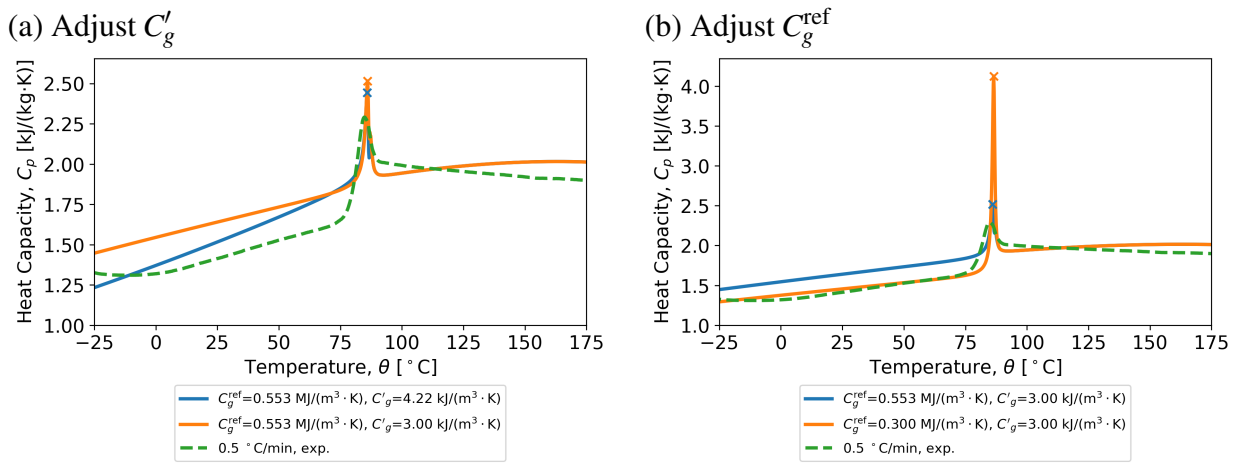

Figure 5-11. Adjustments to the glassy heat capacity starting from the modified DSC fit in Fig. 5-10 that used a cooling rate of $0.5\,^{\circ}\text{C}/\text{min}$. (a) Adjust the glassy heat capacity slope, C'_g, blue curve to orange curve. (b) Then adjust the glassy heat capacity reference value, C_g^{ref}, blue curve to orange curve. Peak heat capacities are marked with an "x". Experimental data from Fig. 3-7.

Since fitting the heat capacity parameters to the experiment with a slow cooling rate did not produce a better result than the using the original cooling rate, investigations are refocused on the first DSC calibration step presented Section 5.1.5. Parameter studies were conducted to determine if the peak heat capacity be reasonably fit by adjusting $f_4(t)$. Fig. 5-12 shows the heat capacity when the baseline 828DEA calibration is adjusted by changing (a) τ_4 and (b) β_4. In Fig. 5-12a, the characteristic time, τ_4, is varied up and down by three orders of magnitude in while keeping β_4 fixed. Over six orders of magnitude for τ_4, the peak heat capacity has a range of $1.5\,\text{kJ}/(\text{kg}\cdot\text{K})$, but a decrease of $3\,\text{kJ}/(\text{kg}\cdot\text{K})$ is needed to match the experimental value. Therefore, reasonable variations to τ_4 still do not decrease the heat capacity to the experimental value. The behavior is not monotonic, as the highest peak occurs for the middle value of τ_4. Furthermore, the shortest τ_4 presents a "double structure" during the transition in that two local maximums occur. In Fig. 5-12b, the breadth of the relaxation function, β_4, is varied by ± 0.2 while keeping τ_4 fixed. Once again, despite the extreme changes to β_4 the range of peak heat capacities is only $1.5\,\text{kJ}/(\text{kg}\cdot\text{K})$. Based on the parameter studies in Figs. 5-12, changes to $f_4(t)$ alone are not sufficient to fit DSC results that exhibit a heat capacity spike. Also taking into account the parameter studies shown in Fig. 5-11, there appears to be a conflict between matching both $C_D(\theta)$ and the peak heat capacity, at least given the parameters found from calibration steps prior to DSC step.

Since changes to $f_4(t)$ were not able to affect the peak heat capacity values enough to align them with experimental measurements, $f_3(t)$ is now investigated. Since $f_3(t)$ drives the thermal history in the material clock, it is especially important for predictions related to physical aging. Fig. 5-13 shows the heat capacity when the baseline 828DEA calibration is adjusted by changing (a) τ_3 and (b) β_3. In Fig. 5-13a, the characteristic time, τ_3, is varied up and down by three orders of magnitude in while keeping β_3 fixed. These changes to τ_3 result in a range in the peak heat

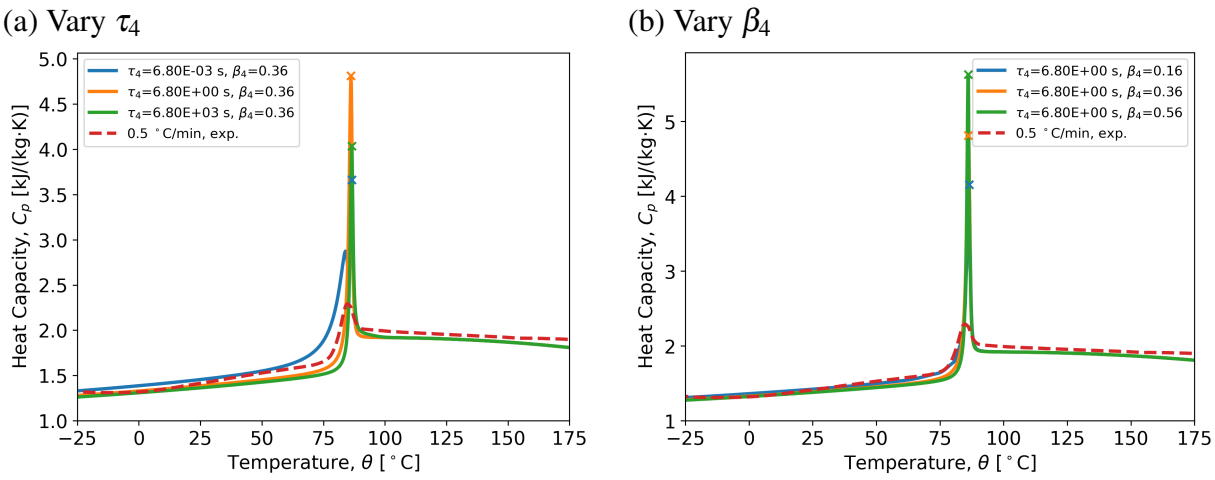

Figure 5-12. Effects of changing (a) τ_4 and (b) β_4 in the baseline calibration for 828DEA on the heat capacity after cooling at $0.5\,^{\circ}\mathrm{C/min}$. Peak heat capacities are marked with an "x". Experimental data from Fig. 3-7.

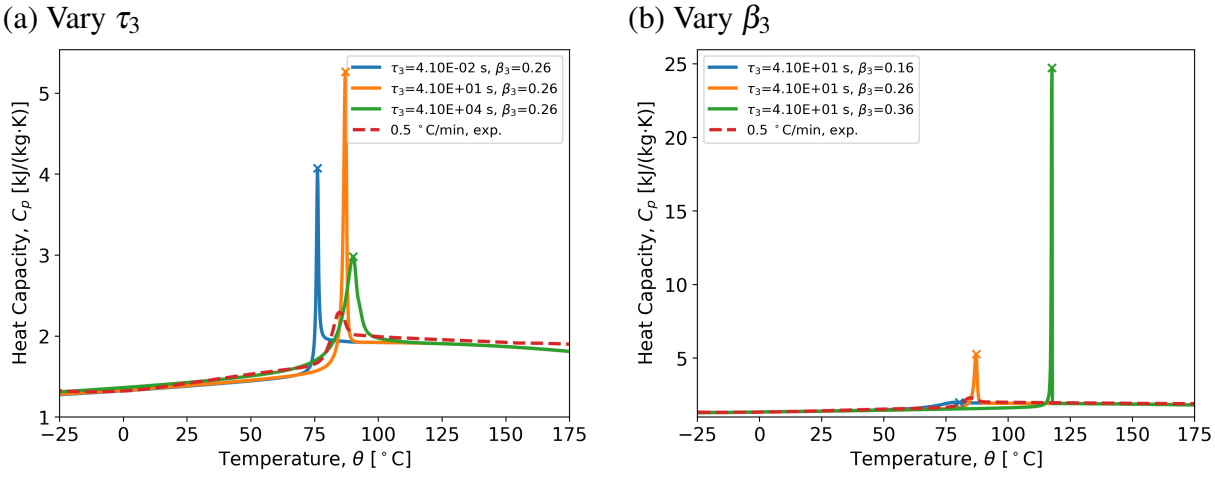

Figure 5-13. Effects of changing (a) τ_3 and (b) β_3 in the baseline calibration for 828DEA on the heat capacity after cooling at $0.5\,^{\circ}\mathrm{C/min}$. Peak heat capacities are marked with an "x". Experimental data from Fig. 3-7.

capacity that varies by $2\,\mathrm{kJ}/(\mathrm{kg}\cdot\mathrm{K})$. Interestingly, the highest peak corresponds to the middle value of τ_3, a trend repeated from the τ_4 study. Unlike τ_4, changes in τ_3 also changed the location of the peak, with shorter characteristic times causing peaks at lower temperatures. In Fig. 5-13b, the breadth of the relaxation function, β_3, is varied by ± 0.1 while keeping τ_3 fixed. The effect of β_3 on the peak heat capacity is enourmous; increasing β_4 from 0.16 to 0.36 changes the peak from $2\,\mathrm{kJ}/(\mathrm{kg}\cdot\mathrm{K})$ (no discernable spike) to $25\,\mathrm{kJ}/(\mathrm{kg}\cdot\mathrm{K})$. Furthermore, the temperature of spike increases dramatically as β_3 increases. These results show that $f_3(t)$ is perhaps the important relaxation function for predicting the peak heat capacity in a DSC experiment. For the baseline approach, when $f_3(t)$ is calibrated using TMA experiments, then there are not enough degrees-of-freedom in the DSC calibration step to fit experiments that exhibit physical aging (a heat capacity spike). This serves as the motivation for a DSC-focused approach.

In the original PEC model [7, 3] there were four relaxation functions, the volumetric, shear, thermal-volumetric, and thermal, $f_1(t)$, $f_2(t)$, $f_3(t)$, and $f_4(t)$, respectively. The thermal history in the material clock is controlled by the thermal relaxation function, $f_4(t)$. When the PEC model was simplified to the SPEC model in [4], only two relaxation were used, one for the volumetric and thermal-volumetric response and one for shear. Since the SPEC model in [4] did not include equations for thermomechanical coupling, there was no thermal relaxation function. The `spectacular` implementation used here once again has four relaxation functions, but the use of $f_3(t)$ with the thermal history in the material clock was maintained from before the introduction of full thermomechanical coupling. However, now that a true thermal relaxation function has been reintroduced to the model, we hypothesize that it should be the relaxation function that stores the thermal memory in the material clock. This hypothesis is the basis for the "DSC-focused" approach, which uses $f_4(t)$ for the thermal history in the material clock by setting $f_3(t) = f_4(t)$. This allows us to test this hypothesis wihtout re-working the implementation of the model. The DSC-focused approach differs from the baseline approach in the following ways. (1) After $f_1(t) = f_3(t)$ is calibrated by fitting the CTE response from a TMA experiment, $f_3(t) = f_4(t)$ is then calibrated by fitting the heat capacity response using a DSC experiment. The end result is that $f_1(t)$ is leftover from the TMA fit, but $f_3(t)$ and $f_4(t)$ are fit to the DSC experiment, and therefore should reflect the thermal (not thermal-volumetric) relaxation function. (2) The heat capacity response is fit to a DSC experiment using a cooling rate of $0.5\,^{\circ}\mathrm{C}/\mathrm{min}$. This forces the optimized $f_3(t) = f_4(t)$ to fit a heat capacity overshoot, which is essentially a manifestation of physical aging. (3) After changing $f_3(t)$ in the DSC experiment, C_4 must be fit to yield stress in glassy compression. Therefore, the DSC-focused approach fits $f_4(t)$ and then C_4, but the order of these two steps are reversed in the baseline approach.

5.2. Compression-Focused Calibration

Based on the discussion in Section 4.1.6, an alternate calibration approach was proposed where $f_3(t)$ was calibrated to fit the yield stress in glassy compression at different rates and temperatures. Although the motivation for the compress-focused calibration was based on the performance of the baseline 828T403 calibration, the procedure is also applied to 828DEA to exercise the procedure on two different materials.

Table 5-4. SPEC parameters produced by the compression-focused calibration for 828DEA. Only parameters that have changed from the baseline approach are listed here, see Table 5-1.

Parameter	Value	Units	Experiment	Reference
C_g^{ref}	1.135	$\text{MJ}/(\text{m}^3 \cdot \text{K})$	DSC	Fig. 5-16
C_g'	1.22	$\text{kJ}/(\text{m}^3 \cdot \text{K}^2)$	DSC	Fig. 5-16
C_∞^{ref}	1.300	$\text{MJ}/(\text{m}^3 \cdot \text{K})$	DSC	Fig. 5-16
C_∞'	0.83	$\text{kJ}/(\text{m}^3 \cdot \text{K}^2)$	DSC	Fig. 5-16
C_4	24800	K	Compression	Fig. 5-14
τ_1	1.42	s	Compression	Fig. 5-14
β_1	0.27	–	Compression	Fig. 5-14
τ_3	1.42	s	Compression	Fig. 5-14
β_3	0.27	–	Compression	Fig. 5-14
τ_4	15.8	s	DSC	Fig. 5-16
β_4	0.34	–	DSC	Fig. 5-16

This calibration approach diverges from the baseline approach at Step 3 in Fig. 4-1. The calibrated volumetric coefficients of thermal expansion from the baseline calibration were kept, but instead of calibrating $f_3(t)$ using the TMA experiment, $f_3(t)$ and C_4 were calibrated from the glassy compression experiments. The calibration of $f_3(t)$ and C_4 to glassy compression data are presented in Section 5.2.1. In Section 5.2.2, the DSC calibration step from the baseline approach is repeated, but new values for τ_4 and β_4 emerge given that a different $f_3(t)$ was used. After finishing the alternate calibration, the TMA simulation is revisited in Section 5.2.3 to assess what trade-offs were necessary betwen the CTE predictions and the yield stress predictions. Since this approach calibrates $f_3(t)$, the relaxation function that drives the material clock, using glassy compression data, it is referred to as the "compression-focused" calibration approach. Parameters that changed from the baseline approach are listed in Table 5-4.

5.2.1. Glassy Compression

After the CTEs are measured, the compression-focused calibration departs from the baseline calibration. Instead of calibrating $f_3(t)$ using the CTE transition measured by the TMA and then calbrating C_4 using glassy compression, $f_3(t)$ and C_4 are both calibrated using glassy compression data. As with the baseline calibration approach, it is assumed that the volumetric and the thermal-volumetric functions are equal, $f_1(t) = f_3(t)$. Details for the experimental data can be found in Section 3.1.4 and results are shown in Figs. 3-4 and 3-5. All nine loading conditions from the baseline approach were also used here (loading temperatures: $-50\,^\circ\text{C}$, $25\,^\circ\text{C}$, $50\,^\circ\text{C}$ and nominal strain rates: $1/\text{min}$, $10^{-1}/\text{min}$, $10^{-2}/\text{min}$) The simulations use the same thermomechanical history described in Section 4.1.4.

The optimization is conducted using the `soga` method in Dakota. One-hundred generations were

(a) Temperature Effect

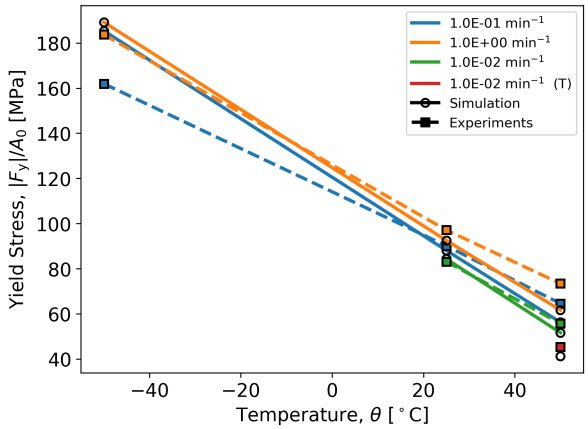

(b) Strain Rate Effect

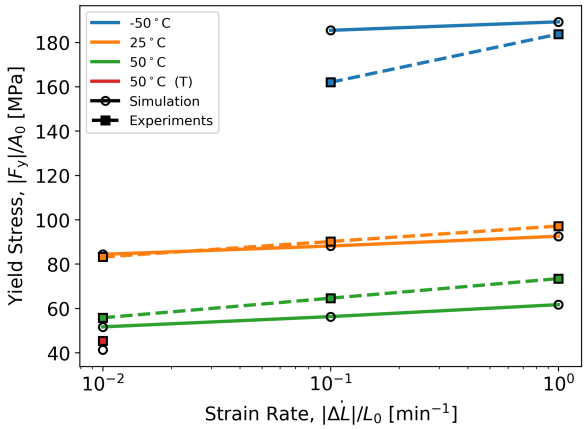

Figure 5-14. Optimized yield stress response from the compression-focused calibration approach for 828DEA. (a) Yield stress versus temperature for constant strain rates, (b) Yield stress versus strain rate for constant temperatures. In the legend, "(T)" denotes tensile experiments. All other experiments are compressive. The optmized parameters included $\tau_1 = \tau_3$, $\beta_1 = \beta_3$, and C_4. Experimental data from Fig. 3-5.

evaluated, with each generation having a population of one-hundred. Three parameters were optimized: the two stretched exponential parameters for the thermal-volumetric relaxation function and the clock parameter controlling the effect of shear strain on the material clock i.e. $\tau_1 = \tau_3$, $\beta_1 = \beta_3$, and C_4. The minimized objective function was composed of the relative errors of the yield stress for all nine loading conditions in the test matrix. The yield stress was calculated as the maximum nominal stress below 0.12 strain. Linear regressions for the yield stress, see Fig. 3-15, were used as the reference value when calculating the relative errors. The same eight compressive loading conditions used for the baseline calibration are used again here.

The simulated yield stress after fitting $\tau_1 = \tau_3$, $\beta_1 = \beta_3$, and C_4 are shown in Fig. 5-14. The same data is shown in Fig. 5-14a and Fig. 5-14b, but the data are organized into iso–strain rate and isothermal lines, respectively. Simulated and experimental stress–strain curves are shown in Fig. 5-15. For glassy compression, the compression-focused fit is similar to the baseline fit. The temperature sensitivity of the yield stress is slightly too high; at high temperatures, yield stress is too low and at low temperatures it is too high. The model predicts that the effect of the strain rate sensitivity on the yield stress is similar at all three temperatures. The predicted strain rate sensitivity is accurate at 50 °C and 25 °C, but is too low at −50 °C. Also, the difference between the tensile and compressive yield stress is nearly the same as the experimental difference. For 828T403, the compression-focused approach significantly improved the glassy compression fit compared to the baseline calibration. For 828DEA, the baseline approach was able to fit glassy compression, and the compression focused approach has not yielded much improvement.

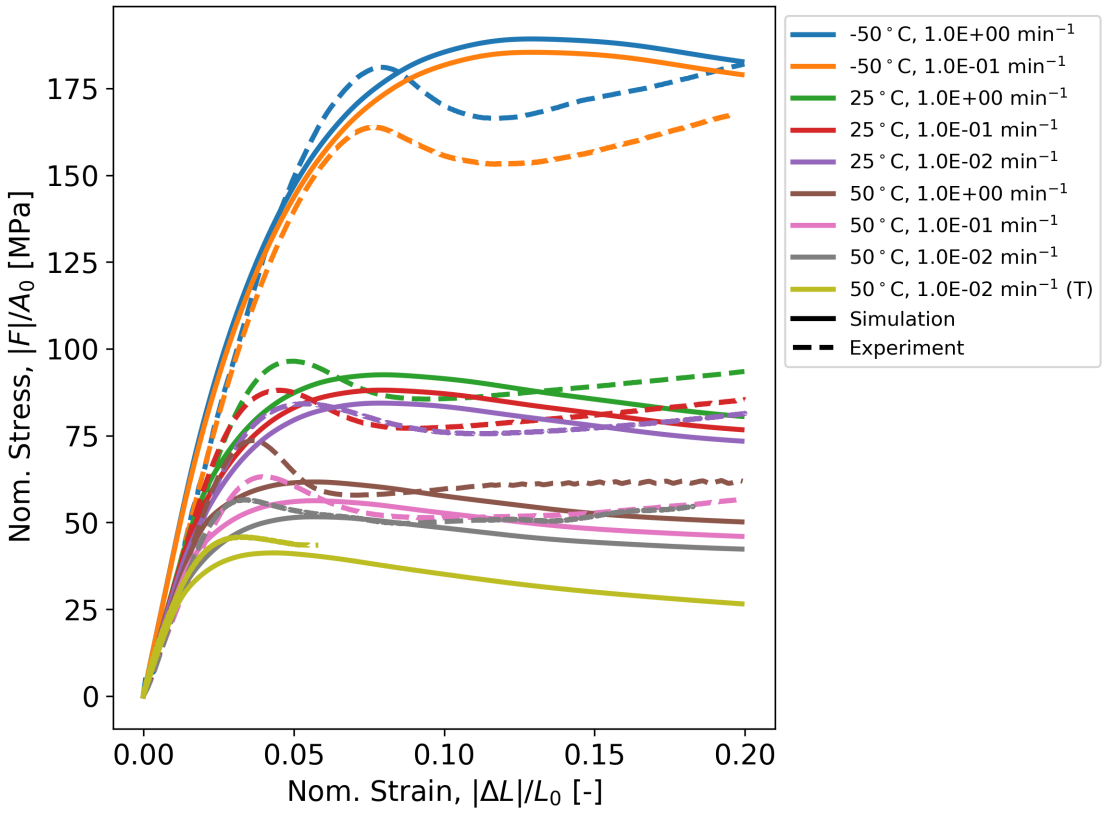

Figure 5-15. Simulated and experimental stress–strain curves. The simulated response was produced by the compression-focused calibration approach for 828DEA. In the legend, "(T)" denotes tensile experiments. All other experiments are compressive. Experimental data from Fig. 3-4.

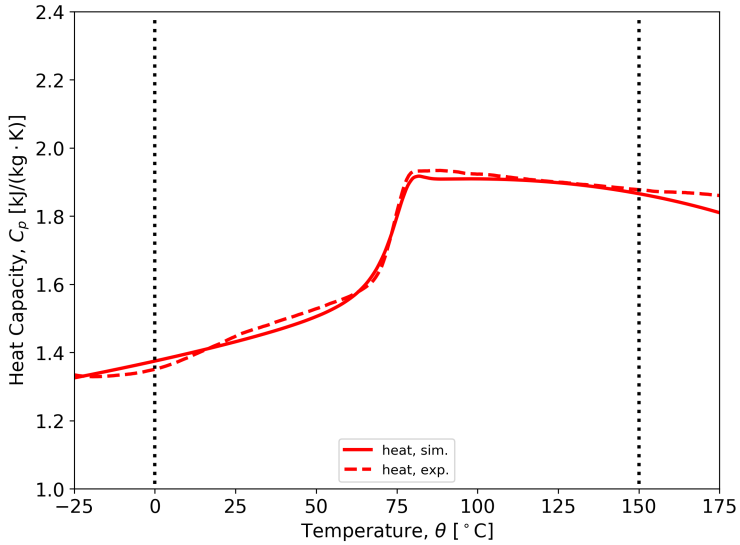

Figure 5-16. Optimized DSC response from the compression-focused calibration approach for 828DEA. Black dotted lines represent the temperature range considered during optimization. Optimized parameters included τ_4, β_4, C_g^{ref}, C_g', C_∞^{ref}, and C_∞'. Experimental data from Fig. 3-7. The cooling rate was $15\,^{\circ}\text{C}/\text{min}$.

5.2.2. Stress-Free Temperature Sweep in a Differential Scanning Calorimeter

For the compression-focused calibration, the DSC calibration step needs to be repeated using the new $f_3(t)$. Since $f_3(t)$ appears in the shift factor definition of the SPEC model, Eq. (2.8), it affects all viscoelastic behaviors predicted by the model, so parameters from the baseline DSC calibration can not be re-used. The exact calibration procedure described in Section 5.1.5 is repeated here.

Fig. 5-16 shows the calibrated constant-pressure heat capacity fit for the compression-focused approach. All regions of the heat capacity curve are well fit to the experimental data, with the caveat that the experimentally observed negative slope is likely an effect of chemical changes, and so it is undesirable that the model has mimicked the negative slope. However, the slope predicted by the model is still fairly flat, at least up to 150 °C, so this particular aspect of the fit is not expected to create major issues.

5.2.3. Revisit the Stress-Free Temperature Sweep in Thermomechanical Analyzer

No relaxation function was optimized to the TMA data in the compression-focused calibration. Therefore, it is important to re-visit the TMA response to evaluate the trade-offs made in order to improve the yield stress behavior. Details on the thermal history used to simulate the TMA experiment are provided in Section 5.1.3.

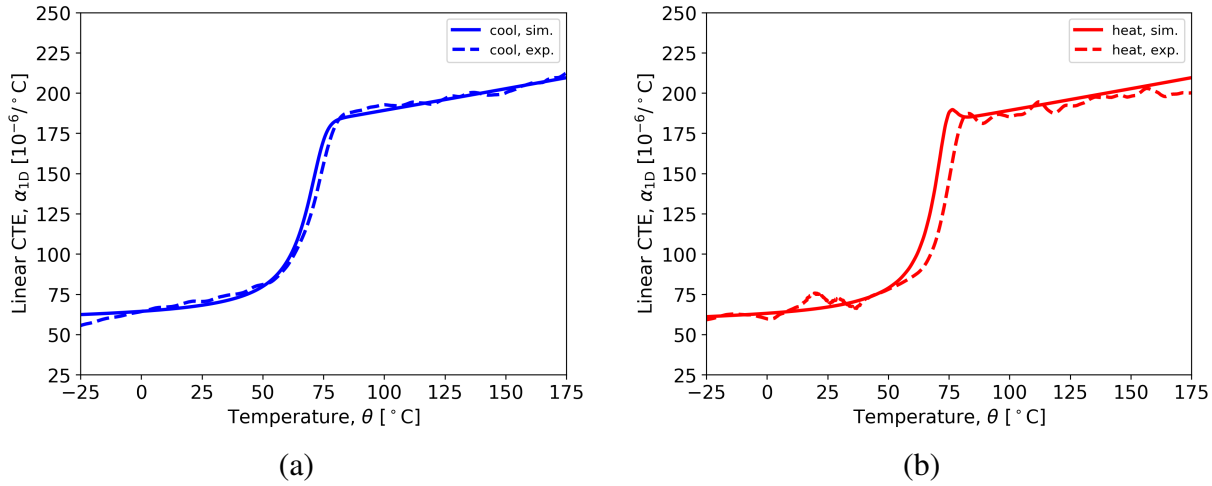

Figure 5-17. Experimental TMA response compared to the simulated response from the compression-focused calibration for 828T403 during (a) cooling and (b) heating.

Fig. 5-17 shows the simulated and experimental linear CTE on cooling (a) and heating (b). For the compression-focused approach, the TMA response is still well fit, even without optimizing any relaxation functions to fit the TMA experiment. The compression-focused approach was much less impactful for 828DEA than for 828T403. For 828T403, the yield stress fit for the baseline approach was only mediocre, but was improved by the compression focused fit. The 828T403 baseline calibration had $\tau_1 = \tau_3 = 0.835\,\text{s}$ and $\beta_1 = \beta_3 = 0.25$, and the compression-focused approach had $\tau_1 = \tau_3 = 129\,\text{s}$ and $\beta_1 = \beta_3 = 0.15$. The large increase in the characteristic time and the breadth for the compression-focused approach had an adverse effect on the CTE response for the TMA experiment. On the other hand, for 828DEA, the baseline calibration approach already predicted the yield stress fairly well, and the compression-focused approach did not signficantly improve the already acceptable fit. Consequently, the thermal-volumetric relaxation functions changed less between the baseline and compression-focused calibrations for 828DEA than for 828T403. The 828DEA baseline calibration had $\tau_1 = \tau_3 = 41.0\,\text{s}$ and $\beta_1 = \beta_3 = 0.26$, and the compression-focused approach had $\tau_1 = \tau_3 = 1.42\,\text{s}$ and $\beta_1 = \beta_3 = 0.27$, so the compression-focused calibration had a shorter characteristic time by one order-of-magnitude, with a similar breadth. On the other hand, for 828T403, the characteristic time increased by two orders-of-magnitude and became much broader (baseline $\tau_1 = \tau_3 = 0.835\,\text{s}$, compression-focused $\tau_1 = \tau_3 = 129\,\text{s}$ baseline $\beta_1 = \beta_3 = 0.25$, compression-focused $\beta_1 = \beta_3 = 0.15$, see Table 4-5).

5.3. DSC-Focused Calibration

Based on the discussion in Section 5.1.6, an alternate calibration approach was proposed where $f_3(t) = f_4(t)$ are calibrated to fit the constant pressure heat capacity from a DSC experiment using a slow cooling rate. The goal of this approach was to predict the height of the heat capacity spike that occurs on reheating when the material was cooled into the glass at a low cooling rate. The

Table 5-5. SPEC parameters produced by the DSC-focused calibration for 828DEA. Only parameters that have changed from the baseline approach are listed here, see Table 5-1.

Parameter	Value	Units	Experiment	Reference
C_g^{ref}	1.172	$\text{MJ}/(\text{m}^3 \cdot \text{K})$	DSC	Fig. 5-18
C_g'	2.16	$\text{kJ}/(\text{m}^3 \cdot \text{K}^2)$	DSC	Fig. 5-18
C_∞^{ref}	1.381	$\text{MJ}/(\text{m}^3 \cdot \text{K})$	DSC	Fig. 5-18
C_∞'	0.69	$\text{kJ}/(\text{m}^3 \cdot \text{K}^2)$	DSC	Fig. 5-18
C_4	9900	K	Compression	Fig. 5-19
τ_3	890.	s	DSC	Fig. 5-18
β_3	0.22	–	DSC	Fig. 5-18
τ_4	890.	s	DSC	Fig. 5-18
β_4	0.22	–	DSC	Fig. 5-18

parameter studies in Section 5.1.6 reveal that calibrating $f_4(t)$ alone is not sufficient to adjust the aging response of the heat capacity, since $f_3(t)$ controls the thermal history in the material response. Furthermore, the slow cooling rate is necessary for this calibration approach, since it invokes physical aging behavior in the heat capacity experiment, thus making it more discerning for calibrating relaxation functions.

In this calibration approach, the heat capacity fitting step is executed followed by the glassy compression fitting (in the baseline approach, glassy compression fitting step is before the heat capacity fitting). The modified heat capacity step in this approach is different in two ways. First, the experimental data that is fit during optimization uses a cooling rate of $0.5\,^\circ\text{C}/\text{min}$ instead of a cooling rate of $15\,^\circ\text{C}/\text{min}$, which was used in Sections 5.1.5 and 5.2.2. The slower cooling rate allows some physical aging, which results in an overshoot in the constant-pressure heat capacity when the material is reheated, followed quickly by a return to the equilibrium heat capacity value. This manifests in the heat capacity curve as a "spike". Second, the thermal-volumetric and thermal relaxation functions are set equal, $f_3(t) = f_4(t)$. The bulk relaxation function during the TMA calibration step in Section 5.1.3 is not changed. Results from the modified DSC calibration step are shown in Section 5.3.1. After $f_3(t) = f_4(t)$ is fit to the DSC data using a slower cooling rate, C_4 must be adjusted to refit the glassy compression data using the new $f_3(t)$. The results from this calibration step are shown in Section 5.3.2. Finally, the TMA predictions are revisited in Section 5.3.3 using the $f_3(t)$ found from the DSC calibration step using the slower cooling rate. No relaxation functions are calibrated using the TMA data. Since this calibration approach calibrates $f_3(t)$, the relaxation function that appears in the material clock, using DSC data, it is referred to as the "DSC-focused" calibration approach. Parameters that changed from the baseline approach are listed in Table 5-5.

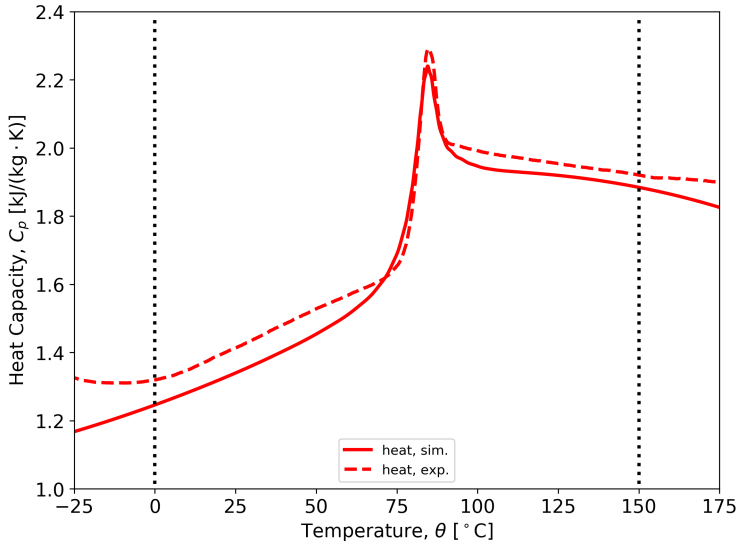

Figure 5-18. Optimized DSC response from the DSC-focused calibration approach for 828DEA. Black dotted lines represent the temperature range considered during optimization. Optimized parameters included $\tau_3 = \tau_4$, $\beta_3 = \beta_4$, C_g^{ref}, C_g', C_∞^{ref}, and C_∞'. Experimental data from Fig. 3-7. The cooling rate was $0.5\,^{\circ}\text{C}/\text{min}$**.**

5.3.1. Stress-Free Temperature Sweep in a Differential Scanning Calorimeter

After calibrating $f_1(t) = f_3(t)$ using the TMA data the DSC-focused approach departs from the baseline approach. Instead of using the $f_3(t)$ found from the TMA data, $f_3(t)$ and $f_4(t)$ were calibrated using the heat capacity response measured by DSC. However, $f_1(t)$ is not changed from the TMA calibration step, and the thermal and thermal-volumetric relaxation functions were set equal, $f_3(t) = f_4(t)$.

The calibration procedure described in Section 5.1.5 is repeated here, with two exceptions. First, the experimental data used for calibration used a slower cooling rate of $0.5\,^{\circ}\text{C}/\text{min}$. The slower cooling was useful for invoking a physical aging response, which manifested as a spike in the heat capacity response upon reheating, since this behavior was poorly predicted in the baseline calibration, which was calibrated using an experiment with a cooling rate of $15\,^{\circ}\text{C}/\text{min}$. Second, the thermal and thermal-volumetric relaxation functions were set to be equal, $f_3(t) = f_4(t)$. Otherwise, the same six parameters in Section 4.1.5 were also recalibrated here, τ_4, β_4, C_g^{ref}, C_g', C_∞^{ref}, and C_∞'.

The optimized DSC response for the DSC-focused approach is shown in Fig. 5-18. Overall, this calibration step produced a good fit the the DSC experiment using a slow cooling rate. Most importantly, the height of the heat capacity spike matches the experimental data. This was not possible without optimzing both $f_3(t)$ and $f_4(t)$, see Section 5.1.6 and Fig. 5-10. Outside of the transition region, the rubbery and glassy heat capacity are well matched, even if they are slightly low. Once again, it should be noted that the decreasing rubbery heat capacity with temperature is

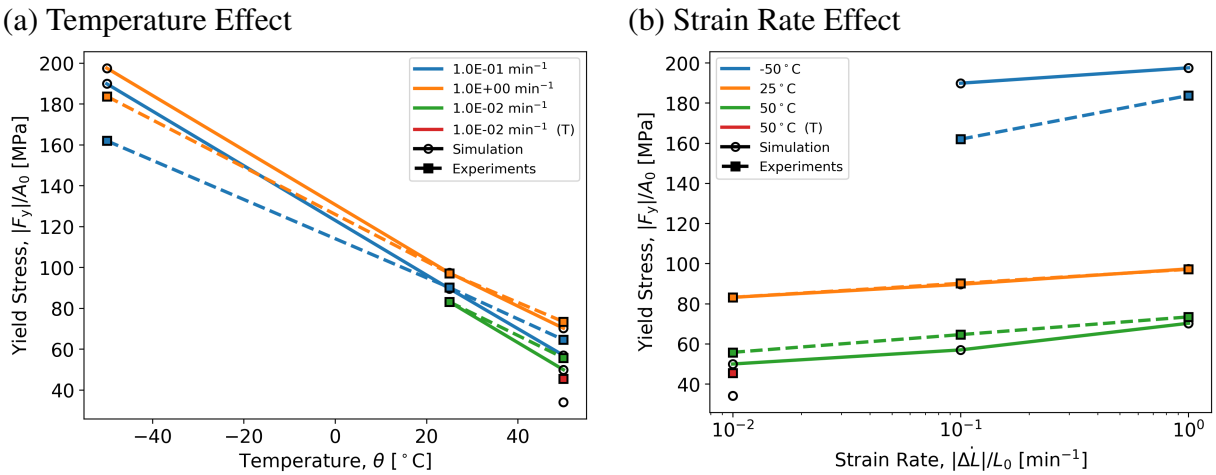

Figure 5-19. Optimized yield stress response from the DSC-focused calibration approach for 828DEA. (a) Yield stress versus temperature for constant strain rates, (b) Yield stress versus strain rate for constant temperatures. The only optimized parameter was C_4. Experimental data from Fig. 3-5.

an artifact from the experiments that the model was able to fit. Physically, the heat capacity should increase with temperature.

5.3.2. Glassy Compression

After changing $f_3(t)$, a new C_4 is needed to best fit the glassy compression response. Only C_4 is recalibrated using the glassy compression response, so the parameter is manually adjusted within 100 K of the best fit. The best fit is defined by minimizing the relative error of the yield stress at the nine loading conditions used in Section 5.1.4. The simulated yield stress was calculated as the maximum nominal stress prior to a strain of 0.12. Regressions of the yield stress, see Fig. 3-5, served as the reference values when calculating the relative errors. All loading conditions were also weighted equally in the objective function.

The simulated yield stresses after fitting C_4 are shown in Fig. 5-19. The same data is shown in Fig. 5-19(a) and Fig. 5-19(b), but the data are organized into iso–strain rate and isothermal lines, respectively. Simulated and experimental stress–strain curves are shown in Fig. 5-20. The DSC-focused fit for glassy compression is quantiatively similar to both the baseline and compression-focused fit. This in contrast to 828T403, where the glassy fit is similar for the baseline and DSC-focused approaches, but is noticably better for the compression-focused approach. The similarity of the glassy compression fit across all three calibration approaches for 828DEA is peculiar, since a fairly wide range of C_4 and $f_3(t)$ are produced from the procedures. The parameter C_4 varies from 9900 K (DSC-focused) to 24 800 K (compression-focused) and τ_3 varies from 1.42 s (compression-focused) to 890 s (DSC-focused). The β_3 is less varied; the lowest value corresponds to the DSC-focused approach, 0.22, and the highest value corresponds to the compression-focused approach, 0.27. Among the 828T403 fits for glassy compression, the

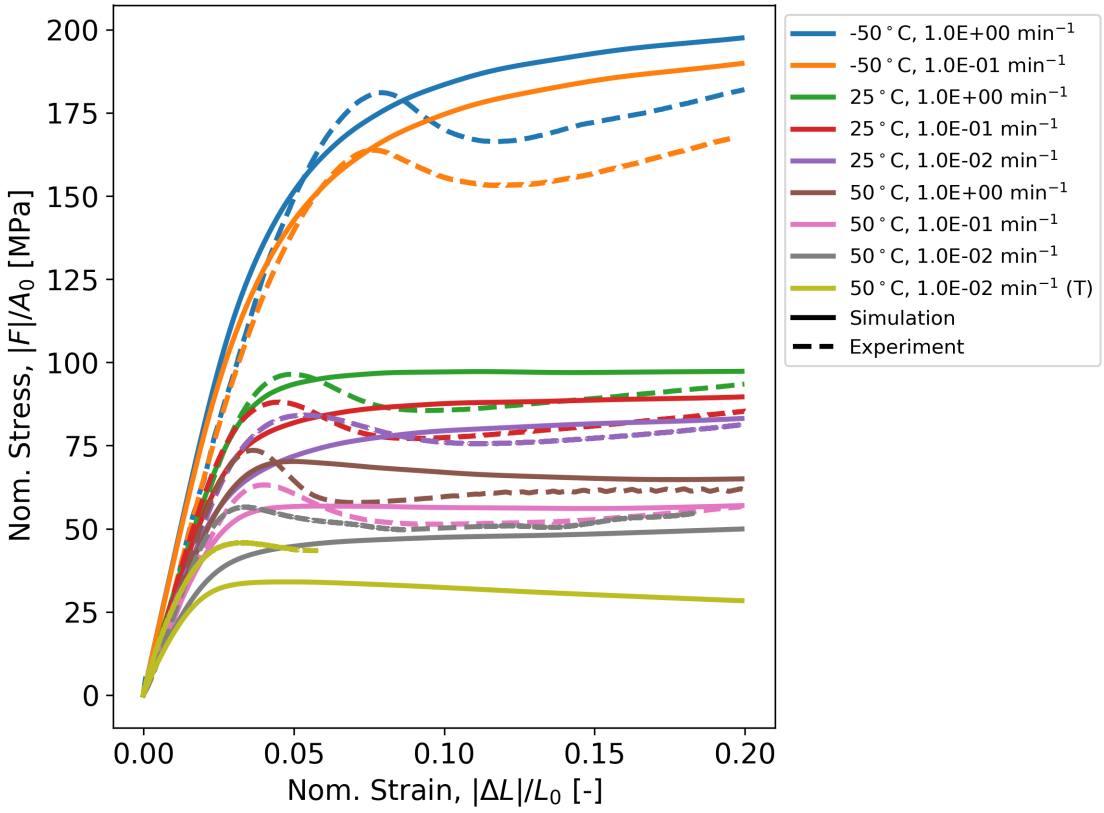

Figure 5-20. Optimized glassy compression response from the DSC-focused calibration approach for 828DEA. The only optimized parameter was C_4. Experimental data from Fig. 3-4.

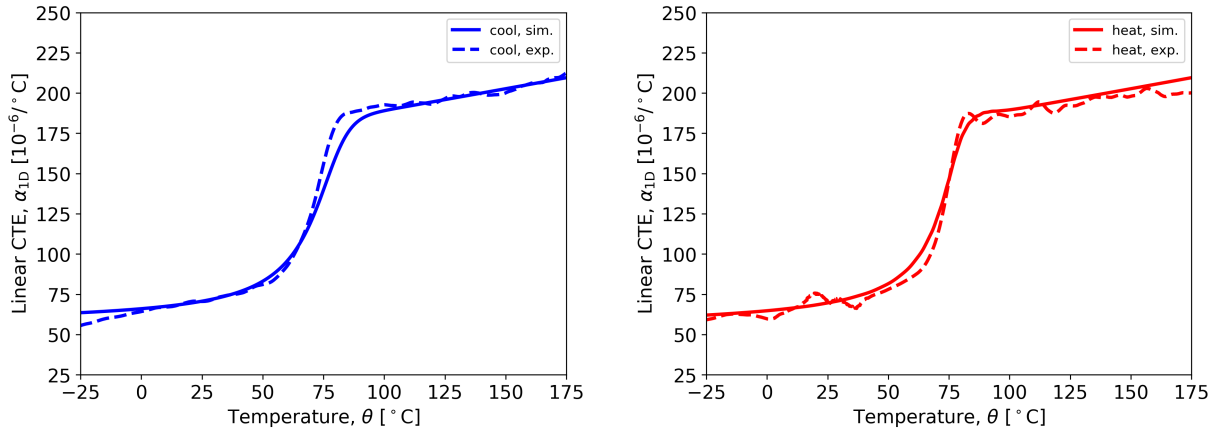

(a) (b)

Figure 5-21. Experimental TMA response compared to the simulated response from the DSC-focused calibration for 828DEA during (a) cooling and (b) heating.

β_3 value varies by a wider range, suggesting that this parameter should be investigated further to understand how to calibrate the effect of temperature and strain rate on the glassy yield stress.

The DSC-focused approach over-predicts the difference between the tensile and compressive yield strength, see Fig. 5-19, but the yield stress difference is better by the baseline calibration, see Fig. 5-6. This is unsurprising, since C_3 was borrowed from an older parameterization where the calibration approach was closer to the baseline approach executed here. A new C_3 suited for a DSC-focused calibration is needed, but preliminary attempts yielded values that were too low, see Appendix B.

5.3.3. Revisit the Stress-Free Temperature Sweep in a Thermomechanical Analyzer

No relaxation function was optimized to the TMA data in the DSC-focused calibration. Therefore, it is important to re-visit the TMA response to evaluate the trade-offs made in order to improve the DSC response for slow cooling rates. Details on the thermal history used to simulate the TMA experiment are provided in Section 5.1.3.

Fig. 5-21 shows the simulated and experimental linear CTEs on cooling (a) and heating (b). DSC-focused calibration accurately predicts the TMA experiment, even without calibrating any relaxation functions directly to the data. The CTE during the glass transition is slightly to broad on both heating a cooling, but the predictions are better than the compression-focused approach. Although the baseline approach has a better TMA fit, this is not surprising since the thermal-volumetric relaxation function was fit directly the data.

Table 5-6. Relaxation functions and changed parameters for all three calibration approaches for 828DEA.

Parameter	Baseline	Compression-focused	DSC-focused	Units
C_g^{ref}	1.146	1.135	1.172	$\text{MJ}/(\text{m}^3 \cdot \text{K})$
C_g'	1.29	1.22	2.16	$\text{kJ}/(\text{m}^3 \cdot \text{K}^2)$
C_∞^{ref}	1.379	1.300	1.381	$\text{MJ}/(\text{m}^3 \cdot \text{K})$
C_∞'	0.65	0.83	0.69	$\text{kJ}/(\text{m}^3 \cdot \text{K}^2)$
C_4	13700	24800	9900	K
τ_1	41.0	1.42	41.0	s
β_1	0.26	0.27	0.26	–
τ_2	1.25	1.25	1.25	s
β_2	0.23	0.23	0.23	–
τ_3	41.0	1.42	890.	s
β_3	0.26	0.27	0.22	–
τ_4	6.80	15.8	890.	s
β_4	0.36	0.34	0.22	–

5.4. DEA Aging Predictions Across Calibrations

In this section, each of the three calibrations for 828DEA are subjected to a suite of physical aging simulations. The reponse from each simulation will be compared to experimental data to make qualitative assessments of the strengths and weaknesses of each calibration. In addition, predictions from a legacy calibration [4] are also presented. Parameters for the 828DEA legacy calibration can be found in Appendix A.

Prior to executing the physical aging simulations, the key differences betweeen the calibrations are highlighted. Table 5-6 lists the stretched exponential functions for all four relaxation functions from all three 828DEA calibrations and the parameters that changed between each calibration. The most fundamental difference between each calibration is the type of experiment used to calibrate $f_3(t)$, which is the relaxation function that stores the thermal history in the shift factor definition, see Eq. (2.8). The characteristic time for $f_3(t)$ varies from 1.42 s to 890 s and the breadth varies from 0.22 to 0.27. Based on the parameter studies that are discussed in Sections 4.1.6 and 5.1.6, the model responses are less sensitive to $f_1(t)$ and $f_4(t)$. The shear relaxation function, $f_2(t)$, is the same across all three calibrations, since they were all calibrated from the same shear master curve. Different C_4 arise from fitting the glassy compression data based on the different $f_3(t)$ functions. As τ_3 increases, C_4 must decrease to maintain the same yield stress. Values for the heat capacity parameters also vary for each calibration, but these changes are of secondary importance to the aging response. Fig. 5-22 shows compares $f_3(t)$ for all three calibrations along with the common $f_2(t)$. The $f_3(t)$ and $f_2(t)$ from a legacy calibration are also shown. Unlike 828T403, the legacy and current $f_2(t)$ have characteristic times that are about an order of magnitude apart. This is likely due to different thermal histories, as it is

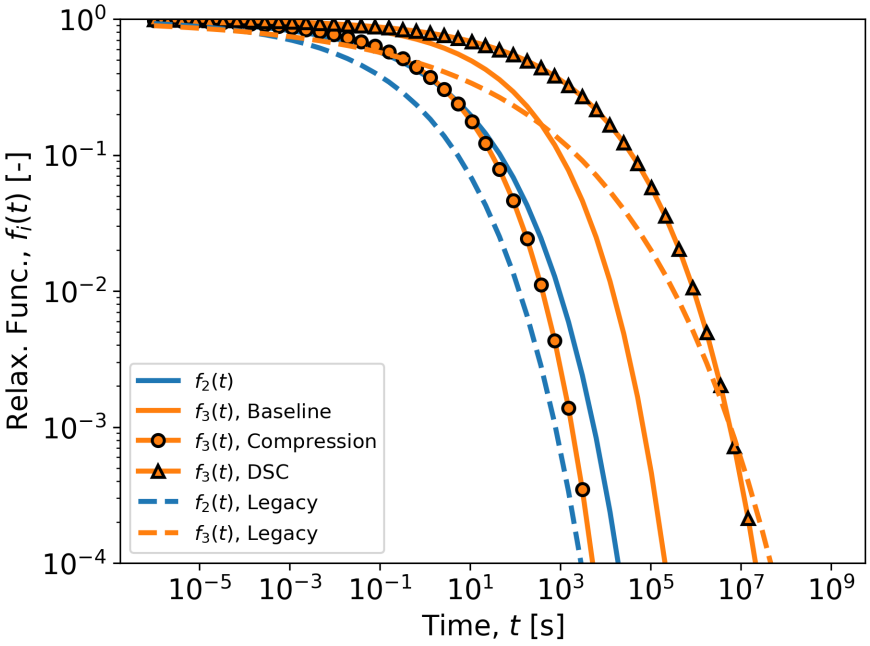

Figure 5-22. Comparison of the different functions for $f_3(t)$ found from the three calibrations of 828DEA and the $f_2(t)$ common to all three. Also shown are the $f_2(t)$ and $f_3(t)$ from a legacy calibration [4].

demonstrated in Section 3.1.2 that the shear master curve for 828DEA is very sensitive to the specific thermal history used to construct it. As with 828T403, the functions for $f_3(t)$ appear very different depending on what experiment was used to calibrate it. The compression-focused $f_3(t)$ is shortest and relaxes-out around the same time as $f_2(t)$. The DSC-focused $f_3(t)$ is the longest, and the baseline (TMA-focused) is intermediate. This ordering is different from 828T403, which was ordered from shortest to longest as baseline, DSC-focused, compression-focused. The legacy $f_3(t)$ begins to relax sooner than the baseline and DSC-focused $f_3(t)$ functions, but due to its high breadth, the legacy $f_3(t)$ finishes relaxing after the others.

5.4.1. Stress-Free Aging Followed by Compression Through Yield

The calibrations were benchmarked against the evolution of the mechanical behavior after stress-free aging. Experimental details are found in Section 3.1.8 and results are shown in Fig. 3-9. Aging times between 0 h and 10 143 h were explored. Stress-free aging followed by compression through yield was simulated using the following thermomechanical history applied to a single element in Sierra: (1) anneal at 105 °C for 30 min, (2) cool to 25 °C at a rate of 0.8 °C/min, (3) sit at 25 °C for 60 min, (4) heat to the aging temperature, θ_{age} over 30 min, (5) hold at the aging temperature for the aging time, less 30 min for the time it took to heat to the aging temperature, (6) cool to 25 °C over 30 min, (7) sit at 25 °C for 1 h, (8) heat to the loading temperature, θ_{load} over 30 min, (9) load at a nominal strain rate of 0.089/min. The yield stress is

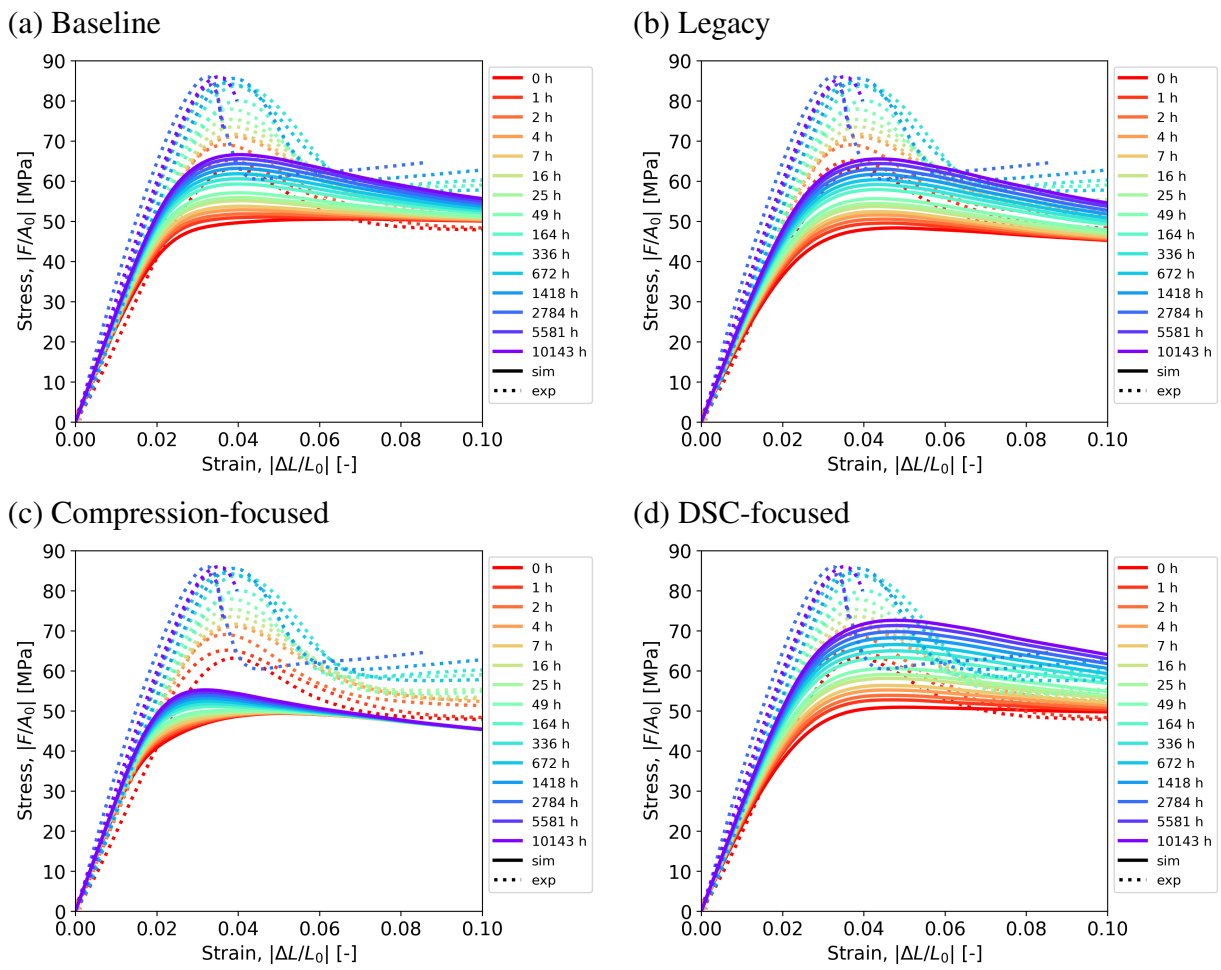

Figure 5-23. 828DEA calibration assessment of stress–strain curves after stress-free aging. (a) Baseline calibration, (b) Legacy calibration [4], (c) Compression-focused calibration, (d) DSC-focused calibration. The loading temperature and aging temperature are both 55 °C. Experimental data from Fig. 3-9a.

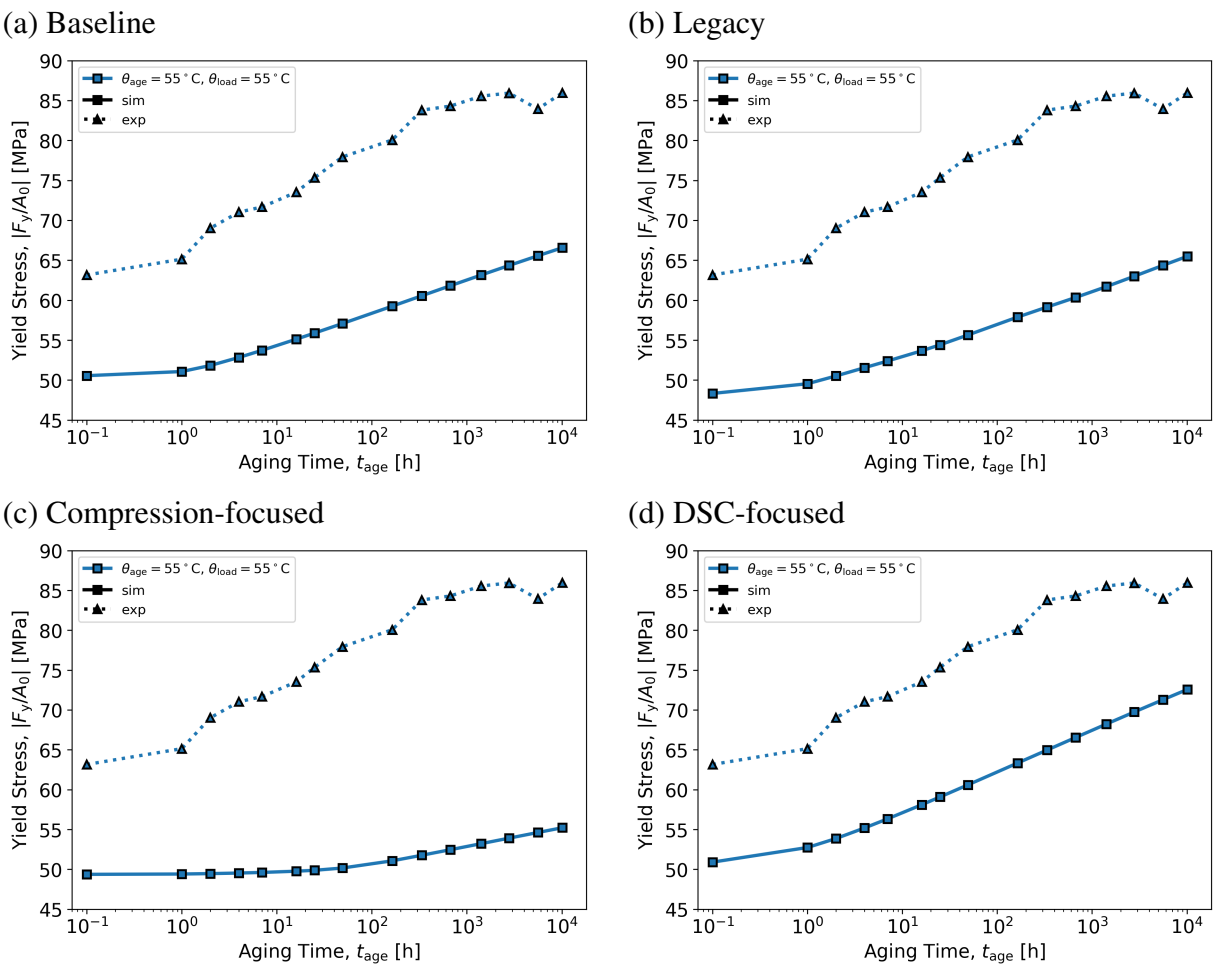

Figure 5-24. 828DEA calibration assessment for yield stress evolution with aging time for stress-free aging. The aging and loading temperature are both 55 °C. (a) Baseline calibration, (b) Legacy calibration [4], (c) Compression-focused calibration, (d) DSC-focused calibration. Experimental data from Fig. 3-9c.

chosen as a convenient metric for physical aging, which is calculated from the simulations as the local maximum in the nominal stress.

Fig. 5-23 shows predicted stress–strain curves after aging for each of the four calibrations compared to experimental data. The predicted and experimental evolution of the yield stress with aging time is then shown in Fig. 5-24. To faciliate plotting on a log scale, aging times of zero are plotted as 0.1 h. In the experiments, the unaged yield stress is around 65 MPa and increases to 85 MPa at around 10 000 h for a total increase of 20 MPa. For all four calibrations, the unaged yield stress is too low, 50 MPa, but some calibrations are better at predicting the change in the yield stress. In the baseline calibration and legacy calibrations, Fig. 5-23a, b , the yield stress increases by 15 MPa over the range of aging times, which is fairly close to the experimental target. The compression-focused calibration, Fig. 5-23c, performs the worst, as the yield stress only increases by 5 MPa over 10 000 h. The DSC-focused calibration, Fig. 5-23d, matches the experimental changes in the yield stress very well; it shows a 20 MPa increase over 10 000 h.

5.4.2. Low-Stress Creep

The calibrations were benchmarked against the creep experiments. Experimental details are found in Section 3.1.7 and results are shown in Fig. 3-8. Creep was simulated using the following thermomechanical history applied to a single element in Sierra: (1) Anneal at 105 °C for 30 min, (2) cool to 25 °C at 1 °C/min, (3) sit at 25 °C for 1 h, (4) heat from 25 °C to the creep temperature over 30 min, (5) Load to the creep stress over 5 min, (6) Hold at the creep stress and the creep temperature for 30 h. The creep temperature was 50 °C, and creep stresses of 5 MPa, 10 MPa, and 20 MPa were simulated.

Creep strain and compliance predictions from each calibration are compared to experimental data in Figs. 5-25 and 5-26 for three different stress levels. The baseline calibration, Fig. 5-25a, has the most accurate creep strain prediction after 1000 min. The legacy and DSC-focused calibrations, Fig. 5-25b, d, over-predict the creep strain and the compression-focused, Fig. 5-25c, calibration under-predicts the creep strain. In the experiments, linear viscoelasticity holds for stresses up to 20 MPa; all three experimental creep compliance curves essentially overlap. In the model, the compliance is similar for 5 MPa and 10 MPa, but is higher for 20 MPa.

5.4.3. Age-Under-Load Followed by Compression Through Yield

The calibrations were benchmarked against experiments that were aged-under-load followed and then compressed through yield. Experimental details are found in Section 3.1.9 and results for an aging temperature of 65 °C and an aging stress of 30 MPa are shown in Fig. 5-27. Age-under-load followed by compression through yield was simulated using the following thermomechanical history applied to a single element in Sierra: (1) Anneal at 105 °C for 30 min, (2) cool at 0.8 °C to 25 °C, (3) heat to the aging temperature over 30 °C, (4) load to the aging stress at an approximate strain rate of 0.1/min (using a force boundary condition)[1], (5) age for the aging time, (6) unload

[1]The element is loaded up to the aging stress using force boundary conditions. The stress rate is caculated from the input strain rate assuming linear elasticity and using the glassy elastic constants.

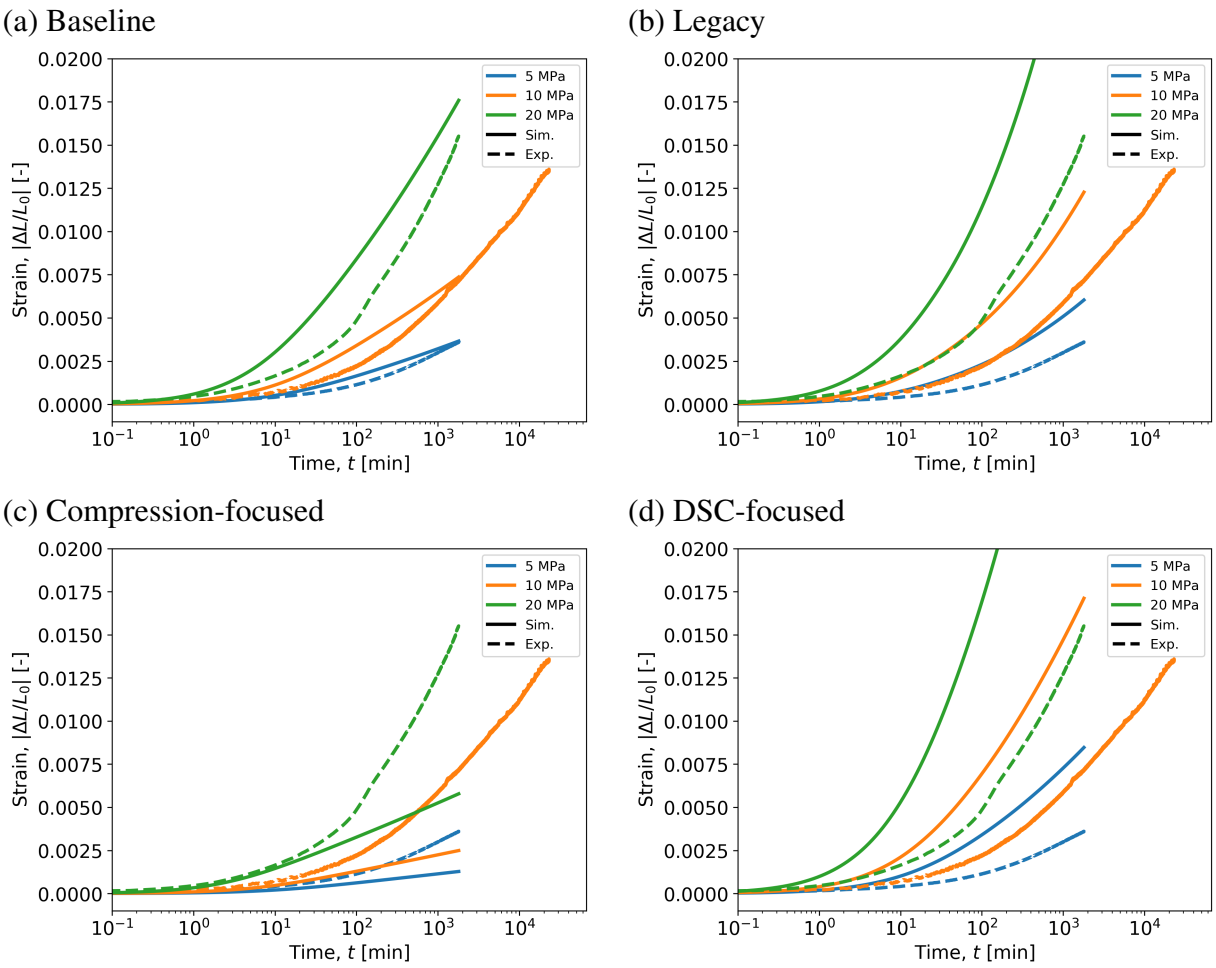

Figure 5-25. 828DEA calibration assessment for low-stress creep strain. (a) Baseline calibration, (b) Legacy calibration [4], (c) Compression-focused calibration, (d) DSC-focused calibration. Experimental data from Fig. 3-8.

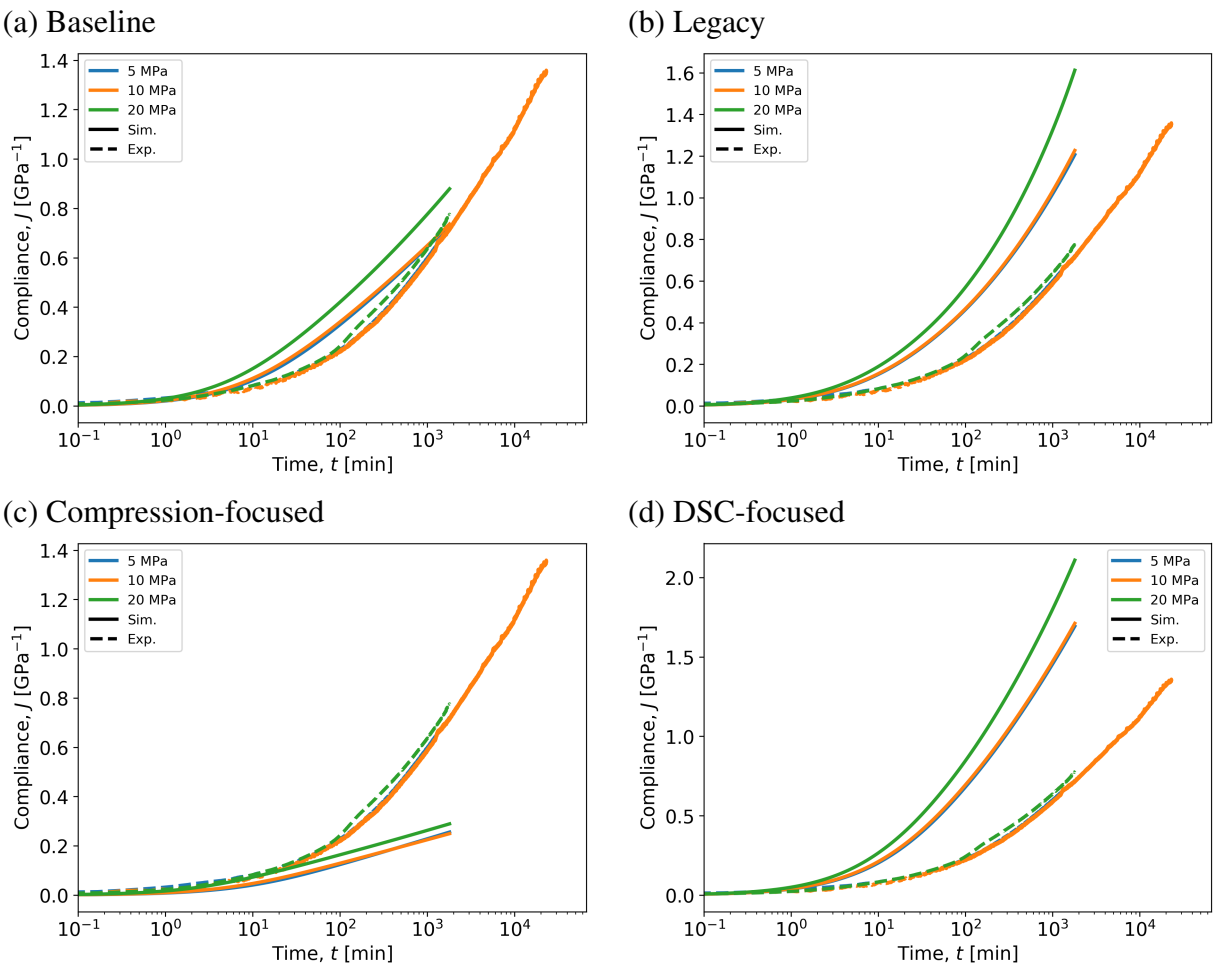

Figure 5-26. 828DEA calibration assessment for low-stress creep compliance. (a) Baseline calibration, (b) Legacy calibration [4], (c) Compression-focused calibration, (d) DSC-focused calibration. Experimental data from Fig. 3-8.

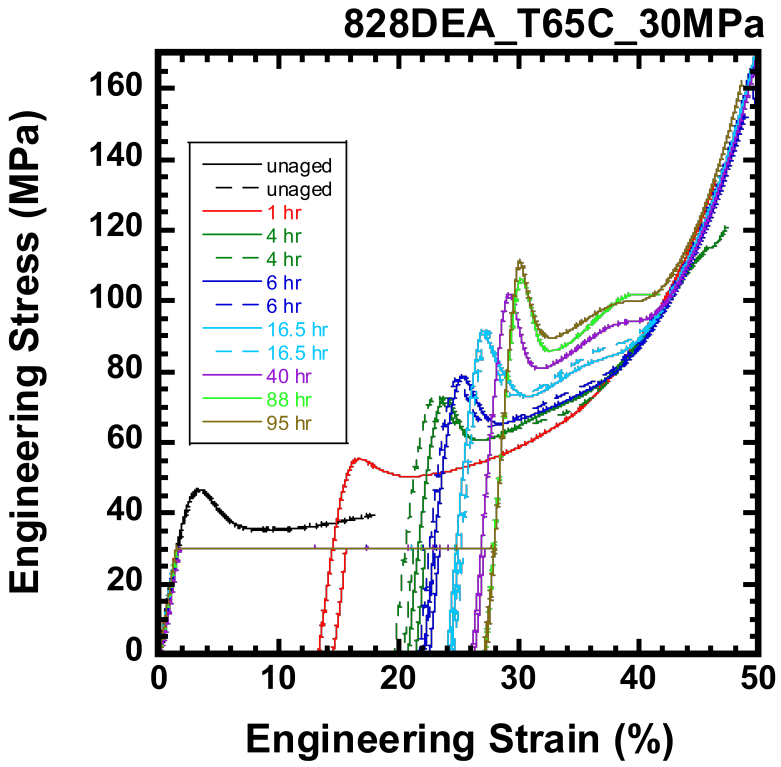

Figure 5-27. 828DEA experimental results for aging-under-load followed by compression through yield. The experiments used an aging temperature of 65 °C and an aging stress of 30 MPa. See additional experimental details in Section 3.1.9.

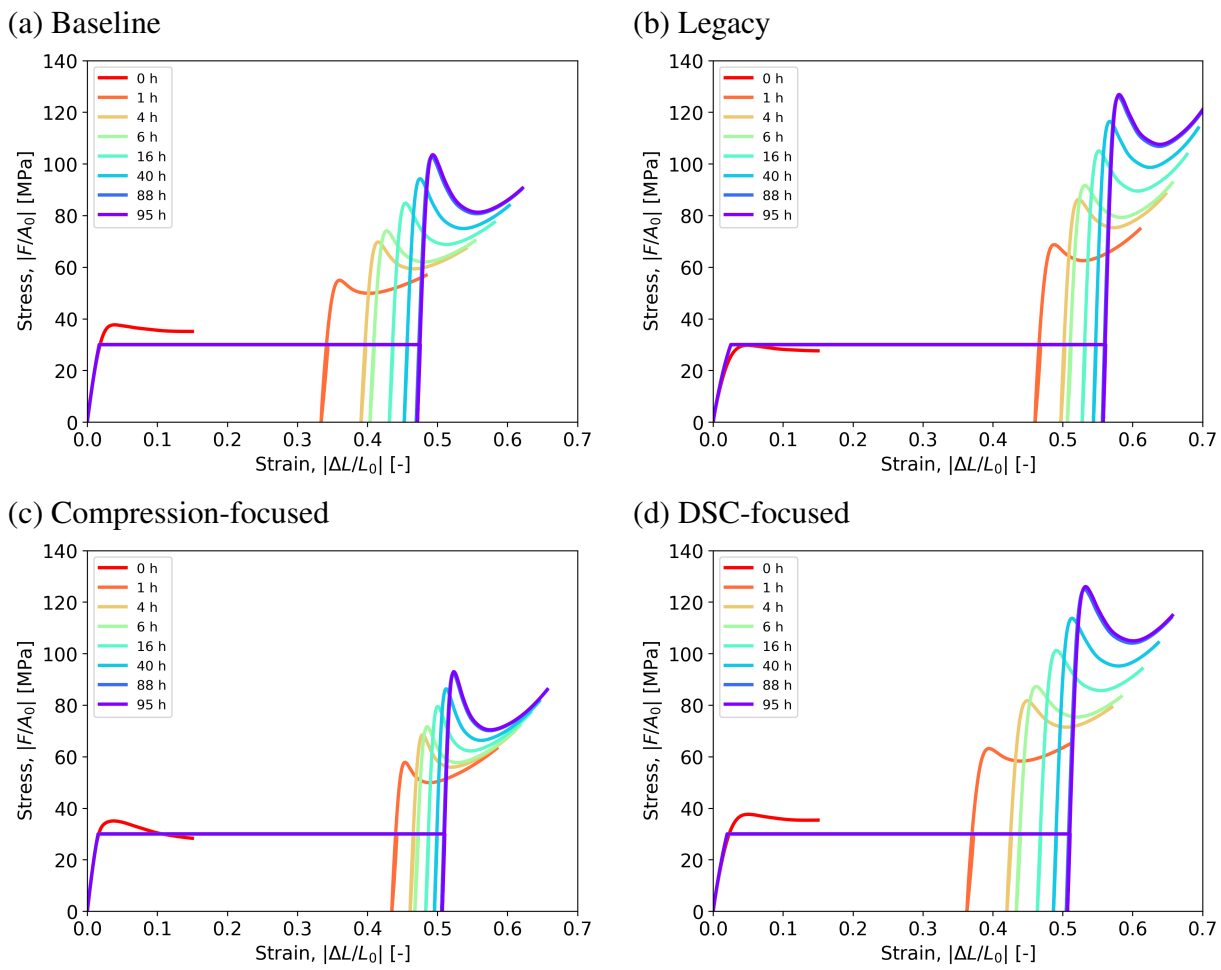

Figure 5-28. 828DEA calibration assessment for aging-under-load followed by compression through yield. The experiments and simulations used an aging temperature of 65 °C and an aging stress of 30 MPa. (a) Baseline calibration, (b) Legacy calibration [4], (c) Compression-focused calibration, (d) DSC-focused calibration.

to zero stress using an approximate strain rate of $0.1/\text{min}$ (also using a force boundary condition), (7) load at a strain rate of $0.1/\text{min}$ (using a displacement boundary condition).

Fig. 5-28 shows predictions for the age-under-load at 65 °C and 30 MPa followed by compression through yield for all four calibrations. Aging times between 0 h and 95 h are investigated. In the experiments, the strain at the end of aging for 1 h is around 0.14, and after 95 h it is around 0.28. All calibrations significantly over-predict the strain after aging under load, but the baseline and DSC-focused calibrations produce the lowest strain, and therefore they give the best predictions of the strain after aging-under-load. In the experiments, the yield stress evolves from around 45 MPa at 0 h to 110 MPa at 95 h. The baseline calibration is the closest to predicting the yield stress evolution, with an unaged yield of 40 MPa and the yield stress after 95 h is 110 MPa. The DSC-focused gives the second best prediction of the yield stress, with an unaged yield stress of 40 MPa, but the yield stress at 95 h is too high by approximately 10 MPa, where the baseline is almost exactly on-target here. The compression-focused calibration does not show enough yield stress evolution (40 MPa at 0 h to 90 MPa at 95 h). The legacy calibration's unaged yield stress is too low, and the yield stress at 95 h is too high.

5.4.4. Isothermal Volume Relaxation Under Near Stress-Free Conditions

The calibrations were benchmarked against the evolution of the volume strain during a nearly stress-free isothermal hold. Experimental details are shown in Section 3.1.10 with experimental results shown in Fig. 3-10. The isothermal hold experiment was simulated by applying the following thermomechanical history to a single element in Sierra: (1) anneal at 150 °C for 5 min, (2) cool to 30 °C at 1 °C/min, (3) heat to the aging temperature at 1 °C/min, (4) hold at the aging temperature for 60 d. Since contact from a probe is required to measure the volume, the experiment is nearly stress-free. A token stress of 1 Pa is applied to the $+y$-face of the element.

The isothermal volume relaxations for each calibration are compared to experimental data in Fig. 5-29. Experimentally, the isothermal hold at 75 °C shows the most volume relaxation. This is most likely not an effect of physical aging, since this temperature is near the glass transition, and therefore the material should already be very close to, or already at, equilibrium when the isothermal hold begins. Therefore, the large volume decrease is likely due to shrinkage from chemical aging, which the `spectacular` model cannot predict. The baseline and compression-focused calibrations predict almost no volume relaxation at 75 °C, but the DSC focused does predict some, likely due to its extremely long characteristic time for the thermal-volumetric relaxation function, τ_3. At 70 °C, the the compression-focused calibration still predicts the least amount of volume relaxation, consistent with it having the smallest τ_3, while the baseline and DSC-focused calibrations predict similar amounts of volume relaxation. The predictions still show less volume strain than the experimental data. At 55 °C, all three of the new calibrations show a similar amount of volume relaxation, which is actually close to the experimental data. It is difficult to draw conclusions about which calibrations perform the best for this experiment, since it appears that chemical shrinkage is occuring, which cannot be predicted by the model.

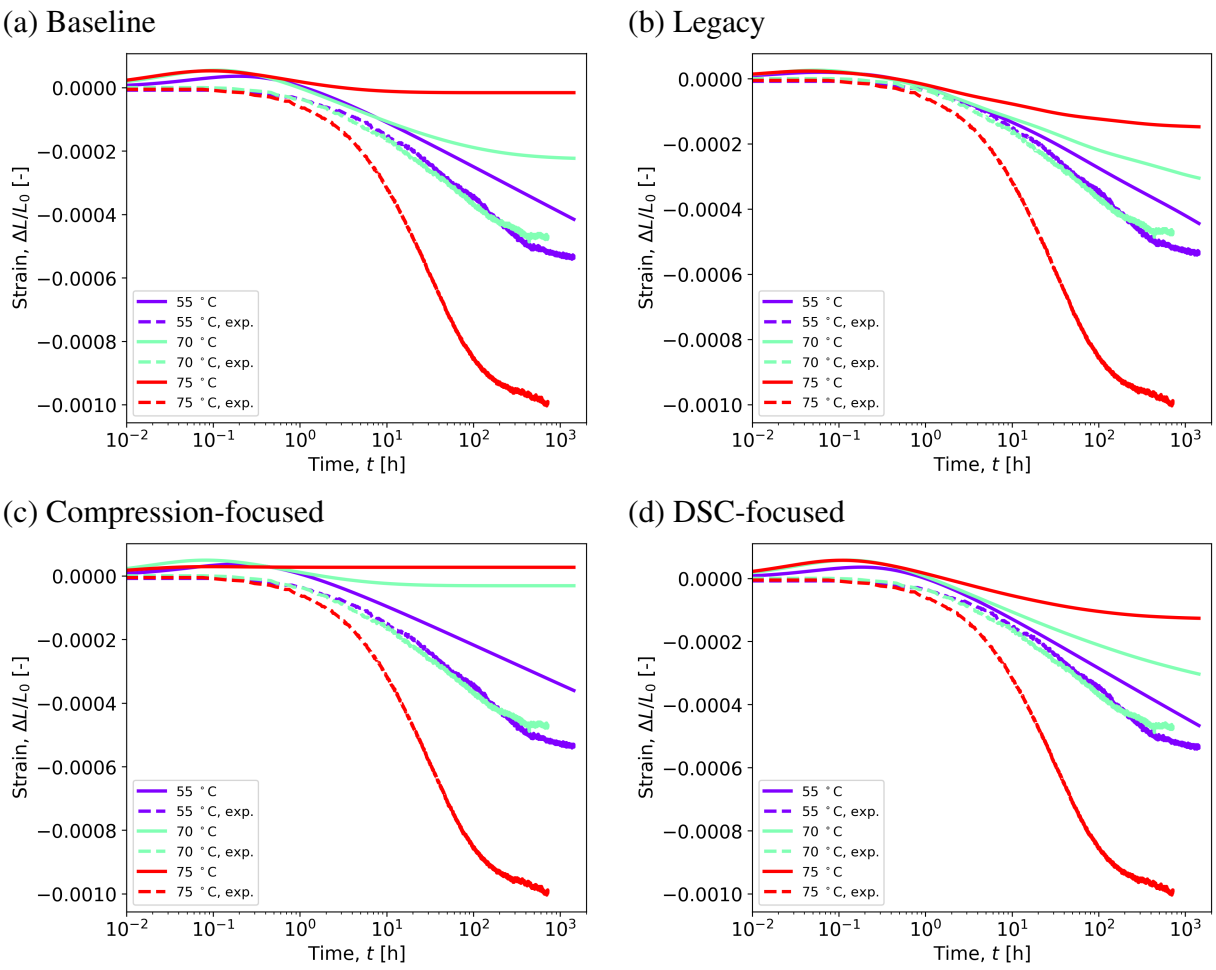

Figure 5-29. 828DEA calibration assessment for isothermal volume relaxation. (a) Baseline calibration, (b) Legacy calibration [4], (c) Compression-focused calibration, (d) DSC-focused calibration. Experimental data from Fig. 3-10.

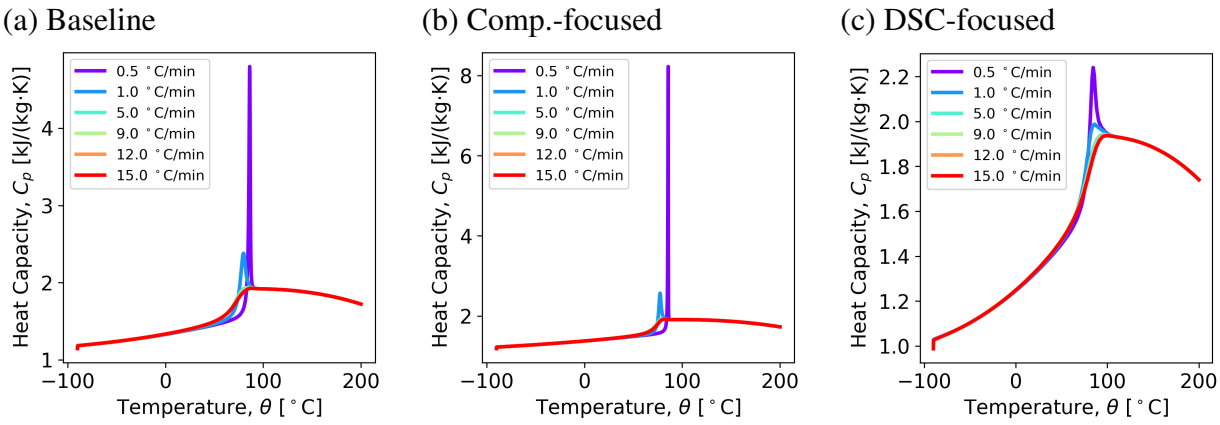

Figure 5-30. The effect of cooling rate on the constant pressure heat capacity upon reheating for three calibrations of 828DEA. (a) Baseline calibration, (b) compression-focused calibration, (c) DSC-focused calibration.

5.4.5. Effect of Cooling Rate on the Heat Capacity Overshoot

The calibrations were benchmarked against the heat capacity measured during a stress-free temperature increase. The thermal history involved cooling into the glass and then reheating at 10 °C/min. The experimental database included tests using different cooling rates. At slower cooling rates, a small amount of physical aging occurs, so that upon reheating, enthalpy recovery results in a spike in the heat capacity curve [9]. Experimental details can be found in Section 3.1.6 with results shown in Fig. 3-7. The DSC experiments were already used during the calibration step, but each of the three procedures used only a single cooling rate; the baseline and compression-focused calibrations used 15 °C/min, while the DSC-focused used 0.5 °C/min. Here, all three calibrations are tested at multiple cooling rates. The thermal history used to simulate these experiments is listed in Section 4.1.5, except that the applied cooling rate is variable.

The effect of the cooling rate on the heat capacity during the reheat is shown for all three calibrations in Fig. 5-30. For the baseline and compression-focused calibrations, unrealistic heat capacity spikes are predicted at 0.5 °C/min. For all three calibrations, a spike is only apparent at 0.5 °C/min and 1.0 °C/min. Fig. 4-27 compares the model responses to experimental data. The figures are organized to show a single calibration per row and a single cooling rate per column. The fits for the baseline and compression-focused calibrations are similar. They dramatically over-predict the heat capacity for a cooling rate of 0.5 °C/min, slightly over-predict the spike for a cooling rate of 1.0 °C/min, but are fit fairly well for a cooling rate of 15.0 °C/min. This indicates that fitting to the a DSC experiment that doesn't exhibit physical aging through a heat capacity spike may not be sufficiently discerning for calibrating $f_3(t) = f_4(t)$. On the other hand, the DSC-focused approach was fit very well to the 0.5 °C/min condition and the prediction for the 1.0 °C/min condition is still fairly good. For the 15.0 °C/min condition, the DSC-focused prediction is reasonable, even if the transition is slightly too broad. Overall, the DSC-focused fit is able to give the best predictions for the heat capacity on reheating after cooling into the glass at

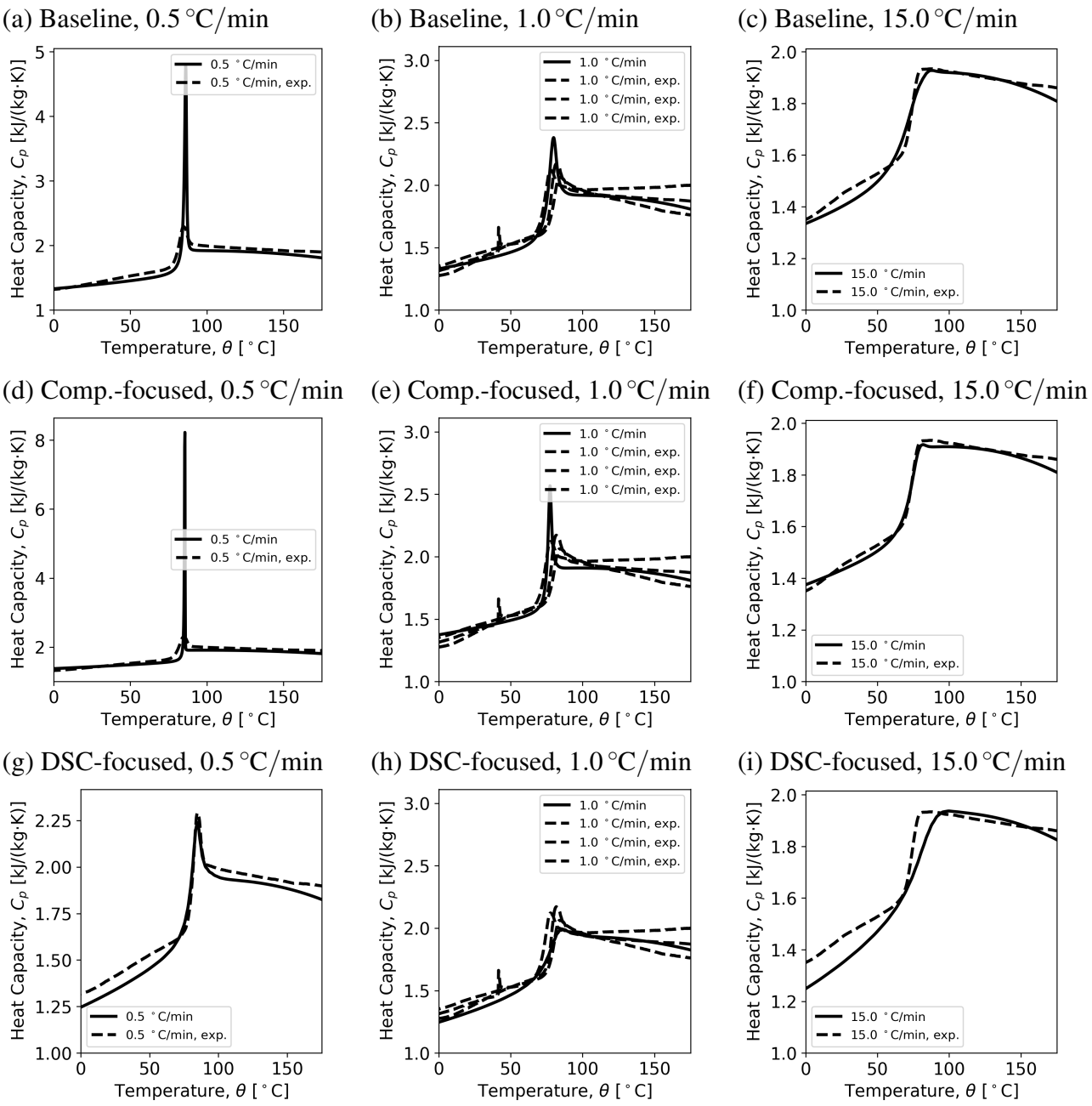

Figure 5-31. 828DEA calibration assessment for the effect of cooling rate on the constant pressure heat capacity upon reheating. The different calibrations are organized in rows; (a, b, c) baseline, (d, e, f) compression-focused, (g, h, i) DSC-focused; and different cooling rates are organized in columns; (a, d, g) 0.5 °C/min**, (b, e, h)** 1.0 °C/min**, (c, f, i)** 15.0 °C/min**. Experimental data from Fig. 3-7.**

different rates.

5.4.6. Effect of Isothermal Aging on the Heat Capacity Overshoot

The calibrations were benchmarked against the heat capacity measured by a DSC during a stress-free temperature increase after aging during an isothermal hold. The available experimental data did not include tests of this type for 828DEA, but the simulations are run to evaluate if the behavior is qualitatively realistic. The aged DSC experiments are simulated by applying the following thermomechanical history to a single element in Sierra: (1) anneal at 120 °C for 30 min, (2) cool to 30 °C at 1 °C/min, (3) hold at 30 °C for 5 min, (4) heat to the aging temperature, θ_{age}, at 10 °C/min, (5) hold at the aging temperature, θ_{age} for the aging time, t_{age}, (6) cool to 30 °C at 10 °C/min, (7) hold at 30 °C for 5 min, (8) heat to 120 °C at 10 °C/min.

The heat capacity after aging for all three calibrations are shown in Fig. 5-32. The peak heat capacity and the temperature of the peak are plotted versus aging time in Fig. 5-33. For an aging temperature of 55 °C, the peak aging temperature is extremely large, which is unlikely to be corroborated by experiments. Additionally, for high aging times, the temperature of the peak dramatically exceeds the glass transition temperature, which is also physically unrealistic. For the aging temperature of 65 °C, the predictions are more reasonable, but the peaks still seem a little higher than what is reasonable to expect, and the temperature of the peak is too high, except perhaps for the compression-focused calibration. Similar results were obtained for 828T403, see Fig. 5-33. The unrealistic predictions of the heat capacity could support the following hypothesis for future work: (1) the equilibrium behavior of the shift factor is making it impossible to predict aging behaviors very deep in the glass or (2) the DSC experiment cooled slowly into the glass is still not discerning enough for calibrating $f_4(t)$.

5.5. 828DEA Summary and Recommendations

Three calibration procedures were executed for 828DEA. The fundamental difference between each calibration procedure is the experiment used to calibrate $f_3(t)$, the relaxation function that controls the thermal memory in the shift factor definition. For the baseline approach, $f_3(t)$ is calibrated from the coefficient of thermal expansion measured by a thermo-mechanical analyzer, for the compression-focused approach, $f_3(t)$ is calibrated from the yield stress in glassy compression at different strain rates and temperatures, and for the DSC-focused approach, $f_3(t)$ is calibrated from the heat capacity measured from a differential scanning calorimeter experiment and the experiment used a procedure where the material was cooled slowly into the glass so that a heat capacity spike is observed.

All calibration procedures produced reasonable fits to the suite of calibration experiments (TMA, glassy compression, DSC). However, the DSC-focused approach was able to fit the DSC experiment when the material was cooled slowly and quickly into the glass, but the other two procedures failed to accurately predict the heat capacity spike after slowly cooling into the glass. Therefore, the DSC-focused approach produced the best overall fit to calibration data. The $f_3(t)$ relaxation functions produced from the different calibrations had the following order, from

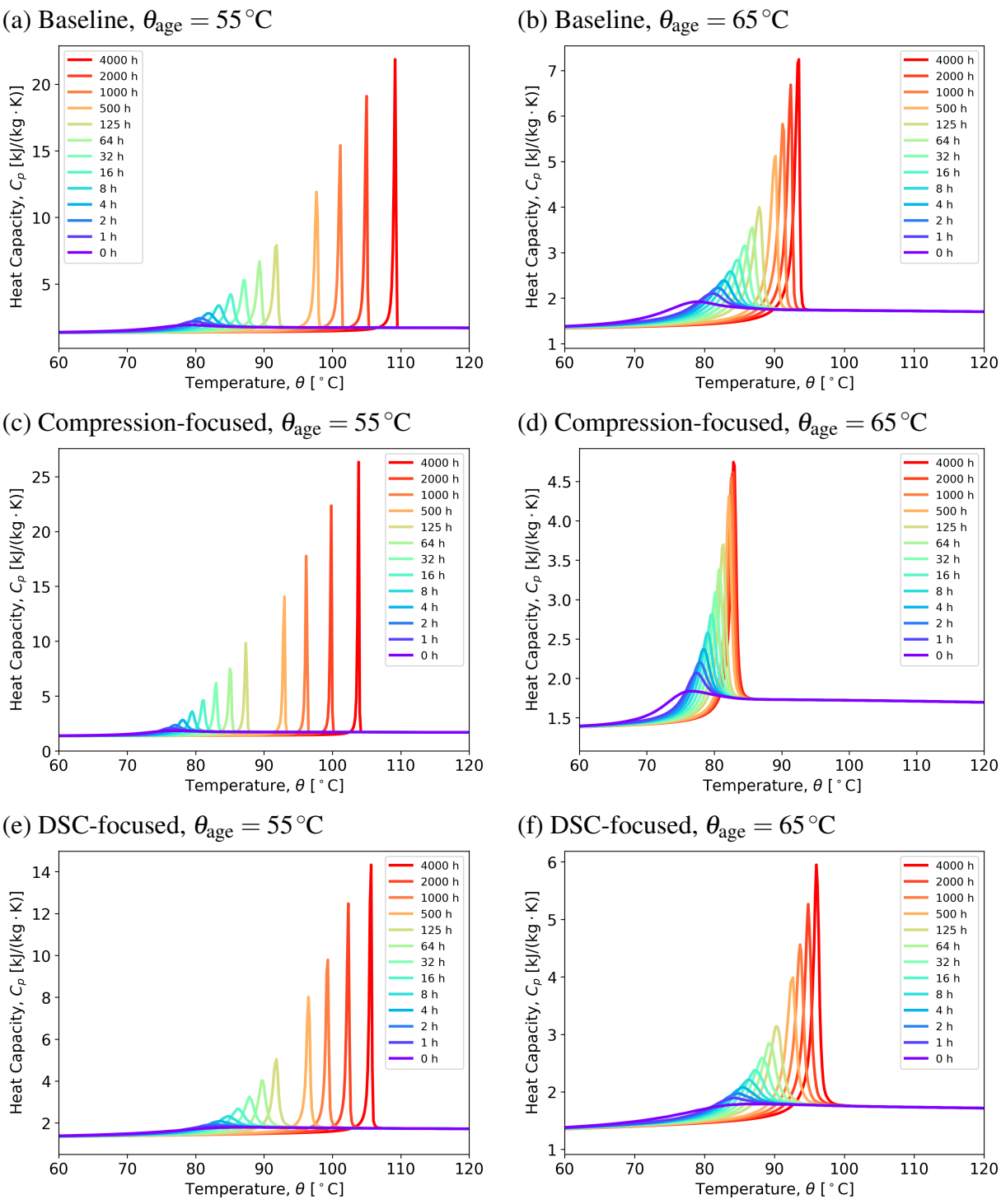

Figure 5-32. 828DEA calibration assessment for the effect of isothermal aging on the constant pressure heat capacity upon reheating. Calibrations are organized in rows; (a, b) baseline, (c, d) compression-focused, (d, e) DSC-focused, and different aging temperatures are organized in columns; (a, c, e) $\theta_{age} = 55\,^{\circ}C$ **and (b, d, f)** $\theta_{age} = 65\,^{\circ}C$**.**

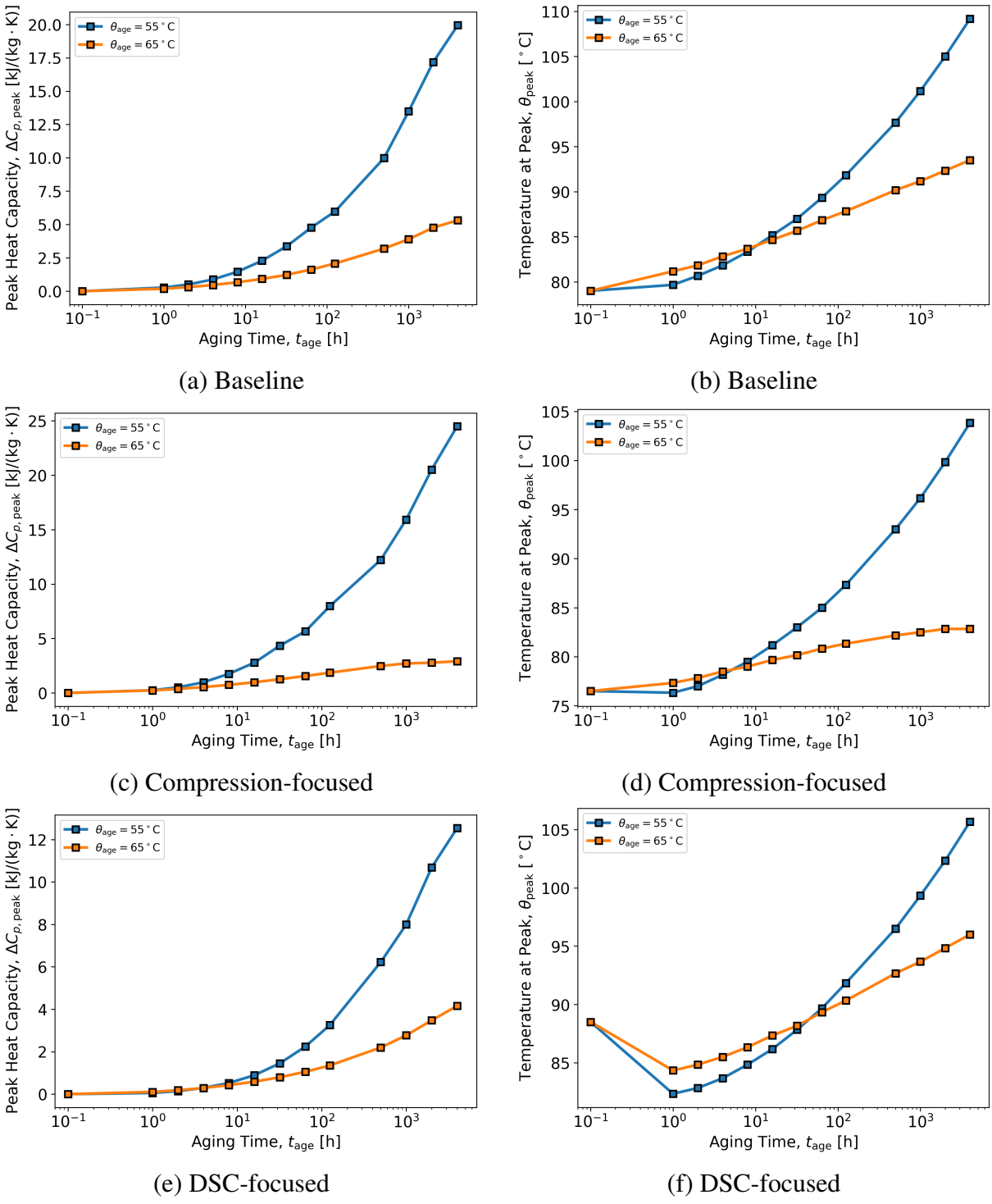

(a) Baseline

(b) Baseline

(c) Compression-focused

(d) Compression-focused

(e) DSC-focused

(f) DSC-focused

Figure 5-33. 828DEA calibration assessment for the effect of isothermal aging on the (a, c, e) peak heat capacity and (b, d, f) temperature of the peak heat capacity. Calibrations are organized in rows; (a, b) baseline, (c, d) compression-focused, (d, e) DSC-focused.

shortest to longest, compression-focused, baseline (TMA-focused), and DSC-focused. This is a different ordering of $f_3(t)$ than for 828T403.

Across the suite of physical aging experiments, the baseline and DSC-focused approach perform the best, while the compression-focused performs the worst. For stress-free aging followed by compression, the DSC-focused accurately predicts the rate of change in the yield stress with the log of the aging time, the baseline slightly underpredicts the rate, and the compression-focused significantly underpredicts the rate. All three under-predict the magnitude of the yield stress. For low-stress creep predictions, the baseline accurately predicts the creep strain at three different stresses, the compression-focused under-predicts the creep strain, and the DSC-focused over-predicts the creep strain. For aging-under-load followed by compression, all calibrations over-predict the strain at the end of aging, but the baseline focused has the lowest strain, making it the best. The baseline calibration also matches the evolution of the yield stress after aging under load, but the DSC focused is only slightly worse. Overall, the DSC-focused approach produces the best predictions and fits to experimental data, but when it is not the best, it is a close second. Therefore, the DSC-focused is deemed the best calibration approach.

Given that the DSC-focused approach is the best for both 828DEA and 828T403, this suggests that the thermal relaxation function should be implemented as the relaxation function that drives the thermal history in the shift factor definition.

As with 828T403, all calibrations performed poorly when predicting the aged DSC experiments. Their heat capacity spikes were generally too high, and occurred at temperatures too far above the glass transtion temperature. Parameter studies in Section 5.1.6 indicate that lowering β_3 might reduce the height and temperature of the peaks, but the inability of any calibration to predict the aged DSC behavior might indicate one or both of the following. First, the DSC experiment cooled slowly into the glass may be insufficiently discerning for calibrating $f_3(t)$. It was already shown that cooling slowly was more discerning than cooling quickly, see Section 5.1.6, so perhaps an even more discerning DSC experiment needs a period of isothermal aging. Second, this could be related to issues with the sub–glass transition equilibrium behavior of the model, especially since the over-predictions of the peak heat capacity are more pronounced at lower temperatures.

6. PARAMETRIC STUDIES TO FIND PARAMETER CORRELATIONS THAT PRODUCE AGING BEHAVIOR

In this chapter, parameter relationships necessary to produce physical aging behavior are explored through parameter studies. In Section 6.1, parameter studies for stress-free aging followed by compression through yield are explored. Then, in Section 6.2, the parameter relationships that are found to promote physical aging behavior are discussed in the context of the three different calibration procedures from Chapters 4 and 5.

6.1. Parameter Studies for Stress-Free Aging Followed by Compression Through Yield

Parameter studies on simulations of stress-free aging followed by compression through yield are described here. Stress-free aging followed by compression through yield was simulated using the following thermomechanical history applied to a single element in Sierra: (1) anneal at 105 °C for 30 min, (2) cool to 25 °C at a rate of 0.8 °C/min, (3) sit at 25 °C for 60 min, (4) heat to the aging temperature, θ_{age} over 30 min, (5) hold at the aging temperature for the aging time, less 30 min for the time it took to heat to the aging temperature, (6) cool to 25 °C over 30 min, (7) sit at 25 °C for 1 h, (8) heat to the loading temperature, θ_{load} over 30 min, (9) load at a nominal strain rate of 10^{-3}/s. The yield stress is chosen as a convenient metric for physical aging, which is calculated from the simulations as the local maximum in the nominal stress. For all simulations conducted here, the aging temperature and the loading temperature are the same.

In each parameter study, the average rate of the change in the yield stress per log aging time is investigated across two different parameters. Eight different parameter studies were conducted and are listed in Table 6-1. To reduce complexity of the results, two very simple model parameterizations were employed for the parameter studies. All temperature derivative parameters are zero in both parameterizations. The first parameterization is defined in Table 6-2. It represents an ideal two-spectrum model, using $f_2(t)$ and $f_3(t)$. The bulk modulus is purely elastic, $K_g(\theta) = K_\infty(\theta)$, the coefficients of thermal expansion are zero, and the volume strain does not influence the material clock, $C_3 = 0$. Given these parameters, $f_1(t)$ is irrelevant to the model. The second parameterization is defined in Table 6-3. In this parameterization, $f_1(t)$ is allowed to influence the behavior. The parameters in Table 6-2 and 6-3 represent nominal parameters used in the studies; the parameters that are changed in a study are mentioned in context.

The results from a parameter study exploring τ_2 and τ_3/τ_2 for an aging temperature of 45 °C and the nominal parameters in Table 6-2 are summarized in Fig. 6-1. A total of 25 conditions were run, five different values for τ_2 and five for τ_3/τ_2. The stress and shift factor are plotted versus the strain during loading for different aging times in Fig. 6-1(a) for $\tau_2 = 0.01$ s and $\tau_3/\tau_2 = 0.01$ and

Table 6-1. Summary of parameter studies for stress-free aging followed by compression through yield.

Param. 1	Param. 2	Nominal Parameters	$\theta_{\text{age}} = \theta_{\text{load}}$	Figure	Notes
τ_2	τ_3/τ_2	Table 6-2	45 °C	Fig. 6-1	
τ_2	τ_3/τ_2	Table 6-2	65 °C	Fig. 6-2	
C_4	τ_3/τ_2	Table 6-2	45 °C	Fig. 6-3	
C_3	τ_3/τ_2	Table 6-2, see Notes	45 °C	Fig. 6-4	CTEs activated
β_2	τ_3/τ_2	Table 6-2	45 °C	Fig. 6-5	
β_3	τ_3/τ_2	Table 6-2	45 °C	Fig. 6-6	
τ_1/τ_2	τ_3/τ_2	Table 6-3, see Notes	45 °C	Fig. 6-7	CTEs deactivated
τ_1/τ_2	τ_3/τ_2	Table 6-3	45 °C	Fig. 6-8	
τ_1/τ_2	τ_3/τ_2	Table 6-3	35 °C	Fig. 6-9	

Table 6-2. First set of nominal parameters used for stress-free yield stress evolution parameter studies.

Parameter	Value	Units
K_g^{ref}	5	GPa
K_∞^{ref}	5	GPa
G_g^{ref}	1	GPa
G_∞^{ref}	5	MPa
α_g^{ref}	0	$10^{-6}/\text{K}$
$\alpha_\infty^{\text{ref}}$	0	$10^{-6}/\text{K}$
θ_{ref}	75	°C
$\hat{C}_1$	20	–
$\hat{C}_2$	50	K
C_3	0	K
C_4	10000	K
τ_2	0.1	s
β_2	0.2	–
τ_3	10	s
β_3	0.2	–

Table 6-3. Second set of nominal parameters used for stress-free yield stress evolution parameter studies.

Parameter	Value	Units
K_g^{ref}	5	GPa
K_∞^{ref}	2	GPa
G_g^{ref}	1	GPa
G_∞^{ref}	5	MPa
α_g^{ref}	200	$10^{-6}/\text{K}$
$\alpha_\infty^{\text{ref}}$	600	$10^{-6}/\text{K}$
θ_{ref}	75	°C
$\hat{C}_1$	20	–
$\hat{C}_2$	50	K
C_3	1000	K
C_4	10000	K
τ_1	10.0	s
β_1	0.2	–
τ_2	0.1	s
β_2	0.2	–
τ_3	100	s
β_3	0.2	–

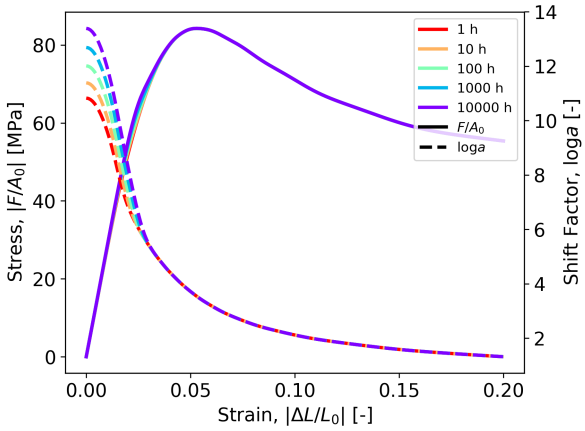

(a) $\tau_2 = 0.01\,\mathrm{s}$, $\tau_3/\tau_2 = 0.01$

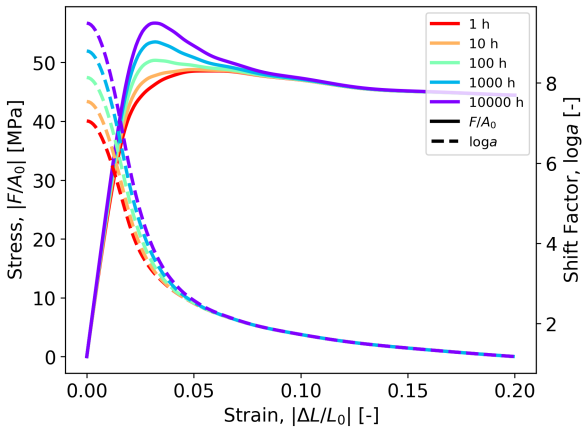

(b) $\tau_2 = 0.01\,\mathrm{s}$, $\tau_3/\tau_2 = 100$

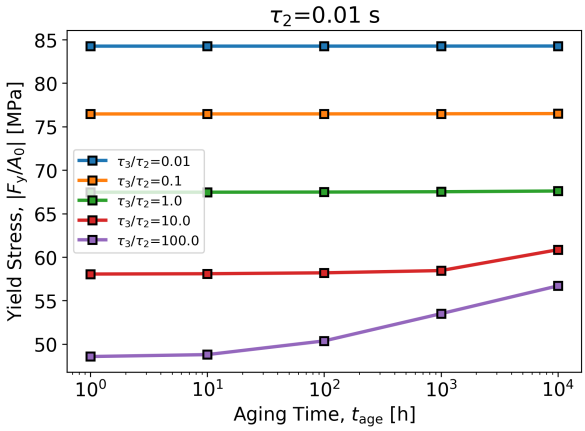

(c)

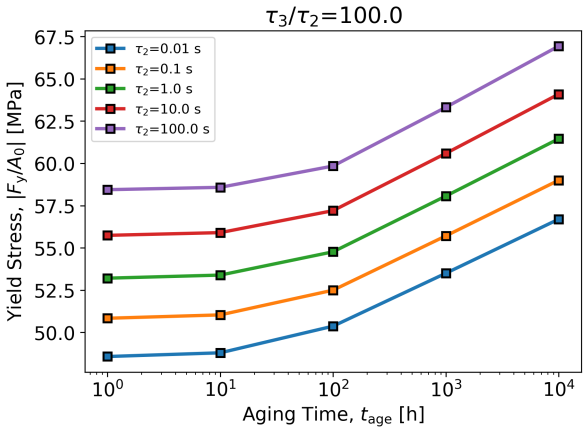

(d)

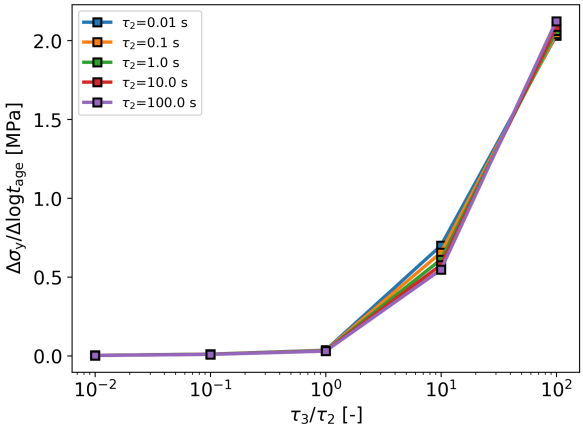

(e)

Figure 6-1. Stress-free yield stress evolution parameter study on τ_2 and τ_3/τ_2. The aging and loading temperatures are both $45\,^{\circ}\mathrm{C}$. Nominal parameters are listed in Table 6-2. (a) and (b) Effect of aging time on the stress and shift factor during loading for two different combinations of parameters. (c) Yield stress versus aging time organized by lines of constant τ_3/τ_2. (d) Yield stress versus aging time organized by lines of constant τ_2. (e) Secant slope of the yield stress versus the $\log$ of aging time from $0\,\mathrm{h}$ to $10\,000\,\mathrm{h}$ versus τ_3/τ_2.

Fig. 6-1(b) for $\tau_2 = 0.01\,\text{s}$ and $\tau_3/\tau_2 = 0.01$. The explored aging times vary from 1 h to 10 000 h. In Fig. 6-1(a), the shift factors at the start of loading vary by almost two orders of magnitude, but the $\log a$–strain curves all collapse onto the same curve before yield, so the yield stress is apparently unaffected by aging. In Fig. 6-1(b), the shift factors at the start of loading still vary by almost two orders of magnitude, but the $\log a$–strain curves are distinct until after yield, and so the yield stress is able to evolve with the aging time. Plots of the yield stress versus aging time are then built from the stress–strain curves. Fig. 6-1(c) shows the yield stress versus aging time for all conditions using $\tau_2 = 0.01\,\text{s}$. The stress–strain curves in Fig. 6-1(a) and Fig. 6-1(b) are used to construct the blue curve and purple curves in Fig. 6-1(c). Fig. 6-1(c) shows that increasing τ_3/τ_2 decreases the yield stress. For $\tau_3/\tau_2 \leq 1$, no yield stress evolution occurs. For $\tau_3/\tau_2 > 1$, increasing the τ_3/τ_2 increases the change in the yield stress from 1 h to 10 000 h. Fig. 6-1(d) shows the yield stress versus aging time for all conditions using $\tau_3/\tau_2 = 100$. The stress–strain curves in Fig. 6-1(b) are used to construct the purple curve in Fig. 6-1(d). Fig. 6-1(d) shows that changing τ_2 does not influence the rate of yield stress evolution, but increasing τ_2 increases the yield stress at all aging times. All 25 conditions explored produce a single yield stress versus aging time curve, and each curve is reduced to a single point by measuring its secant from 1 h to 10 000 h. The secant slopes from all 25 conditions are plotted against τ_3/τ_2 for curves with constant τ_2 in Fig. 6-7(e). The secant slope of the yield stress with the log of the aging time will be referred to simple as the yield stress evolution rate. Fig. 6-7(e) suggests that the relationship between τ_3 and τ_2 is more important than their absolute values. In this parameter study, the yield stress evolution rate is nearly independent of τ_2 and is instead driven by τ_3/τ_2. For $\tau_3/\tau_2 \leq 1$, the yield stress evolution rate is essentially zero. The stress–strain and $\log a$–strain curves in Figs. 6-1(a) and 6-1(b) reveal why $\tau_3/\tau_2 > 1$ is necessary for yield stress evolution. For both $\tau_3/\tau_2 = 0.01$ and 100, the shift factor varies at the start of aging. However, for $\tau_3/\tau_2 = 0.01$, the shift factors for different aging times all become the same before yield, but for $\tau_3/\tau_2 = 100$, the shift factors remain distinct until after yield. Yield occurs when the shear strain accelerates the material clock (though the term C_4) enough that the shear relaxation function relaxes quickly, so the stress in the material drops. If $\tau_3/\tau_2 < 1$ (for similar β_2 and β_3), then the thermal history, stored in $f_3(t)$ through a hereditary integral, is erased before yield. On the other hand, if $\tau_3/\tau_2 > 1$, then the shear relaxation function can relax without erasing the thermal history accumulated during aging. The remaining parameter studies in this chapter investigate the importance of τ_2/τ_3 for predicting the yield stress evolution rate.

The next study repeated the previous investigation of τ_2 and τ_3/τ_2, but at an aging temperature of 65 °C was used, which is much closer to the reference temperature of 75 °C. The results from this parameter study are shown in Fig. 6-2. Examples of stress–strain curves at different aging times are show in Figs. 6-2(a) and 6-2(b), and plots of the yield stress versus aging temperature are shown in Figs. 6-2(c) and 6-2(d). Plots of the yield stress evolution rate are shown in Fig. 6-2(e), which shows that the yield stress evolution rate increases with τ_2 and τ_3/τ_2. The plot also shows non-zero yield stress evolution rates when $\tau_3/\tau_2 < 1$. Apparently, when the material is close to the reference temperature, it is possible for thermal history to affect yield even when $\tau_3/\tau_2 < 1$. Fig. 6-2(c) shows that the yield stress evolution rate increases for longer τ_3/τ_2. At the higher temperature, there are two contributing factors to the relationship between τ_3/τ_2 and the yield stress evolution rate. First, as with the lower temperature study, a larger τ_3/τ_2 allows the thermal history stored in the hereditary integral during aging to be remembered after the shear relaxation

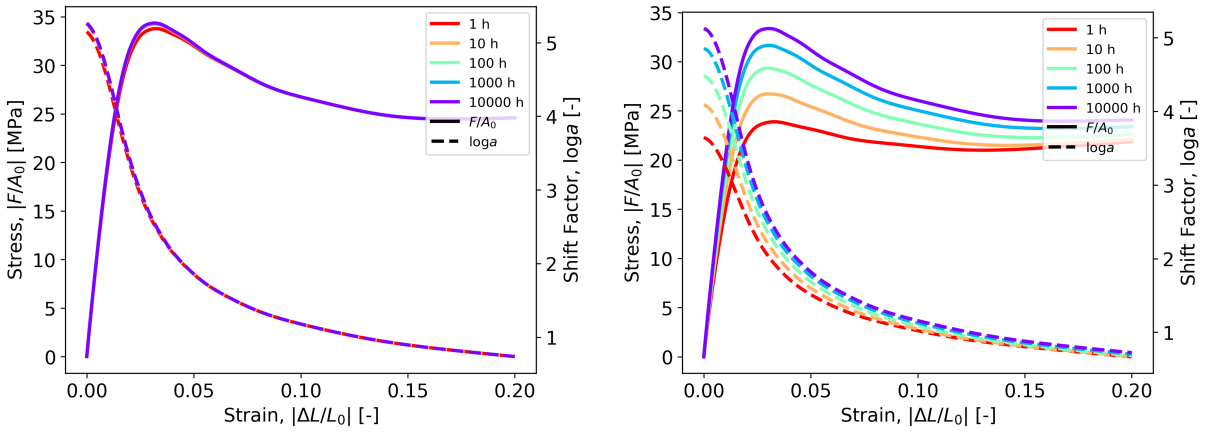

(a) $\tau_2 = 0.01\,\mathrm{s}$, $\tau_3/\tau_2 = 0.01$

(b) $\tau_2 = 0.01\,\mathrm{s}$, $\tau_3/\tau_2 = 100$

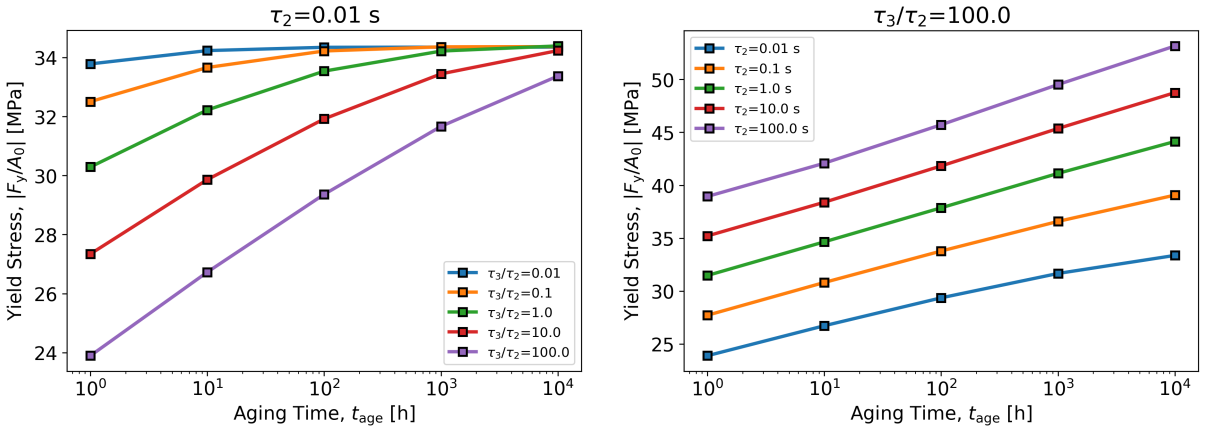

(c)

(d)

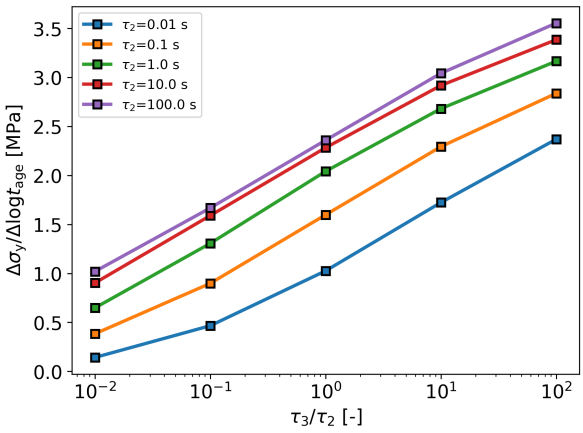

(e)

Figure 6-2. Stress-free yield stress evolution parameter study on τ_2 and τ_3/τ_2. The aging and loading temperatures are both $65\,^{\circ}\mathrm{C}$. Nominal parameters are listed in Table 6-2. (a) and (b) Effect of aging time on the stress and shift factor during loading for two different combinations of parameters. (c) Yield stress versus aging time organized by lines of constant τ_3/τ_2. (d) Yield stress versus aging time organized by lines of constant τ_2. (e) Secant slope of the yield stress versus the $\log$ of aging time from $0\,\mathrm{h}$ to $10000\,\mathrm{h}$ versus τ_3/τ_2.

function relaxes out when yielding occurs. Second, when τ_3/τ_2 is small, τ_3 is also smaller, so the material reaches equilibrium sooner. This is clear in Fig. 6-2(c), where the yield stress approaches 34 MPa for all five curves, but the 1 h aging condition starts closer to the equilibrium value when τ_3/τ_2 is smaller. This effect is also evident in Fig. 6-2(a), which shows an extremely small spread in the shift factor at the start of loading, since for this extremely short τ_3, equilibrium occurs almost immediatley during the aging period.

Next, the effects of C_4 and τ_3/τ_2 on the yield stress evolution rate were investigated for an aging temperature and loading temperature of 45 °C and the nominal parameters in Table 6-2. The results from this parameter study are shown in Fig. 6-3. Examples of stress–strain curves at different aging times are show in Figs. 6-3(a) and 6-3(b). Fig. 6-3(a) uses a smaller C_4 value and Fig. 6-3(a) uses a larger C_4 value. Accordingly, the $\log a$–strain curves for each aging time remain distinct much longer than in Fig. 6-1(a) than Fig. 6-3(b), since more shear strain is required to accelerate the clock to erase the thermal history accrued during aging. Plots of the yield stress versus aging time are shown for different values of τ_3/τ_2 in Fig. 6-3(c) and for different values of C_4 in Fig. 6-3(d). The secant slopes for all conditions are presented in Fig. 6-3(e), which reveal once again that yield stress evolution does not occur unless $\tau_3/\tau_2 > 1$. When $\tau_3/\tau_2 > 1$ is satisfied, lower values for C_4 result in a higher yield stress evolution rate.

Next, the effects of C_3 and τ_3/τ_2 on the yield stress evolution rate were investigated for an aging temperature and loading temperature of 45 °C and the nominal parameters in Table 6-2, except that the CTE parameters have been activated, so C_3 can influence the mechanical behavior, and $f_1(t) = f_3(t)$. The results from this parameter study are shown in Fig. 6-4. The parameter C_3 controls the effect of the volume strain on the material clock. In compression, the volume strain is negative, so C_3 slows down the material clock. Therefore, it is expected that C_3 will have the opposite effect as C_4. Examples of stress–strain curves at different aging times are show in Figs. 6-4(a) and 6-4(b). Fig. 6-4(a) uses a smaller C_3 value and Fig. 6-4(a) uses a larger C_3 value. The expected trends are apparent, showing that C_3 is in opposition to C_4 in compression; Figs. 6-4(a) and 6-4(b) show the thermal history from aging is erased at higher strains when C_3 is increased. Plots of the yield stress versus aging time are shown for different values of τ_3/τ_2 in Fig. 6-4(c) and for different values of C_3 in Fig. 6-4(d). The secant slopes for all conditions are presented in Fig. 6-4(e), which reveal once again that yield stress evolution does not occur unless $\tau_3/\tau_2 > 1$. When $\tau_3/\tau_2 > 1$ is satisfied, higher values for C_3 result in a higher yield stress evolution rate.

So far, the breadth of the relaxation functions have not been varied. However, the breadths of $f_2(t)$ and $f_3(t)$ are likely important, considering that the parameter studies thus far have indicated that yield stress evolution occurs when $f_2(t)$ is able to fully relax out before $f_3(t)$, at least for temperatures far away from the reference temperature. The results from a parameter study on β_2 and τ_3/τ_2 are shown in Fig. 6-5 and the results from a parameter study on β_3 and τ_3/τ_2 are shown in Fig. 6-6. Both investigations use an aging and loading temperature of 45 °C and the nominal parameters in Table 6-2. Now that the breadth of the relaxation functions are varied, the ratio of the characteristic times does not accurately determine which relaxation function will decay first. Therefore, for the studies using β_2 and β_3, the ratio of times required for a function to decay to a certain value are used. For a stretched exponential function with characteristic time τ_i and breadth

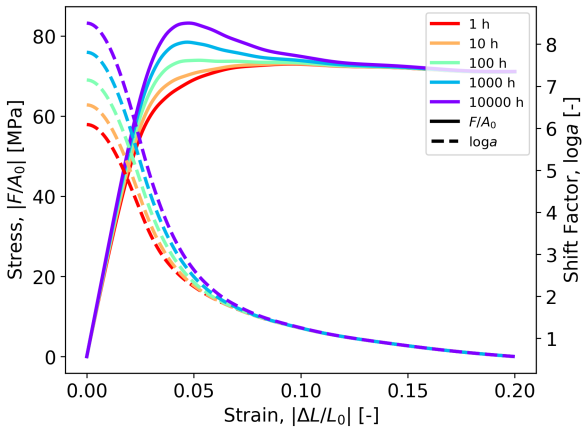

(a) $C_4 = 5000\,\mathrm{K}$, $\tau_3/\tau_2 = 100$

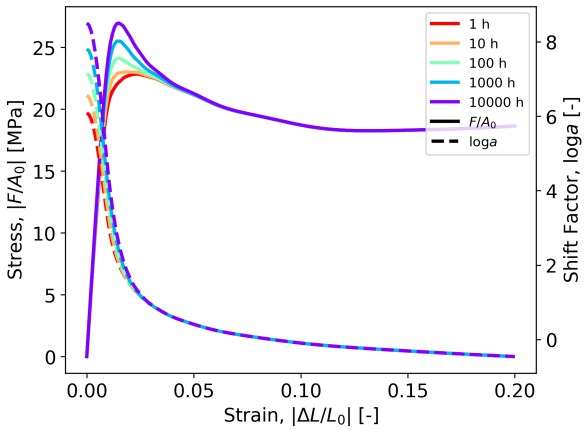

(b) $C_4 = 50000\,\mathrm{K}$, $\tau_3/\tau_2 = 100$

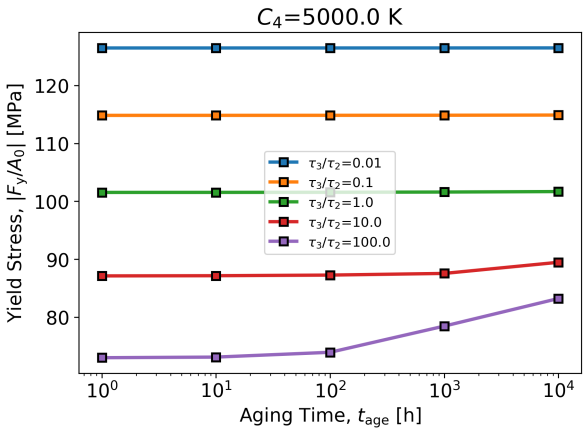

(c)

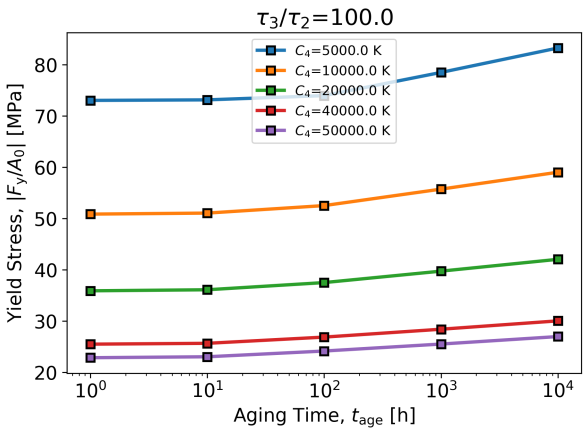

(d)

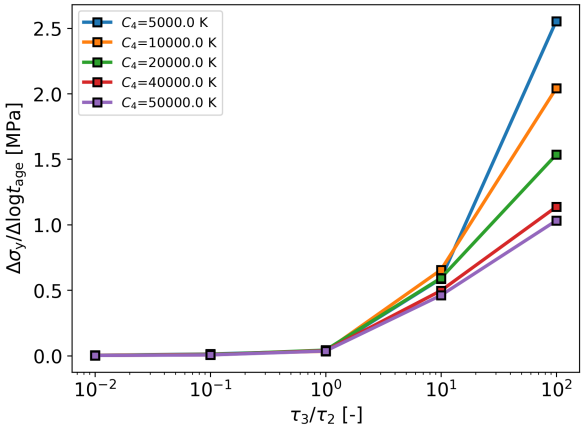

(e)

Figure 6-3. Stress-free yield stress evolution parameter study on C_4 and τ_3/τ_2. The aging and loading temperatures are both $45\,^{\circ}\mathrm{C}$. Nominal parameters are listed in Table 6-2. (a) and (b) Effect of aging time on the stress and shift factor during loading for two different combinations of parameters. (c) Yield stress versus aging time organized by lines of constant τ_3/τ_2. (d) Yield stress versus aging time organized by lines of constant C_4. (e) Secant slope of the yield stress versus the $\log$ of aging time from $0\,\mathrm{h}$ to $10000\,\mathrm{h}$ versus τ_3/τ_2.

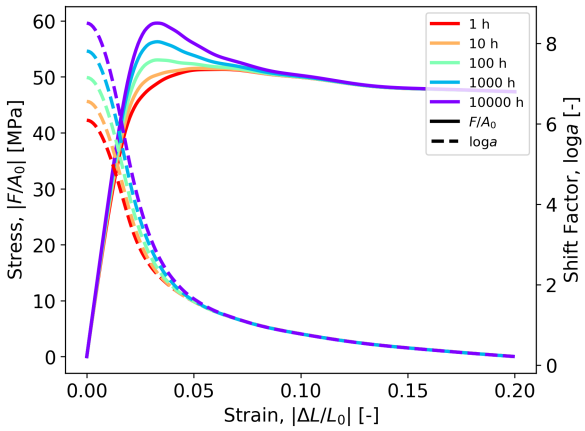

(a) $C_3 = 0\,\mathrm{K}$, $\tau_3/\tau_2 = 100$

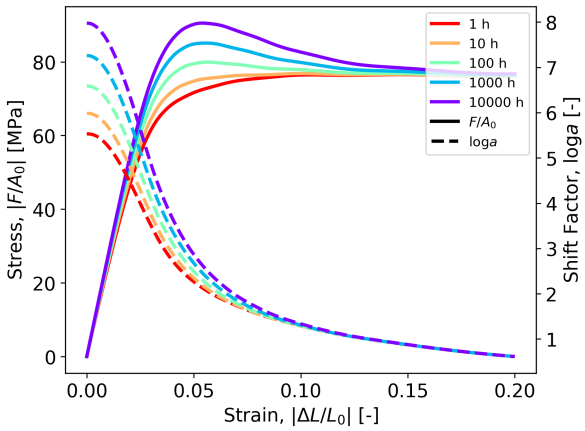

(b) $C_4 = 2000\,\mathrm{K}$, $\tau_3/\tau_2 = 100$

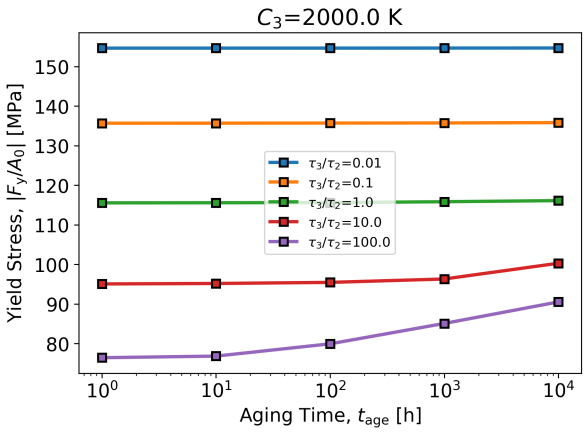

(c)

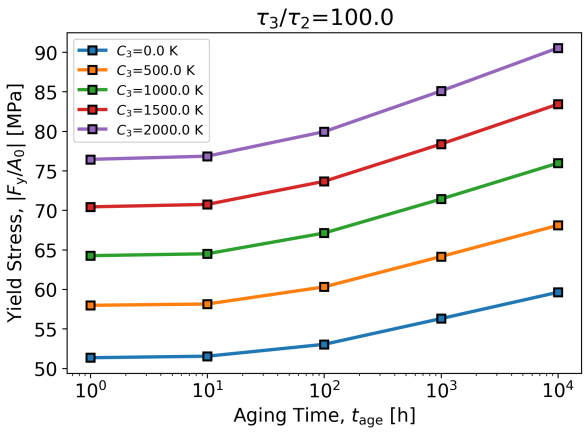

(d)

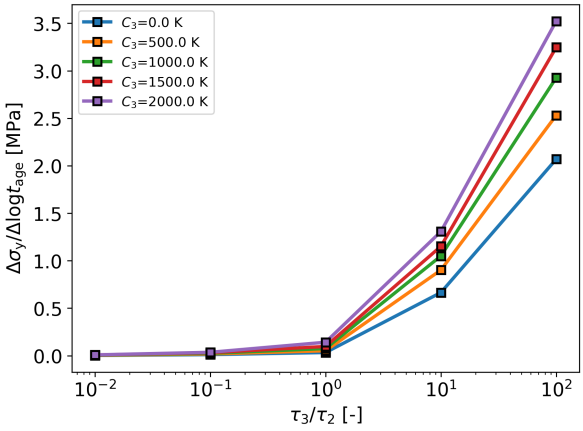

(e)

Figure 6-4. Stress-free yield stress evolution parameter study on C_3 and τ_3/τ_2. The aging and loading temperatures are both $45\,^{\circ}\mathrm{C}$. Nominal parameters are listed in Table 6-2, except CTE parameters have been activated, $\alpha_g^{\mathrm{ref}} = 200 \times 10^{-6}/\mathrm{K}$ and $\alpha_\infty^{\mathrm{ref}} = 600 \times 10^{-6}/\mathrm{K}$. (a) and (b) Effect of aging time on the stress and shift factor during loading for two different combinations of parameters. (c) Yield stress versus aging time organized by lines of constant τ_3/τ_2. (d) Yield stress versus aging time organized by lines of constant C_3. (e) Secant slope of the yield stress versus the $\log$ of aging time from $0\,\mathrm{h}$ to $10\,000\,\mathrm{h}$ versus τ_3/τ_2.

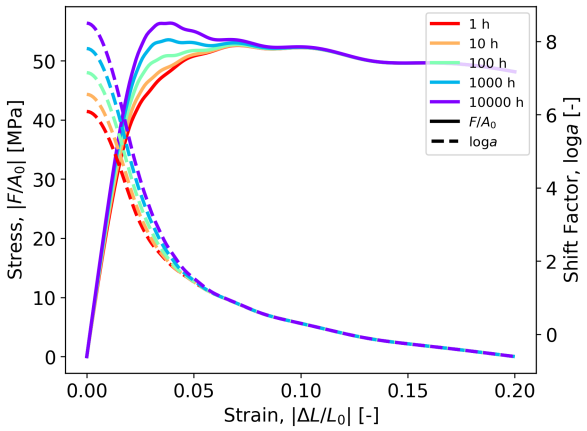

(a) $\beta_2 = 0.15$, $\tau_3/\tau_2 = 100$

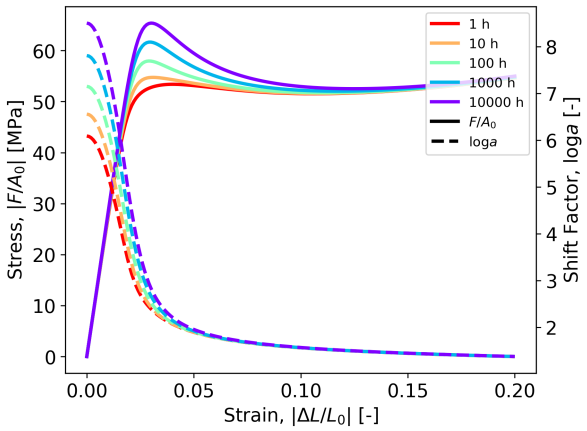

(b) $\beta_2 = 0.35$, $\tau_3/\tau_2 = 100$

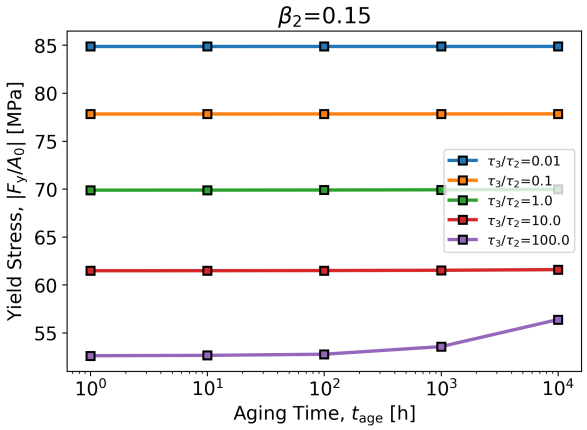

(c)

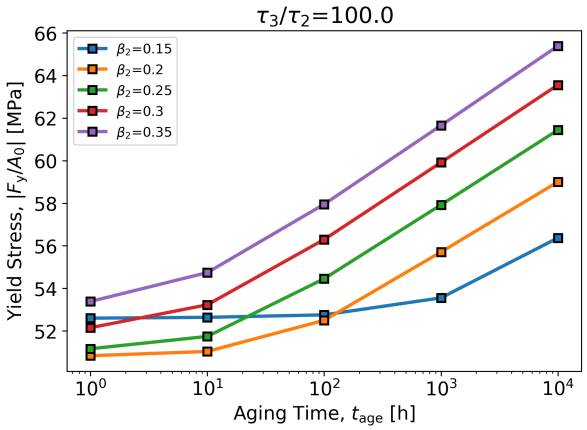

(d)

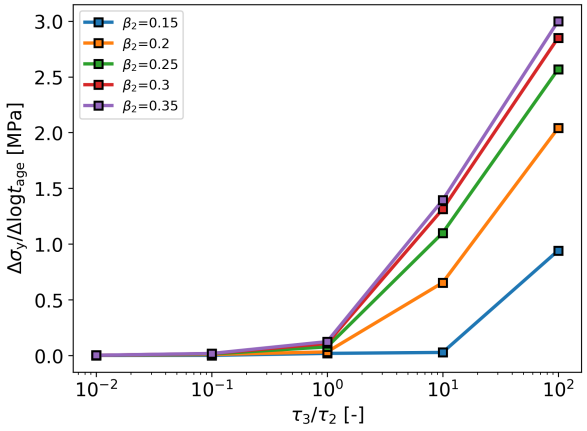

(e)

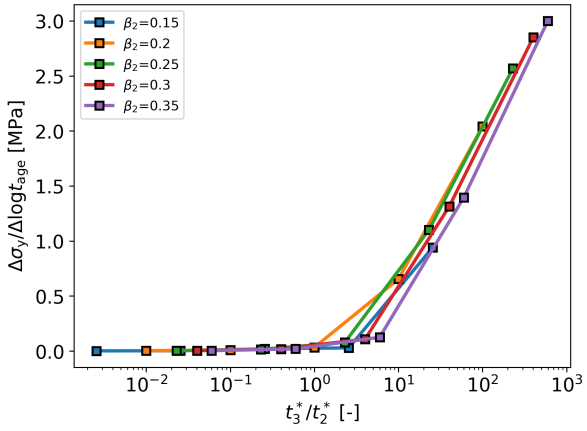

(f)

Figure 6-5. Stress-free yield stress evolution parameter study on β_2 and τ_3/τ_2. The aging and loading temperatures are both $45\,^{\circ}\mathrm{C}$. Nominal parameters are listed in Table 6-2. (a) and (b) Effect of aging time on the stress and shift factor during loading for two different combinations of parameters. (c) Yield stress versus aging time organized by lines of constant τ_3/τ_2. (d) Yield stress versus aging time organized by lines of constant β_2. (e) Secant slope of the yield stress versus the log of aging time from $0\,\mathrm{h}$ to $10000\,\mathrm{h}$ versus τ_3/τ_2. (f) Secant slope versus the ratio of times for a relaxation function to decay to $10\,\%$, t_3^*/t_2^*.

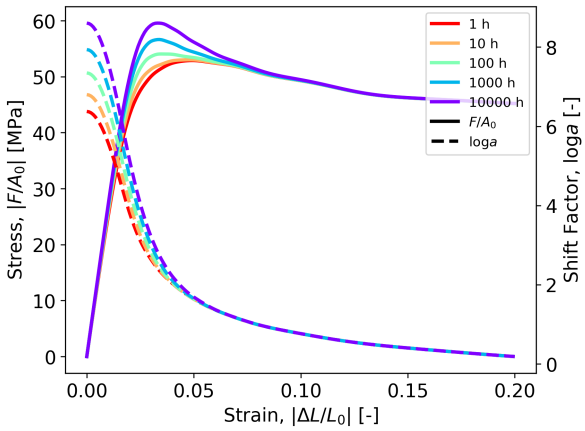

(a) $\beta_3 = 0.15$, $\tau_3/\tau_2 = 100$

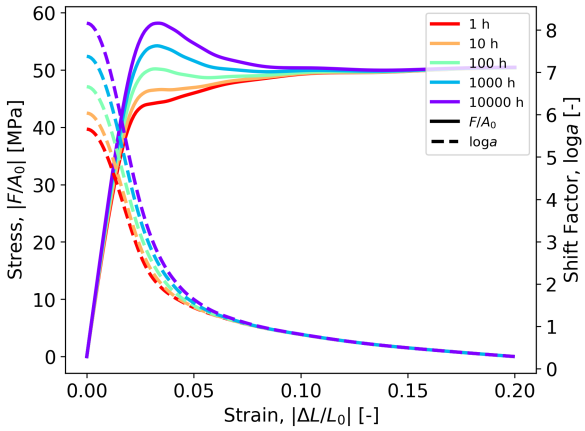

(b) $\beta_3 = 0.35$, $\tau_3/\tau_2 = 100$

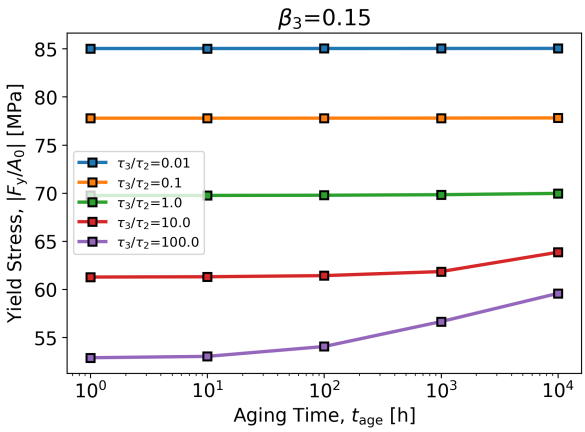

(c)

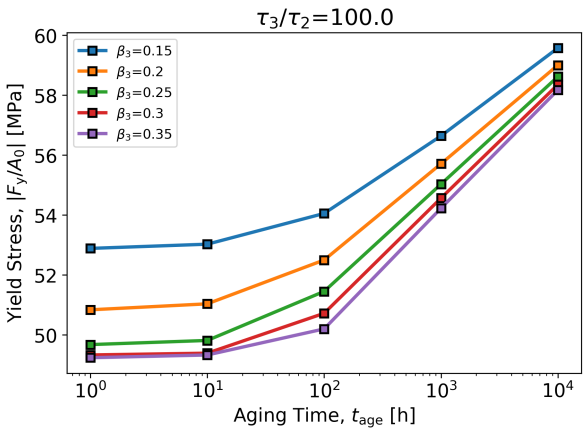

(d)

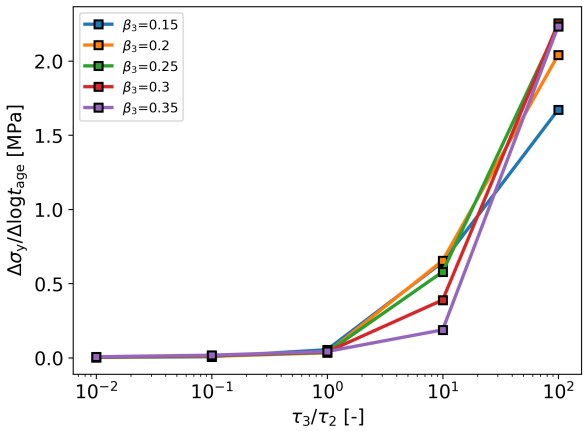

(e)

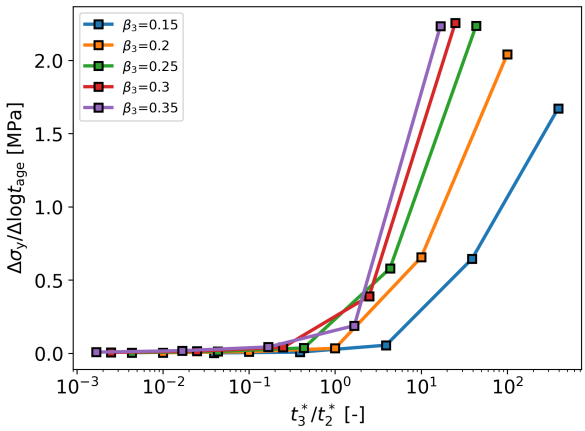

(f)

Figure 6-6. Stress-free yield stress evolution parameter study on β_3 and τ_3/τ_2. The aging and loading temperatures are both $45\,^{\circ}\mathrm{C}$. Nominal parameters are listed in Table 6-2. (a) and (b) Effect of aging time on the stress and shift factor during loading for two different combinations of parameters. (c) Yield stress versus aging time organized by lines of constant τ_3/τ_2. (d) Yield stress versus aging time organized by lines of constant β_3. (e) Secant slope of the yield stress versus the log of aging time from $0\,\mathrm{h}$ to $10000\,\mathrm{h}$ versus τ_3/τ_2. (f) Secant slope versus the ratio of times for a relaxation function to decay to $10\,\%$, t_3^*/t_2^*.

β_i, it will decay to a value c at time t_i^*;

$$t_i^* = -\tau_i (\ln c)^{\frac{1}{\beta_i}} . \tag{6.1}$$

As a metric for which relaxation function relaxes-out first, compare the ratio of the times for the thermal-volumetric and shear functions to relax to 0.1 (the choice of 0.1 is somewhat arbitrary);

$$\frac{t_3^*}{t_2^*} = -\frac{\tau_3}{\tau_2} (\ln 0.1)^{\frac{1}{\beta_3} - \frac{1}{\beta_2}} . \tag{6.2}$$

When comparing the yield stress evolution rate versus t_3^*/t_2^* for the study on β_2 in Fig. 6-5(f) and β_3 in Fig. 6-6(f), it is apparent that which relaxation function relaxes-out first is still important to predicting a non-zero yield stress evolution rate, as $t_3^*/t_2^* < 1$ shows no physical aging.

Studies using the two-function parameterization clearly show that $f_3(t)$ must relax-out after $f_2(t)$ for yield stress evolution to occur at temperatures deep into the glass. Next, the parameter studies are expanded to investigate the three-function parameterization in Table 6-3. Additionally, the parameter studies will now explore up to $\tau_3/\tau_2 = 1000$, which is approximately the ratio calibrated from the DSC-focused approaches in Chapters 4 and 5. In the first parameter study using the three-spectrum parameterization, τ_1/τ_2 and τ_3/τ_2 are investigated at $\theta_{\text{age}} = \theta_{\text{load}}$, but the CTEs are deactivated. With the CTEs set to zero, $f_1(t)$ only influences the mechanical behavior during the loading step. The results from this parameter study are shown in Fig. 6-7. This study indicates that τ_1/τ_2 is irrelevant to the yield stress evolution rate, and $\tau_3/\tau_2 > 1$ is necessary for a non-zero yield stress evolution rate. A follow-up parameter study, shown in Fig. 6-8, repeats the same conditions as Fig. 6-7 except that the CTEs are activated using the nominal values listed in Table 6-3. When the CTEs are on, a non-zero yield stress evolution rate is seen for $\tau_3/\tau_2 < 1$, provided that $\tau_1/\tau_2 > 1$. To check the robustness of these results, the study on τ_1/τ_2 and τ_3/τ_2 is repeated for 35 °C in Fig. 6-9. With non-zero values for the CTEs and C_3, the memory of aging can be stored either through the temperature hereditary integral in the material clock, associated with $f_3(t)$, or the volume strain hereditary integral in the material clock, associated with $f_1(t)$. As long as either $\tau_1/\tau_2 > 1$ or $\tau_3/\tau_2 > 1$, then some memory of aging survives after yield, which allows the yield stress to grow with the aging time. After the yield stress evolution is activated by either $\tau_1/\tau_2 > 1$ or $\tau_3/\tau_2 > 1$, it continues to increase with increases to either ratio.

6.2. Discussion Regarding Parameter Relationships and the Different Calibration Procedures

In Section 6.1, parameter studies revealed important relationships between parameters for predicting yield stress evolution. It was found that either $\tau_1/\tau_2 > 1$ or $\tau_3/\tau_2 > 1$ must be true for the yield stress to evolve under stress-free aging. Furthermore, increasing either τ_1/τ_2 or τ_3/τ_2 beyond unity increases the rate of change of the yield stress per log of the aging time. These ratios are important because relaxation functions must relax-out in a certain order for yield stress evolution to occur. The "memory" of stress-free aging is stored in the thermal history hereditary integral associated with $f_3(t)$, or the volume strain history (if the CTEs are non-zero) associated with $f_1(t)$. The thermal history hereditary integral is essential to the material clock, and the

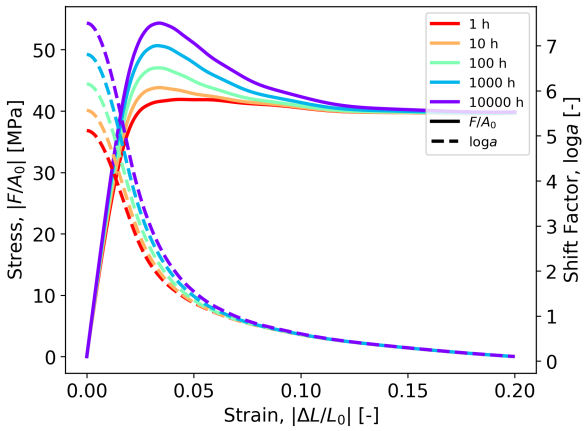

(a) $\tau_1/\tau_2 = 0.01$, $\tau_3/\tau_2 = 1000$

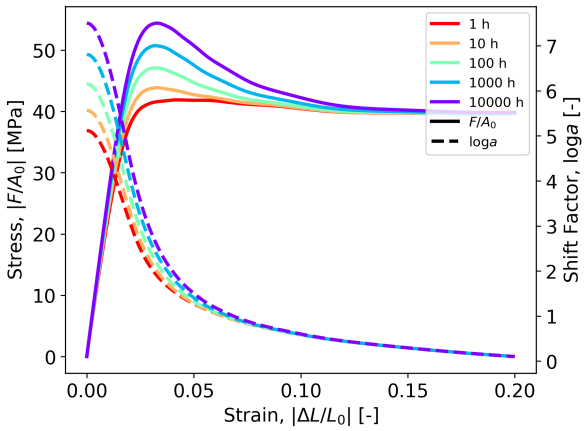

(b) $\tau_1/\tau_2 = 100$, $\tau_3/\tau_2 = 1000$

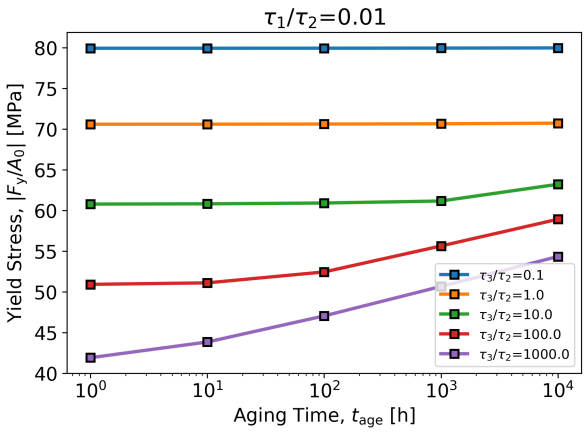

(c)

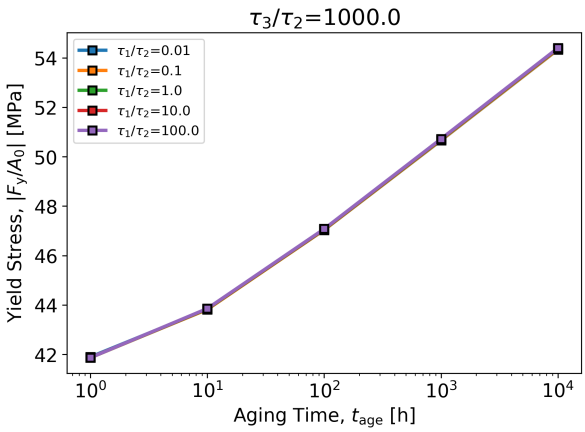

(d)

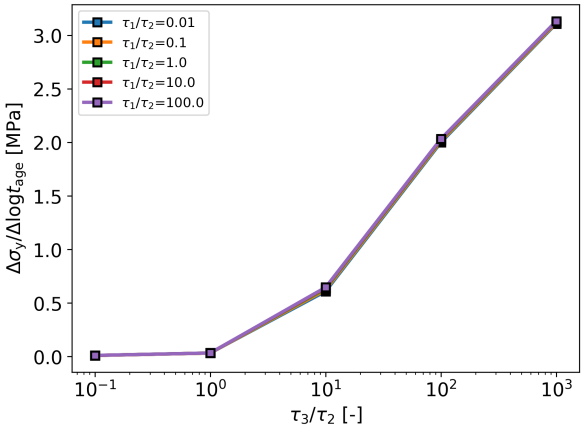

(e)

Figure 6-7. Stress-free yield stress evolution parameter study on τ_1/τ_2 and τ_3/τ_2. The aging and loading temperatures are both $45\,^{\circ}\mathrm{C}$. Nominal parameters are listed in Table 6-3, except that CTE parameters have been deactivated, $\alpha_g^{\mathrm{ref}} = \alpha_\infty^{\mathrm{ref}} = 0$. (a) and (b) Effect of aging time on the stress and shift factor during loading for two different combinations of parameters. (c) Yield stress versus aging time organized by lines of constant τ_1/τ_2. (d) Yield stress versus aging time organized by lines of constant τ_2. (e) Secant slope of the yield stress versus the $\log$ of aging time from $0\,\mathrm{h}$ to $10\,000\,\mathrm{h}$ versus τ_3/τ_2.

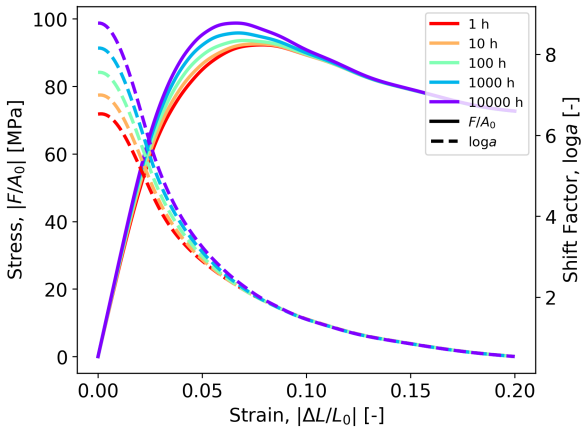

(a) $\tau_1/\tau_2 = 0.01$, $\tau_3/\tau_2 = 1000$

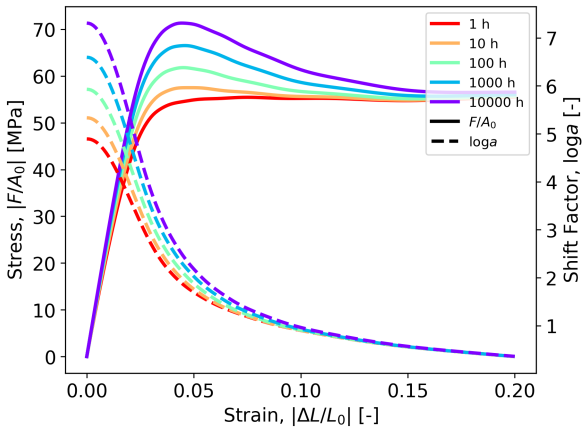

(b) $\tau_1/\tau_2 = 100$, $\tau_3/\tau_2 = 1000$

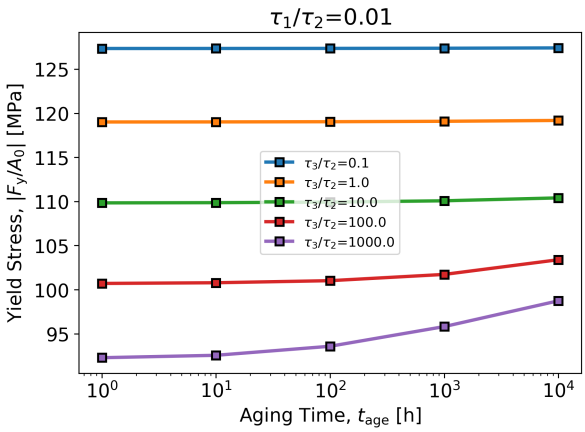

(c)

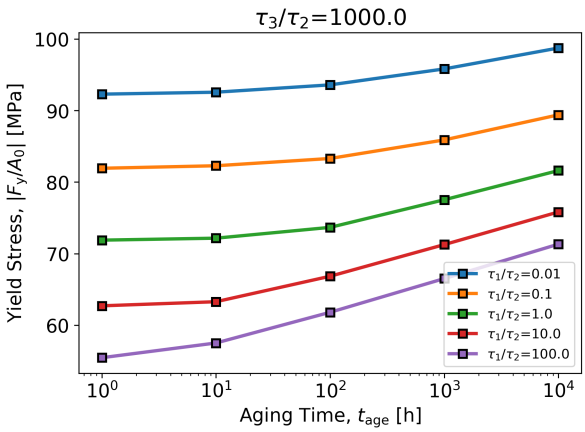

(d)

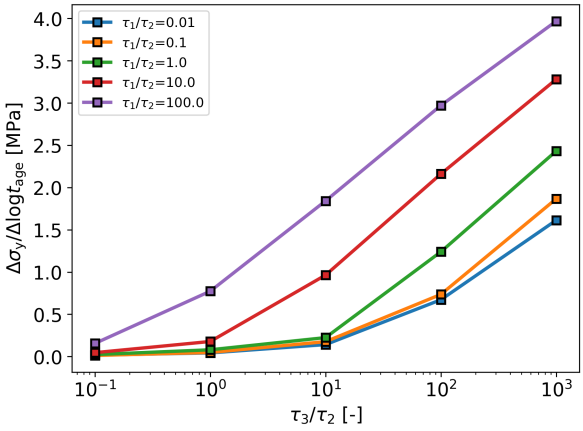

(e)

Figure 6-8. Stress-free yield stress evolution parameter study on τ_1/τ_2 and τ_3/τ_2. The aging and loading temperatures are both $45\,^{\circ}\mathrm{C}$. Nominal parameters are listed in Table 6-3. (a) and (b) Effect of aging time on the stress and shift factor during loading for two different combinations of parameters. (c) Yield stress versus aging time organized by lines of constant τ_1/τ_2. (d) Yield stress versus aging time organized by lines of constant τ_2. (e) Secant slope of the yield stress versus the $\log$ of aging time from $0\,\mathrm{h}$ to $10\,000\,\mathrm{h}$ versus τ_3/τ_2.

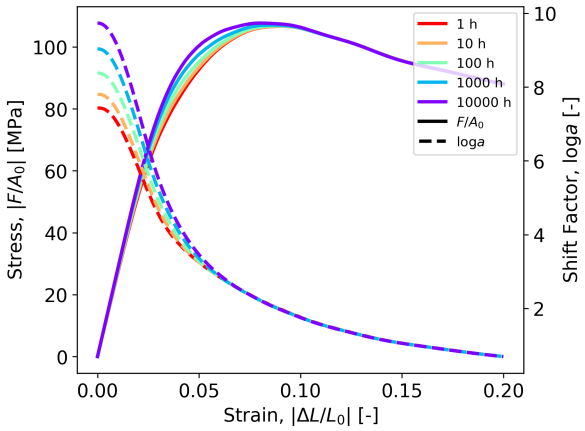

(a) $\tau_1/\tau_2 = 0.01$, $\tau_3/\tau_2 = 1000$

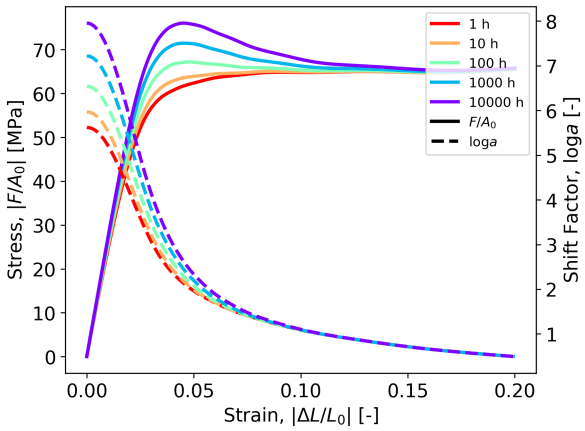

(b) $\tau_1/\tau_2 = 100$, $\tau_3/\tau_2 = 1000$

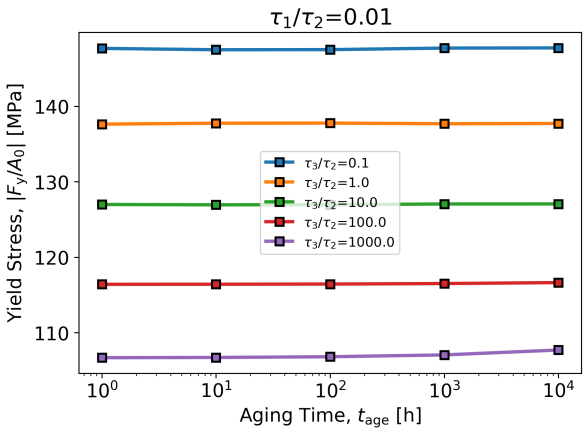

(c)

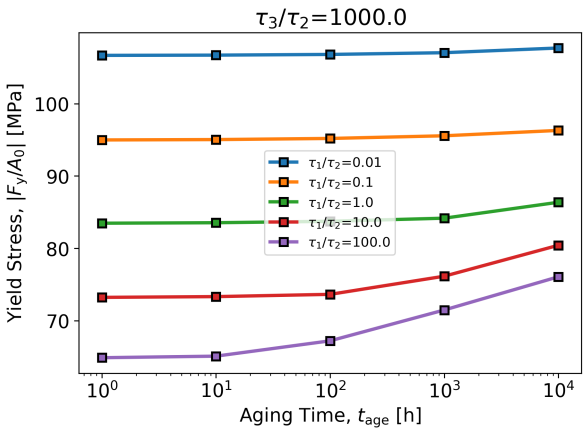

(d)

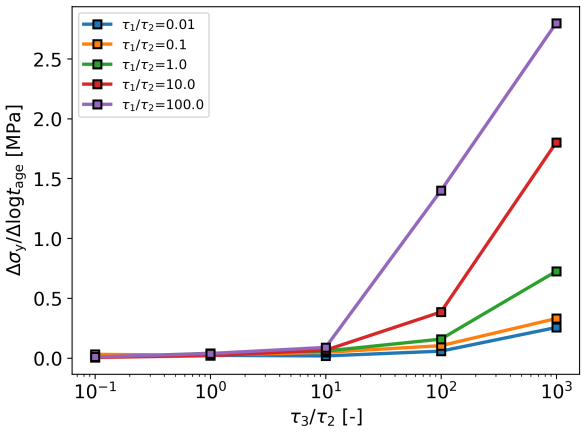

(e)

Figure 6-9. Stress-free yield stress evolution parameter study on τ_1/τ_2 and τ_3/τ_2. The aging and loading temperatures are both $35\,^{\circ}\mathrm{C}$. Nominal parameters are listed in Table 6-3. (a) and (b) Effect of aging time on the stress and shift factor during loading for two different combinations of parameters. (c) Yield stress versus aging time organized by lines of constant τ_1/τ_2. (d) Yield stress versus aging time organized by lines of constant τ_2. (e) Secant slope of the yield stress versus the $\log$ of aging time from $0\,\mathrm{h}$ to $10\,000\,\mathrm{h}$ versus τ_3/τ_2.

Experiment	T403 TMA	T403 Comp	T403 DSC	DEA TMA	DEA Comp	DEA DSC
TMA	1	3	2	1	3	2
Compression, No aging	3	1	2	3	1	2
Compression, No-load aging	3	2	1	2	3	1
Linear Creep				1	2	3
Compression, Aging with Load				1	3	2
DSC, cool rates	3	1	2	2	3	1
DSC, aging	3	1	2	3	2	1
SUM	**13**	**8**	**9**	**13**	**17**	**12**
BOTH MATERIALS	**26**	**25**	**21**			

Figure 6-10. Qualitative ranksings of different calibration procedures for 828T403 and 828DEA across available data.

importance of the volume strain history to the material clock scales with C_3. If both $f_1(t)$ and $f_3(t)$ relax-out faster than $f_2(t)$, then deformation leading up to yielding erases the thermomechanical history of aging before yield occurs, and thus aging can have no effect on the observed yield stress. There are two caveats to the importance of these characteristic time ratios. The first is that τ_3/τ_2 is not sufficient to describe which relaxation function will relax-out first if their breadths (β_i) are significantly different. If β_3 and β_2 are too different, then another metric is needed to describe which function relaxes-out first. In Section 6.1, the time required for the function to decay to 0.1 was used, although this measure was somewhat arbitrarily chosen and the robustness of the metric is untested. The second caveat is that when the material is aged near equilibrium, it is possible for aging to occur when $\tau_3/\tau_2 < 1$, although the change is small and increasing τ_3/τ_2 increases the yield stress evolution rate. In this section, the relationships that promote physical aging that were uncovered by the parameter studies are discussed within the context of the three calibration procedures executed in Chapters 4 and 5.

We first rank the three calibration procedures, across all fittings and predictions, for each material in order to establish which ones did best. In Fig. 6-10, the calibration procedures are ranked as either first, second, or third best. These rankings are qualitative and open to interpretation. Here, for example, compression comparisons focused on yield strength comparisons, and DSC predictions focused on peak heat capacity and glass transition onset.

For T403, the compression- and DSC-focused approaches produce the best fit across the suite of experimental data, while for 828DEA the baseline (TMA-focused) and DSC-focused approaches produce the best fit. For both materials, the DSC-focused is either the best or a close second. Since the DSC-focused approach performs reasonably well for both materials, we recommended this approach for future model calibration efforts.

Given that the DSC-focused procedure performed well for both 828T403 and 828DEA, it is especially important to discuss in the context of the parameter studies presented in this chapter. All stretched exponential parameters from the DSC-focused approach for both materials in Table 6-4. Table 6-4 also lists the characteristic times normalized by the shear characteristic time

Table 6-4. Comparison of stretched exponential function parameters obtained from the DSC-focused calibration for 828T403 and 828DEA.

Parameter	828T403	828DEA	Units
τ_1	0.835	41.0	s
β_1	0.25	0.26	
τ_2	0.0186	1.25	s
β_2	0.21	0.23	
$\tau_3 = \tau_4$	17.6	890.	s
$\beta_3 = \beta_4$	0.21	0.22	
τ_1/τ_2	45	33	
$\tau_3/\tau_2 = \tau_4/\tau_2$	946	712	

for that material. Relaxation functions for both materials are plotted in Fig. 6-11(a). Since the parameter studies show that ratios of τ_i/τ_2 are important for yield stress evolution, Fig. 6-11(b) plots relaxation functions relative to the shear relaxation, i.e. their argument is normalize by the shear characteristic time, $f_i(t/\tau_2)$, which is equivalent to plotting a relaxation function with τ_i/τ_2 and β_i. For both 828T403 and 828DEA, the relationships between the relaxation functions are nearly identical; $\tau_1/\tau_2 \approx 50$ and $\tau_3/\tau_2 \approx 1000$, see Table 6-4. For the DSC-focused approach, all β_i are nearly the same (0.21 to 0.26), so comparing ratios of the characteristic times are appropriate. The relaxation functions exhibit a clear ordering across both materials. From shortest to longest, $f_2(t)$, $f_1(t)$, $f_3(t) = f_4(t)$. This ordering is in accord with what the parameter studies suggest is important for yield stress evolution, which is that $f_3(t)$ and $f_1(t)$ should both be bigger than $f_2(t)$, but $f_3(t)$ is likely more important. Given this, it is not surprising that the best predictions of the stress-free yield stress evolution come from the DSC-focused calibration. Unfortunately, this ordering is in conflict with the order expected in the literature. The bulk relaxation function $f_1(t)$ is shorter than the shear relaxation function $f_2(t)$ [20], but the thermal relaxation function $f_4(t)$ is potentially longer than the shear relaxation function [27]. If it is taken for granted that $f_4(t)$ should replace $f_3(t)$ in the thermal hereditary integral in the clock, then the only conflict between the relaxation functions in the DSC-focused approach and those expected by the literature is that $f_1(t)$ should be shorter than $f_2(t)$. Although $f_1(t)$ being longer than $f_2(t)$ promotes yield stress evolution, it is possible for yield stress evolution to occur if $f_1(t)$ is shorter than $f_2(t)$, provided that $f_3(t) = f_4(t)$ is still longer than $f_2(t)$, see Fig. 6-8. Recall that $f_1(t)$ in the DSC-focused approach is fit to the CTE transition during a TMA experiment, and so was not directly measured. A parameterization that utilized a direct measurement of $f_1(t)$ would help resolve the discrepancy between the ordering of relaxation functions found the by the DSC-focused approach and the ordering expected by the literature.

The relaxation function parameters for the baseline calibration (TMA-focused) are listed in Table 6-5. Plots of the relaxation functions and relative relaxation functions for the baseline calibration shown in Fig. 6-12. For the baseline calibration, $f_1(t) = f_3(t)$ are fit to a TMA experiment. The relative relaxation functions for $f_1(t) = f_3(t)$ are similar for both experiments. In contrast, the relative relaxation functions for $f_4(t)$ look noticably different; although they have

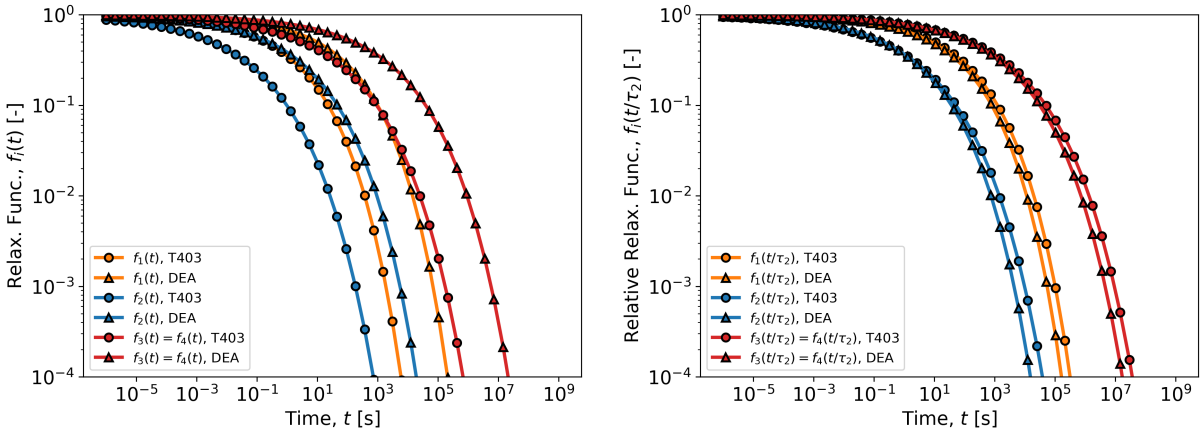

(a) Relaxation functions

(b) Relative relaxation functions

Figure 6-11. Comparison of (a) relaxation functions and (b) relaxation functions relative to the shear characteristic time τ_2, obtained from the DSC-focused calibration procedures for 828T403 and 828DEA.

similar ratios of τ_4/τ_2, the 828DEA calibration is much narrower than the other relaxation functions. The literature suggests that the heat capacity relaxation function drives the thermal history of the shift factor [3]. Since, in the baseline calibration approach, $f_4(t)$ was fit while using $f_3(t)$ to drive the thermal history in the shift factor, the thermal relaxation function may be altered by the baseline calibration process, i.e. the $f_4(t)$ from the baseline calibration may not be physically meaningful. This may explain why the (relative) $f_4(t)$ from the baseline calibrations are much more different in each material than they are for the DSC-focused process. Overall, this process does not fit the calibration data as well as the DSC-focused process, nor does it predict physical aging for either material.

The relaxation function parameters for the compression-focused calibration are listed in Table 6-6. Plots of the relaxation functions and relative relaxation functions for the compression-focused calibration shown in Fig. 6-13. The compression focused calibration process found very different parameterization spaces for 828DEA and 828T403 suggesting that the overall staged optimization compression-oriented approach does not have the sensitivity to uniquely identify parameters. Therefore, this method may produce very different responses based on the input data. For 828T403, the compression-focused calibration found a very long $f_3(t)$, and therefore predicted yield stress evolution fairly well given the high τ_3/τ_2. On the other hand, for 828DEA, the compression-focused found a short $f_3(t)$ with $\tau_3/\tau_2 \approx 1$. Accordingly, the rate of the yield stress evolution was much lower than experimental data.

The parameter studies on stress-free aging followed by compression through yield indicate that a large τ_3/τ_2 or τ_1/τ_2 increase the rate of yield stress evolution with the log of the aging time and if both ratios drop below unity, then no yield stress evolution occurs with stress-free aging, at least when the model simulates aging at temperatures deep in the glass. These findings are consistent with the predictions from the baseline, compression-focused, and DSC-focused calibrations for both 828403 and 828DEA. Additionally, the best calibration procedure, the DSC-focused,

Table 6-5. Comparison of stretched exponential function parameters obtained from the baseline (TMA-focused) calibration for 828T403 and 828DEA.

Parameter	828T403	828DEA	Units
$\tau_1 = \tau_3$	0.835	41.0	s
$\beta_1 = \beta_3$	0.25	0.26	
τ_2	0.0186	1.25	s
β_2	0.21	0.23	
τ_4	0.132	6.80	s
β_4	0.22	0.36	
$\tau_1/\tau_2 = \tau_3/\tau_2$	45	33	
τ_4/τ_2	7	5	

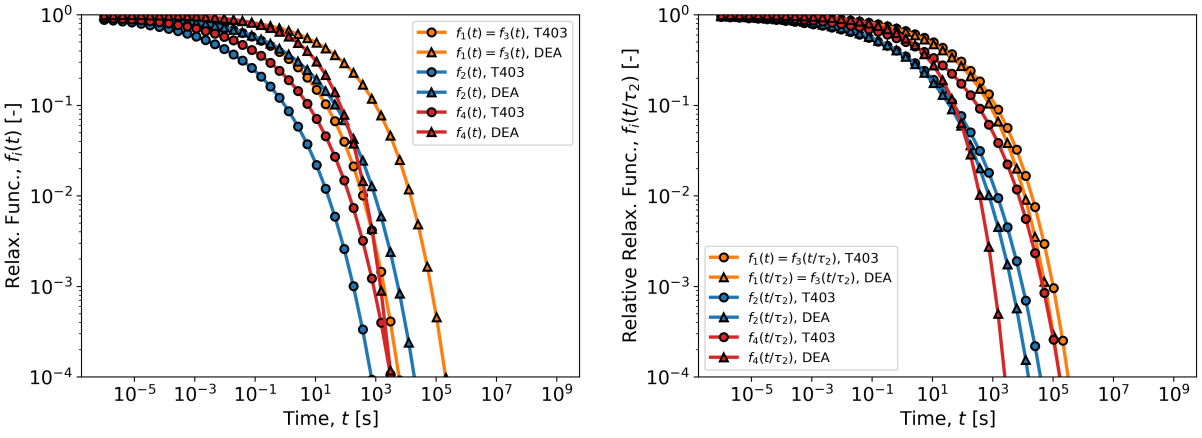

(a) Relaxation functions

(b) Relative relaxation functions

Figure 6-12. Comparison of (a) relaxation functions and (b) relaxation functions relative to the shear characteristic time τ_2, obtained from the baseline (TMA-focused) calibration procedures for 828T403 and 828DEA.

Table 6-6. Comparison of stretched exponential function parameters obtained from the compression-focused calibration for 828T403 and 828DEA.

Parameter	828T403	828DEA	Units
$\tau_1 = \tau_3$	129	1.42	s
$\beta_1 = \beta_3$	0.15	0.27	
τ_2	0.0186	1.25	s
β_2	0.21	0.23	
τ_4	49.8	15.8	s
β_4	0.67	0.34	
$\tau_1/\tau_2 = \tau_3/\tau_2$	6935	1.1	
τ_4/τ_2	2667	13	

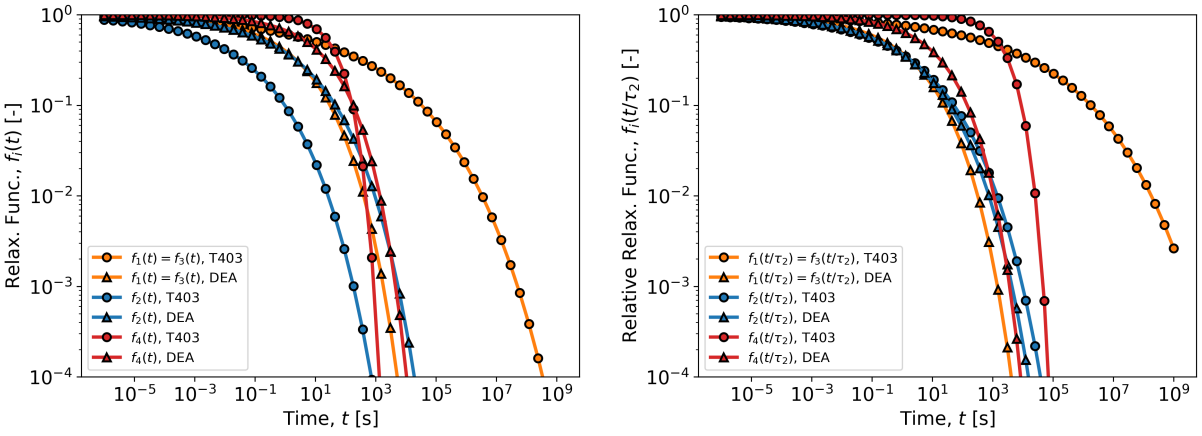

(a) Relaxation functions

(b) Relative relaxation functions

Figure 6-13. Comparison of (a) relaxation functions and (b) relaxation functions relative to the shear characteristic time τ_2, obtained from the compression-focused calibration procedures for 828T403 and 828DEA.

produced similar relationships between relaxation functions in both materials; $\tau_1/\tau_2 \approx 50$ and $\tau_3/\tau_2 \approx 1000$, both of which are greater than unity. However, these relationships are in conflict with the literature, which suggests that the bulk relaxation function should be shorter than the shear relaxation function, $\tau_1/\tau_2 < 1$.

7. CONCLUSION

Both a briefing of the main findings are laid and an assessment of the `spectacular` model's ability to predict physical aging are given in Section 7.1. Remaining gaps and proposed future work are discussed in Section 7.2. Finally, milestone completion evidence is summarized in Section 7.3.

7.1. Summary of the Main Findings and Assessment of the Capability to Predict Physical Aging

7.1.1. Summary of Main Findings

1. A qualitative ranking of the different calibration procedures (shown in Fig. 6-10) determined that the DSC-focused procedure was the best for 828DEA and second best for 828T403, making it the most reliable overall calibration procedure.

2. For the DSC-focused calibration for both materials, relaxation functions normalized by the shear characteristic relaxation time, $f_i(t/\tau_2)$, are nearly identical for both materials (Fig. 6-11). The same finding does not hold for the other two calibration procedures (Figs. 6-12 and 6-13).

3. Parameter studies for stress-free aging followed by compression through yield indicate that $\tau_2 < \tau_1 < \tau_3 = \tau_4$ is best for predicting yield stress evolution. This finding is in agreement with the ordering of characteristic relaxation times found by the DSC-focused approach (Fig. 6-1).

4. At 30 °C below Tg, the stress-free aging parameter studies also found that if both τ_1/τ_2 and τ_3/τ_2 are less than unity, then the yield stress does not evolve after stress-free aging. The aging history is stored in $f_3(t)$ via the thermal history and $f_1(t)$ via the volume strain history (and scaled by C_3). When the material compresses, the shear strain accelerates the material clock through C_4. When this happens, if both $f_1(t)$ and $f_3(t)$ are shorter than $f_2(t)$, then the aging history is erased before yield. See Figure 6-1 for the case where $\tau_1 = \tau_3$ and Figure 6-8 for the cases where τ_1 is not equal to τ_3.

5. Near the glass transition, stress-free aging parameter studies showed that yield strength evolution is possible when τ_1/τ_2 and τ_3/τ_2 are both less than unity, although the rate of yield strength evolution with aging time clearly increases with both characteristic time ratios, see Fig. 6-2.

6. The heat capacity relaxation function, $f_4(t)$, should be driving the temperature history in the material clock in the SPECTACULAR model. Our evidence is two fold. First the DSC-focused calibrations used $f_3(t) = f_4(t)$ (essentially placing $f_4(t)$ into the thermal hereditary integral), and this approach was reliably accurate accross both materials, while the other two methods for calibrating $f_3(t)$ only performed well on one material. Second, in the original formulation of the SPEC model, the thermal hereditary integral in the material clock is multiplied by a heat capacity term, suggesting that the thermal hereditary integral should use the heat capacity relaxation function in a four-spectrum model. See Equation (16) in [4].

7. In conjunction with the previous finding, DSC measurements are important for calibrating the SPEC model to predict a wide range of physical aging responses.

8. If $f_1(t)$ is distinct from $f_3(t)$, then $f_3(t)$ has a stronger influence on the temperature dependence of the compressive yield stress than $f_1(t)$. See Section 4.1.6. Bulk moduli were borrowed in this work and should be re-measured.

9. If $f_4(t)$ is distinct from $f_3(t)$, then $f_3(t)$ has a stronger influence on the heat capacity transition during a stress-free temperature sweep. See Section 5.1.6.

10. The best ordering of the characteristic relaxation times found from parameter studies and the DSC-focused calibration, $\tau_2 < \tau_1 < \tau_3 = \tau_4$, are in conflict with the literature [20, 27], which suggests $\tau_1 < \tau_2 < \tau_4$. Direct measurements of $f_1(t)$ would be helpful for resolving this apparent conflict.

11. Efforts to determine C_3 from tension–compression asymmetry of yield identified C_3 values significantly smaller than in past work. Direct measurements of C_3 are needed. C_3 was borrowed in this work.

7.1.2. What Physical Aging Behavior Can the SPEC Model Predict Today?

For the DSC-focused calibration, the spectacular model is good at fitting and/or predicting the following experiments, but some issues persist:

1. The thermal strain during a stress-free temperature sweep in a TMA experiment.

2. The (unaged) heat capacity during a stress-free temperature sweep in a DSC experiment. It can also predict small amounts of enthalpy recovery (which manifests as a heat capacity spike) that occur during heating after the material is slowly cooled into the glass. This result is very clear for 828DEA, see Fig. 5-31. For 828T403, the transition predicted by the DSC-focused calibration is too broad, but the heat capacity spike is not overly high as in the baseline calibration approach, see Fig. 4-27.

3. For the yield stress after isothermal stress-free aging well below Tg, predictions of the yield stress qualitatively agree over most timescales, see Fig. 4-23. Near Tg, the model does not correctly equilibriate, as discussed in the sub-Tg equilibrium gap.

4. For isothermal aging under load followed by compression through yield, the nominal yield stress versus aging time is accurately predicted (with 15 % error for the conditions studied here), even if the strain at the end of loading is off by around a factor of two.

5. The temperature dependence of the yield stress in glassy compression was not always accurate. For 828T403, temperature dependence could be improved by optimizing $f_3(t)$ to match the yield stress in glassy compression (see Section **??**) but doing so decreased the quality of the CTE transition during a stress-free temperature sweep (see Fig. 4-16). For 828DEA, all three calibration approaches produced reasonable fits for the temperature dependence of the yield stress.

6. The strain-rate dependence of the yield stress in glassy compression was accurate at high tempertures, but not at low temperatures. Typically, the model fits predicted a yield slope of yield stress versus the log of the strain rate that was constant with temperature, but experiments showed an increased slope at $-50\,^{\circ}\mathrm{C}$. In general, the strain-rate dependence in glassy compression is not well understood.

7. Predicting the shape of the stress–strain curve. Simulations here, which assumed homogenous motion and ignored self-heating, generally produce a yield strain that is much higher than what is experimentally observed.

8. When C_3 is measured from the pressure dependence of Tg, tension–compression asymmetry can be predicted, see Figure 5-6 where C_3 was borrowed from Ref. [4]. However, efforts to use tension–compression asymmetry were unsuccesful in identifying confidently the C_3 parameter for 828DEA, see Appendix B.

For the DSC-focused calibration, the `spectacular` model is unreliable for fitting and/or predicting the following experiments:

1. The linear creep response. Both the model and experiments show linear viscoelastic behavior (common creep compliance curves at different stresses). But, the model is more compliant than the experiments for the conditions studied here, see Fig. 5-25(d). Note, the baseline calibration procedure did noticeably better in predicting the low stress creep response, but its still over-predicted the creep compliance in the high stress creep response.

2. The non-linear creep response. The model substantially over predicts the creep compliance for all large stresses and holding times, generally by a factor of two. Note, the compression-focused calibration under-predicted the linear creep compliance, but still over-predicted the non-linear creep compliance.

3. Predictions of enthalpy recovery after isothermal aging, measured by a DSC experiment. It is not clear if this problem is related to the shift factor sub-Tg equilibration behavior or whether we used sufficiently discerning data during the DSC-focused calibration procedure to define $f_4(t)$.

7.2. SPEC Prediction Gaps and Future Work

The most important gaps identified during the milestone are,

1. The sub-Tg equilibration model form and implementation requires more work before we can conclude if it fills the gap in model predictions of equilibrated sub-Tg behavior. Note that if the sub-Tg issues are resolved, then the model parameterizations and predictions must be re-done. This may also improve predictions of the yield stress evolution after stress-free aging for temperatures around 10 °C–15 °C below Tg.

2. Implement $f_4(t)$ as the relaxation function used in the thermal history hereditary integral in the material clock (see Item 6 in Section 7.1.1). The following implications of this change should be investigated.

   - This change would necessitate a rearrangement of the calibration procedure, since $f_4(t)$ would affect all viscoelastic behaviors. A new "baseline" calibration approach might use the following process (1) Calibrate the WLF parameters, $f_2(t)$, and the shear moduli from the shear master curve. (2) Calibrate $f_4(t)$ and the heat capacity from the heat capacity measured by a DSC. (3) Calibrate $f_3(t)$ and the CTEs from the thermal strain measured by a TMA. (4) Calibrate C_4 from glassy compression. Methods to fit the bulk moduli, C_3, and $f_1(t)$ still need to be inserted into this process depending on the availability of data.

   - With $f_3(t)$ in the thermal hereditary integral of the material clock, it was found that $f_1(t)$ was of secondary importance to $f_3(t)$ when fitting the temperature dependence of yield in glassy compression (Section 4.1.6). With $f_4(t)$ in the thermal hereditary integral, it is expected to be dominant over $f_1(t)$ or $f_3(t)$ for predicting the yield stress in glassy compression, but all three relaxation functions will play different roles in the behavior. This rich interaction between all three relaxation functions should be investigated in the context of glassy compression.

   - With $f_3(t)$ in the thermal hereditary integral of the material clock, it was found that $f_4(t)$ was of secondary importance to $f_3(t)$ when fitting the heat capacity during a stress-free temperature sweep (Section 5.1.6). With $f_4(t)$ in the thermal hereditary integral, it is expected to be dominant over $f_1(t)$ and $f_3(t)$ for predicting the heat capacity, but all three relaxation functions will play different roles in the behavior. This rich interaction between all three relaxation functions should be investigated in the context of heat capacity predictions.

   - It is expected that this change will make $f_4(t)$ dominant over $f_3(t)$ for predictions of the thermal strain measured during a stress-free temperature sweep. The implications of this change should be investigated.

3. The DSC aging predictions are highly sensitive to model parameters, and we are not confident we can accurately predict DSC aging through calibrations that use DSC cool-reheat tests at different cooling rates. In particular, parametric studies show that the width of $f_3(t)$ (i.e. β_3) strongly affects the DSC isothermal aging predictions and must be more accurately determined in the calibration process, see Fig. 5-13. We should either

consider calibrating directly to the isothermally aged DSC data or improve the optimization problem to focus more carefully on the glass transition.

4. The best calibration procedure and parameter studies found that when the bulk charateristic time is greater than the shear characteristic time, $\tau_1 > \tau_2$, then the yield stress evolution with aging time is higher and closer to the experimentally measured rate. However, the literature suggests that $\tau_1 < \tau_2$ [20]. The un-physical relationship should be resolved by exploring parameter spaces where $\tau_1 < \tau_2$ that also produce good predictions of physical aging. If this parameter space cannot produce good physical aging predictions, this may indicate a model form error.

Secondarily, other known gaps of lesser or unknown importance to physical aging predictions are,

1. The Helmholtz Free Energy produces non-intuitive heat capacity behavior, and new model forms should be considered that do not produce a dependence of the heat capacity on absolute temperature. Additionally, a term-by-term analysis of the constant-pressure heat capacity should be conducted to understand why the temperature sensitivites of the bulk moduli (K_g', K_∞') have such a strong influence. If the Helmholtz free energy is not reformulated, a reduced parameter space (e.g. $K_g' = K_\infty' = 0$) should be considered to avoid the unintuitive and non-physical behaviors that are currently produced.
2. C_3 and the bulk moduli were borrowed parameters from prior work. Inverse modeling to identify C_3 was not selective, see Appendix B. Refinements to the optimization problem or more data for the tensile yield stress may enable selective inverse modeling of C_3. Additional data would be especially helpful if the tension–compression asymmetry could be spread out by testing at lower temperatures. Direct measurements of C_3 would be useful to validate and guide the inverse identification of C_3.
3. While $f_1(t)$ played a minimal role in the calibration process and parametric studies on its influence on yield strength evolution suggested its importance was small, the role of $f_1(t)$ on other physical aging behaviors has not been studied. Specifically, $f_1(t)$ and C_3 could be analyzed parametrically to understand their influence on creep behavior. Direct measurements of $f_1(t)$ would also be helpful.
4. To improve linear creep predictions, a calibration procedure that utilizes a linear creep mastercurve to define $f_1(t)$ should be explored.
5. Previous work could be leveraged to improve predictions of non-linear creep, see Ref. [22].
6. In general, the strain-rate dependence of the yield stress in glassy compression is not well understood.
7. Boundary value problems that incorporate the full specimen geometry, heat transfer, self-heating, and large-strain hardening may be necessary to further assess the quality of stress–strain fitting and predictions.

7.3. Milestone Criteria Completed

The completion summary for the five milestone criteria is provided in Table 7-1.

Table 7-1. Milestone Completion Criteria Evidence Summary

Criterion	Report Location	Summary
Model Development	Section 2.4	Theory was developed and implemented.
Calibration	Sections 4.1–4.3 and Sections 5.1–5.3	We found the DSC-focused calibration procedure produced the most reasonable predictions for both materials simultaneously.
Physical Aging Prediction	Section 4.4 and Section 5.4	Predictions of aging included stress-free aging followed by compression through yield, creep, aging-under-load followed by compression through yield, volume relaxation, heat capacity response after cooling into the glass at different rates, and heat capacity response after isothermal aging
Uncertainty Analysis	Section 5.1.6 and Chapter 6	A parameter study on stress-free aging followed by compression through yield revealed important relationships between relaxation functions that are necessary for SPEC to predict yield stress evolution. The relationships uncovered by the parameter studies emerged naturally from the DSC-focused calibration.
SAND Report		This document completes this criterion

REFERENCES

[1] Brian M. Adams, William J. Bohnhoff, Keith R. Dalbey, Mohamed S. Ebeida, John P. Eddy, Michael S. Eldred, Russell W. Hooper, Patricia D. Hough, Kenneth T. Hu, John D. Jakeman, Mohammad Khalil, Kathryn A. Maupin, Jason A. Monschke, Elliott M. Ridgway, Ahmad A. Rushdi, D. Thomas Seidl, J. Adam Stephens, Laura P. Swiler, , and Justin G. Winokur. Dakota, a multilevel parallel object-oriented framework for design optimization, parameter estimation, uncertainty quantification, and sensitivity analysis: Version 6.14 user's manual. SAND 5822, Sandia National Laboratories, 2021.

[2] D. Adolf, S. Spangler, K. Austin, M. Neidigk, M. K. Neilsen, and R. S. Chambers. Packaging strategies for printed circuit board components volume i materials and thermal stresses. *SANDIA REPORT Unlimited Release*, SAND4751:1–114, 2011.

[3] D. B. Adolf, R. S. Chambers, and J. M. Caruthers. Extensive validation of a thermodynamically consistent, nonlinear viscoelastic model for glassy polymers. *Polymer*, 45(13):4599–4621, 2004.

[4] D. B. Adolf, R. S. Chambers, and M. A. Neidigk. A simplified potential energy clock model for glassy polymers. *Polymer*, 50(17):4257–4269, 2009.

[5] D. B. Adolf, M. E. Stavig, S. Kawaguchi, and R. S. Chambers. Time-dependence of epoxy debonding. *Journal of Adhesion*, 83(1-3):85–104, 2007.

[6] J. M. Caruthers, D. B. Adolf, R. S. Chambers, and P. Shrikhande. A thermodynamically consistent, nonlinear viscoelastic approach for modeling glassy polymers. *Polymer*, 45(13), 2004. Times Cited: 58.

[7] J. M. Caruthers, D. B. Adolf, R. S. Chambers, and P. Shrikhande. A thermodynamically consistent, nonlinear viscoelastic approach for modeling glassy polymers. *Polymer*, 45(13):4577–4597, 2004.

[8] Robert S. Chambers, Rajan Tandon, and Mark E. Stavig. Characterization and calibration of a viscoelastic simplified potential energy clock model for inorganic glasses. *Journal of Non-Crystalline Solids*, 432, Part B:545 – 555, 2016.

[9] Caitlyn M. Clarkson, John D. McCoy, and Jamie M. Kropka. Enthalpy recovery and its relation to shear response in an amine cured {DGEBA} epoxy. *Polymer*, 94:19 – 30, 2016.

[10] B. D. Coleman and W. Noll. Foundations of linear viscoelasticity. *Reviews of Modern Physics*, 33(2), 1961. Times Cited: 498.

[11] Jr. E. D. Reedy, R. S. Chambers, L. G. Hughes, J. M. Kropka, M. E. Stavig, and M. J. Stevens. A process and environment aware sierra/solidmechanics cohesive zone modeling capability for polymer/solid interfaces. SAND 8066, Sandia National Laboratories, 2015.

[12] Yael S. Elmatad, David Chandler, and Juan P. Garrahan. Corresponding states of structural glass formers. *The Journal of Physical Chemistry B*, 113(16):5563–5567, 2009.

[13] John D Ferry. *Viscoelastic properties of polymers*. John Wiley and Sons Ltd. Sons, 1980.

[14] G.A. Holzapfel. *Nonlinear Solid Mechanics*. John Wiley and Sons Ltd., The Atrium, Southern Gate, Chichester, West Sussex PO19 8SQ, England, 2000.

[15] Jamie M. Kropka, Douglas B. Adolf, Scott Spangler, Kevin Austin, and Robert S. Chambers. Mechanisms of degradation in adhesive joint strength: Glassy polymer thermoset bond in a humid environment. *International Journal of Adhesion and Adhesives*, 63:14 – 25, 2015.

[16] Jamie M. Kropka and Kevin N. Long. Predicting the counter-intuitive stress relaxation behavior of glass forming materials. *Polymer*, 145:54 – 61, 2018.

[17] John D. McCoy, Windy B. Ancipink, Caitlyn M. Clarkson, Jamie M. Kropka, Mathias C. Celina, Nicholas H. Giron, Lebelo Hailesilassie, and Narjes Fredj. Cure mechanisms of diglycidyl ether of bisphenol a (dgeba) epoxy with diethanolamine. *Polymer*, 105:243 – 254, 2016. Structure and Dynamics of Polymers studied by X-ray, Neutron and Muon Techniques.

[18] Gregory B. McKenna. *Physical Aging in Glasses and Composites*, chapter 7, pages 237–309. Springer US, Boston, MA, 2012.

[19] A.D. Mulliken and M.C. Boyce. Mechanics of the rate-dependent elastic–plastic deformation of glassy polymers from low to high strain rates. *International Journal of Solids and Structures*, 43:1331–1356, 2006.

[20] Connie B. Roth, editor. *Polymer Glasses*. Number 978-1498711876. CRC Press, 1 edition, December 2016.

[21] William Scherzinger and Brian Lester. Library of advanced materials for engineering (lame) 4.56. UUR SAND2020-3408, Sandia National Laboratories, March 2020.

[22] Alyssa Skulborstad, Jamie M. Kropka, and Kevin N. Long. Age under load validation efforts for the physical aging of 828 dea. Memo, Sandia National Laboratories, 2020.

[23] I.S. Sokolnikoff. *Mathematical Theory of Elasticity*. McGraw-Hill, 2nd edition, 1956.

[24] Brandon Talamini and Kenneth N. Cundiff. Extension of SPECTACULAR constitutive model for full thermomechanical coupling. Sand2021-9851 ctf, Sandia National Laboratories, 2021.

[25] SIERRA Solid Mechanics Team. *Sierra/SolidMechanics 4.48 User's Guide*. Computational Solid Mechanics and Structural Dynamics Department Engineering Sciences Center Sandia National Laboratories, Box 5800 Albuquerque, NM 87185-0380, 4.48 (sand202018-2961) edition, March 2018.

[26] Craig M. Tenney, Kevin N. Long, and Jamie M. Kropka. Predictions of yield strength evolution due to physical aging of 828 dgeba/dea using the simplified potential energy clock model. Sand2019-2248 r (uur), Sandia National Laboratories, February 2019.

[27] Kelsey M Wilson. Physical aging in a polyether-amine cured dgeba epoxy. Master's thesis, New Mexico Institute of Mining and Technology, Socorro, New Mexico, August 2018.

APPENDIX A. Legacy SPEC Parameterizations

When benchmarking the new calibrations to physical aging data in Sections 4.4 and 5.4, simulations using legacy calibrations are also included for comparison. The parameters used for the legacy calibrations are listed in this appendix. Table A-1 shows the legacy parameterization used for 828DGEBA/T403, which is taken from [11] and Table A-2 shows the legacy parameterization used for 828DGEBA/DEA, which is taken from [4], Table 3.

Table A-1. Legacy SPEC parameters for 828DGEBA/T403 [11].

Parameter	Value	Units
K_g^{ref}	4.9	GPa
K_g'	−12	MPa/K
K_∞^{ref}	3.5	GPa
K_∞'	−12	MPa/K
G_g^{ref}	0.75	GPa
G_g'	−2.7	MPa/K
G_∞^{ref}	9.0	MPa
G_∞'	0	kPa/K
α_g^{ref}	265	10^{-6}/K
α_g'	0.6	10^{-6}/K^2
$\alpha_\infty^{\mathrm{ref}}$	500	10^{-6}/K
α_∞'	0.9	10^{-6}/K^2
θ_{ref}	90	°C
$\hat{C}_1$	16.5	–
$\hat{C}_2$	54.5	K
C_3	900	K
C_4	30000	K
τ_1	0.001	s
β_1	0.20	–
τ_2	0.1	s
β_2	0.25	–
τ_3	0.001	s
β_3	0.20	–

Table A-2. Legacy SPEC parameters for 828DGEBA/DEA [4], Table 3.

Parameter	Value	Units
K_g^{ref}	4.9	GPa
K_g'	-12	MPa/K
K_∞^{ref}	3.2	GPa
K_∞'	-12	MPa/K
G_g^{ref}	0.9	GPa
G_g'	-4.2	MPa/K
G_∞^{ref}	4.5	MPa
G_∞'	0	kPa/K
α_g^{ref}	170	10^{-6}/K
α_g'	0.2	10^{-6}/K^2
$\alpha_\infty^{\mathrm{ref}}$	600	10^{-6}/K
α_∞'	0.4	10^{-6}/K^2
θ_{ref}	75	°C
$\hat{C}_1$	16.5	–
$\hat{C}_2$	54.5	K
C_3	1000	K
C_4	11800	K
τ_1	6.0	s
β_1	0.14	–
τ_2	0.12	s
β_2	0.22	–
τ_3	6.0	s
β_3	0.14	–

APPENDIX B. Calibrating C_3 from the Tension–Compression Asymmetry of the Yield Stress

B.1. Motivation and Summary

The parameter C_3 controls the effect of the volume strain on the material clock. Historically, it has been calibrated by measuring the glass transition temperature as a function of pressure and volume [4], but such tests are difficult to conduct. In searching for other methods for calibrating C_3, it was hypothesized that it could be calibrated from the asymmetry of the yield stress in tension and compression. In compression, the volume strain is negative, so C_3 increases the shift factor, therefore yield is shifted to a higher stress. In tension, the volume strain is positive, so C_3 decreases the shift factor, therefore yield is shifted to a lower stress.

This method of calibrating C_3 was attempted for 828DGEBA/DEA, since data in both tension and compression were available. The calibration of C_3 was intended to replace the glassy compression calibration step in the baseline calibration for 828DGEBA/DEA, see Section 5.1.4. Unfortunately, this method produced C_3 values much smaller than expected, and so was not included in the main calibration. The thermomechanical history used to simulate yield in already described in Section 5.1.4, and is not repeated here. Two attempts to calibrate C_3 were attempted. In the first, both C_3 and C_4 were optimized to fit all 8 compression loading conditions and a single tension loading condition. In the second, C_3 and C_4 were optimized to fit one pair of tension and compression loading conditions.

B.2. Calibrating C_3 and C_4 Using the Full Uniaxial Loading Test Matrix

In the first calibration attempt, eight different compression loading conditions and one tensile loading conditions were considered in the construction of the objective function. The parameters C_3 and C_4 were first optimized using the `soga` genetic algorithm in Dakota, and then the parameter were refined using the `conmin_frcg` method in Dakota, a gradient-based optimization method. All compression experiments were weighted equally in the objective function, but the tensile loading condition was given a weight of 8 so that the total number of tesnile and compressive yield stresses had similar weights. The yield stress for each objective function was calculated as the relative error of the yield stress, calculated as the maximum nominal stress below 0.15 strain. Regressions of the yield stress from all experimental realizations, see Fig. 3-5, served as the reference values when calculating the relative errors. The fits produced from this procedure are shown in Figs. B-1 and B-2. The fit found $C_3 = 0$ and $C_4 = 8300\,\mathrm{K}$. This C_3 is much lower than previously found values, which are around $1000\,\mathrm{K}$ [4].

(a) Temperature Effect

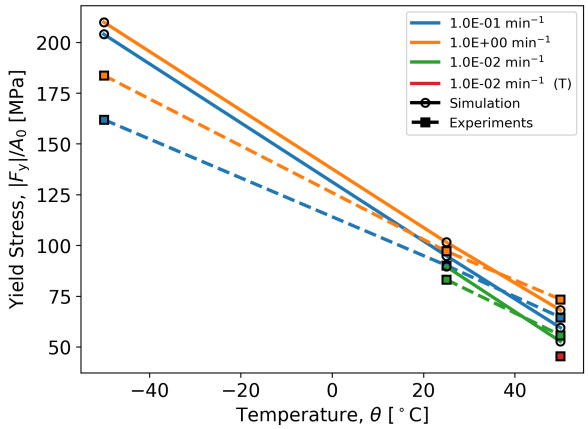

(b) Strain Rate Effect

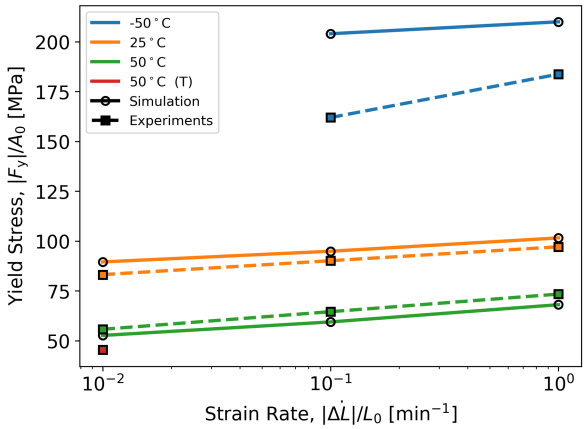

Figure B-1. Optimized yield stress response from the baseline calibration approach for 828DGEBA/DEA. (a) Yield stress versus temperature for constant strain rates, (b) Yield stress versus strain rate for constant temperatures. In the legend, "(T)" denotes tensile experiments. All other experiments are compressive. The optimized parameters included C_3 and C_4. For this optimization, all depicted loading conditions were included in the objective function. Experimental data from Fig. 3-5.

B.3. Calibrating C_3 and C_4 Using One Tension and One Compression Loading Condition

In the second calibration attempt, a single tension–compression pair was considered, that is a compressive loading condition and a tensile loading condition that use the same temperature and strain rate. Each test in the pair received the same weight in the objective function. Otherwise, all details from the Section B.2 are repeated here. The fits produced from this procedure are shown in Figs. B-3 and B-4. The fit found $C_3 = 360\,\mathrm{K}$ and $C_4 = 8300\,\mathrm{K}$. This C_3 is much lower than previously found values, which are around 1000 K [4].

B.4. Conclusion

Both attempts to fit C_3 and C_4 using the tension–compression asymmetry of yield produced values of C_3 that are much lower than what is expected based on past measurements. This indicates that tension–compression asymmetry is not discerning enough for calibrating C_3. This is partially due to the fact that some portion of the tension–compression asymmetry of the nominal yield stress is due to geometric effects. Furthermore, the specific value found C_3 using this method is very sensitive to how the objective function is formulated.

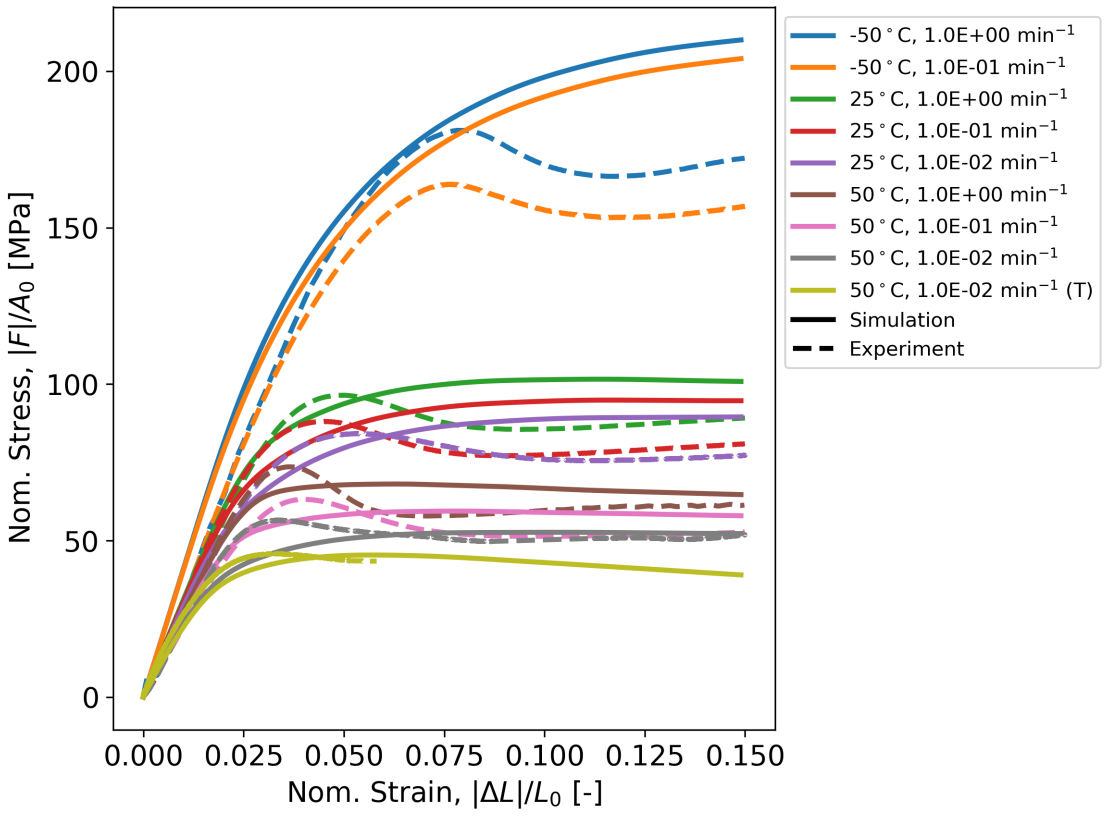

Figure B-2. Simulated and experimental stress–strain curves after fitting C_3 and C_4 to the full uniaxial loading test matrix. The simulated response was produced by the baseline calibration approach for 828DGEBA/DEA. In the legend, "(T)" denotes tensile experiments. All other experiments are compressive. Experimental data from Fig. 3-4.

(a) Temperature Effect

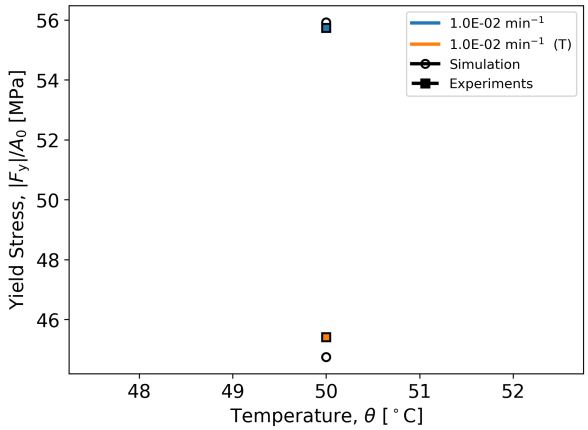

(b) Strain Rate Effect

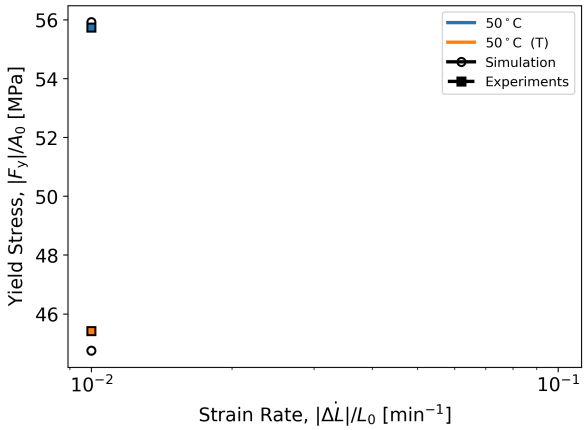

Figure B-3. Optimized yield stress response from the baseline calibration approach for 828DGEBA/DEA. (a) Yield stress versus temperature for constant strain rates, (b) Yield stress versus strain rate for constant temperatures. In the legend, "(T)" denotes tensile experiments. All other experiments are compressive. The optimized parameters included C_3 and C_4. For this optimization, a tension–compression pair is considered in the objective function. Experimental data from Fig. 3-5.

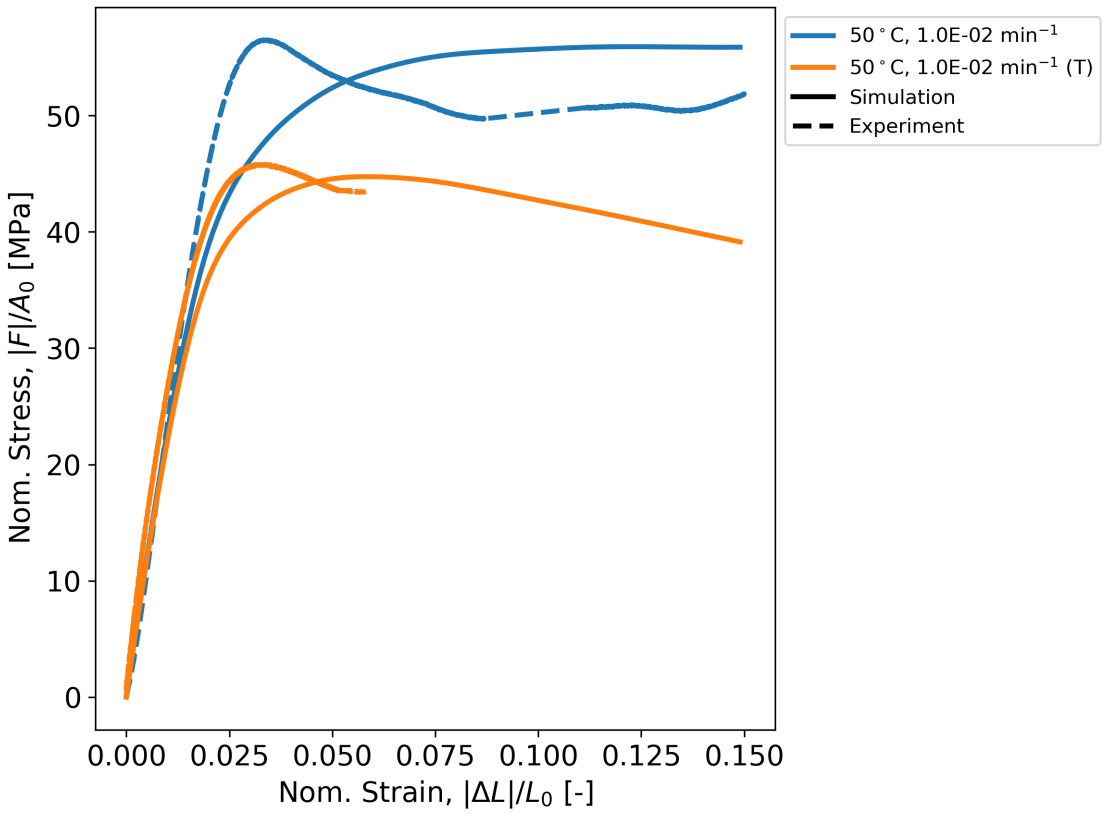

Figure B-4. Simulated and experimental stress–strain curves after fitting C_3 and C_4 to a single tension–compression condition pair. The simulated response was produced by the baseline calibration approach for 828DGEBA/DEA. In the legend, "(T)" denotes tensile experiments. All other experiments are compressive. Experimental data from Fig. 3-4.

DISTRIBUTION

Email—External [redacted]

Name	Company Email Address	Company Name
John D. McCoy	john.mccoy@nmt.edu	New Mexico Tech.

Email—Internal [redacted]

Name	Org.	Sandia Email Address
Alyssa Skulborstad	8752	ajskulb@sandia.gov
Brandon Talamini	8363	btalami@sandia.gov
Brian Lester	1558	btleste@sandia.gov
Brenton Elisberg	1556	belisbe@sandia.gov
Catherine Groves	1853	bsong@sandia.gov
Christine Northrop	10615	csalaz@sandia.gov
Coby Davis	1854	cldavis@sandia.gov
H. Eliot Fang	1558	hefang@sandia.gov
Jeffrey Payne	1510	jlpayne@sandia.gov
Jason Dugger	2585	jwdugge@sandia.gov
Jamie Kropka	1853	jmkropk@sandia.gov
Kelsey Wilson	2491	kelwils@sandia.gov
Mike Neilsen	1558	mkneils@sandia.gov
Nicholas Wyatt	1852	nbwyatt@sandia.gov
Shianne Carrol	1853	shicarr@sandia.gov
Stacy Nelson	8752	smnelso@sandia.gov
Technical Library	1911	sanddocs@sandia.gov

Sandia National Laboratories

Sandia National Laboratories is a multimission laboratory managed and operated by National Technology & Engineering Solutions of Sandia LLC, a wholly owned subsidiary of Honeywell International Inc., for the U.S. Department of Energy's National Nuclear Security Administration under contract DE-NA0003525.